

# Over-the-air characterization of millimeter-wave integrated antenna systems

**Citation for published version (APA):**

van den Biggelaar, A. J. (2020). *Over-the-air characterization of millimeter-wave integrated antenna systems*. [Phd Thesis 1 (Research TU/e / Graduation TU/e), Electrical Engineering]. Technische Universiteit Eindhoven.

**Document status and date:**

Published: 11/11/2020

**Document Version:**

Publisher's PDF, also known as Version of Record (includes final page, issue and volume numbers)

**Please check the document version of this publication:**

- A submitted manuscript is the version of the article upon submission and before peer-review. There can be important differences between the submitted version and the official published version of record. People interested in the research are advised to contact the author for the final version of the publication, or visit the DOI to the publisher's website.
- The final author version and the galley proof are versions of the publication after peer review.
- The final published version features the final layout of the paper including the volume, issue and page numbers.

[Link to publication](#)

**General rights**

Copyright and moral rights for the publications made accessible in the public portal are retained by the authors and/or other copyright owners and it is a condition of accessing publications that users recognise and abide by the legal requirements associated with these rights.

- Users may download and print one copy of any publication from the public portal for the purpose of private study or research.
- You may not further distribute the material or use it for any profit-making activity or commercial gain
- You may freely distribute the URL identifying the publication in the public portal.

If the publication is distributed under the terms of Article 25fa of the Dutch Copyright Act, indicated by the "Taverne" license above, please follow below link for the End User Agreement:

[www.tue.nl/taverne](http://www.tue.nl/taverne)

**Take down policy**

If you believe that this document breaches copyright please contact us at:

[openaccess@tue.nl](mailto:openaccess@tue.nl)

providing details and we will investigate your claim.



Over-the-Air Characterization of Millimeter-Wave Integrated Antenna Systems

A. J. van den Biggelaar

# Over-the-Air Characterization of Millimeter-Wave Integrated Antenna Systems

A. J. van den Biggelaar

# **Over-the-Air Characterization of Millimeter-Wave Integrated Antenna Systems**

PROEFSCHRIFT

ter verkrijging van de graad van doctor aan de  
Technische Universiteit Eindhoven, op gezag van de  
rector magnificus, prof.dr.ir. F. P. T. Baaijens, voor een  
commissie aangewezen door het College voor  
Promoties in het openbaar te verdedigen op  
woensdag 11 november 2020 om 16.00 uur

door

Antonius Johannes van den Biggelaar

geboren te Gemert

Dit proefschrift is goedgekeurd door de promotoren en de samenstelling van de promotiecommissie is als volgt:

voorzitter: prof.dr.ir. M. J. Bantum  
promotor: prof.dr.ir. A. B. Smolders  
copromotor: dr. U. Johannsen  
leden: prof.dr.ir. P. G. M. Baltus  
prof.dr.ir. F. E. van Vliet (Universiteit Twente & TNO)  
prof.dr.ir. H. Rogier (Universiteit Gent)  
dr. D. F. Williams (NIST)  
adviseur: ir. M. Geurts (NXP Semiconductors)

*Het onderzoek of ontwerp dat in dit proefschrift wordt beschreven is uitgevoerd in overeenstemming met de TU/e Gedragscode Wetenschapsbeoefening.*

Over-the-Air Characterization of Millimeter-Wave Integrated Antenna Systems  
A. J. van den Biggelaar  
Technische Universiteit Eindhoven, 2020

A catalogue record is available from the Eindhoven University of Technology Library  
ISBN: 978-90-386-5125-5  
NUR: 959

This thesis was prepared with the  $\text{\LaTeX} 2_{\epsilon}$  documentation system  
Reproduction: Gildeprint, Enschede, the Netherlands  
Cover photo: Bart van Overbeeke Fotografie, Eindhoven, the Netherlands

Copyright ©2020 by A. J. van den Biggelaar, all rights reserved



# Contents

---

<b>Summary</b>	<b>ix</b>
<b>List of Abbreviations</b>	<b>xi</b>
<b>1 Introduction</b>	<b>1</b>
1.1 Societal relevance of mobile cellular communication . . . . .	1
1.2 5G mm-wave cellular network . . . . .	3
1.3 Outline of the thesis . . . . .	4
1.4 Original contributions of the thesis . . . . .	6
<b>2 Effect of Random Errors in the Element Excitations on the Array Pattern</b>	<b>9</b>
2.1 Introduction . . . . .	9
2.2 The array amplitude pattern including excitation errors . . . . .	10
2.3 Statistical quantities of the array amplitude pattern . . . . .	11
2.3.1 Mean value . . . . .	12
2.3.2 Variance . . . . .	12
2.3.3 Correlation . . . . .	12
2.4 Magnitude of the array amplitude pattern . . . . .	14
2.4.1 Rician distribution . . . . .	14
2.4.2 Beckmann distribution . . . . .	15
2.5 Simulation results . . . . .	16
2.6 Physical interpretation of the acquired results . . . . .	20
2.6.1 Variance . . . . .	20
2.6.2 Correlation . . . . .	21
2.6.3 Effect on magnitude . . . . .	24
2.6.4 Effect of scanning . . . . .	27
2.7 Conclusion . . . . .	27
<b>3 5G Millimeter-Wave Phased Array Design, Characterization &amp; Calibration</b>	<b>29</b>
3.1 Introduction . . . . .	29

3.2	Active phased array design . . . . .	30
3.2.1	Design specifications . . . . .	30
3.2.2	PCB stack-up . . . . .	31
3.2.3	PCB layout . . . . .	33
3.2.4	Analog beamformer ICs . . . . .	33
3.2.5	Wilkinson versus T-junction . . . . .	34
3.2.6	Beamformer network implementation . . . . .	35
3.2.7	Patch antenna elements . . . . .	38
3.2.8	Assessment on stability . . . . .	40
3.2.9	Heat sink assembly . . . . .	40
3.3	Characterization of the active phased array . . . . .	42
3.3.1	Reflection coefficient measurement . . . . .	44
3.3.2	Performance analysis of the beamforming network . . . . .	44
3.3.3	Normalized ABF IC response . . . . .	46
3.3.4	Load pull effects on the ABF IC response . . . . .	48
3.3.5	Embedded element patterns . . . . .	48
3.4	Calibration of the active phased array . . . . .	50
3.4.1	Shaping the array radiation pattern . . . . .	51
3.4.2	Phase calibration and EIRP . . . . .	53
3.4.3	Online calibration . . . . .	54
3.5	Conclusion . . . . .	59
<b>4</b>	<b>Accurate Gain Measurement Technique for Limited Antenna Separations</b>	<b>61</b>
4.1	Introduction . . . . .	61
4.2	Phase and amplitude center . . . . .	62
4.3	Antenna gain measurement technique . . . . .	63
4.4	Measurement results . . . . .	66
4.4.1	Relative-distance sweep: OEWG and SGH . . . . .	66
4.4.2	Isotropic radiator model . . . . .	67
4.4.3	Relative-distance sweep: SGH and SGH . . . . .	69
4.4.4	Determining the realized gain . . . . .	71
4.5	Evaluation of the gain measurement technique . . . . .	76
4.5.1	Comparison to different choices of reference points . . . . .	76
4.5.2	Comparison phase and amplitude center . . . . .	76
4.5.3	Number of measurements in the distance sweep . . . . .	79
4.5.4	Connection to the extrapolation measurement technique . . . . .	80
4.6	Conclusion . . . . .	82
<b>5</b>	<b>Contactless Characterization of Millimeter-Wave Integrated Antennas</b>	<b>83</b>
5.1	Introduction . . . . .	83
5.2	Contactless characterization method . . . . .	85



5.2.1	Determining the input impedance using the CCM . . . . .	85
5.2.2	Determining the realized gain using the CCM . . . . .	86
5.3	Analysis of the CCM in far-field conditions . . . . .	87
5.3.1	Reflected signal of interest . . . . .	87
5.3.2	Displacement errors . . . . .	89
5.3.3	Load uncertainty . . . . .	89
5.3.4	Impact of noise and drift . . . . .	91
5.3.5	Optimal distance between the RA and AUT . . . . .	92
5.4	Experimental evaluation . . . . .	92
5.4.1	Measurement setup . . . . .	92
5.4.2	Choice of RA and AUT . . . . .	93
5.4.3	Stability of the measurement setup . . . . .	93
5.4.4	Impact of noise . . . . .	94
5.4.5	Distance between the RA and AUT . . . . .	94
5.5	Measurement results . . . . .	94
5.6	Complex radiation pattern measurement . . . . .	95
5.7	Conclusion . . . . .	98
<b>6</b>	<b>Antenna Functionality Testing for High-Volume AoC &amp; AiP Manufacturing</b>	<b>99</b>
6.1	Introduction . . . . .	99
6.2	Analysis of the CCM in near-field conditions . . . . .	101
6.2.1	Setup of the CST model . . . . .	101
6.2.2	Distance between the AUT and RA . . . . .	101
6.2.3	Sensitivity to positioning errors . . . . .	103
6.2.4	Sensitivity to a dynamic setup . . . . .	105
6.2.5	Integrated monopole and dipole antenna . . . . .	105
6.3	Measurement results . . . . .	107
6.4	Conclusion . . . . .	109
<b>7</b>	<b>Modeling of Artificial Magnetic Conductors for AoC Applications</b>	<b>111</b>
7.1	Introduction . . . . .	111
7.2	IC manufacturing process . . . . .	112
7.3	Equivalent circuit models of AMCs . . . . .	113
7.3.1	Modeling of an AMC having a lossless substrate . . . . .	113
7.3.2	Modeling of an AMC having a lossy substrate . . . . .	114
7.4	Bandwidth of AMCs . . . . .	116
7.4.1	Bandwidth of an AMC in the metal stack . . . . .	116
7.4.2	Bandwidth of an AMC utilizing the silicon substrate . . . . .	119
7.5	Minimizing the dielectric losses of an AMC . . . . .	119
7.6	Realization of an AoC including an AMC . . . . .	122
7.7	Angular stable AMC for TM plane wave excitations . . . . .	123

---

7.7.1	Design procedure and simulation results . . . . .	123
7.7.2	Comparison to 2D surface impedance sheets . . . . .	124
7.8	Conclusion . . . . .	127
<b>8</b>	<b>Conclusions and recommendations</b>	<b>129</b>
<b>A</b>	<b>Derivation of Statistical Quantities of the Array Amplitude Pattern</b>	<b>133</b>
A.1	Introduction . . . . .	133
A.2	Mean value . . . . .	134
A.3	Variance . . . . .	134
A.4	Correlation . . . . .	136
<b>B</b>	<b>Derivation of a Beamforming Algorithm for Arbitrary Antenna Arrays</b>	<b>139</b>
B.1	Introduction to the algorithm . . . . .	139
B.2	Steering the main lobe and minimizing radiation . . . . .	140
B.3	Solving the real counterpart . . . . .	141
B.4	Suppressing the side lobes . . . . .	142
<b>C</b>	<b>Derivation of the Bandwidth of a Lossless Artificial Magnetic Conductor</b>	<b>145</b>
	<b>List of Publications</b>	<b>149</b>
	<b>Bibliography</b>	<b>153</b>
	<b>Acknowledgments</b>	<b>163</b>
	<b>Curriculum Vitae</b>	<b>165</b>

# Summary

---

The society as we know it today relies heavily on wireless communication. To prevent congestion in our current cellular infrastructure, hence, to maintain the quality of service that users are experiencing at present, the 4G cellular network has to be upgraded. This results in the current development of the fifth generation mobile communications, or in short 5G. To accommodate a higher data rate, the so-called 5G mm-wave frequency band will be utilized. The increased path loss and attenuation associated with the exploitation of mm-waves demands new antenna concepts for 5G mm-wave base stations. One promising concept for a new 5G mm-wave base station antenna system is a phased array. The main goal of this thesis is to address challenges with respect to the design and characterization of these new phased array systems operating at mm-waves. The challenges addressed in this thesis are summarized below.

Phased array systems consist by definition of multiple individual radiating antenna elements. By controlling the excitation of each element, array radiation patterns having desired radiation characteristics can be obtained. Due to errors in the phase and amplitude of the element excitations, however, the array pattern gets distorted. To statistically model the magnitude of the array pattern, the use of a Beckmann distribution is suggested as a replacement of the conventionally used Rician distribution. The proposed model can be used by engineers or regulatory agencies to define specifications on tolerable excitation errors by the electronics to ensure compliance with future 5G protocols, based on desired radiation characteristics such as a certain side lobe level or null depth.

To understand the design and characterization challenges associated with 5G mm-wave phased array systems, a 28 GHz 8-by-8 dual-polarized analog active phased array is realized. The array is the university's first prototype of a 5G mm-wave active phased array and is developed as testbed to experiment with over-the-air (OTA) characterization and phased array calibration methods. Using these techniques, it is demonstrated that the performance of individual components can be deduced and that array radiation patterns can be synthesized. The OTA characterization techniques also revealed that some components of the phased array can be improved. These results can serve as input for new phased array designs and, in turn, improve future realizations of 5G mm-wave base station antenna systems.

The limited size of typical 5G mm-wave arrays allows for antenna measurement ranges

that are small in size while still fulfilling far-field conditions. To determine the gain of an antenna accurately for antenna separations in the order of one to two times the Fraunhofer distance, a good estimate of the distance between the antennas is required. To acquire a good estimate, a novel antenna gain measurement method based on a relative-distance sweep is presented, allowing for an accurate gain determination. Moreover, this sweep can be used to determine whether or not the non-uniform phase distribution over the aperture of the receiver is significant. This, in turn, allows for accurate far-field measurements at minimum antenna separations.

The short wavelength associated with the 5G mm-wave frequency band results in individual antenna elements having a size in the order of a typical integrated circuit (IC). This miniaturization opens up the possibility to create an antenna-on-chip (AoC) or antenna-in-package (AiP), potentially reducing manufacturing costs and decreasing losses. The characterization of these integrated antennas is challenging as they usually do not provide a suitable direct interface for the measurement equipment. To measure typical antenna parameters of an integrated antenna, such as the input impedance or the antenna gain, a contactless measurement method (CCM) can be used as this method does not require a cable or probe to be connected to the device. The CCM has been experimentally verified at 5G mm-wave frequencies, enabling the characterization of future 5G mm-wave integrated antennas that can serve as individual radiating elements in a phased array antenna system.

Designing the antenna on-chip makes direct matching to on-chip amplifiers possible, allowing us to leave the standard  $50\ \Omega$  interface impedance. The IC manufacturing process is highly optimized to maximize the performance of the electronics, but is typically not well suited for antennas. Artificial magnetic conductors (AMCs) can be used to reduce dielectric losses caused by the silicon substrate, and to tune the antenna at the same time. The utilization of AMCs for AoC applications is investigated and modeling techniques are presented, with the aim of stimulating future research to enable the production of low-loss AoCs using AMCs.

# List of Abbreviations

---

3GPP	3 <sup>rd</sup> Generation Partnership Project
4G	4 <sup>th</sup> generation mobile communications
5G	5 <sup>th</sup> generation mobile communications
ABF	Analog beamformer
ADS	Keysight Advanced Design System
AiP	Antenna-in-Package
AMC	Artificial magnetic conductor
AoC	Antenna-on-Chip
AUT	Antenna-under-test
BER	Bit error rate
(Bi-)CMOS	(Bipolar) complementary metal-oxide-semiconductor
BFN	Beamformer network
BW	Bandwidth
CCM	Contactless characterization method
CDF	Cumulative distribution function
CLT	Central limit theorem
CPU	Central processing unit
CST	CST Microwave Studio
EBG	Electromagnetic bandgap
EEP	Embedded element pattern
EIRP	Equivalent isotropic radiated power
EM	Electromagnetics
EVM	Error vector magnitude
FR	Frequency range
FSPL	Free-space path loss
GSG	Ground-signal-ground
HPBW	Half-power beamwidth
IC	Integrated circuit
IFBW	Intermediate frequency bandwidth
IoT	Internet-of-Things
LNA	Low-noise amplifier
MIMO	Multiple-input-multiple-output
mm-wave	Millimeter-wave
MR	Measurement range

NIST	National Institute of Standards and Technology
OEWG	Open-ended waveguide
OTA	Over-the-air
P1dB	1-dB compression point
PA	Power amplifier
PCB	Printed circuit board
PDF	Probability density function
PEC	Perfect electric conductor
PMC	Perfect magnetic conductor
RA	Reference antenna
RCS	Radar-cross-section
RF	Radio frequency
RMS	Root mean square
RP	Reference plane
RSI	Reflected signal of interest
Rx	Receive
SGH	Standard gain horn
SIW	Substrate integrated waveguide
SLL	Side lobe level
SOL	Short-open-load
SOLT	Short-open-load-thru
TDD	Time division duplex
TE	Transverse electric
TIM	Thermal interface material
TL	Transmission line
TM	Transverse magnetic
TU/e	Eindhoven University of Technology
Tx	Transmit
VM	Vector modulator
VNA	Vector network analyzer

## CHAPTER ONE

# Introduction

---

### 1.1 Societal relevance of mobile cellular communication

Transferring money from a savings to a checking account while in the queue of a grocery store, navigating and avoiding traffic jams based on real-time road conditions, making a telephone call while driving on the highway (hands-free of course), streaming Dutch music on a party, translating some unknown English words on the spot, and sending live footage of amazing landscapes when standing on the top of a mountain to impress family and friends; just a few examples of how I relied on a 4G internet connection during the last month of my stay as guest researcher at NIST in the United States.

Needless to say, the society as we know it today relies heavily on wireless communication. Almost everyone around us has (at least) one mobile phone which is connected to a cellular network. In fact, more mobile phones are currently connected to a cellular network than the amount of people living on this planet [1], [2]. Especially with the rise of the so-called Internet-of-Things (IoT), the number of devices using the cellular network will only increase in the future. It is predicted that in the coming five years, more than four billion additional devices will be connected to a cellular network [2]. This prediction is visualized in Fig. 1.1.

An obvious consequence of connecting more devices to a cellular network is that the overall data traffic grows. Additionally, as the performance of our electronic devices increases, so does the data traffic. For instance, why use only voice in a call with family or friends when a mobile phone allows for high-quality video calls, even in remote mountain areas? Both consequences translate to an exponential growth of data traffic that the cellular network has to accommodate [2], which is depicted in Fig. 1.2. To prevent congestion in our current cellular infrastructure, hence, to maintain the quality of service that users are experiencing at present, the 4G cellular network has to be upgraded. This results in the current development of the fifth generation mobile communications, or in short 5G.

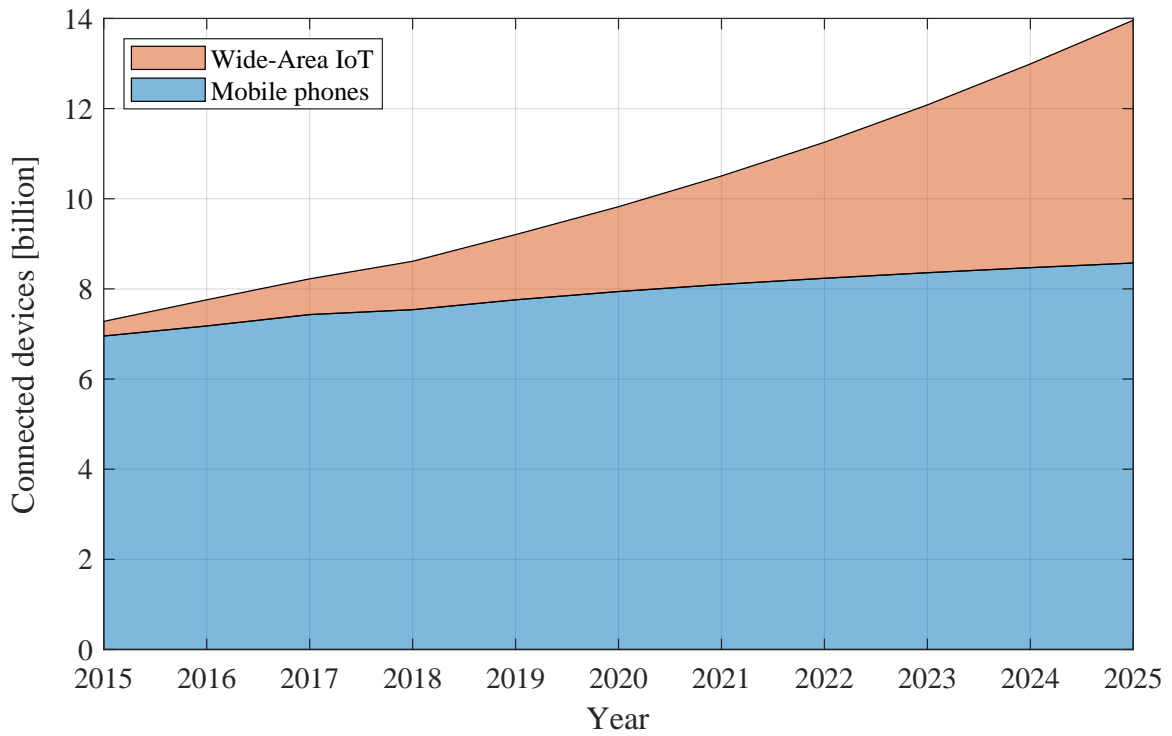


**Figure 1.1:** Amount of devices connected to a cellular network (forecasted beyond 2019). This figure is based on [2].

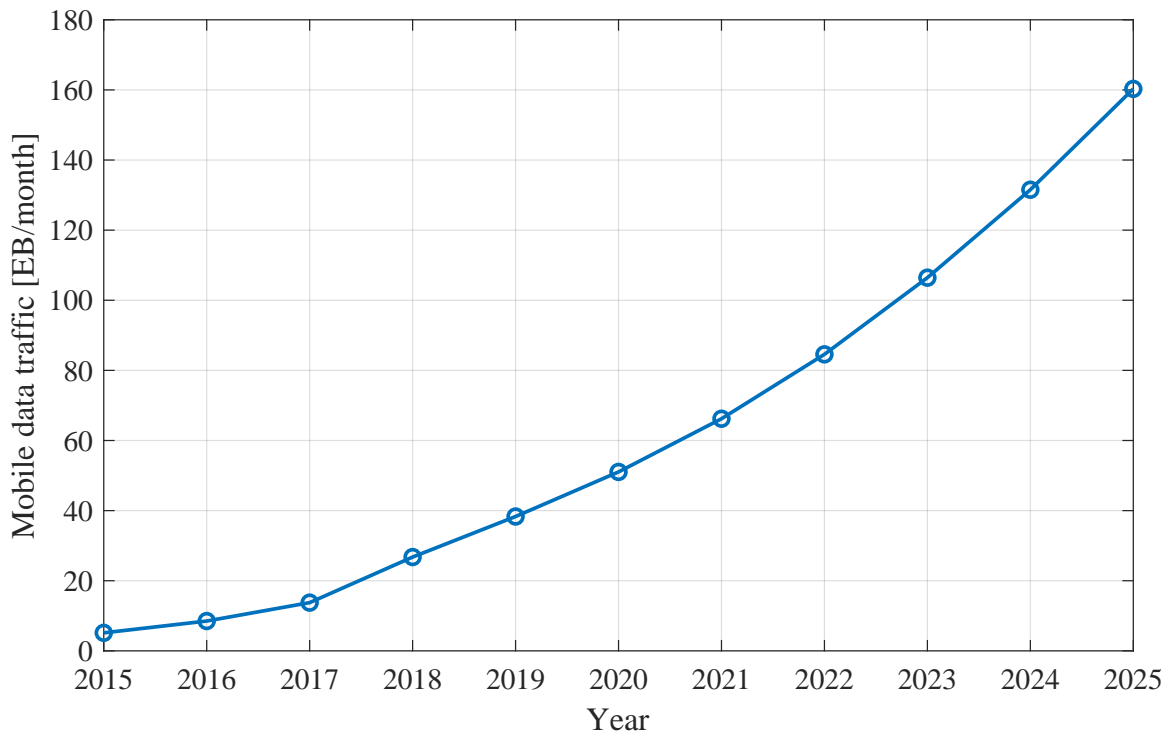


**Figure 1.2:** Global mobile data traffic (forecasted beyond 2019). This figure is based on [2].



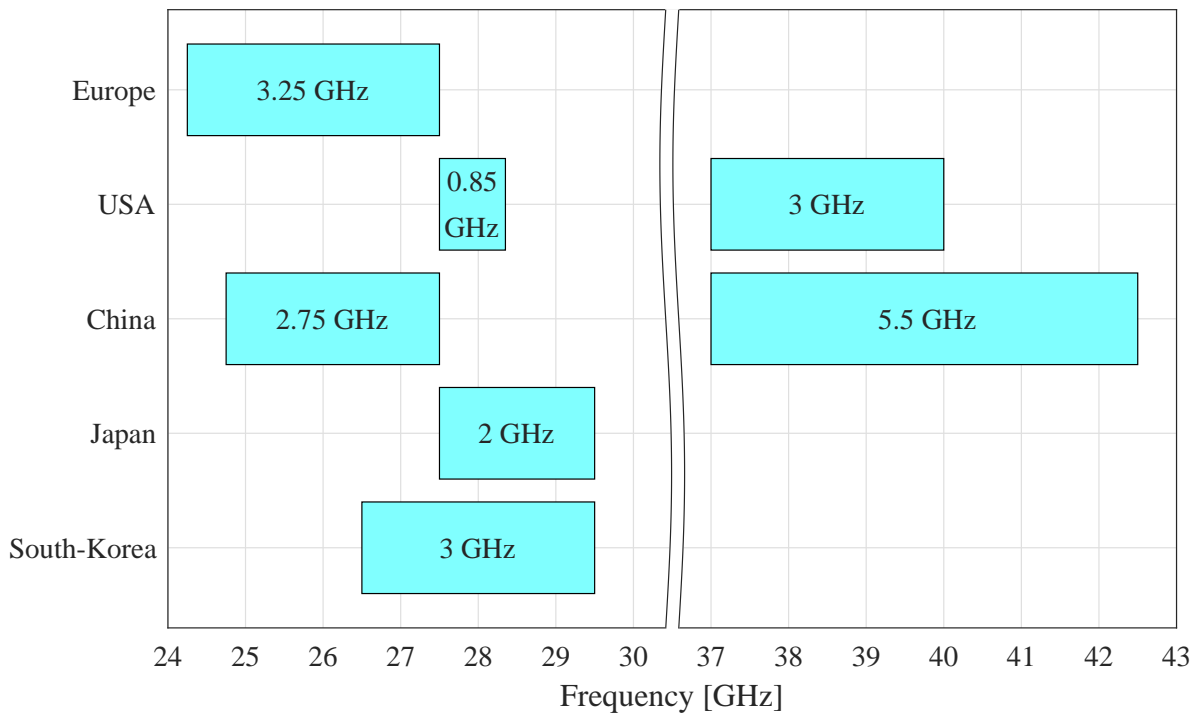


**Figure 1.3:** Allocated 5G mm-wave frequency bands including their bandwidth for different regions. This figure is based on [9].

## 1.2 5G mm-wave cellular network

Compared to 4G, the promise of 5G is to have higher peak data rates, lower latency, more data traffic, and higher connection density, among other improvements [3]-[7]. For these improvements to become reality, additional frequency bands compared to 4G have to be used. Despite the fact that the exact allowable frequency bands are region dependent, the frequency bands which are going to be used for 5G are typically divided in two frequency ranges; FR1 and FR2 [8], or often referred to as the sub-6 GHz and mm-wave frequency bands.<sup>1</sup> In Fig. 1.3, the mm-wave frequency bands allocated for 5G for some regions are shown [9].

Although the 5G wireless systems utilizing the sub-6 GHz frequency band will be using new waveforms [10], [11] and new technologies like MIMO [7], [12], these frequencies are similar to the frequencies used in current 4G systems. From an RF research point of view, the antenna design and characterization challenges, therefore, are more interesting in the mm-wave frequency band compared to the sub-6 GHz band. Hence, at the Electromagnetics (EM) group of the Eindhoven University of Technology (TU/e), the present research to 5G cellular networks is focused on challenges and implications associated with the utilization of 5G antenna systems operating at mm-wave frequencies. Especially the frequency band from 26.5 to 29.5 GHz (sometimes referred to as the n257 frequency band) is of interest as NXP

<sup>1</sup>3GPP has defined FR1 from 0.41 GHz to 7.125 GHz and FR2 from 24.25 GHz to 52.6 GHz [8], so the terms ‘sub-6 GHz’ and ‘mm-wave’ may be misleading. Nonetheless, these terms are often used to refer to FR1 and FR2, as will also be the case in this thesis.

Semiconductors is able to provide integrated circuits (ICs) for prototyping purposes that are operational in this frequency range.

Exploiting the 5G mm-wave frequency band comes at the cost of a decreased communication range compared to 4G frequencies [13]. The 5G mm-wave frequency band suffers from an increased free-space path loss (FSPL) and is more prone to attenuation and blockage by objects like trees and buildings, for instance. One solution to cope with this decrease in communication range is to install more base stations, allowing the cell size of a 5G mm-wave network to be a lot smaller than the cell size of a typical 4G network. An additional measure is to increase the gain of the antenna system at the base station. At the EM group, three different concepts of high-gain antenna systems for 5G mm-wave base stations are currently being investigated, realized and evaluated.

The first concept is a static antenna system based on cell partitioning [14]. Using this approach, the base station is equipped with tens of high-gain antennas and each antenna is used to illuminate a small part of the cell. The second concept is a phased-array-fed reflector system [P6]. In this concept, a phased array is used to illuminate a reflector, in turn creating a very directional beam to each mobile user. By changing which elements of the phased array are active, it is possible to dynamically adjust the beam, therefore, maintaining a high-quality data link. The third concept is based on using a phased array antenna system to perform beamforming without utilizing a reflector. This phased array concept is the focus of this thesis. Multiple challenges in the design and characterization of these phased array systems have to be overcome before a large-scale roll-out of the 5G mm-wave network is possible. The challenges addressed in this thesis are discussed below.

### 1.3 Outline of the thesis

Antenna arrays consist by definition of multiple individual radiating elements. By controlling the excitation of each element, array radiation patterns having desired radiation characteristics can be obtained. Due to errors in the phase and amplitude of the element excitations, however, the array pattern gets distorted. In Chapter 2, the impact of these errors on the array radiation pattern is assessed. It is suggested to use a Beckmann distribution to statistically model the magnitude of the array pattern, instead of the conventionally used Rician distribution. The presented model yields accurate estimations of, for instance, the likelihood that the obtained array pattern exceeds a specified side lobe level (SLL). In turn, the proposed model can be used by engineers or regulatory agencies to define specifications on tolerable excitation errors by the electronics to ensure compliance with future 5G protocols, based on desired radiation characteristics such as a certain SLL or null depth.

Chapter 3 is devoted to the design and realization of a 28 GHz 8-by-8 dual-polarized analog active phased array. This array is the university's first prototype of a 5G mm-wave base station and is developed to perform in-house experiments. Contrary to typical conventional sub-6 GHz antenna systems, in the prototype, the ICs and antennas are highly integrated. Due

to this high level of integration, it is not possible to connect measurement equipment directly to the individual components. This implies that conductive measurements to characterize individual components of the prototype are impossible and that these measurements have to be performed in a radiative manner instead. In the chapter, several over-the-air (OTA) measurements are presented that are used to deduce the functionality of individual components. Based on these OTA measurements, the design choices are critically evaluated with the aim of improving future realizations of 5G mm-wave base stations.

Although characterizing individual components of an integrated phased array is important to (in)validate models and manufacturing processes, eventually the system performance of the complete array has to be determined. Since typical 5G mm-wave arrays are small in size, far-field conditions are met for small antenna separations, allowing for antenna measurement ranges that are limited in size as well. To determine the gain of an antenna in a far-field setup accurately, a good estimate of the distance between the reference antenna (RA) and antenna-under-test (AUT) in the anechoic chamber is required. An antenna has a certain size and the antenna's radiation does not originate from one single point. This makes it sometimes unclear what the exact distance between the antennas is, increasing the measurement uncertainty. In Chapter 4, a novel antenna gain measurement method based on a relative-distance sweep is presented. Using this technique, the absolute distance between the RA and AUT can be determined, which reduces the uncertainty in determined gain. Moreover, it can be assessed at what antenna separation far-field conditions are met, allowing for accurate far-field measurements at minimum antenna separations. This, in turn, also improves the accuracy of other OTA measurements requiring far-field conditions, such as error-vector-magnitude (EVM) or bit-error-rate (BER) measurements, for instance, ultimately enhancing the reliability of the 5G cellular network.

The antenna system shown in Chapter 3 is highly integrated, but the individual antenna elements and ICs are designed separately and are both matched to  $50 \Omega$ . The short wavelength associated with the 5G mm-wave frequency band, however, results in individual antenna elements having a size in the order of a typical IC. This miniaturization opens up the possibility to create an antenna-on-chip (AoC) or antenna-in-package (AiP), potentially reducing manufacturing costs, decreasing RF losses and eliminating the  $50 \Omega$  boundary. Processes suitable for high-volume manufacturing of AoCs or AiPs are currently under development. Being able to measure typical antenna parameters, such as the input impedance or the antenna gain, without having physical access to the antenna terminals, is useful to validate models which are used to design integrated antennas produced using high-volume manufacturing processes. The OTA characterization methods presented in Chapter 3 are used to deduce the performance of several individual components in a phased array. However, the gain or the input impedance of an individual antenna element cannot be extracted using the presented methods. In Chapter 5, a contactless characterization method (CCM) is presented that allows for determining the input impedance and gain of an integrated antenna without having to connect the integrated antenna to a measurement device. The method is verified using a connectorized mm-wave open-ended waveguide (OEWG). This potentially enables the characterization of

**Table 1.1:** Structure and coherence of Chapter 2 to 7.

	<b>Modeling and design</b>	<b>OTA characterization</b>
<b>Integrated phased array systems</b>	Chapter 2 & 3	Chapter 3 & 4
<b>Integrated antenna elements</b>	Chapter 7	Chapter 5 & 6

mm-wave integrated antennas and can be used to validate models used to design the AoCs and AiPs using new high-volume manufacturing technologies. In turn, these integrated antennas can be used as building blocks for antenna arrays, potentially reducing the design time of antenna systems.

The method presented in Chapter 5 does require calibration, an anechoic chamber, and the measurement equipment to have a large dynamic range. While this method is suited for validating a high-volume manufacturing process, these requirements might not be realistic for antenna functionality testing of the individual (packaged) dies in a conventional production facility. In Chapter 6, a variant of the CCM as presented in Chapter 5 is used to determine the reflection coefficient of a connectorized mm-wave patch antenna in a contactless manner. This variant does not require an anechoic chamber or calibration. Moreover, the measurements are conducted when the antennas are in each other's near-field region, drastically reducing the required dynamic range of the measurement system. Due to these advantages it is possible to create compact antenna functionality testing solutions for mass-produced integrated antennas, ensuring reliability of the products.

Integrating the antenna on an IC can potentially decrease RF losses and reduce the manufacturing costs. On the other hand, the IC manufacturing process is highly optimized to maximize the performance of the electronics, but is typically not well suited for antennas. The dielectric losses induced by the IC's silicon are generally high and impacts the radiation efficiency of the antenna significantly. Moreover, the IC is typically placed on a ground plane or heat sink to distribute the generated heat, which often decreases the efficiency of the antenna at the same time. To (partly) shield an antenna from these unwanted effects, artificial magnetic conductors (AMCs) can be used. In Chapter 7, the utilization of AMCs for AoC applications is examined and modeling techniques are presented, with the aim of stimulating future research to enable the production of low-loss AoCs using AMCs.

As a summary, the structure and coherence of Chapter 2 to 7 is shown in Table 1.1. Finally, in Chapter 8, the conclusions and recommendations based on the research reported in this thesis are presented.

## 1.4 Original contributions of the thesis

The work that is presented in this thesis contains the following original contributions.

- As a replacement for the conventionally used Rician distribution, the Beckmann distribution is proposed to assess the impact of random errors in the excitations of individual

antenna elements on the array radiation pattern, see Chapter 2 and Appendix A.

- It is shown that the maximum probability of exceeding a certain SLL does not have to be at the position(s) of the highest side lobe(s) in the error-free case, see Chapter 2.
- The design and characterization of a 5G mm-wave 8-by-8 dual-polarized analog active phased array based on analog beamformer (ABF) ICs that are produced using a low-cost silicon-based high-volume manufacturing process is presented, see Chapter 3.
- The beamforming algorithm reported in [15] is extended to shape the 3D radiation pattern, rather than a planar cut, see Chapter 3 and Appendix B.
- An antenna gain measurement technique using a relative-distance sweep is developed that allows for accurate gain measurements for minimum antenna separations, see Chapter 4.
- The Fraunhofer far-field distance associated with the largest antenna is often used to determine the distance between two antennas in a far-field gain measurement setup. It is experimentally proven, however, that the required separation before far-field conditions are achieved does depend on the smallest antenna as well, see Chapter 4.
- Although the phase center is often used as the reference point of an antenna in gain measurements, it is shown that the amplitude center better serves this purpose, see Chapter 4.
- The input impedance and realized gain of a connectorized OEWG operating in the  $K_a$ -band has been determined in a contactless manner, see Chapter 5.
- The aforementioned method also yields phase information, enabling complex radiation pattern measurements of integrated antennas, see Chapter 5.
- It is experimentally shown that using the CCM, the reflection coefficient can be determined when the antennas are in each other's near-field, see Chapter 6.
- A concept of a pick-and-place handler, combining both the RF testing and pick-and-place functionality is developed, see Chapter 6.
- The maximum achievable bandwidth of an AMC and a theoretical minimum dielectric loss induced by an AMC, excited by plane waves of normal incidence, is derived, see Chapter 7 and Appendix C.
- A design methodology of an angular stable AMC for transverse magnetic (TM) plane wave excitations up to grazing incidence is developed, see Chapter 7.



# Effect of Random Errors in the Element Excitations on the Array Pattern<sup>1</sup>

---

## 2.1 Introduction

Electronically controlled antenna arrays are utilized in a lot of applications, mainly due to their adaptive radiation characteristics. Many synthesis techniques are available that allow for the determination of the correct element excitations that result in a desired array radiation pattern. Due to errors in the phase and amplitude of the element excitations, however, the array radiation pattern gets distorted. The excitations generated by ICs that are produced using a high-volume manufacturing process typically show small deviations compared to their designed values as a result of manufacturing tolerances. Moreover, deviations between the ICs can also be observed, making the response and the quantization of every IC in a sense unique. Although these excitation errors can be taken into account when synthesizing the array radiation pattern, characterizing every setting of every IC in an antenna array having tens to hundreds elements is very time consuming and is not desired for high-volume fabrication of 5G mm-wave antenna systems. Alternatively, since the error excitation for every element will be different, these errors can be modeled as random errors. In the past, a lot of effort had already been done in order to derive statistical results of the array radiation pattern subject to random errors. In fact, in 1952 the first statistical results on distorted array radiation patterns were already obtained by Ruze [16]. In [16], the claim has been made that if the individual array elements are subject to random excitation errors, the magnitude of the array amplitude pattern follows a modified Rayleigh (nowadays commonly known as Rician) distribution. Many publications addressing this problem followed, see for instance [17]-[22], and this Rician distribution is used in all these publications to model the distribution of the magnitude of the array amplitude pattern. However, as presented in this chapter, in some cases the use

---

<sup>1</sup>This chapter is based on [P1].

of the Rician distribution leads to incorrect results, whereas the Beckmann distribution yields more accurate results. Using the Beckmann distribution, a seemingly counterintuitive result is obtained, i.e., that the maximum probability of exceeding a certain SLL does not have to be at the position(s) of the highest side lobe(s) in the error-free case. Therefore, angular probability plots are introduced, which cover the whole angular domain, rather than only assessing the distribution of the highest side lobe(s).

The outline of this chapter is as follows. In Section 2.2, the random errors and the random variables for the real and imaginary values of the distorted array amplitude pattern are introduced. In Section 2.3, statistical quantities of these random variables are presented. Section 2.4 is devoted to choosing the proper distribution of the magnitude of the array amplitude pattern. Here, both the Rician and Beckmann distribution are discussed. Section 2.5 introduces the angular probability plots and compares the Rician and Beckmann cumulative distribution functions (CDFs) to Monte Carlo simulations. Here, it is shown that the usage of the Beckmann CDF yields more accurate results compared to using the Rician CDF. Section 2.6 is devoted to a physical interpretation of the obtained results. Finally, in Section 2.7, the conclusion is presented.

## 2.2 The array amplitude pattern including excitation errors

For a linear-polarized one-dimensional linear antenna array, the complex-valued array amplitude pattern  $F_0(\theta)$  (sometimes also called array field or voltage pattern) in the azimuth plane can be expressed as

$$F_0(\theta) = \sum_{n=1}^N g_n(\theta) a_n e^{jk_0 d(N-n) \sin \theta}. \quad (2.1)$$

Here,  $N$  is the number of antenna elements,  $g_n(\theta)$  and  $a_n$  are the complex-valued embedded element pattern<sup>2</sup> (EEP) and excitation coefficient of the  $n^{\text{th}}$  antenna element, respectively,  $k_0$  is the wave number in vacuum and  $d$  is the spacing between the individual antenna elements. The array amplitude pattern as given in (2.1) can be split in a real and imaginary field component using Euler's formula, i.e.,

$$\begin{aligned} \operatorname{Re}[F_0(\theta)] &= \sum_{n=1}^N A_n(\theta) \operatorname{Re}[e^{jC_n(\theta)}] = \sum_{n=1}^N A_n(\theta) \cos C_n(\theta), \\ \operatorname{Im}[F_0(\theta)] &= \sum_{n=1}^N A_n(\theta) \operatorname{Im}[e^{jC_n(\theta)}] = \sum_{n=1}^N A_n(\theta) \sin C_n(\theta), \end{aligned} \quad (2.2)$$

where,

$$\begin{aligned} A_n(\theta) &= |g_n(\theta)| |a_n|, \\ C_n(\theta) &= k_0 d(N-n) \sin \theta + \arg(a_n) + \arg(g_n(\theta)). \end{aligned} \quad (2.3)$$

---

<sup>2</sup>Effects due to mutual coupling are captured in the EEP and are taken into consideration in this model. Load pull effects, however, are ignored in this model.



Here,  $\arg(\cdot)$  represents the function to calculate the argument (or phase) of a complex number. In the remainder of the chapter, the notation of  $F_0(\theta)$ ,  $g_n(\theta)$ ,  $A_n(\theta)$  and  $C_n(\theta)$  is shortened by omitting the explicit mentioning of the  $\theta$ -dependency.

The phase and amplitude of the element excitations are assumed to be subject to non-deterministic noise and errors. Hence, two random variables are introduced for each individual element. The random variables  $\delta_{pn}$  and  $\delta_{an}$  represent the phase and relative amplitude error of the  $n^{\text{th}}$  antenna element, respectively. Both random variables are Gaussian distributed and have zero mean, but have, in general, a different variance. The variance in the phase error is assumed to be identical among the different elements. The same holds for the variance of the amplitude error. This can be expressed as

$$\begin{aligned}\delta_{pn} &\sim \mathcal{N}(0, \sigma_p^2), \\ \delta_{an} &\sim \mathcal{N}(0, \sigma_a^2), \\ \text{where } n &= 1, \dots, N,\end{aligned}\tag{2.4}$$

with  $\sigma_p^2$  and  $\sigma_a^2$  the variance of the phase and relative amplitude error, respectively. Furthermore, no correlation between errors is assumed, i.e.,

$$\begin{aligned}\text{corr}(\delta_{pn}, \delta_{pm}) &= 0, \text{ for } n \neq m, \\ \text{corr}(\delta_{an}, \delta_{am}) &= 0, \text{ for } n \neq m, \\ \text{corr}(\delta_{an}, \delta_{pm}) &= 0, \text{ for all } n, m, \\ \text{where } n &= 1, \dots, N, \text{ and } m = 1, \dots, N.\end{aligned}\tag{2.5}$$

The error-free array amplitude pattern  $F_0$  will be distorted as a result of the introduced random errors. The distorted array amplitude pattern  $F_d$  can be written as

$$F_d = \sum_{n=1}^N A_n (1 + \delta_{an}) e^{j\delta_{pn}} e^{jC_n}.\tag{2.6}$$

This distorted array amplitude pattern can also be split in a real and imaginary component using Euler's formula, i.e.,

$$\begin{aligned}X = \text{Re}[F_d] &= \sum_{n=1}^N A_n (1 + \delta_{an}) (\cos \delta_{pn} \cos C_n - \sin \delta_{pn} \sin C_n), \\ Y = \text{Im}[F_d] &= \sum_{n=1}^N A_n (1 + \delta_{an}) (\cos \delta_{pn} \sin C_n + \sin \delta_{pn} \cos C_n).\end{aligned}\tag{2.7}$$

## 2.3 Statistical quantities of the array amplitude pattern

According to the Central Limit Theorem (CLT), for sufficiently large  $N$ , the random variables  $X$  and  $Y$  will follow a Gaussian distribution. In the following subsections, some statistical quantities of these Gaussian distributions are presented. In Appendix A, a complete derivation of these statistical quantities can be found.

### 2.3.1 Mean value

The mean values of  $X$  and  $Y$  can be written as

$$E[X] = \mu_x = e^{-\frac{\sigma_p^2}{2}} \operatorname{Re}[F_0], \quad (2.8)$$

$$E[Y] = \mu_y = e^{-\frac{\sigma_p^2}{2}} \operatorname{Im}[F_0]. \quad (2.9)$$

### 2.3.2 Variance

The variances of  $X$  and  $Y$  can be written as

$$\operatorname{Var}(X) = \sigma_x^2 = \frac{1}{2}(1 + \sigma_a^2)(1 - e^{-2\sigma_p^2}) \sum_{n=1}^N A_n^2 + \left( (1 + \sigma_a^2)e^{-2\sigma_p^2} - e^{-\sigma_p^2} \right) \sum_{n=1}^N A_n^2 \cos^2 C_n, \quad (2.10)$$

$$\operatorname{Var}(Y) = \sigma_y^2 = \frac{1}{2}(1 + \sigma_a^2)(1 - e^{-2\sigma_p^2}) \sum_{n=1}^N A_n^2 + \left( (1 + \sigma_a^2)e^{-2\sigma_p^2} - e^{-\sigma_p^2} \right) \sum_{n=1}^N A_n^2 \sin^2 C_n. \quad (2.11)$$

In first instance it might not be evident, but note that  $C_n$  has a  $\theta$ -dependency (see (2.3)), hence, the variance of  $X$  and  $Y$  are dependent on  $\theta$  as well. In Fig. 2.1, this dependency is shown. To generate this result, and the results in the upcoming sections, an array of  $N = 16$  elements with half-wavelength spacing  $d = \frac{1}{2}\lambda_0$  has been chosen. Chebyshev tapering with a designed SLL of  $\text{SLL}_0 = -40$  dB has been applied to this array. The standard deviation of the phase and amplitude errors were chosen to be  $\sigma_p = 5^\circ$  and  $\sigma_a = 0.1$  dB, respectively. Furthermore, the amplitude pattern of the individual elements  $g_n$  is isotropic (i.e.,  $g_n = 1$ ), unless specified otherwise. The following derived results and drawn conclusion are in principle, however, valid for other sets of parameters as well.

Note that in Fig. 2.1, around  $\theta = -90^\circ$ ,  $\theta = 0^\circ$  and  $\theta = 90^\circ$ , the variances show large variations. In Section 2.6, a physical interpretation for these large variations is presented.

### 2.3.3 Correlation

The correlation coefficient  $\rho_{xy}$  between random variables  $X$  and  $Y$  with expected values  $\mu_x$  and  $\mu_y$  and standard deviations  $\sigma_x$  and  $\sigma_y$  is defined as

$$\rho_{xy} = \frac{\operatorname{cov}(X, Y)}{\sigma_x \sigma_y} = \frac{\operatorname{cov}(X, Y)}{\sqrt{\operatorname{Var}(X) \operatorname{Var}(Y)}}. \quad (2.12)$$

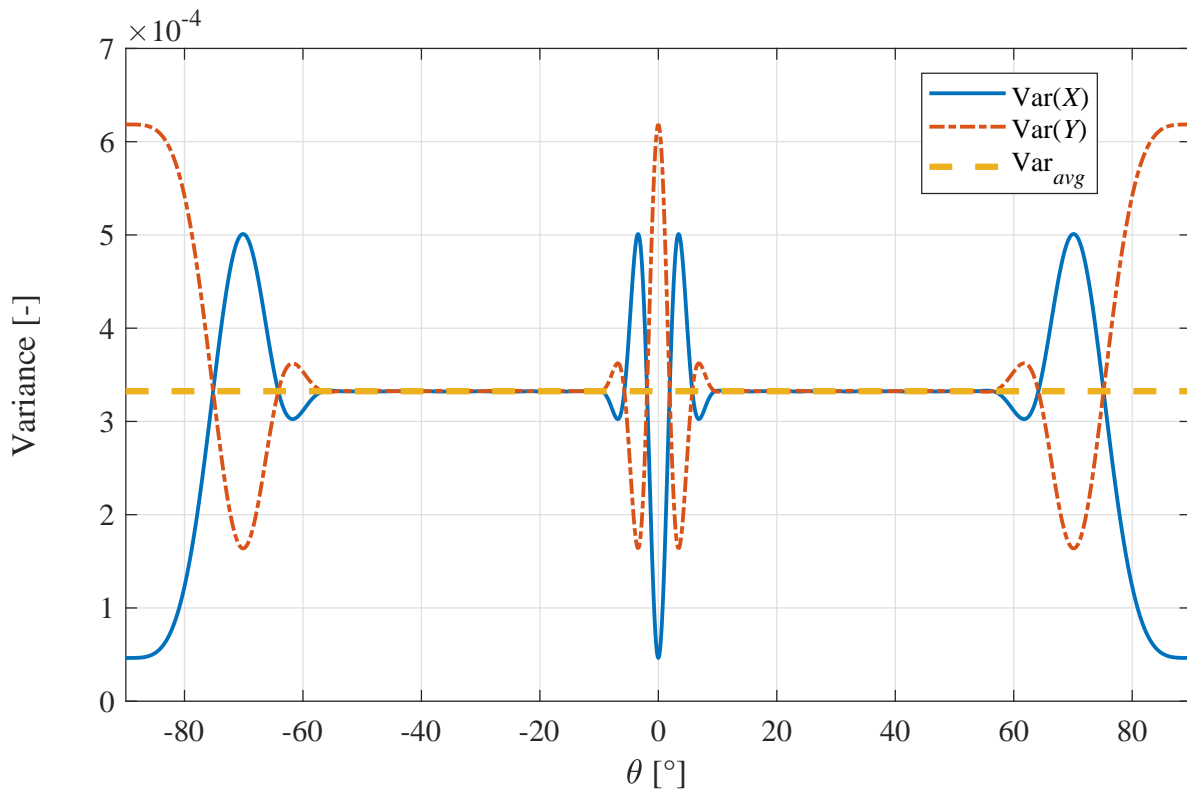


**Figure 2.1:** Variance of  $X$ ,  $Y$ , and its average. The values of the parameters used to generate this figure are given in Section 2.3.2.

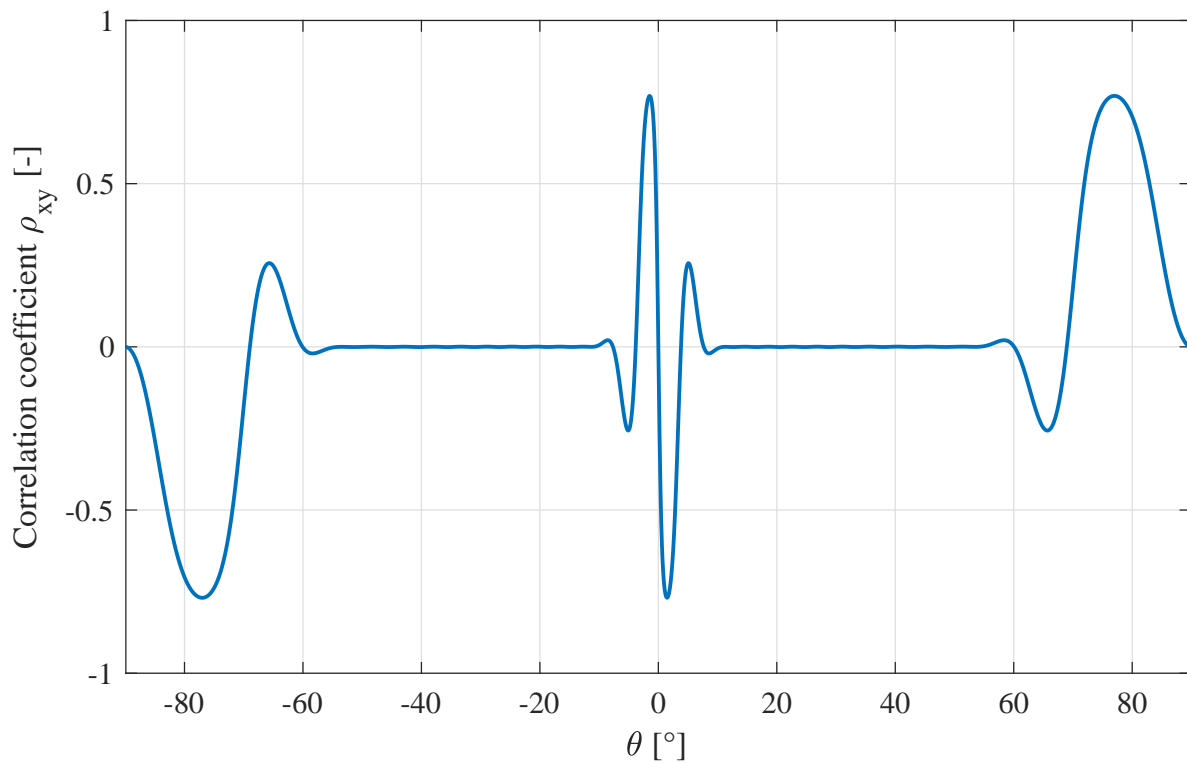


**Figure 2.2:** Correlation between  $X$  and  $Y$ . The values of the parameters used to generate this figure are given in Section 2.3.2.

The covariance between the random variables  $X$  and  $Y$  can be written as

$$\text{cov}(X, Y) = \left( (1 + \sigma_a^2) e^{-2\sigma_p^2} - e^{-\sigma_p^2} \right) \sum_{n=1}^N A_n^2 \cos C_n \sin C_n. \quad (2.13)$$

By substituting (2.10), (2.11) and (2.13) into (2.12), an expression for the correlation coefficient  $\rho_{xy}$  can be found. This will give rise to a tedious expression and, therefore, this expression has been omitted in this chapter and in Appendix A. For implementation purposes, it is recommended to calculate the variances of  $X$  and  $Y$ , and the covariance between  $X$  and  $Y$ , and substitute the results in (2.12), rather than implementing (2.12) in one single expression.

In Fig. 2.2, the correlation between  $X$  and  $Y$  is shown as function of  $\theta$  for the parameters as specified in Section 2.3.2. As can be seen in Fig. 2.2, there is a strong correlation at certain angles. This means that although the phase and relative amplitude errors are uncorrelated, the real and imaginary value of the distorted array amplitude pattern can, in general, be highly correlated at certain angles. In Section 2.6, a physical interpretation for this observed correlation is presented.

## 2.4 Magnitude of the array amplitude pattern

In the previous section, statistical quantities are presented which allow the calculation of the distribution of the real and imaginary value of the array amplitude pattern. From an engineer's perspective, however, it is more interesting to be able to calculate the distribution of the magnitude of the array amplitude pattern. It is often assumed that the magnitude of the array amplitude pattern follows a Rician distribution. However, by using the Rician distribution, two assumptions are implicitly made that are not made when using a Beckmann distribution. In this section, both distributions are discussed and compared.

### 2.4.1 Rician distribution

Suppose there are two orthogonal and uncorrelated Gaussian distributions. If these Gaussian distributions have a nonzero and unidentical mean  $\mu_x$  and  $\mu_y$ , but share the same variance  $\sigma^2$ , then the magnitude  $r$  of the sum of these Gaussian distributions will follow a Rician distribution [23]. The Rician probability density function (PDF) is defined as

$$\text{PDF}_{\text{rice}}(r) = \frac{r}{\sigma^2} \exp\left(-\frac{r^2 + v^2}{2\sigma^2}\right) I_0\left(\frac{rv}{\sigma^2}\right). \quad (2.14)$$

Here,  $I_0$  is the modified Bessel function of the first kind with order zero and  $v$  is defined as

$$v = \sqrt{\mu_x^2 + \mu_y^2}. \quad (2.15)$$

The CDF of a Rician distribution is given by

$$\text{CDF}_{\text{rice}}(r) = 1 - Q_1\left(\frac{v}{\sigma}, \frac{r}{\sigma}\right), \quad (2.16)$$

with  $Q_1$  the Marcum Q-function [24].

This Rician PDF is often used to describe the distribution of the magnitude of the array amplitude pattern. However, by using the Rician distribution, two assumptions on the statistic quantities of the random variables  $X$  and  $Y$  are implicitly made; the variances of  $X$  and  $Y$  are identical, and the correlation between  $X$  and  $Y$  has to be zero. In [16], the variances of  $X$  and  $Y$  are averaged and zero correlation between  $X$  and  $Y$  is assumed. In [19]-[22] the result found in [16] is followed. In [17], [18], the authors report the same expressions for the variances and correlation as presented in Section 2.3. However, when assessing the distribution of the magnitude of the array amplitude pattern, the same assumptions on the variances and correlation as in [16] are made.

Following the approach in [16] and averaging the variance found in (2.10) and (2.11) yields

$$\text{Var}_{avg} = \frac{\text{Var}(X) + \text{Var}(Y)}{2} = \frac{1}{2}(1 + \sigma_a^2 - e^{-\sigma_p^2}) \sum_{n=1}^N A_n^2. \quad (2.17)$$

As can be seen in (2.17), the averaged variance is constant with respect to  $\theta$ . In Fig. 2.1, the averaged variance is compared to the variance of  $X$  and  $Y$  for the parameters as specified in Section 2.3.2. Hence, if one is interested in the maximum probability of exceeding a specified SLL, the Rician CDF only has to be calculated at the angle with the highest value of  $v$  to obtain the maximum probability of exceeding a specified SLL. This turns out to be at the position(s) of the highest side lobe(s).

## 2.4.2 Beckmann distribution

The Beckmann distribution is a more general distribution compared to the Rician distribution. Again, supposing there are two orthogonal Gaussian distributions, but in this case these distributions can be correlated, i.e.,  $\rho_{xy} \neq 0$ . These Gaussian distributions can have a nonzero and unidentical mean  $\mu_x$ ,  $\mu_y$  and variance  $\sigma_x^2$ ,  $\sigma_y^2$ . Then, the magnitude  $r$  of the sum of these Gaussian distributions will follow a Beckmann distribution. Note that for the case that  $\sigma_x^2 = \sigma_y^2$  and  $\rho_{xy} = 0$ , the Beckmann distribution reduces to a Rician distribution.

The Beckmann PDF is defined by [25]

$$\text{PDF}_{\text{beck}}(r) = \frac{r}{2\pi\sigma_x\sigma_y\sqrt{1-\rho_{xy}^2}} \int_0^{2\pi} \exp\left(-\frac{z}{1-\rho_{xy}^2}\right) d\theta, \quad (2.18)$$

with

$$z = \frac{(r \cos \theta - \mu_x)^2}{2\sigma_x^2} + \frac{(r \sin \theta - \mu_y)^2}{2\sigma_y^2} - \frac{\rho_{xy}(r \cos \theta - \mu_x)(r \sin \theta - \mu_y)}{\sigma_x\sigma_y}. \quad (2.19)$$

The CDF can then be calculated by

$$\text{CDF}_{\text{beck}}(r) = \int_0^r \text{PDF}_{\text{beck}}(r') dr'. \quad (2.20)$$

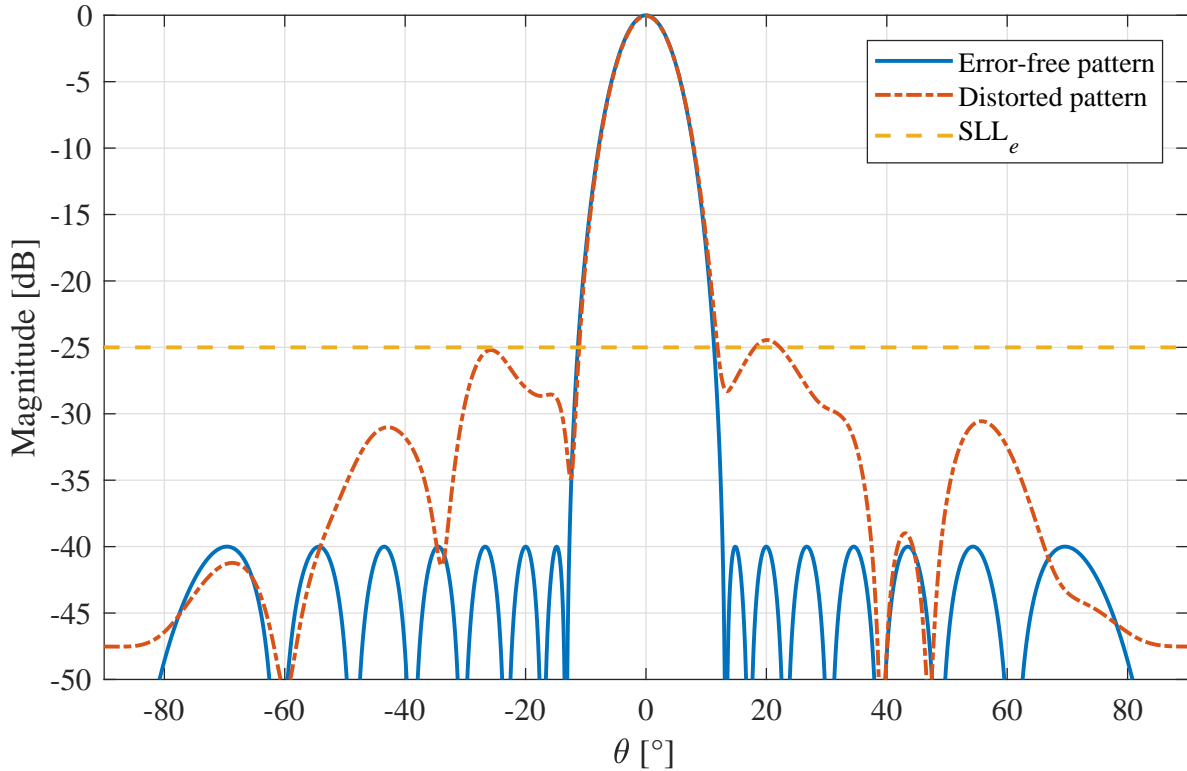


**Figure 2.3:** Error-free pattern and an example of one out of the one million Monte Carlo simulations. Around  $18^\circ < \theta < 22^\circ$ , the distorted pattern exceeds  $SLL_e$ .

Equation (2.20) unfortunately does not have a closed-form solution and has to be calculated numerically.

## 2.5 Simulation results

To verify that the magnitude of the array amplitude pattern follows a Beckmann distribution instead of a Rician distribution, the CDF of (2.16) and (2.20) are compared to Monte Carlo simulations. For each Monte Carlo simulation, a phase and amplitude error is generated for each element according to the probability distributions as defined in (2.4), where  $\sigma_p = 5^\circ$  and  $\sigma_a = 0.1$  dB. The resulting array power pattern is calculated and for each simulation, as function of angle, is determined whether a certain desired side lobe level  $SLL_e$  [dB], with respect to the error-free case, is exceeded. In Fig. 2.3, an example of this process is shown. Here, the error-free array radiation pattern and one of the calculated distorted array radiation patterns is shown. At  $18^\circ < \theta < 22^\circ$ , the distorted pattern exceeds  $SLL_e$ . For these angles the value 1 is assigned, whereas for the other angles the value 0 is assigned. Averaging these values over all simulations leads to an estimate of the probability of exceeding  $SLL_e$  as function of angle. This estimate is compared to the probability determined by the Rician and Beckmann CDF. In the upcoming angular probability plots, the desired side lobe level is set to  $SLL_e = -25$  dB and the yellow dashed line denoted by ‘Monte Carlo simulation’ is the

estimated probability of exceeding  $SLL_e$  as a result of one million simulations.

Figure 2.4 shows an angular probability plot with the parameters as given in Section 2.3.2. The main lobe can, in general, be discarded from the analysis and is illustrated by a gray area. The Monte Carlo simulation is compared to the results of the conventional Rician CDF (blue) and the proposed Beckmann CDF (red). One can see that the three methods agree for  $|\theta| < 60^\circ$ . For  $|\theta| > 60^\circ$ , the calculated values of the Rician CDF starts to show a deviation compared to the calculated values of the Beckmann CDF and Monte Carlo simulations. The Beckmann CDF, however, still agrees with the Monte Carlo simulations over the whole angular domain.

The results of the Monte Carlo simulations and Beckmann CDF beyond  $|\theta| = 60^\circ$  may seem counterintuitive. Although the side lobes of the error-free pattern have equal amplitudes (see Fig. 2.3), the most outward side lobes dominate in this case the probability of exceeding a certain radiation level. A physical interpretation of these results is given in Section 2.6.

One may argue that for a lot of practical antennas, the radiation pattern of the individual elements used in antenna arrays hardly has a significant contribution in the end-fire direction, hence, the discrepancy observed in Fig. 2.4 is not of high importance. However, in Fig. 2.5, the same angular probability plot is shown, but now a linear phase distribution is applied, such that the beam is scanned to  $45^\circ$ . Here, one can see that the increase in probability is shifted to the region  $-25^\circ < \theta < -10^\circ$ . The question might arise why this shift occurs and whether the location of the probability increase is predictable. In Section 2.6, insight in this shift is given and a method is presented that enables the prediction of the location of the increased probability.

To illustrate that this sudden increase in probability can impose a problem for a practical antenna array, a configuration with a different individual radiation pattern has been chosen. In this case, the power pattern of the individual elements follows a cosine shape, i.e.,  $g_n^2(\theta) = \cos(\theta)$  for  $n = 1, \dots, N$ . In Fig. 2.6 the result is shown. Again, the beam is scanned to  $45^\circ$  using a linear phase distribution.

A few things have to be noted here. Chebyshev tapering does not take into account the cosine-shaped radiation pattern of the individual elements. Therefore, the side lobes of the error-free radiation pattern are not constant. Instead, the envelope of the array radiation pattern follows a cosine shape, as can be observed in Fig. 2.7. Due to this, the envelope of a large part of the probability curve in Fig. 2.6 also follows a cosine shape. Moreover, the overall probability of exceeding the threshold value is increased compared to the case where only uniform radiators were being used. Furthermore, by inspecting Fig. 2.6 and 2.7, it can be seen that the highest probability of exceeding  $SLL_e$  is not at the location of the largest side lobe in the error-free case. For such a practical setting, the discrepancy between the Rician CDF and the Monte Carlo simulations is large, making the usage of the Beckmann CDF preferable compared to the Rician CDF in terms of accuracy.

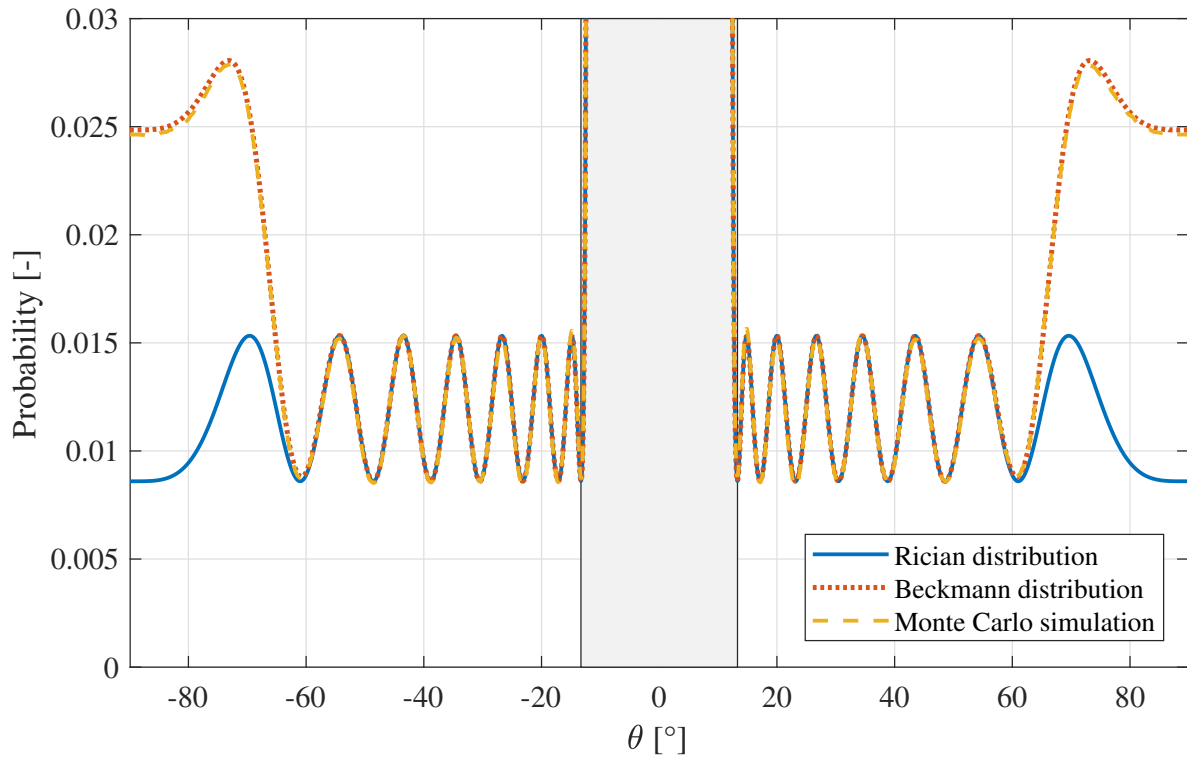


**Figure 2.4:** Angular probability plot. For  $|\theta| > 60^\circ$ , the Rician CDF starts to deviate from the Beckmann CDF and Monte Carlo simulation.

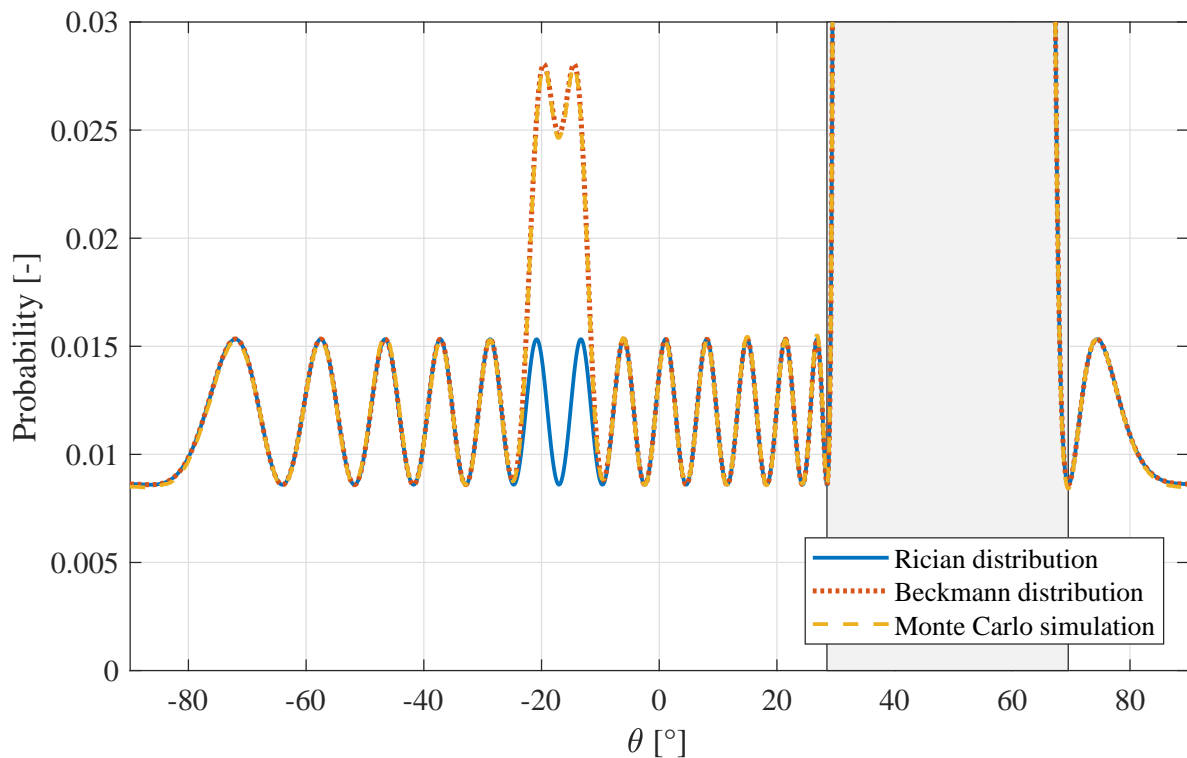


**Figure 2.5:** Angular probability plot with a scan angle of  $45^\circ$ . The increase in probability is shifted to the region  $-25^\circ < \theta < -10^\circ$ .



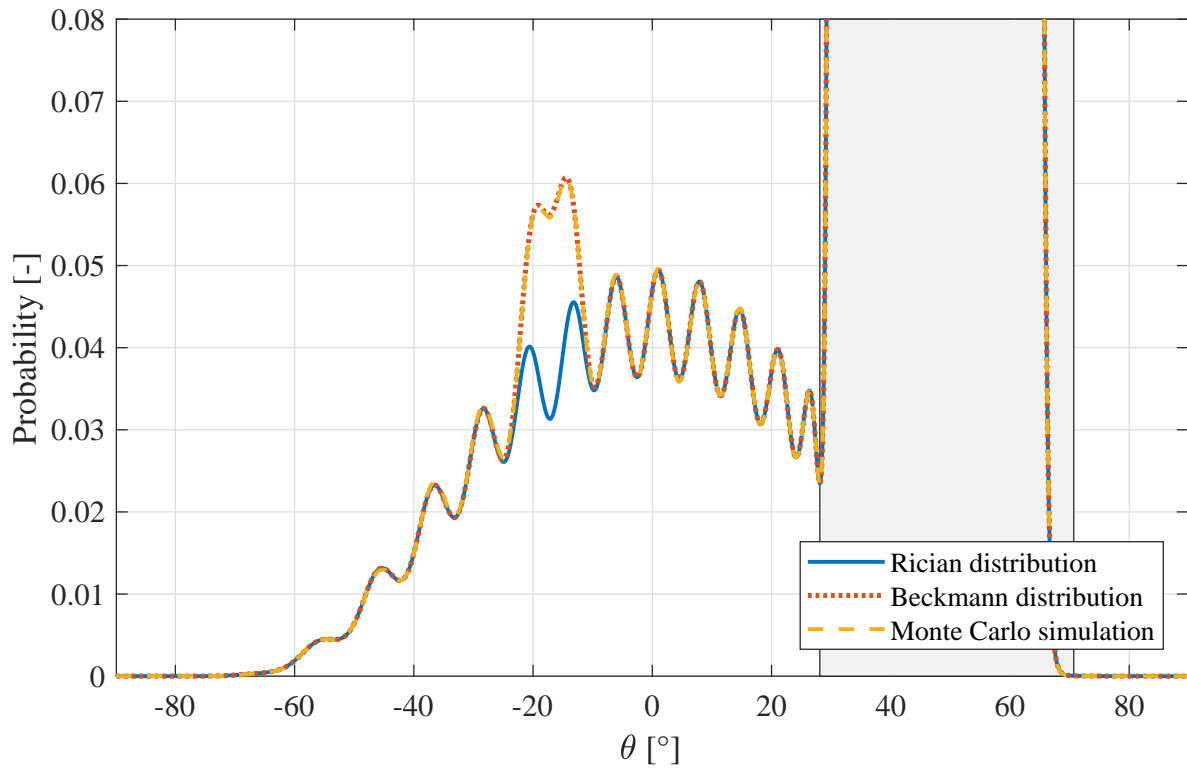


**Figure 2.6:** Angular probability plot with  $g_n^2(\theta) = \cos(\theta)$ , and scanning to  $45^\circ$ . For this practical setting, the performance of the Rician CDF is not sufficient.

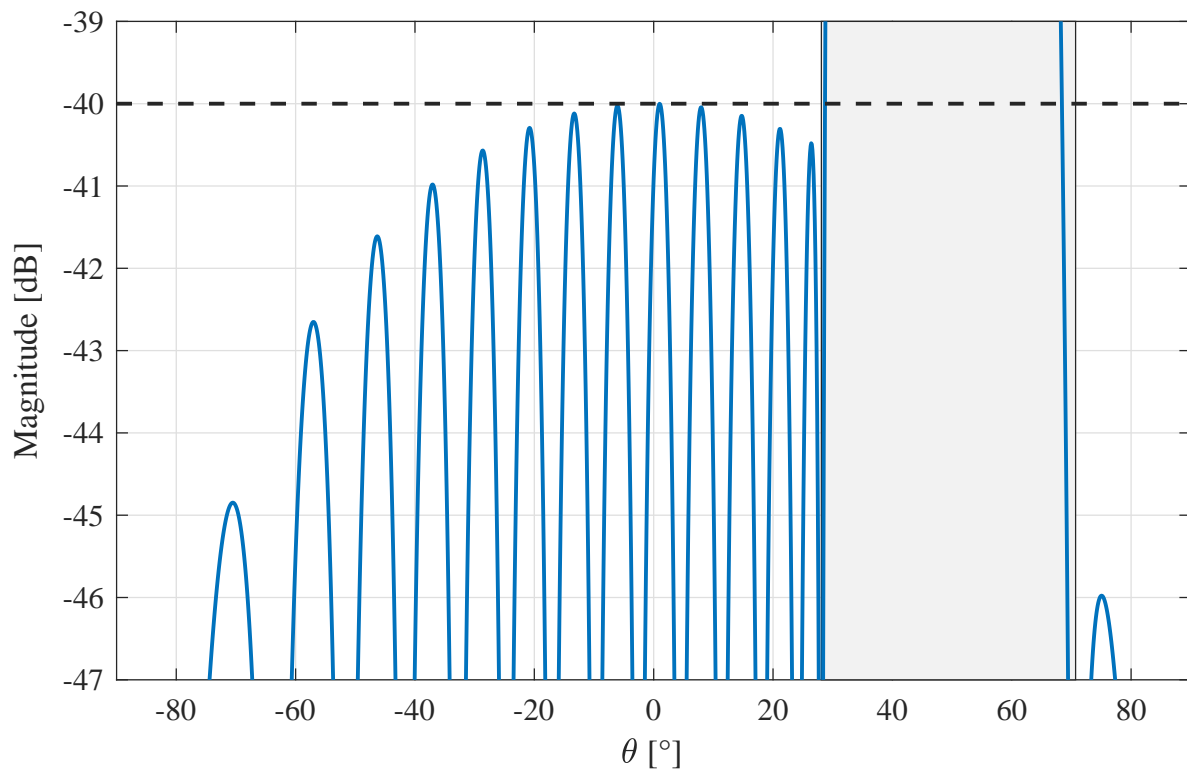


**Figure 2.7:** Zoom of the error-free radiation pattern with  $g_n^2(\theta) = \cos(\theta)$  and a scan angle of  $45^\circ$ . Note that the side lobes do not have the same magnitude.

## 2.6 Physical interpretation of the acquired results

In the previous section, results are presented which might seem counterintuitive at first. To give a physical interpretation of these results, instead of only relying on the derived mathematical descriptions, a step back has to be taken. In this section, first the root cause of the largely varying variances around the angles  $\theta = -90^\circ$ ,  $\theta = 0^\circ$  and  $\theta = 90^\circ$  (see Fig. 2.1) is presented. Next, the nonzero correlation between  $X$  and  $Y$  (see Fig. 2.2) is examined. After that, the impact of this unidentical variance and the nonzero correlation on the distribution of the magnitude of the array amplitude pattern is explained. Finally, the impact of scanning on the angular probability plots is explained as well.

### 2.6.1 Variance

In order to interpret the results of the variance, the effect of the phase and amplitude errors are examined separately. First, the amplitude error is assumed to be zero and only the phase is distorted. In this case, (2.6) reduces to

$$F_d = \sum_{n=1}^N A_n e^{j\delta_{pn}} e^{jC_n} = \sum_{n=1}^N V_n e^{j\delta_{pn}} = \sum_{n=1}^N V_{n,p}. \quad (2.21)$$

Equation (2.21) represents a summation of vectors in the complex plane, where  $V_n$  and  $V_{n,p}$  are the error-free and distorted vector of the  $n^{\text{th}}$  element, respectively. Each error-free vector  $V_n$  is distorted by the  $e^{j\delta_{pn}}$ -term. This error-term only accounts for a change in angle of the vector in the complex plane, but the amplitude of the error-free vector and the distorted vector will remain the same, i.e.,  $|V_n| = |V_{n,p}|$ .

In Section 2.3, a sufficiently large  $N$  was assumed to let  $X$  and  $Y$  approach a Gaussian distribution. However, the definitions of variance of a random variable and correlation between two random variables are independent of the underlying distribution(s), hence, the choice of  $N$  is not of high importance in the upcoming analysis. For visualization purposes, the array contains only  $N = 2$  elements in the upcoming analysis. Moreover,  $A_n = 1$ ,  $d = \frac{1}{2}\lambda_0$  and no phase difference is applied among the elements.

For  $\theta = 0^\circ$ , the resulting individual error-free vectors are  $V_1 = V_2 = 1$ . These vectors are visualized in the unit circle in Fig. 2.8(a). Additionally, one example of the distorted variants  $V_{1,p}$  and  $V_{2,p}$  is visualized in Fig. 2.8(a). Here one can see that for a relatively small phase error, the resulting error in  $X$  is small compared to the error in  $Y$ . This gives rise to a large variance in  $Y$  and only a small variance in  $X$ .

Next,  $\theta = 90^\circ$  is considered. In this case the resulting vectors are in antiphase and a null is created in the error-free radiation pattern in that direction. The variance of  $Y$ , however, is large in this case. This scenario is visualized in Fig. 2.8(b). Note that the scenario of  $\theta = 90^\circ$  gives rise to exactly the same variance in  $X$  and  $Y$  as in the case of  $\theta = -90^\circ$  and  $\theta = 0^\circ$ .

Another interesting scenario to consider is when the variance in  $X$  and  $Y$  are equal. It is geometrically straightforward to see in Fig. 2.8(c) that the variances in  $X$  and  $Y$  are equal

for a  $90^\circ$  phase difference between  $V_1$  and  $V_2$  in the complex plane. This corresponds to the following values of  $\theta$

$$\begin{aligned}\pi \sin \theta &= \frac{1}{2}\pi \rightarrow \theta = 30^\circ, \\ \pi \sin \theta &= -\frac{1}{2}\pi \rightarrow \theta = -30^\circ.\end{aligned}\tag{2.22}$$

The variances of  $X$  and  $Y$  for  $\sigma_a = 0$  dB and  $\sigma_p = 5^\circ$  are calculated according to (2.10) and (2.11), and visualized in Fig. 2.8(d). Note that for the special cases which are visualized in Fig. 2.8(a)-(c), the graph of Fig. 2.8(d) matches the expectations denoted above.

As a second step, an amplitude error is assumed and the error in phase is omitted. In this case, (2.6) reduces to

$$F_d = \sum_{n=1}^N A_n(1 + \delta_{an})e^{jC_n} = \sum_{n=1}^N V_n(1 + \delta_{an}) = \sum_{n=1}^N V_{n,a},\tag{2.23}$$

with  $V_{n,a}$  the vector distorted by an amplitude error. Again, (2.23) represents a summation of vectors in the complex plane. However, the error term now results in a change in magnitude, rather than changing the angle of the vector.

The resulting individual error-free vectors  $V_1$  and  $V_2$  for  $\theta = 0^\circ$  are visualized in the unit circle in Fig. 2.8(e). One example of the distorted variants  $V_{1,a}$  and  $V_{2,a}$  is also visualized in Fig. 2.8(e). It can be observed that for an amplitude error, the resulting error in  $X$  is large, whereas the error in  $Y$  is zero. This gives rise to a large variance in  $X$  and zero variance in  $Y$ .

In Fig. 2.8(f),  $\theta = 90^\circ$  is considered. The variance of  $X$  is in this case large, whereas the variance in  $Y$  is again zero. Also here, note that the scenario of  $\theta = 90^\circ$  gives rise to exactly the same variance in  $X$  and  $Y$  as in the case of  $\theta = -90^\circ$  and  $\theta = 0^\circ$ .

Figure 2.8(g) illustrates the scenario where the variance in  $X$  and  $Y$  are equal. As calculated in (2.22), this scenario corresponds to  $\theta = 30^\circ$  and  $\theta = -30^\circ$ .

The variances of  $X$  and  $Y$  for  $\sigma_a = 0.1$  dB and  $\sigma_p = 0^\circ$  are calculated according to (2.10) and (2.11), and visualized in Fig. 2.8(h). Note that for the special cases which are visualized in Fig. 2.8(e)-(g), the graph of Fig. 2.8(h) again matches the expectations denoted above.

## 2.6.2 Correlation

The nonzero correlation between  $X$  and  $Y$  can be explained by using a similar analysis as used in previous subsection. However, in this analysis, certain ranges of  $\theta$  are explored rather than looking at a few specific special cases.

Again, first the amplitude error is omitted. In Fig. 2.9a, the error-free and distorted vectors are depicted. One can see that if an error is made in  $V_2$ , the error made in  $X$  and  $Y$  are uncorrelated. On the other hand, if an error has been made in  $V_1$ , the error in  $X$  and  $Y$  show opposite behavior. If the error in  $Y$  is positive, the error in  $X$  is negative, and vice versa. Therefore, the total error in  $X$  and  $Y$  has a negative correlation coefficient in this case. Note that this behavior is present in the whole first quadrant.

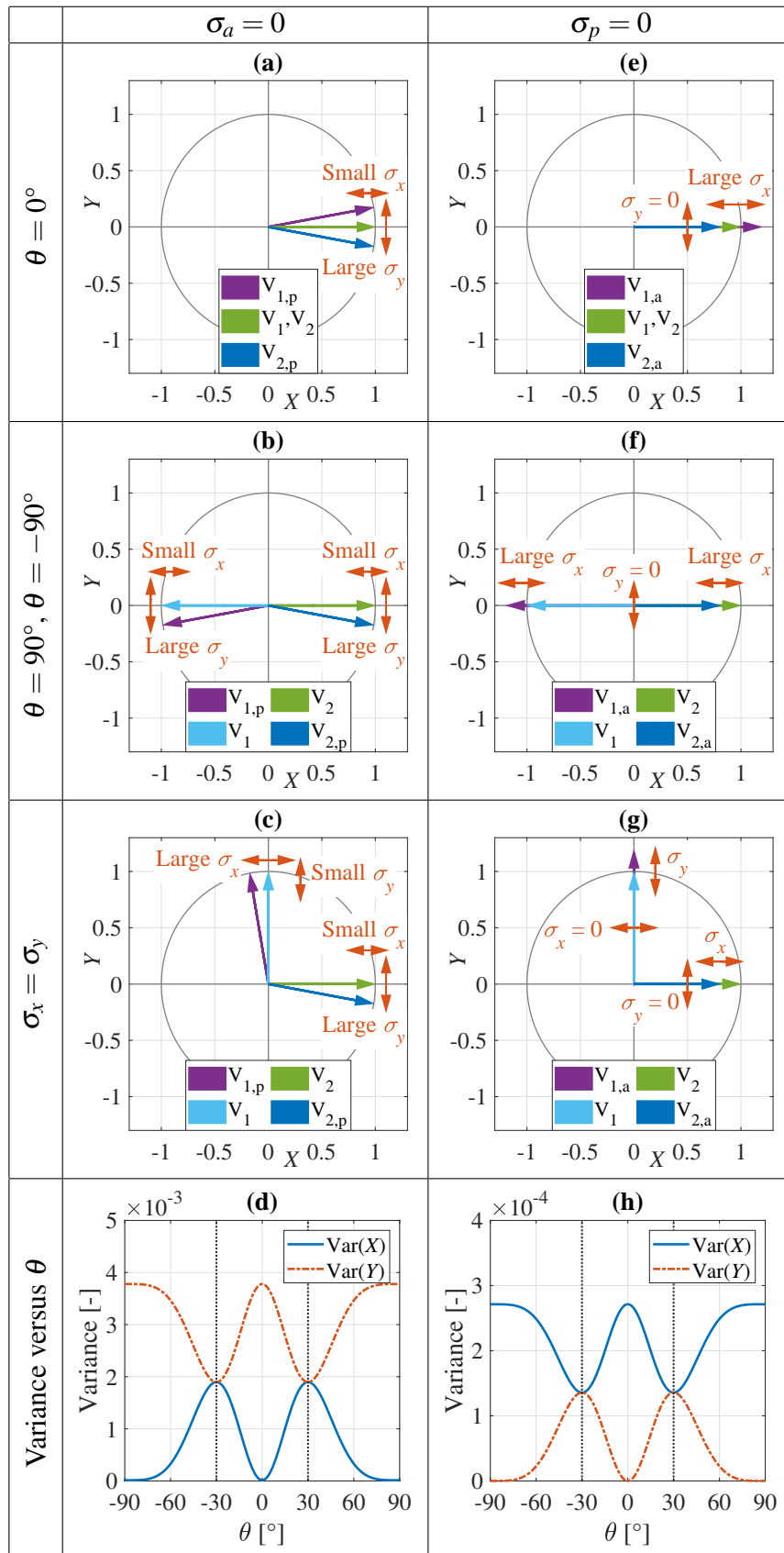


Figure 2.8: Vector representation of the element excitations to explain the variance,  $N = 2$ .

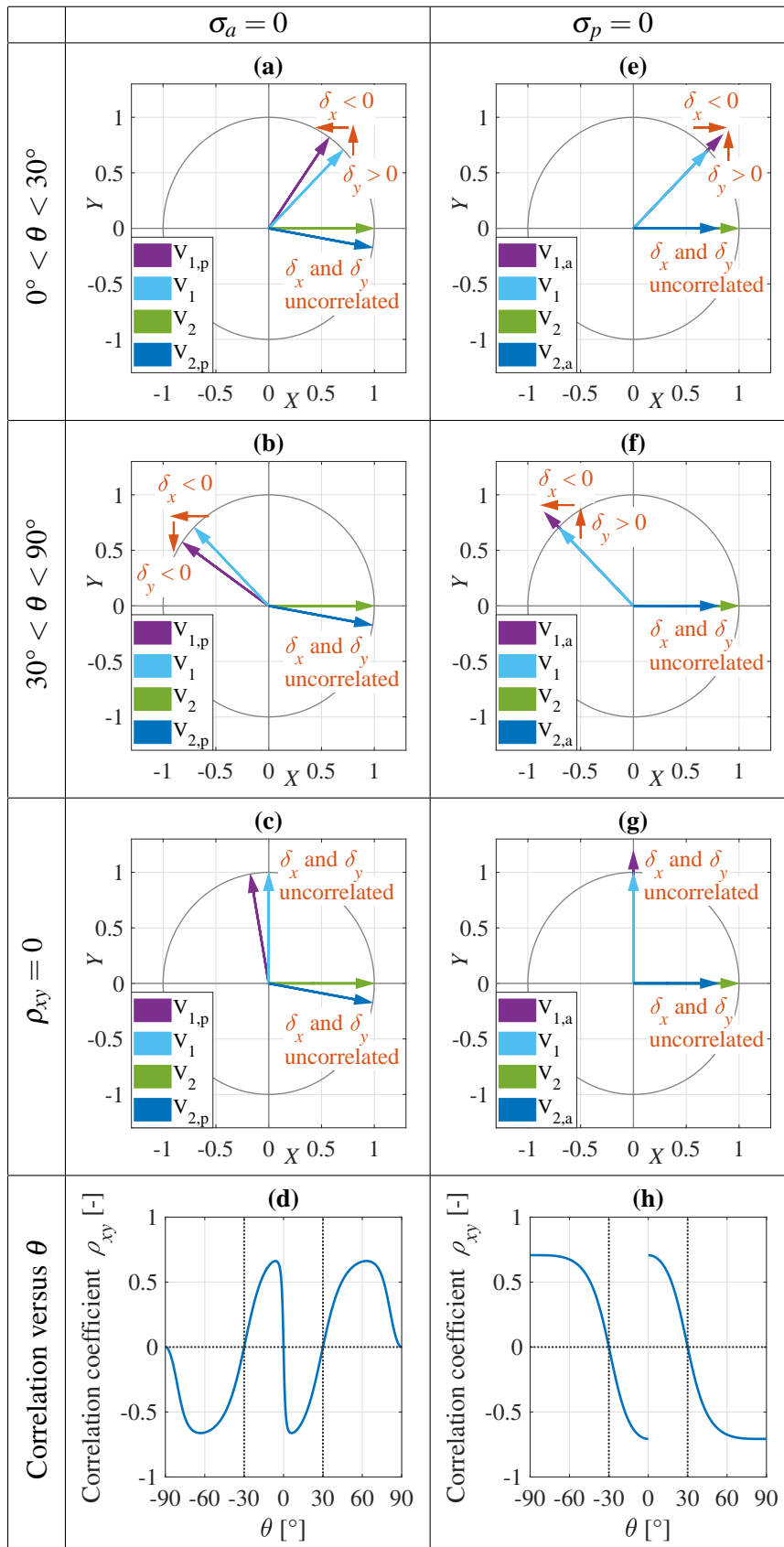


Figure 2.9: Vector representation of the element excitations to explain the correlation,  $N = 2$ .

If  $V_1$  is somewhere in the second quadrant, the errors in  $X$  and  $Y$  show the same behavior. If the error in  $Y$  is positive, the error in  $X$  is also positive, and the same for the errors being negative. This results in a positive correlation coefficient. This situation is visualized in Fig. 2.9b.

Next, the case for no correlation between  $X$  and  $Y$  is examined. In Fig. 2.9c, a phase difference of  $90^\circ$  between  $V_1$  and  $V_2$  is visualized, and it can be seen that the errors in both vectors are uncorrelated. In fact, no correlation between  $X$  and  $Y$  is present when  $V_1$  is parallel to either the x-axis or the y-axis. This corresponds to  $\theta = -90^\circ$ ,  $\theta = -30^\circ$ ,  $\theta = 0^\circ$ ,  $\theta = 30^\circ$  and  $\theta = 90^\circ$ .

The correlation between  $X$  and  $Y$  for  $\sigma_a = 0$  and  $\sigma_p = 5^\circ$  is calculated according to (2.12) and visualized in Fig. 2.9d. Note that for the special cases which are visualized in Fig. 2.9a-c, the graph of Fig. 2.9d matches the expectations denoted above.

If the amplitude error is reintroduced, and the phase error is omitted, one can see in Fig. 2.9e, that if  $V_1$  is located in the first quadrant, the error in  $X$  and  $Y$  show similar behavior. If the error in  $Y$  is positive, the error in  $X$  will also be positive, and the same for the errors being negative. Therefore, the total error in  $X$  and  $Y$  will have a positive correlation coefficient.

On the other hand, if  $V_1$  is somewhere in the second quadrant, the errors in  $X$  and  $Y$  show opposite behavior. If the error in  $Y$  is positive, the error in  $X$  is negative, and vice versa. This results in a negative correlation coefficient. This situation is visualized in Fig. 2.9f.

Next, the case for no correlation between  $X$  and  $Y$  is examined. Again, no correlation between  $X$  and  $Y$  is present when  $V_1$  is parallel to either the x-axis or the y-axis. This corresponds to  $\theta = -90^\circ$ ,  $\theta = -30^\circ$ ,  $\theta = 0^\circ$ ,  $\theta = 30^\circ$  and  $\theta = 90^\circ$ . In Fig. 2.9g, the case of a  $90^\circ$  phase difference between  $V_1$  and  $V_2$  is visualized.

The correlation between  $X$  and  $Y$  for  $\sigma_a = 0.1$  dB and  $\sigma_p = 0^\circ$  is calculated according to (2.12) and visualized in Fig. 2.9h. Note that for the special cases which are visualized in Fig. 2.9e-f, the graph of Fig. 2.9h matches the expectations denoted above. However, Fig. 2.9g matches only partially. The correlation between  $X$  and  $Y$  is zero for  $\theta = -30^\circ$  and  $\theta = 30^\circ$ , but not for  $\theta = -90^\circ$ ,  $\theta = 0^\circ$  and  $\theta = 90^\circ$ . For these angles, the variance of  $Y$  is zero (see Fig. 2.8(h)). This leads to a singularity in (2.12) and the correlation is not defined at these angles.

### 2.6.3 Effect on magnitude

Previous subsections have only given a physical interpretation to the unidentical variance  $\sigma_x^2$  and  $\sigma_y^2$  and the correlation between  $X$  and  $Y$  being nonzero. The impact of this unidentical variance and nonzero correlation on the distribution of the magnitude of the array amplitude pattern is discussed here.

As mentioned in Section 2.4, the magnitude  $r$  of the sum of two orthogonal and uncorrelated Gaussian distributions having mean  $\mu_x$  and  $\mu_y$  and variance  $\sigma^2$ , follows a Rician distribution. This can be graphically visualized as shown in Fig. 2.10. The point  $P$  represents

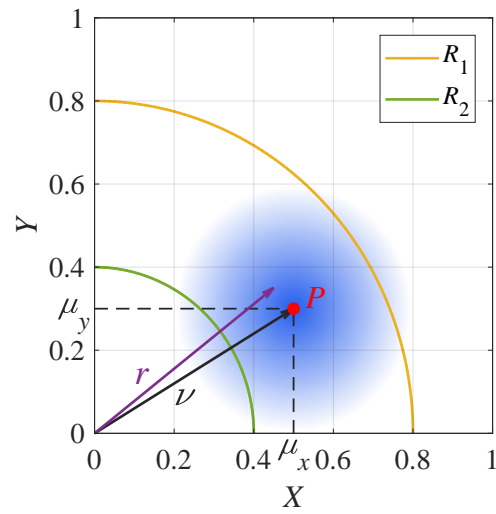


**Figure 2.10:** Depiction of the Rician distribution.

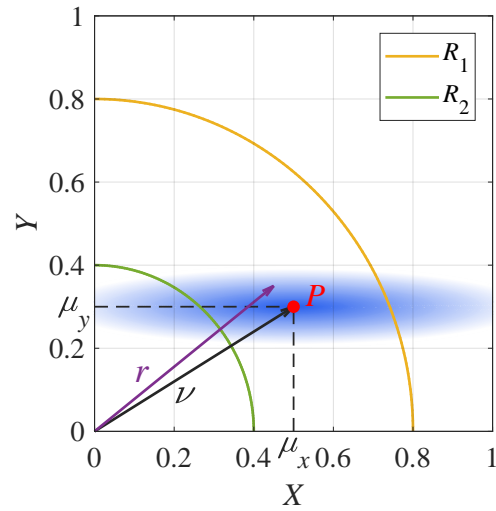


**Figure 2.11:** Depiction of the effect of unequal variance on the Beckmann distribution.

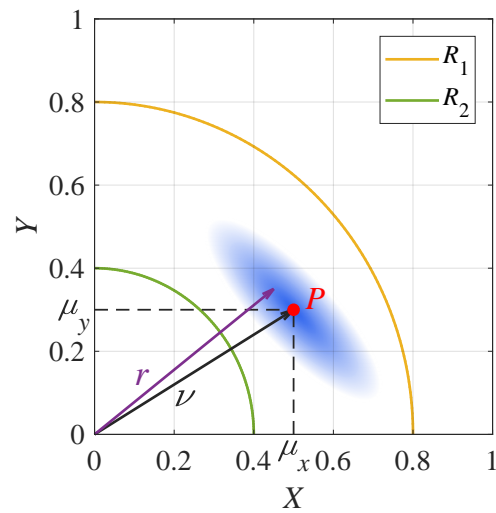


**Figure 2.12:** Depiction of the effect of correlation on the Beckmann distribution.

the expected value of the array amplitude pattern for a particular angle. The parameter  $v$  is the distance between the origin and the point  $P$ . Due to the variance  $\sigma^2$ , each realization of the random variables  $X$  and  $Y$  will be, in general, different from their expected values  $\mu_x$  and  $\mu_y$ . This is illustrated using an intensity profile. The likelihood that a certain combination of  $X$  and  $Y$  is acquired, is represented by the intensity. If the particular position is dark blue, the likelihood of that combination of  $X$  and  $Y$  is high, and vice versa. Note that, since the variances for  $X$  and  $Y$  are equal, the intensity profile has the form of a circle.

Two quarter circles are drawn in Fig. 2.10 to visualize two sets of values with constant magnitude. Using the Rician CDF, the likelihood that the magnitude stays below a certain limit, i.e., the likelihood that the randomly picked points stay below the green curve, can be calculated. As one can see in Fig. 2.10, it is, for example, in this case very likely that a randomly picked combination of  $X$  and  $Y$  stays below  $R_1$ , but likely to be larger than  $R_2$ .

In Fig. 2.11, the effect of the unidentical variance is visualized. In this case  $\sigma_x > \sigma_y$ , hence, the shape of the blue intensity profile is modified into an ellipse. Note that this completely changes the probability of exceeding a certain magnitude. Compared to the circular intensity profile of Fig. 2.10, it is now more likely to exceed  $R_1$ , but at the same time the probability of exceeding  $R_2$  is lower.

In Fig. 2.12, the effect of correlation between  $X$  and  $Y$  is visualized. In this case,  $\sigma_x = \sigma_y$  and  $\rho_{xy} < 0$ . The negative correlation coefficient means that if a positive error in  $X$  is made, it is more likely to make a negative error in  $Y$ . Therefore, due to this negative correlation, the blue intensity profile takes the shape of a 45 degrees tilted ellipse. Note that in this case, it is more likely to stay between  $R_2$  and  $R_1$  compared to both other cases. It is clear that a nonzero correlation coefficient completely changes the probability for the magnitude of exceeding a certain radiation level.<sup>3</sup>

For the values as specified in Section 2.3.2, the large variation in variance (see Fig. 2.1) and strong correlation (see Fig. 2.2) changes the distribution of  $X$  and  $Y$  for  $|\theta| > 60^\circ$  and around  $\theta = 0^\circ$ . For  $\theta = 0^\circ$ , this change in distribution is not visible for the main lobe region in Fig. 2.4, simply because the main lobe region will in principle always exceed the specified radiation level. At  $|\theta| > 60^\circ$ , however, the probability of exceeding the specified SLL is increased compared to the rest of the side lobe region as a result of the variance and the correlation, as shown in this section. Note that, in general, for other values of  $SLL_e$ , the probability of exceeding this level can also be less compared to the rest of the side lobe region.

---

<sup>3</sup>Note that these examples are for illustration purposes only. It is to show the reader how unidentical variances and correlation between  $X$  and  $Y$  can impact the probabilities of exceeding a certain magnitude, rather than showing quantitative results.



### 2.6.4 Effect of scanning

So far in this section, the main lobe has always been pointing towards broadside. However, in practice the beam might be scanned towards other angles. In Fig. 2.5, it can be observed that for a certain scan angle, the peak of higher probability shifted to a different angle of the radiation pattern. In order to understand this shift, one has to go back to the vector representations.

The large variations in the variance in  $X$  and  $Y$  for  $\theta = -90^\circ$  and  $\theta = 90^\circ$  correspond to the angles where  $V_1$  and  $V_2$  are in antiphase. This is the case for  $C_1 = \pi$  or  $C_1 = -\pi$  (see (2.3) for the definition of  $C_n$ ). The linear phase distribution used in Section 2.5 is defined as follows

$$\arg(a_n) = -k_0 d(N - n) \sin \theta_0, \quad (2.24)$$

with  $\theta_0$  the desired scanning angle. By combining (2.3) and (2.24), the following expressions for  $C_1$  can be found

$$C_1 = k_0 d(\sin \theta - \sin \theta_0). \quad (2.25)$$

Solving (2.25) for  $C_1 = -\pi$ ,  $k_0 d = \pi$  and  $\theta_0 = 45^\circ$  gives  $\theta = -17^\circ$ . Note that this result exactly matches the results in Fig. 2.5. This physical interpretation can provide knowledge about where lower or higher probabilities of exceeding a certain radiation level are to be expected.

## 2.7 Conclusion

In this chapter, it is shown that the magnitude of a distorted array amplitude pattern, which is the result of random errors in the phase and amplitude in the element excitations, follows a Beckmann distribution, instead of the often assumed Rician distribution. A practical example is given where the probability of exceeding a certain radiation level is determined. In this example, it is evident that the Beckmann CDF more accurately predicts this probability compared to the Rician CDF. Moreover, the result that the maximum probability of exceeding a certain side lobe level, in general, does not have to be at the angle(s) of the highest side lobe(s) in the error-free case, is obtained. Due to this observation, angular probability plots are shown to be required in properly determining the probability of exceeding a certain radiation level outside the main lobe region. In turn, the proposed Beckmann distribution can be used by engineers or regulatory agencies to, based on desired radiation characteristics such as a certain SLL or null depth, define specifications on tolerable excitation errors by the electronics of a phased array to ensure compliance with future 5G protocols.



# 5G Millimeter-Wave Phased Array Design, Characterization & Calibration<sup>1</sup>

---

## 3.1 Introduction

In the 5G mm-wave band, a wide spectrum is available, which opens up the possibility to enhance the performance of future generation radio access networks. Utilizing this band, however, comes at the cost of a decreased communication range due to the increased path loss at higher frequencies. Phased array antennas enable beamforming, partly overcoming the increase in path loss associated with the 5G mm-wave band. In the past few years, a lot of research is performed by industry and academia to 5G mm-wave analog active phased arrays, see for instance [26]-[35]. In these papers, the resulting equivalent isotropic radiated power (EIRP), radiation patterns, or achieved data rates of the analog active phased array are typically emphasized, but design considerations are sometimes lacking and the design is rarely evaluated in detail. Moreover, due to the high level of integration of the realized arrays, characterization of individual components is often not straightforward, and, therefore, typically omitted. This makes it hard to assess whether the presented arrays and the used design methods are adequate or if there is room for improvement.

To cope with manufacturing errors and to ensure optimum performance, it is common to calibrate a phased array [36]-[40]. It is noteworthy that no calibration procedure is performed on the phased arrays reported in [26]-[33]. Whether or not calibration is required depends on the tolerances of the manufacturing process of the electronics and the printed circuit board (PCB), and of the desired performance for the phased array. For instance, in [32], a root-mean-square (RMS) error of 1.1 dB and 8.9° in the element excitations is reported. It is argued that calibrating the array does not significantly impact the performance as the achieved improvement in gain would be 0.17 dB according to their model. Even though it

---

<sup>1</sup>This chapter is based on [P14] and [P17].

might not be worth performing a calibration procedure to increase the gain by 0.17 dB, it could be worth it to calibrate the array in order to place a null or control the SLL, for instance. A calibration procedure is performed in [34], [35], but it is not reported how much the calibration increased the performance of the array. In [33], no calibration was performed, but it is mentioned in their conclusion that the performance of the array could be improved if the array would be calibrated. Additionally, although in a lab environment calibration might not always be required to achieve good performance, environmental effects might influence the array over time once it is installed in the field. To guarantee reliable operation and to ensure compliance with regulatory agencies, a phased array has to be recalibrated over time. This type of calibration is often referred to as online calibration and has been omitted in [26]-[35].

In this chapter, the design, characterization and calibration of a 28 GHz 8-by-8 analog dual-polarized active phased array is presented. The array is the university's first prototype of a 5G mm-wave active phased array and is developed as testbed to experiment with OTA characterization and phased array calibration methods. Based on these OTA measurements, the performance of the array and its subcomponents can be evaluated. Such an evaluation can provide feedback to design choices and models, which can enable improved designs for future realizations of 5G mm-wave active phased arrays. Moreover, a phased array is an essential component in the phased-array-fed reflector system that is also being investigated at the university as candidate for future 5G mm-wave antenna systems for base stations. Hence, the designed array is also used as feed to illuminate a reflector that is especially designed to achieve a scan angle of  $\pm 30^\circ$ , as can be seen in [P6].

The outline of this chapter is as follows. All the steps taken which were required to arrive at the design are summarized in Section 3.2. Results of OTA measurements to characterize individual components and subsystems of the array are provided in Section 3.3. Section 3.4 is devoted to calibrating the array. Here, beamforming capabilities are presented and a phase calibration is performed to enhance the gain of the array. Moreover, an online calibration procedure is presented that can be used when the array is installed in the field. Finally, in Section 3.5, the conclusion is presented.

## 3.2 Active phased array design

### 3.2.1 Design specifications

The specifications of the active phased array antenna were defined as follows:

- The array should cover the n257 band (26.5 to 29.5 GHz) as much as possible.
- The array should consist of 64 elements (8-by-8).
- The 8-by-8 module has to be stackable in one dimension.
- ABF ICs provided by NXP Semiconductors have to be included to enable scanning and tapering.

- The beamformer network (BFN) and antenna elements should be compatible with standard PCB technology.
- The array has to be dual-polarized, i.e., two data streams can be transmitted or received at the same time.
- Online calibration capabilities should be included.

### 3.2.2 PCB stack-up

The PCB stack-up of the final design is shown in Fig. 3.1. Isola Astra MT77 ( $\tan \delta = 0.0017$ ) has been chosen as dielectric of the PCB. Both the core and prepreg have approximately the same dielectric constant of  $\epsilon_r = 3$ , which simplifies the design process. All dielectric layers have the same thickness of  $127 \mu\text{m}$ , creating symmetry and mitigating warpage of the PCB. The thickness of  $127 \mu\text{m}$  was not enough for the antenna elements to achieve the required bandwidth, hence, multiple dielectric layers are stacked to create sufficient thickness as can be seen in the top part of Fig. 3.1. The board is manufactured using six lamination steps as indicated by the vertical orange bars. This means that in a standard PCB manufacturing process, only six different via types can be used. The vias allowed in the PCB stack-up are indicated by the vertical yellow bars. The implications of having limitations on the vias are discussed in the upcoming subsections.

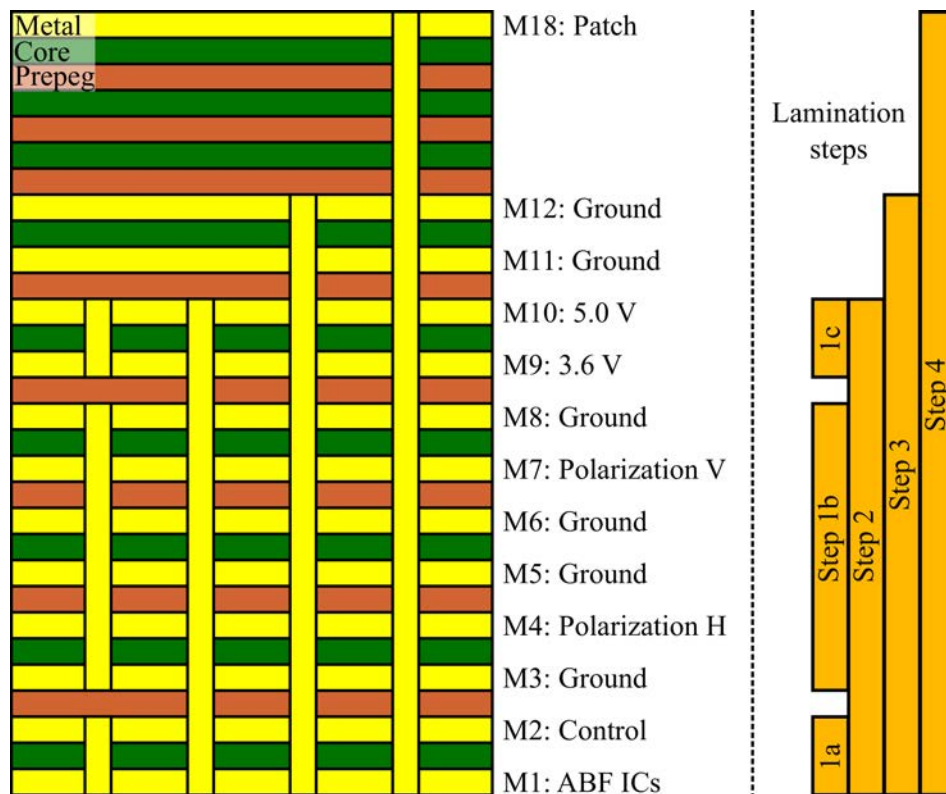
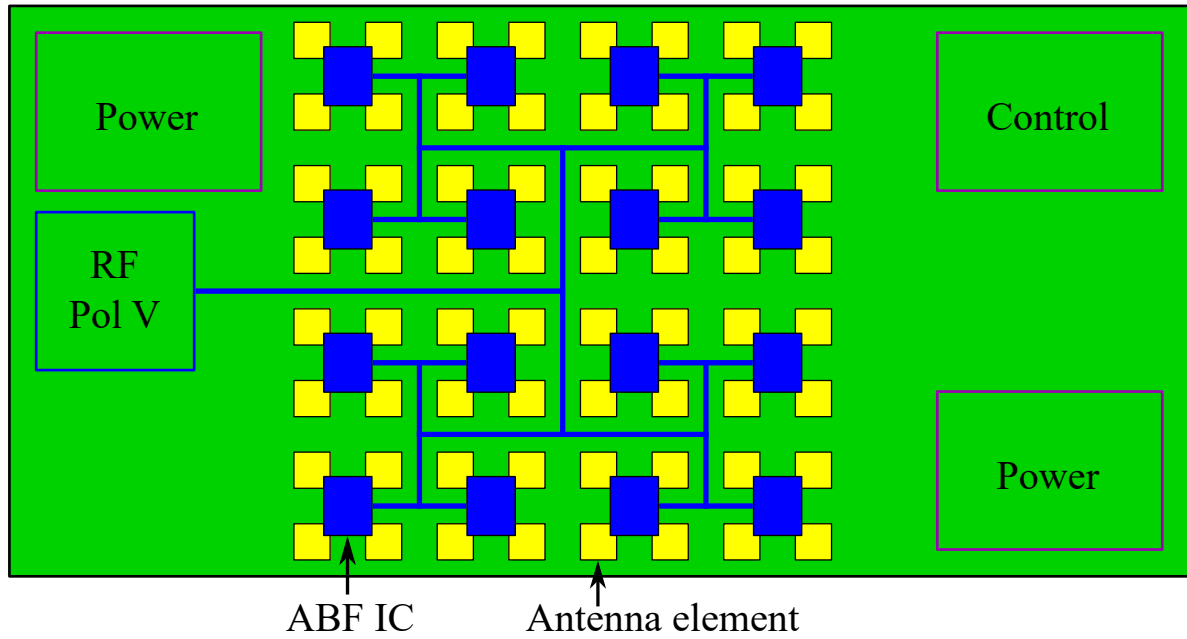
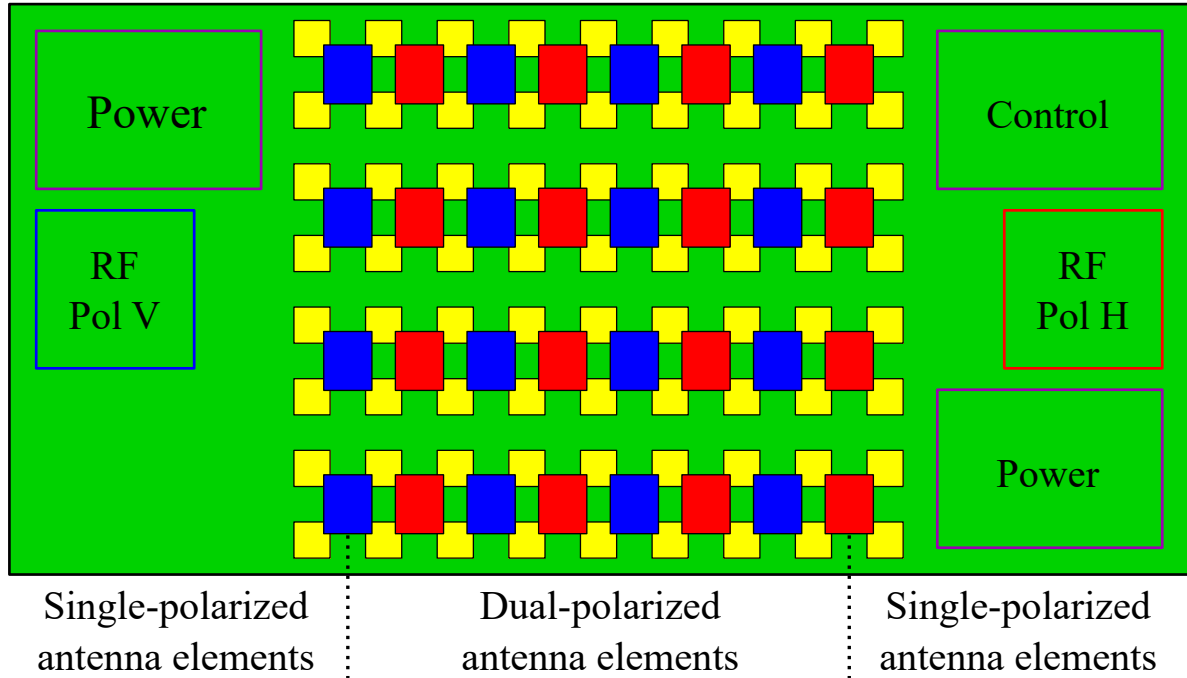


Figure 3.1: PCB stack-up (not to scale).



(a) Sketched PCB layout, showing the 8-by-8 antenna grid, and the ICs and BFN for the vertical polarization.



(b) Sketched PCB layout, showing the 8-by-9 antenna grid and the ICs for both polarizations.

**Figure 3.2:** High-level representation of the PCB layout.

### 3.2.3 PCB layout

In Fig. 3.2(a), a simplified PCB layout, including an 8-by-8 grid of square patch antenna elements, is shown. The topology of the ABF IC allows feeding the antenna elements in a 2-by-2 fashion (see Section 3.2.4). Hence, for feeding one polarization, it is a straightforward choice to position the ABF ICs in a 4-by-4 grid. This also allows for a symmetric BFN, as indicated by the blue traces in Fig. 3.2(a).

To feed the other polarization, another 4-by-4 grid of ABF ICs has to be placed on the PCB. The size of the ABF IC is small enough such that the grids of the two polarizations can be intertwined and most of the antenna elements can be shared. As can be seen in Fig. 3.2(b), the 4-by-4 grid for the horizontal polarization (in red) is simply a translated version of the original ABF IC grid for the vertical polarization (in blue). The translation has been made in the horizontal direction, such that the module remains stackable in the vertical direction. Most of the antenna elements are shared by the ICs for both polarizations, but it is impossible to connect the outermost left column of antennas with the outermost right column of ICs without using complicated feeding traces. Therefore, on the right, an extra column of patches has been added, creating an 8-by-9 grid of antenna elements. This means that the outer columns are single-polarized, and the 8-by-7 grid in the center is dual-polarized, as shown in Fig. 3.2(b). Based on symmetry, a mirrored version of the BFN as shown in Fig. 3.2(a) can be used to feed the horizontal polarization.

### 3.2.4 Analog beamformer ICs

The used ABF ICs are produced using a low-cost silicon-based manufacturing process. In Fig. 3.3, the schematic of the IC is depicted. The IC has five RF ports of which four are connected to antenna elements. The IC is designed for time division duplex (TDD) systems and can, therefore, be used in either a transmit (Tx) or receive (Rx) mode. If the IC is used in Tx, an RF signal can be fed into the common port denoted by  $RF_c$ . The signal is split in four, and each part of the signal is fed in a separate RF chain. In each chain, the signal can

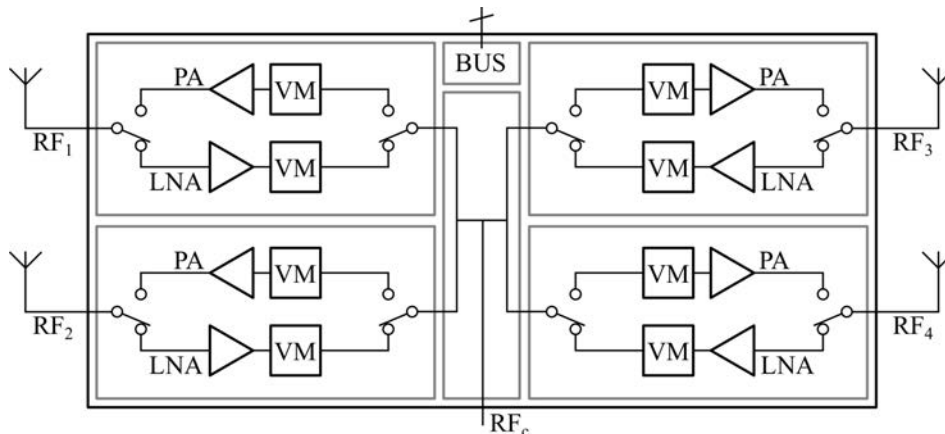


**Figure 3.3:** Schematic of the used ABF ICs.

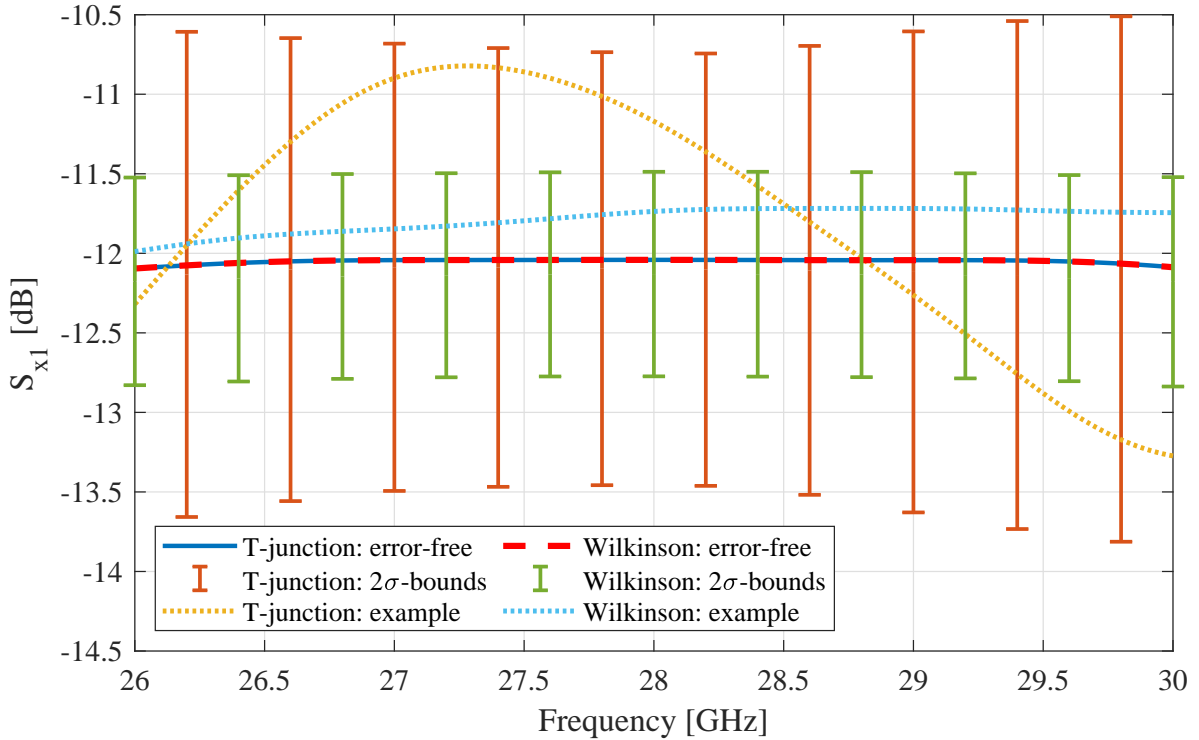


**Figure 3.4:** Comparison of a Wilkinson and a T-junction BFN.

be adjusted by a 6-bit amplitude and 6-bit phase control, before the signal is used to excite an antenna element. If the IC is used in Rx, the signals received by the four antenna elements can also be adjusted by a 6-bit amplitude and 6-bit phase control, before they are combined into the output port  $RF_c$ .

### 3.2.5 Wilkinson versus T-junction

Although the BFN in Fig. 3.2(a) is drawn by lines of equal thickness, properly splitting one or combining two RF signals requires a separate carefully designed structure. Basically, two different options are available for a 1-to-2 splitter/combiner; Wilkinson or T-junctions. The Wilkinson junction requires a resistor and more area compared to a T-junction, but offers better isolation in return. To show the impact of having a better isolation, Monte Carlo simulations were performed using ADS from Keysight. In this simulation, a 1-to-16 splitting network with either 15 Wilkinson or T-junctions has been created. The transmission lines (TLs) used in the junctions and connecting the structures are considered lossless. The splitting network is designed for 28 GHz and a reference impedance of  $50 \Omega$ . In Fig. 3.4, the resulting transfer coefficient for an error-free splitting network that is terminated with matched loads is shown. The transfer of both the Wilkinson and T-junction are on top of each other in the error-free case and are close to -12 dB, as is expected for a lossless 1-to-16 splitting network. In reality, such an error-free network cannot be achieved, and there will be manufacturing errors in the TLs and spread in the impedance of the ABF ICs and resistors. In total, 1000 Monte



Carlo simulations have been performed in which the variation in impedance of the terminations, the  $100\ \Omega$  resistors, and the variation in impedance and lengths of the TLs, are Gaussian distributed with a standard deviation of 5% of its nominal value. The  $2\sigma$ -boundaries of the resulting power transfer of the BFNs are visualized in Fig. 3.4. As can be seen in the figure, the spread in power transfer is much larger in the T-junction BFN than in the Wilkinson junction BFN. On top of that, the frequency dependency of the T-junction BFN is much higher compared to the Wilkinson junction BFN. In Fig. 3.4, one typical example of the simulation for each BFN is shown. In the frequency band of operation, the Wilkinson BFN results in this case in a variation of less than 0.2 dB, whereas the T-junction BFN varies by more than 2 dB. In fact, the standard deviation of the 1000 Monte Carlo samples with respect to the frequency had been determined, and the standard deviation was on average more than 10 times lower for the Wilkinson BFN compared to the T-junction BFN. From an RF performance point of view, a Wilkinson junction BFN outperforms a T-junction BFN due to its higher isolation. A Wilkinson junction BFN requires the use of resistors. Since the BFN is inside the PCB, either these resistors have to be embedded in the PCB as well, or the resistors can be placed on the top layers and vias have to be used to connect to the BFN layer. Embedding the resistors inside the PCB was considered too risky as this manufacturing process was not yet mature. The latter option was difficult to achieve due to space restrictions. Therefore, in this phased array design, T-junctions were eventually chosen over Wilkinson junctions due to their simplicity. In Section 3.3.2, a reflection on this design choice is given.

### 3.2.6 Beamformer network implementation

The BFNs of the two polarizations will need to cross each other. To minimize crosstalk between these signals, both BFNs have been designed inside the PCB on different metal layers, see Fig. 3.1. To prevent leakage and unwanted coupling, a stripline configuration has been used to route the signal, i.e., the signal trace is surrounded by two ground planes on the top and bottom, and vias are positioned on the sides to connect the two ground planes.

To get the signal from the top metal layer to a metal layer inside the PCB, attention has to be paid to two different aspects. First, in standard PCB technology, only a limited amount of via types are available. Due to this limitation, often vias are used that are longer than required. This creates a stub and can cause an impedance mismatch. Second, it is important to prevent leakage of the RF signal. Because not all via sizes are possible, fully shielding the signal via is not always possible and another solution has to be found.

In Fig. 3.5, a cross-section of the transition from the ABF IC to the BFN is shown. Due to manufacturing constraints, the via is too long and sticks out by  $435\ \mu\text{m}$ . For 28 GHz and a dielectric constant of  $\epsilon_r = 3$ , this extra length corresponds to  $0.07\lambda_g$ , with  $\lambda_g$  being the wavelength in the dielectric. This undesired extra via length results in a poorly matched transition and a relatively low power transfer as indicated in Fig. 3.6 by the dashed lines. These results are acquired using CST Microwave Studio. By following a standard matching

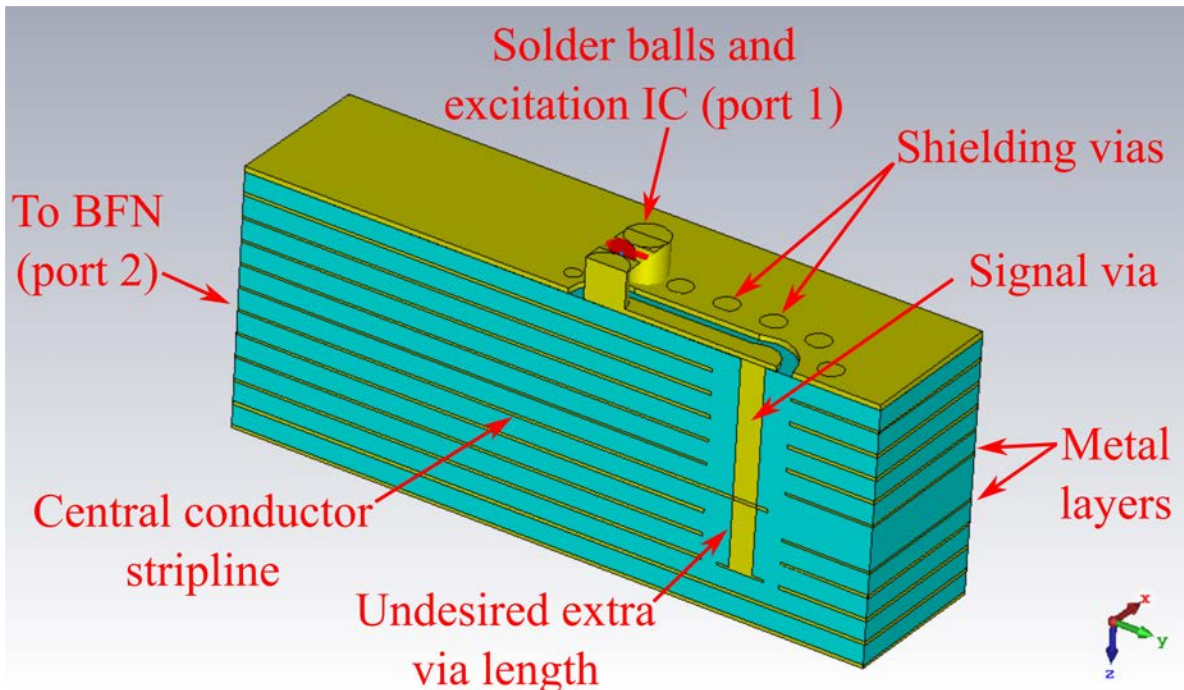


**Figure 3.5:** Cross-section of the ABF IC to BFN transition, indicating the undesired extra via length.

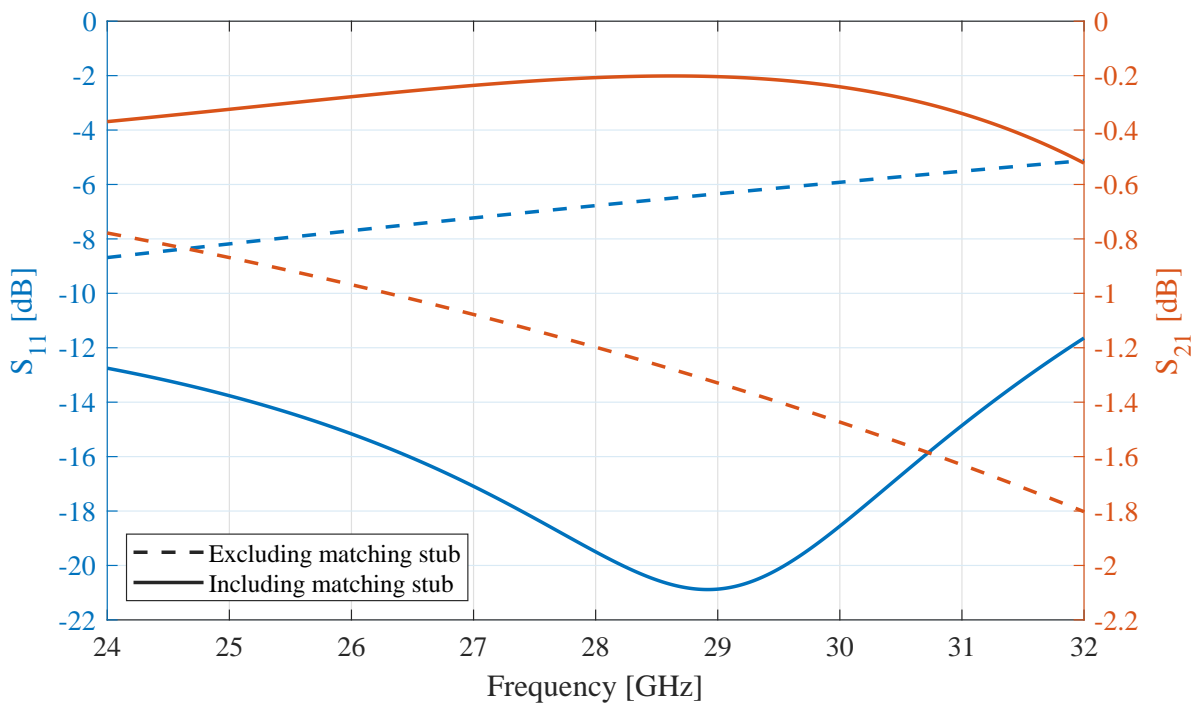
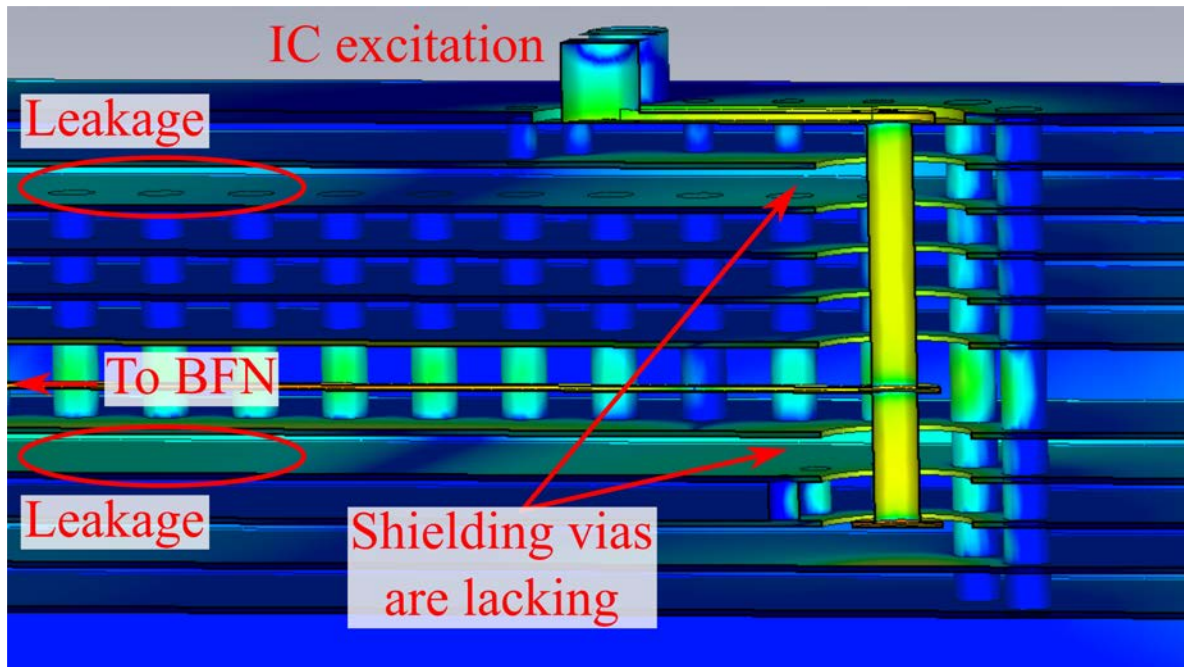
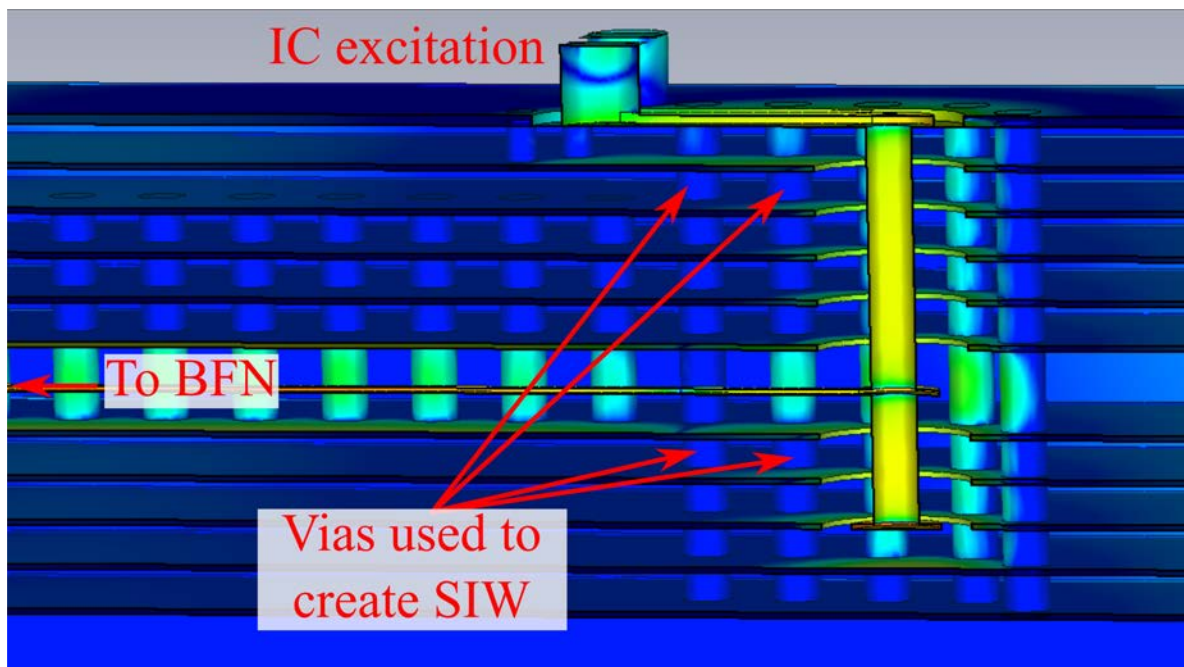


**Figure 3.6:**  $S_{11}$  and  $S_{21}$  of the ABF IC to BFN transition without (dashed) and with (solid) additional matching stub.



(a) Unwanted RF leakage (red ellipses) due to the lack of shielding vias.



(b) Using vias to create a SIW, preventing unwanted RF leakage.

**Figure 3.7:** Calculated E-fields of an IC to BFN transition. A cross-section of the model is shown, and the substrate is removed for visualization purposes.

procedure [41], dimensions of a matching stub have been calculated.<sup>2</sup> The resulting  $S_{11}$  and  $S_{21}$  are shown in Fig. 3.6 using solid lines, and an improvement is clearly visible. This matching procedure has been followed such that the reflection coefficient of every transition is well below -10 dB in the frequency band of interest.

In Fig. 3.5, also some metal layers, which serve as power or ground planes, are indicated. If the signal via is not properly shielded, parallel plate modes can be excited and the RF signal could possibly interfere with itself, degrading the performance of the BFN. As mentioned before, only a limited amount of vias as possible. Hence, due to these manufacturing constraints, surrounding the signal traces and signal vias with shielding vias might not be on all layers as vias needed on one layer would overlap with signal traces on other layers. In Fig. 3.7(a), the resulting E-field of a CST simulation of an IC to BFN transition is shown. It can be seen that between some planes, a shielding via is lacking. Between those metal layers, undesired leakage occurs, as highlighted by the red ellipses.

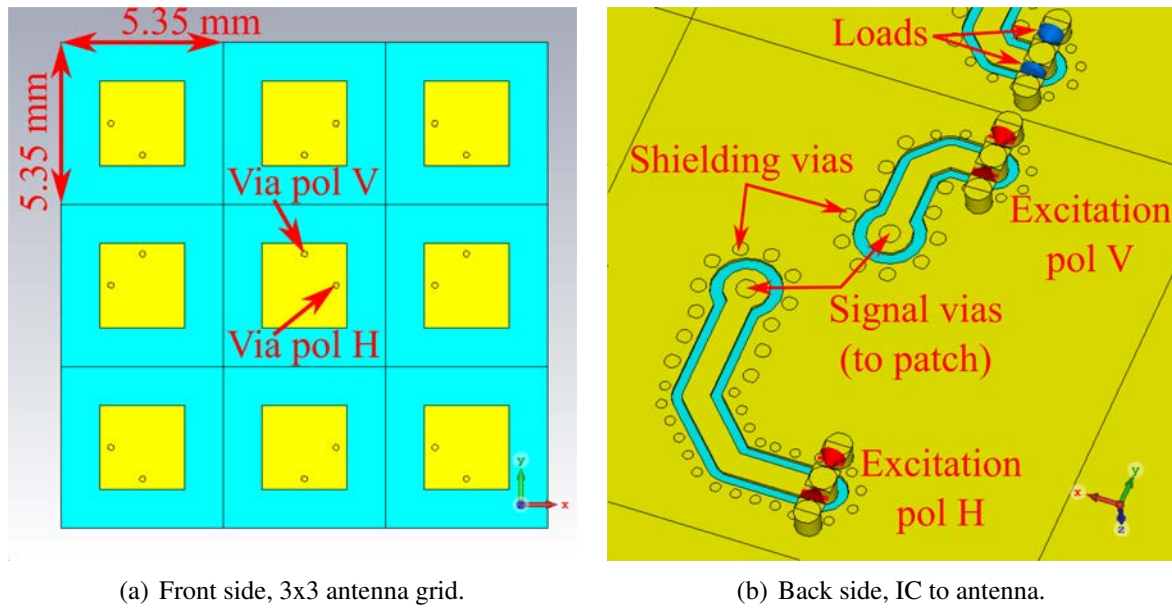
Instead of preventing RF leakage by fully enclosing the signal via, a substrate integrated waveguide (SIW) can be used for that purpose. SIWs are typically constructed by shorting two metal plates with two parallel rows of vias [42]. A SIW has a cut-off frequency, meaning that propagation below that frequency along the SIW is prevented. The manufacturing constraints did allow for creating SIWs having a cut-off frequency of higher than 100 GHz, and is, therefore, suitable for mitigating the undesired RF leakage. The effect of implementing a SIW is shown in Fig. 3.7(b). It can be concluded that by using vias to (locally) short the metal layers, unwanted RF leakage can be prevented, and thus no unwanted coupling through the PCB will occur.

### 3.2.7 Patch antenna elements

The antenna elements are made of square patch antennas and are positioned in an 8-by-9 planar grid. Due to the planar nature of patch antennas, these antenna types allow straightforward integration with the PCB and the electronics. The antennas are via-fed and are mostly dual-polarized. In Fig. 3.8(a), a 3-by-3 grid of the dual-polarized patch antenna is shown. The patch antennas are mirrored, introducing symmetry in the array design, which results in a more symmetric array radiation pattern [43]. In Fig. 3.8(b), the back side of the center antenna is shown. The two 100  $\Omega$  discrete ports represent the ground-signal-ground (GSG) feeding structure of the ABF IC and are used to excite the dual-polarized patch antenna in the simulation model. Figure 3.9 shows the reflection coefficient of the optimized antenna design for both the horizontal and vertical feed. Although the reflection coefficient of the vertically polarized antenna element is not below -10 dB in the entire frequency band of operation, the achieved reflection coefficient was deemed to be sufficient for the current project. In this simulation, the ports of the other eight antenna elements are terminated by two parallel 100  $\Omega$

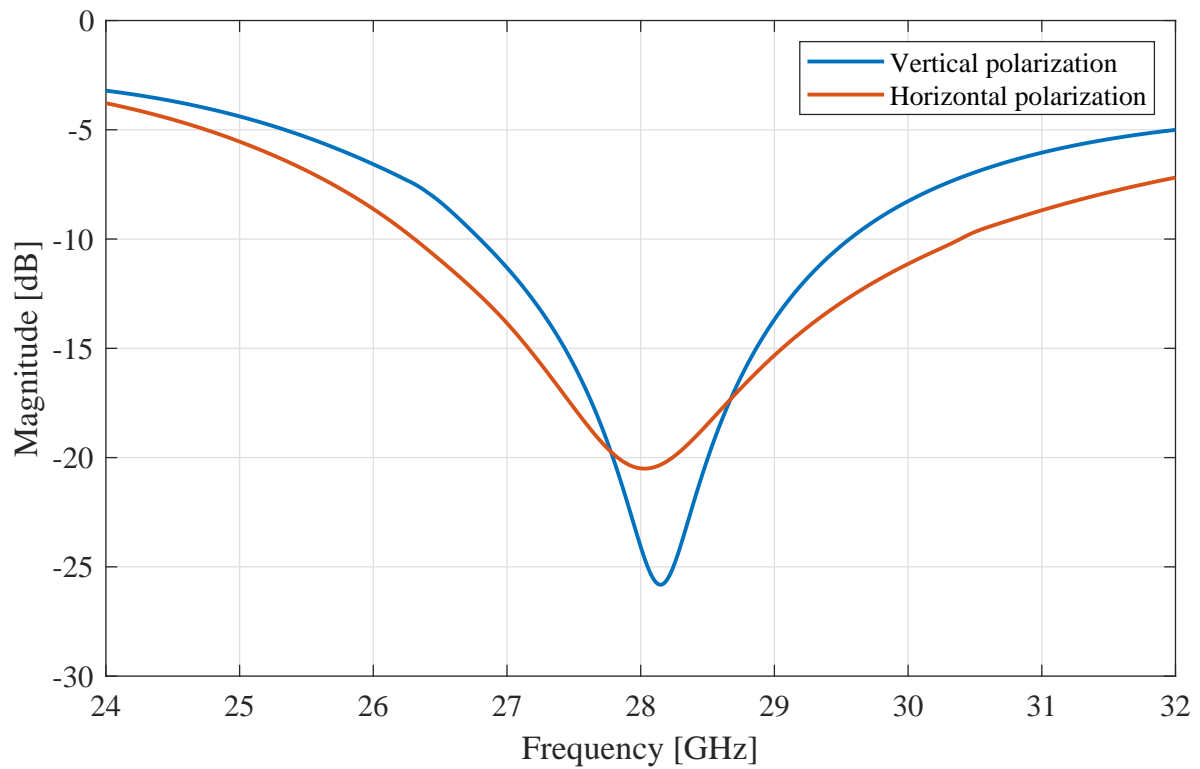
---

<sup>2</sup>Note that it is also possible to extend the signal via such that the extra length corresponds to  $0.25\lambda_g$ , and subsequently terminate it with a short.



(a) Front side, 3x3 antenna grid.

(b) Back side, IC to antenna.

**Figure 3.8:** Dual-polarized antenna model.**Figure 3.9:** Reflection coefficient of the dual-polarized patch.

loads.

To avoid grating lobes, typically, the spacing between antenna elements in the array is taken to be  $0.5\lambda_{\max}$ , with  $\lambda_{\max}$  the free-space wavelength associated with the highest frequency of interest. If, however, the scan angle is limited to a certain angle  $\theta_0$ , the maximum interelement spacing avoiding grating lobes can be calculated as follows [44]

$$d_{\max} = \frac{\lambda_{\max}}{1 + \sin \theta_0}. \quad (3.1)$$

For a maximum frequency of 29.5 GHz and a maximum scan angle of  $50^\circ$ , an interelement spacing of 5.75 mm is determined. In order to fit the dimensions of an off-the-shelf central processing unit (CPU) heat sink (see Section 3.2.9), an interelement spacing of 5.35 mm in both the horizontal and vertical direction has been chosen.

### 3.2.8 Assessment on stability

Since amplifiers are incorporated on the ABF IC, a stability check has to be performed to mitigate the risk of oscillations. Simulated S-parameter data of the ABF IC were available, allowing for the calculation of the K-factor and assessing the stability of the IC [45]. The reference plane of the available S-parameter data is at the solder balls of the ICs and does not include coupling through the PCB. Therefore, the coupling from input to output port when assembled on the PCB has been calculated using CST. Since no accurate 3D model of the IC was available, a few different simulations have been performed in an attempt to mimic the IC and its interaction with the PCB. For instance, the IC has been modeled using a metal plane, a silicon dielectric slab, and a combination of both. In Fig. 3.10, one of the simulation setups is shown in which the IC is replaced by free-space, ignoring the effect of the IC.

The resulting coupling from port 1 to port 2 or port 3 was added to the reverse transmission coefficient of the simulated S-parameter data of the IC and, in turn, the K-factor was calculated. In Fig. 3.11, the lowest determined K-factor is shown for both Tx and Rx. It can be seen that the K-factor is well above 1 over the entire frequency band. Although the K-factor being above 1 does not fully guarantee stability, this result creates confidence that the design will lead to a stable system.

### 3.2.9 Heat sink assembly

Each IC dissipates 1.3 W in Rx and 2.3 W in Tx. This means that if all ABF ICs are set in Tx, a total of 74 W is dissipated in an area as small as  $15.1 \text{ cm}^2$ . A low-cost passive thermal management solution is desired in the high-volume telecommunication industry [P13], hence, a commercially available off-the-shelf CPU heat sink has been selected for this array. The spacing between the antenna elements has been adapted such that the active area of the Mugen MAX CPU cooler from Scythe [46] matches the area of the ABF ICs.

Although the PCB stack-up is symmetric, still the PCB was slightly warped. This resulted in a height variation of the ICs in the order of a millimeter. This means that not all ICs have

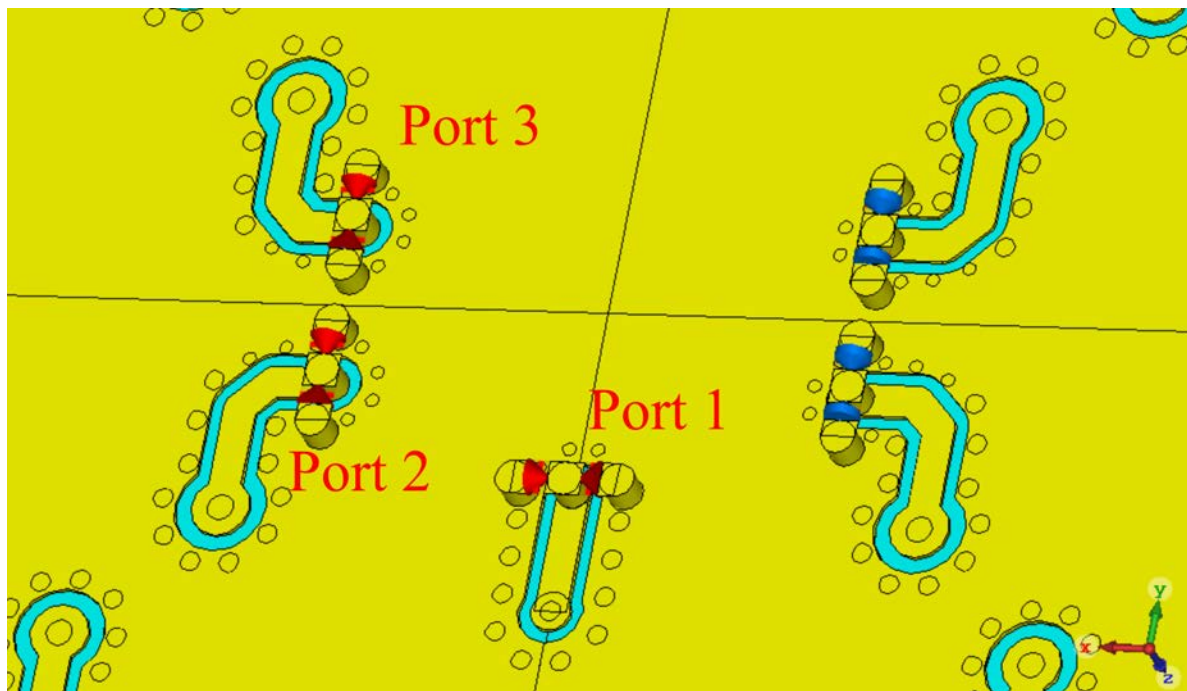


Figure 3.10: Simulation setup to calculate the coupling.

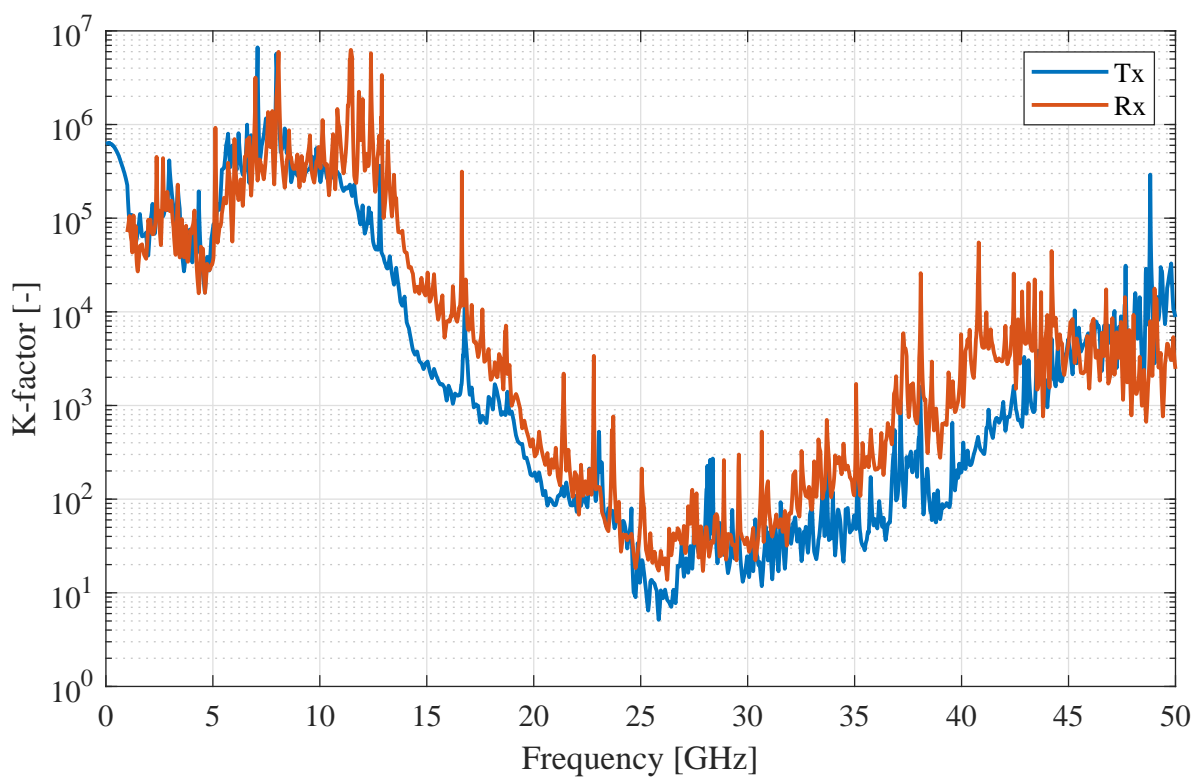
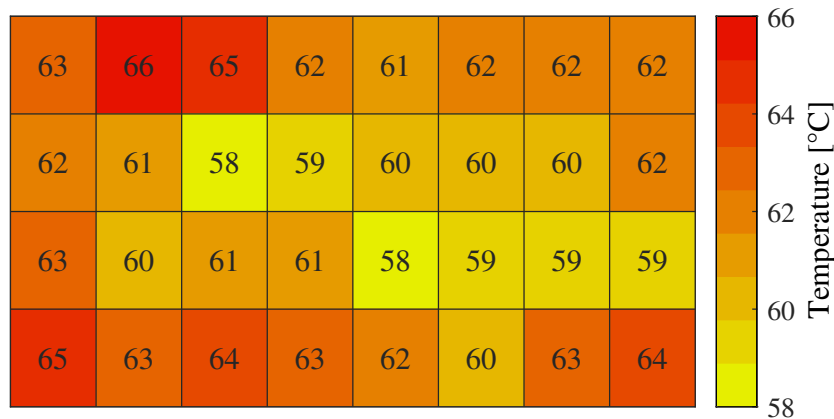


Figure 3.11: Determined K-factor to assess the stability of assembled ICs.



**Figure 3.12:** Steady-state temperatures of all ABF ICs in Tx.

good thermal contact to the heat sink if no additional measures are taken. Putting pressure on the board to enforce proper contact might break solder joints, so the use of a thermal interface material (TIM) layer that can cope with this height variation is desired. Two different types of TIM layers have been assessed; thermally conductive adhesive (SE 4422 from Dow Corning [47]) and soft thermal pads (TG-A1250 from T-global [48]). After assembling the heat sink, it was found that variation in temperature of the ICs was much higher when using the adhesive compared to the pads. Air bubbles were found to be present in the adhesive, most likely causing locally low thermal conductivity. This resulted in temperature variations along the PCB with a maximum of 40 °C. Such large temperature variations could result in a much earlier failure of the electronics of the hottest IC compared to the colder ICs, which is not beneficial in terms of the lifetime of the phased array. The resulting temperature readings of the ICs when using the thermal pad are shown in Fig. 3.12. It can be seen that in this case the deviation in temperature is maximally 8 °C, reducing the risk of one IC failing much earlier than the other ICs.

Note that although the deviation in temperature is only a few degrees Celsius, still the temperature of the ICs in the center is on average lower than the temperature of the ICs on the edges. This difference is most likely caused by the warpage of the PCB. If measures are taken to ensure that the thermal connection of each IC is more uniform, the overall lifetime of the phased array could be increased. Possible measures to balance the thermal conductivity are to introduce more copper symmetry in the PCB which reduces warpage, to create a heat sink that is made conformal to the heights of the ICs, or to strengthen the IC's connection to the PCB such that the PCB can be straightened by force without breaking the solder joints.

### 3.3 Characterization of the active phased array

In Fig. 3.13, the back side of an assembled antenna module is shown. As can be seen in the photo, the realized module is highly integrated. This high level of integration of typical 5G mm-wave arrays does not allow for the characterization of individual components. Char-



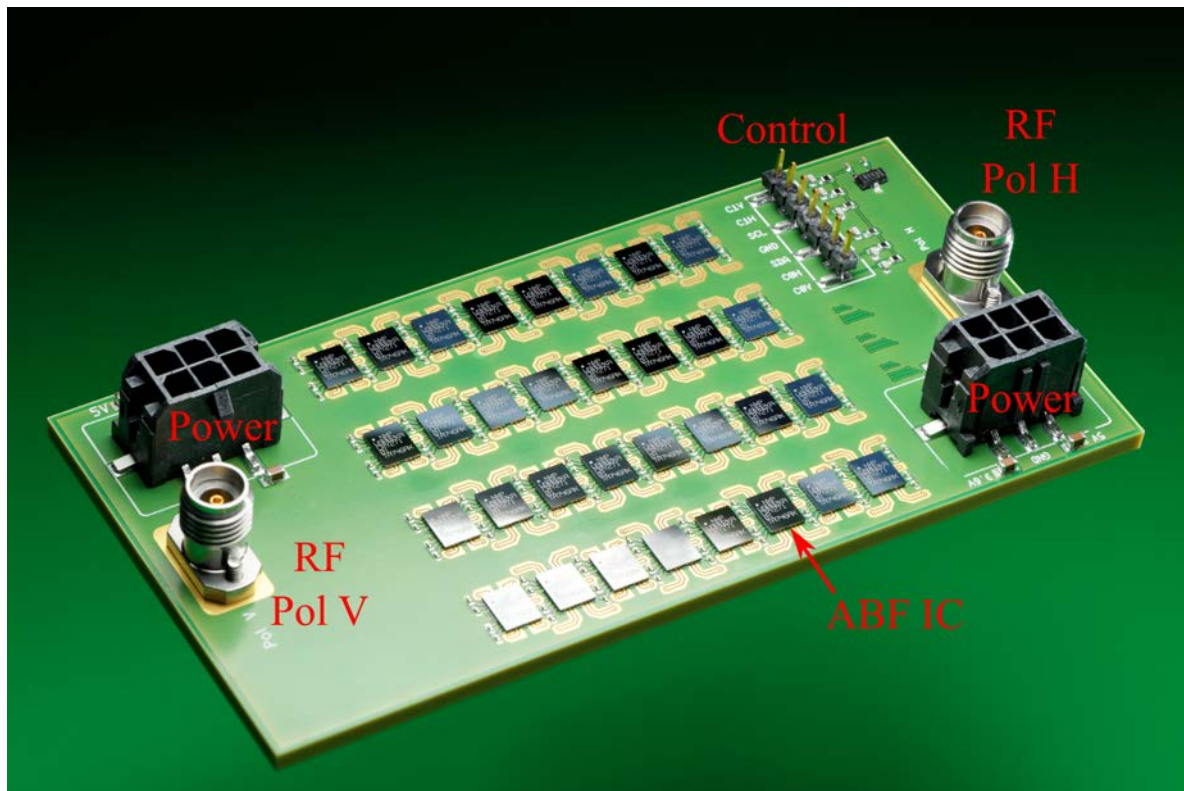


**Figure 3.13:** Assembled PCB of the active phased array.

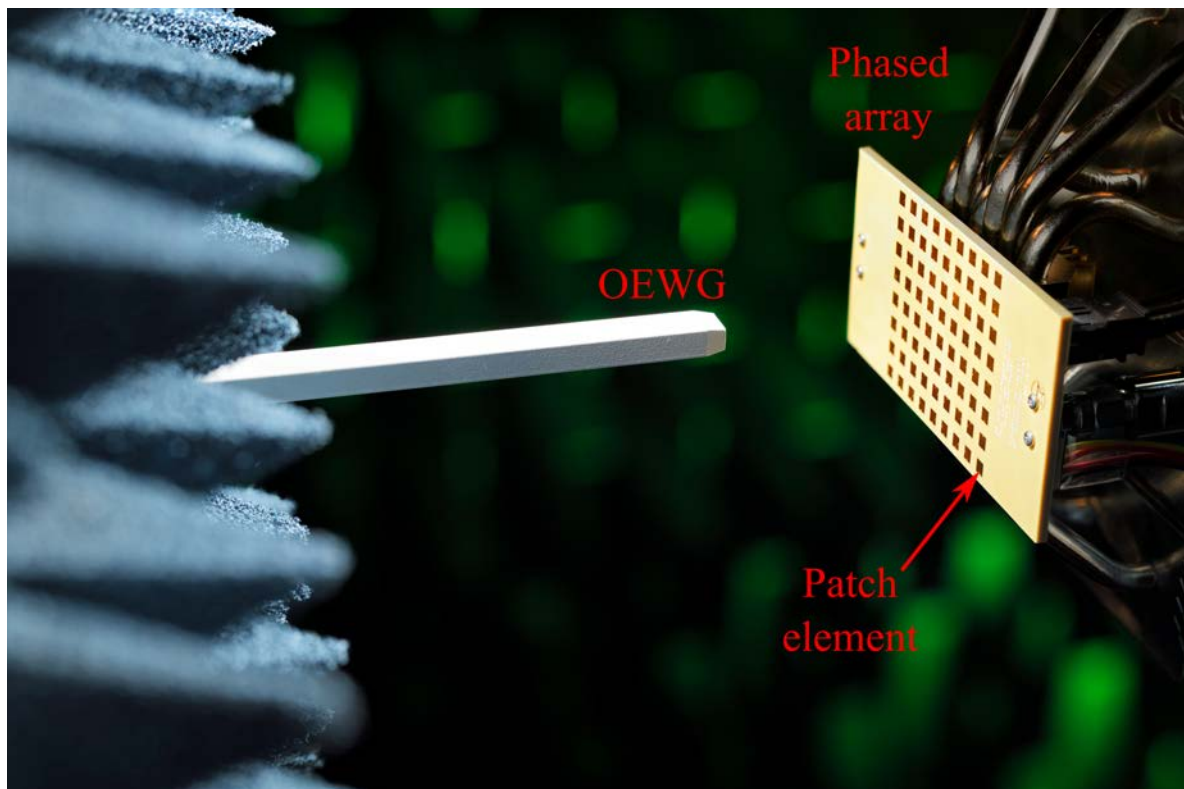


**Figure 3.14:** Measurement setup in the anechoic chamber containing the WR-28 OEWG probe (left) and the active phased array (right).

acterizing these individual components requires a separate prototype, resulting in additional complexity and associated costs. Hence, it is desired to conduct measurements that allow for the verification of one or multiple functionalities of the individual components. In the upcoming subsections, OTA measurement results are presented that are used to deduce the performance of several individual components. These measurements were performed in the anechoic chamber of Eindhoven University of Technology [49]. In Fig. 3.14, the assembled antenna module is shown in the OTA measurement setup that has been used to acquire the results from Section 3.3.2 to Section 3.4.1.

### 3.3.1 Reflection coefficient measurement

The most straightforward measurement to perform first is a reflection coefficient measurement, having the reference planes at the RF connectors of the antenna module. In Fig. 3.15, the result of an  $S_{11}$ -measurement for the horizontal polarization is shown in blue. Using CST, a full-wave simulation was performed on the BFN and its transitions, and the calculated reflection coefficient is shown in Fig. 3.15 in red. It is evident to see that the simulated and measured results do not match. The trough indicating the best impedance match seems to have shifted from around 27 GHz to about 32.5 GHz. Moreover, a large frequency dependent ripple is present in the measured results, whereas this ripple is much lower in the simulated results. After some investigation, it seemed that the electromagnetic 3D model of the RF connector, which was downloadable from the manufacturer's website, was lacking some details. Based on a new 3D connector model, the CST model was updated and resimulated. The resulting reflection coefficient is illustrated in Fig. 3.15 in yellow. The large difference in the two achieved simulation results emphasizes the importance of including an accurate connector model.

The  $S_{11}$ -measurement and simulated results of the vertical polarization showed similar behavior as shown in Fig. 3.15. To prevent repetition of results, the results of the vertical polarization are not shown here and in the remainder of this chapter, unless specified otherwise.

### 3.3.2 Performance analysis of the beamforming network

Although the results of the reflection coefficient measurement and the updated simulation in Fig. 3.15 show a similar trend, still some discrepancies are present. The large ripple, especially in the frequency band of interest, indicates that more reflections are coming from the BFN than initially anticipated. This raises the question whether the BFN performs as expected.

Ideally, if the antenna module is used in Tx, the power is equally split among all 16 ICs, regardless of frequency. If it is assumed that the ICs are approximately the same, it is expected that all the power amplifiers (PAs) inside the ICs reach the 1-dB compression point (P1dB) for equal input power  $P_{in}$ . To verify whether this is the case, a sweep on the input power of the array was performed. In this sweep, only one out of the 16 ICs was active and the

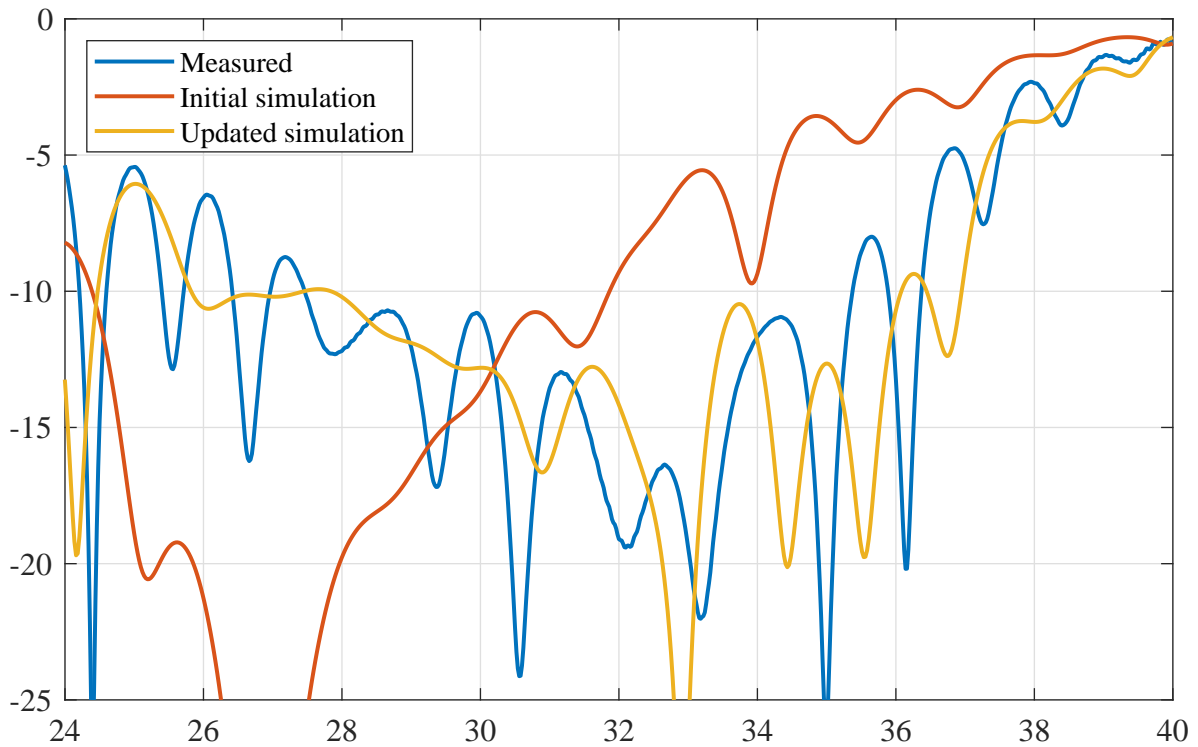


**Figure 3.15:** Simulated and measured reflection coefficient of the module.

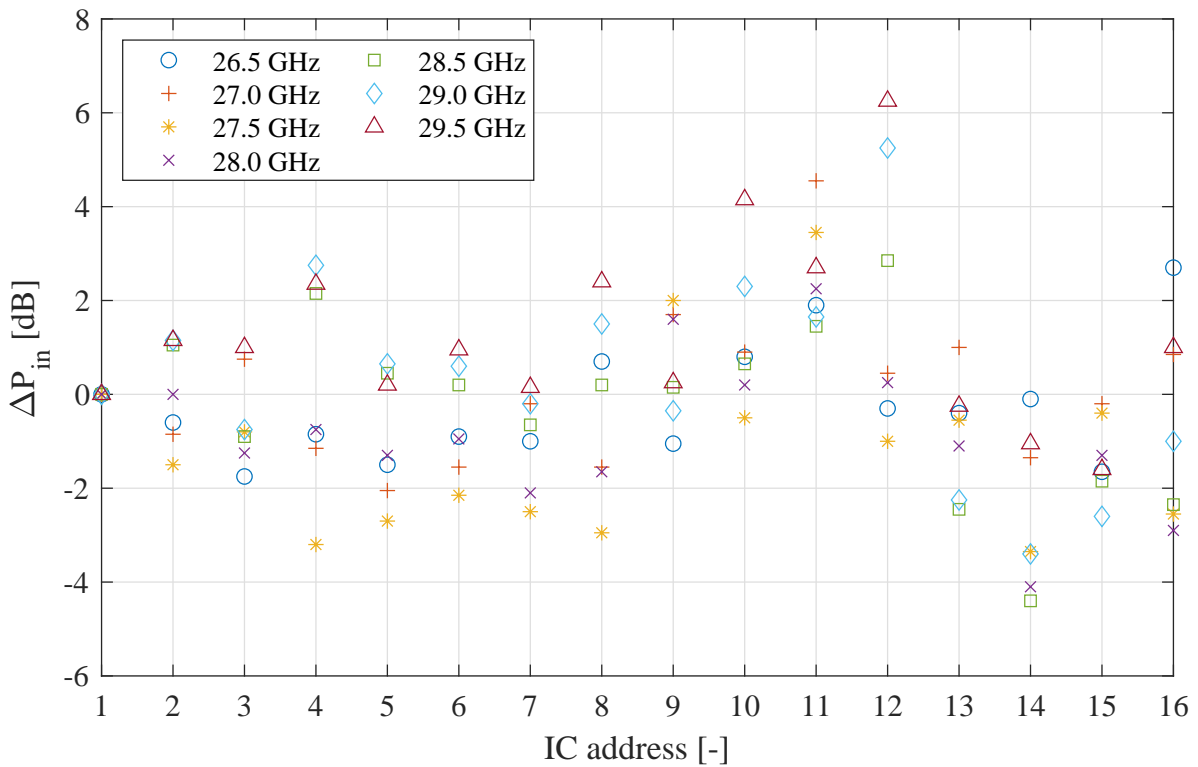


**Figure 3.16:** Difference in input power before reaching compression for 16 ICs connected to the same BFN. The large spread indicates that the BFN does not distribute the power equally to all ICs. The results are normalized to IC address 1.

input power that corresponded to the IC's P1dB was determined using an OTA measurement. The results of this power sweep are shown in Fig. 3.16. Here, the required input powers are normalized to the first IC. If  $\Delta P_{in}$  is positive, the IC required more power before reaching the 1-dB compression point, indicating that the power arriving at the IC was lower compared to the first IC, and vice versa. Due to manufacturing tolerances in the IC manufacturing process, a deviation in the order of 1 dB was expected. However, as can be seen in Fig 3.16, for one frequency, deviations as large as 7 dB were measured, indicating that the BFN does not perform as desired.

In Section 3.2.5, it is shown that the use of T-junctions in a BFN, subject to manufacturing errors and asymmetries, could lead to variations in the order of 3 dB. As can be concluded from Fig. 3.16, that result was underestimated. The large dynamic range of the ICs does partly allow for calibrating the array and compensating for variations of 7 dB. However, since the variation in input power is also highly frequency dependent, calibration will only be suitable for continuous-wave or smallband signals. Since the anticipated maximum bandwidth for the 5G mm-wave frequency band is 400 MHz [8], the use of Wilkinson junctions is recommended in future designs to ensure a smaller frequency dependency of the array's performance, at the cost of increased complexity and associated costs.

### 3.3.3 Normalized ABF IC response

Since only a discrete set of amplitudes and phases can be realized with the ABF ICs, quantization errors will occur. Moreover, the ABF IC exhibits non-linearities, which makes the amplitude and phase response of the IC hard to predict. Furthermore, as a result of tolerances in the IC manufacturing process for mass production, the response of every RF channel of every IC is, in general, different. A typical amplitude and phase response of the IC is shown in Fig. 3.17. The measurements are normalized to the maximum gain and default phase setting since only relative changes are of interest. The contours indicate the response for constant amplitude setting. The small circles indicate the individual measurement points, where the phase setting increases as the color of the small circles changes from light green to black. It can be observed that the phase response is not perfectly linear, and that the amplitude and phase settings are not completely independent.

To select the setting that results in the optimal excitation of an antenna element, a (subset of the) response as shown in Fig. 3.17 has to be determined for that particular element. Since tolerances in the manufacturing process cause the ICs to be different, the response has to be measured for every antenna element individually to find the optimal excitation for a particular array radiation pattern. This is a time consuming task and is not desired for mass-produced phased array systems. Instead, it is possible to treat the excitation errors caused by the spread as random errors, and the model presented in Chapter 2 can be used to analyze the impact of these random errors on the radiation pattern of the phased array. If, based on this analysis, the errors in the excitation do not meet the requirements of, for example, the maximum allowed SLL, either more amplitude and phase combinations have to be measured, or the manufactur-

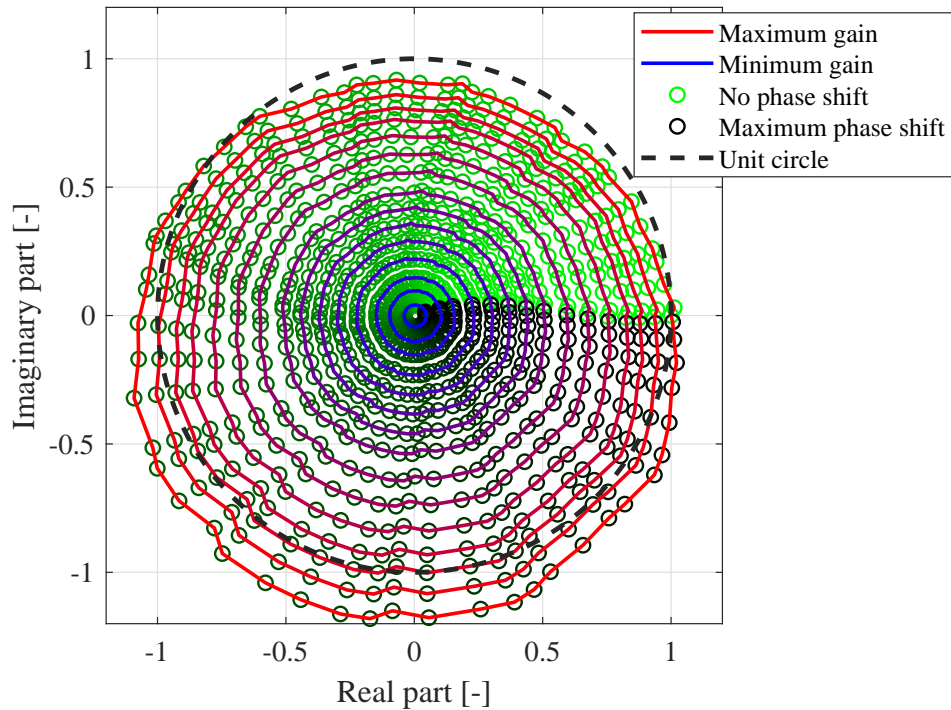


**Figure 3.17:** Measured complex response of one of the elements for a limited amount of different amplitude and phase settings. The measurements are normalized to the response where maximum gain and no phase shift is applied.

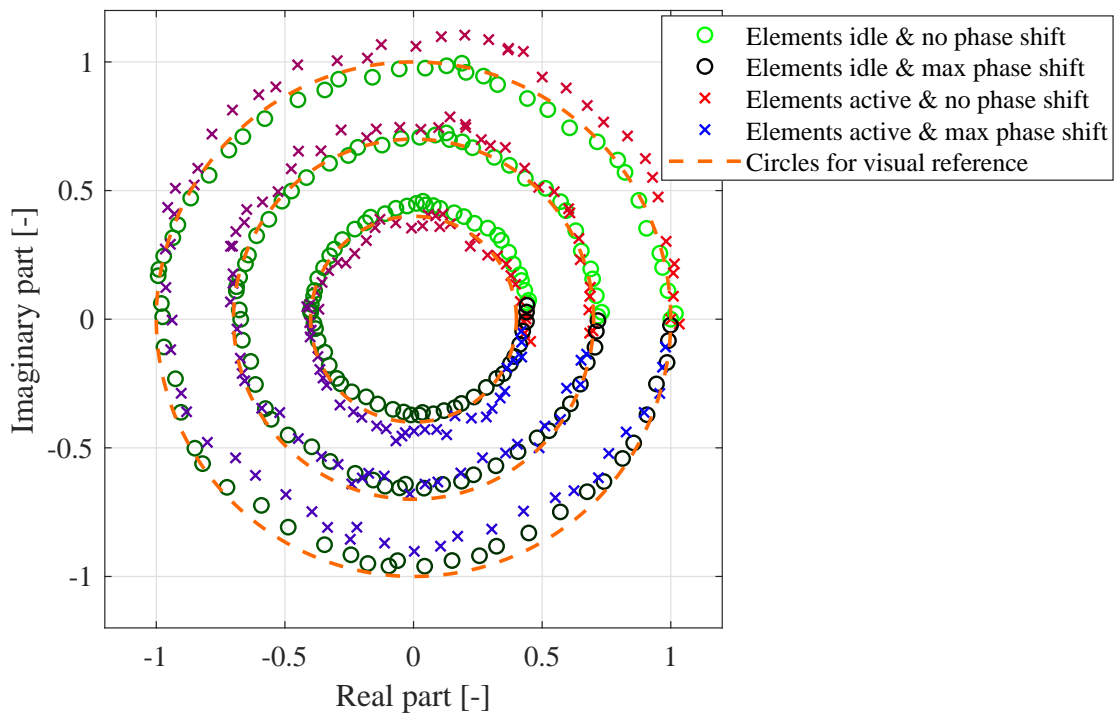


**Figure 3.18:** Measured complex response of one of the elements for a few different amplitude and phase settings, while (o) all other elements are idle and (x) when all other elements are active.

ing process has to be adapted such that the spread from one IC to the other is reduced.

Note that the response in Fig. 3.17 is also dependent on frequency, temperature, bias voltage, and on whether the antenna is used in Tx or Rx. The presented results were obtained at room temperature, while using a fixed bias voltage. The used frequency was  $f = 28$  GHz, and the antenna was used in Tx.

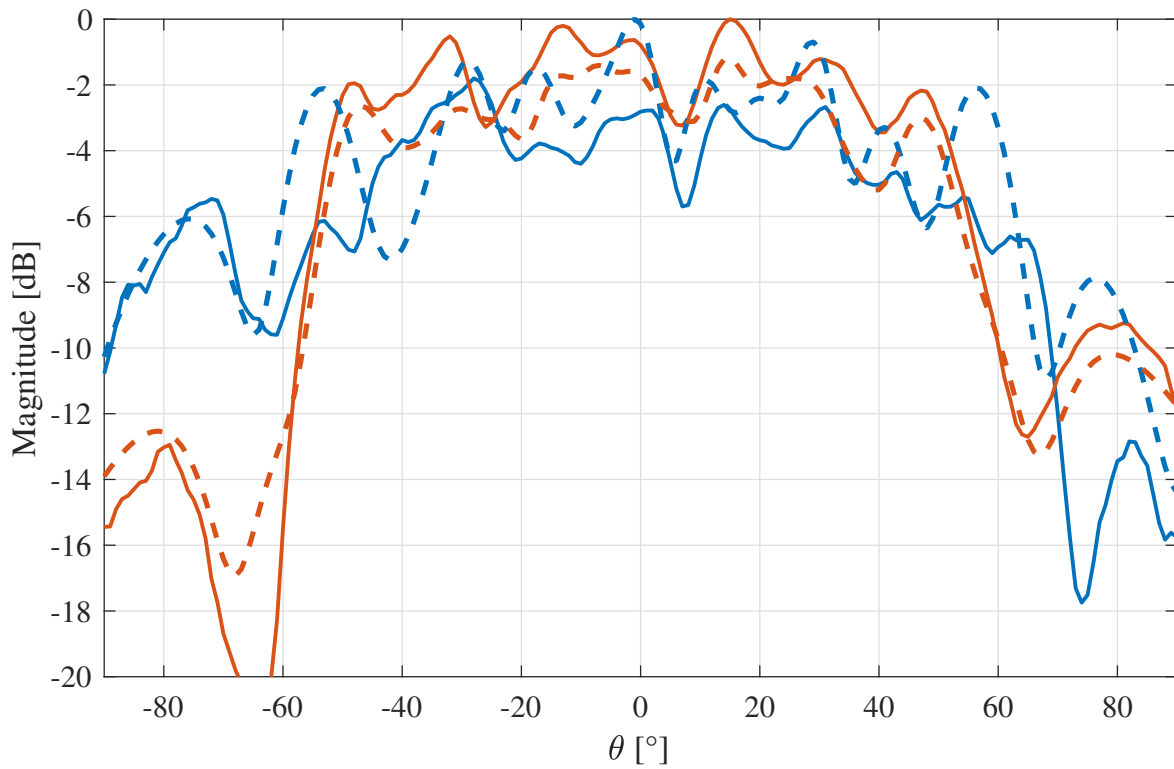
### 3.3.4 Load pull effects on the ABF IC response

The response shown in Fig. 3.17 was measured in isolation, meaning that only that particular element was radiating, whereas all other elements were turned off. During normal operation, all elements will be active and mutual coupling will occur between the elements. This can alter the input impedance of the antenna and can subsequently change the performance of the PA. In Fig. 3.18, the response of a center element is shown for three different amplitude and 64 different phase settings. The small circles represent the element's isolated response in the same way as in Fig. 3.17. The crosses show the individual measurement points where all other elements were active as well. The phase setting increases as the color of the crosses changes from red to blue. If no mutual coupling between the elements was present and/or the PA would be insensitive to load pull effects, the circles and crosses in Fig. 3.18 would be on top of each other. However, it can be observed that the response of the IC is significantly altered by the radiation of the other elements. The impact of this effect is discussed in Section 3.4.1.

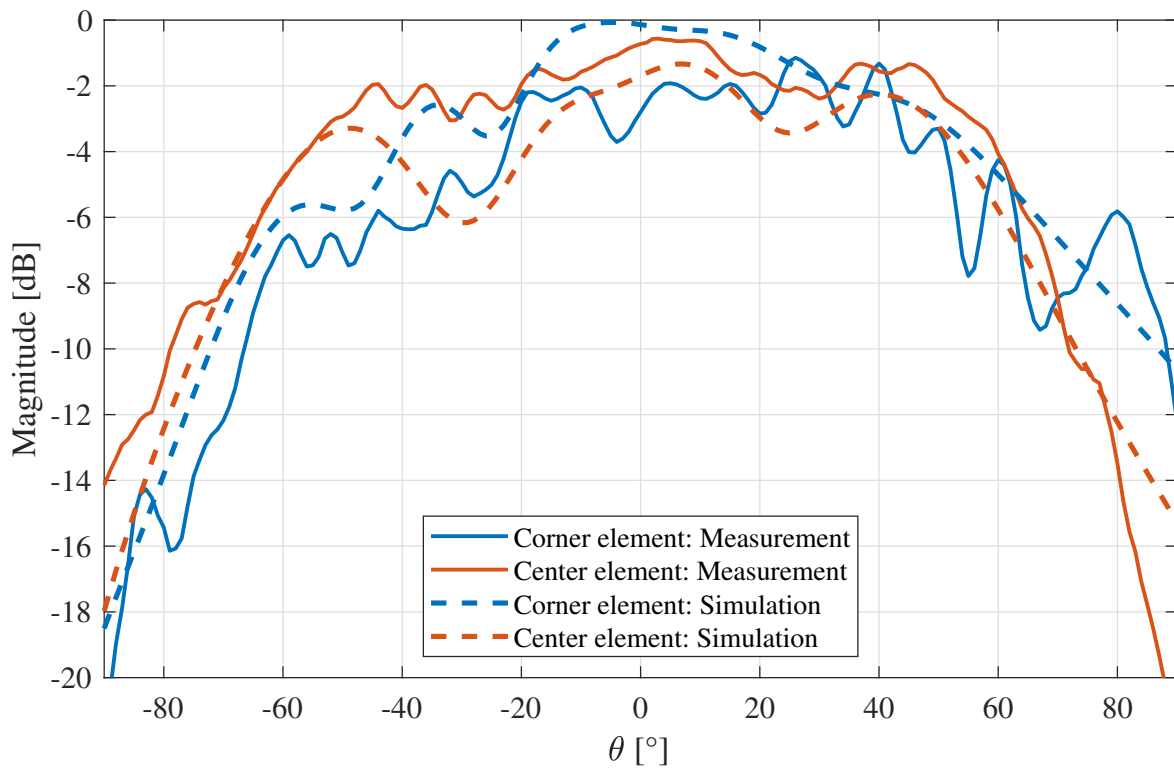
Also here, the response in Fig. 3.18 is also dependent on frequency, temperature, bias voltage, and on whether the antenna is used in Tx or Rx. Moreover, the response also depends on the gain and amplitude settings of all other elements, meaning that the response is also sensitive to scanning and tapering. The presented results were obtained at room temperature, while using a fixed bias voltage. The used frequency was  $f = 28$  GHz, and the antenna was used in Tx. All other elements were phase calibrated using the procedure shown in Section 3.4.2 such that the maximum contribution was in broadside.

### 3.3.5 Embedded element patterns

To measure the EEPs of the patch elements, a planar near-field scanner from NSI-MI Technologies [50] was used. Using a near-field to far-field transformation, the embedded radiation pattern was found. Figure 3.19 shows the obtained embedded radiation patterns of the E- and H-plane for a corner and a center element using solid lines. The EEPs acquired by performing a full-wave simulation of the PCB are depicted as well using dashed lines. Although some similarities can be found between the measured and simulated EEPs, at most angles the results are several dBs off. The main contributor to these discrepancies is most likely the metal heat sink in combination with surface waves and guided waves inside the patch's substrate. No measures were taken that prevent waves to travel towards the edge of the PCB and diffract. A portion of the diffracted waves will excite the heat sink and, in turn, affect the overall radiation pattern. Whereas diffraction of the waves at the edge is taken into account



(a) E-plane.



(b) H-plane.

**Figure 3.19:** The (a) E-plane and (b) H-plane of a measured (solid) and simulated (dashed) embedded element pattern of a corner (blue) and center (red) patch element.

in the full-wave simulations, the heat sink was omitted because otherwise the model became unpractically large in terms of required memory and computation time.

It can also be seen that the corner and center element show significant differences. The radiation pattern of an antenna is, in general, dependent on its direct environment. This dependency can be reduced by isolating the radiating element by adding via fences or electromagnetic bandgap (EBG) structures, for instance. Since no measures were taken to isolate the elements, the corner and the center element were expected to have a different EEP due to their different direct environment. Despite that, it is shown in Section 3.4.1 that by taking into account the EEPs of the elements, the array radiation pattern can be very well controlled. Measuring the EEP of all elements is time consuming, however, making it unpractical for mass-produced phased array systems. Instead, it is recommended to take measures to reduce the mutual coupling from one element to another and make the antenna element less dependent on its direct environment.

### 3.4 Calibration of the active phased array

The overall purpose of an antenna array is, by optimally exciting the individual elements, to realize a radiation pattern that has certain desired characteristics. Due to errors in the design and/or manufacturing tolerances, the achieved element excitations might be different than the optimal element excitations, resulting in a sub-optimal radiation pattern. By calibrating the array, this issue can be overcome. The desired radiation characteristics of a 5G mm-wave phased array depend eventually on the protocols for 5G, which are currently under development, and on regional regulatory agencies. Hence, at the moment of writing, a preferred calibration procedure cannot be determined. Nevertheless, in this section, three different options of array calibration are discussed to show the capabilities of the realized active phased array.

In Section 3.4.1, the ability to shape the radiation pattern of the array is shown. In this case, a beam is formed towards a certain direction, while maintaining an SLL of  $-20$  dB. Having a low SLL is useful to minimize interference from one device to another, but comes at the cost of a lower gain (and thus lower EIRP) of the antenna system due to the required amplitude tapering. Moreover, ensuring low side lobes typically requires good knowledge of the EEPs. This implies that either the simulation models have to be accurate, or that the radiation pattern of each element has to be measured.

If solely the radiated power towards a user is of interest, a phase calibration is sufficient. If it is assumed that the EEPs are equal and that the achieved phase shifts for different phase settings of the IC are equal, a phase calibration has to be performed only once and it will be valid for all other scan angles. If this is not the case, however, the same calibration procedure can be used for different angles as well. In Section 3.4.2, a phase calibration for broadside is performed and the increase in antenna gain is shown.

During operation, environmental effects and aging of the electronics will impact the per-



formance of the antenna array over time. The procedures described in Section 3.4.1 and 3.4.2 are suitable to calibrate the array in a measurement facility, but cannot be used to calibrate the array once installed in the field. To cope with that issue, an online calibration procedure that does not require any additional hardware other than an RF signal source, a receiver and the array itself is presented in Section 3.4.3.

### 3.4.1 Shaping the array radiation pattern

To determine the element excitations required to achieve a certain array radiation pattern, standard synthesis techniques like Dolph-Chebyshev [51] or Taylor [52] tapering are available. These synthesis techniques are computationally inexpensive and readily implemented. By using these techniques, assumptions on the radiation pattern of the individual antenna elements in the phased array are typically made, which in practice often leads to inaccurate results. Other methods have been developed to acquire more accurate results, for example, genetic algorithms [53], [54] or swarm optimization algorithms [55]-[57]. These methods are typically very accurate, but come at the cost of increased computation times, resulting in increased design times.

In [15], a ‘best-of-both-worlds’-method is presented. There, an iterative closed-form optimization algorithm to shape the radiation pattern in one planar cut is presented. This algorithm yields an accurate performance, while maintaining an acceptable calculation time. To achieve the radiation patterns shown in this subsection, the algorithm reported in [15] is extended to shape the full radiation pattern (see Appendix B), instead of controlling the radiation in one planar cut. The main idea of the algorithm and the implemented extension is as follows. First of all, the algorithm requires a mask of the desired radiation pattern. In this subsection, the mask is defined in terms of a steering angle in both the elevation and azimuth direction, denoted by  $el$  and  $az$ , respectively, and a minimum SLL. Moreover, the EEP of every individual element of the antenna array is assumed to be known. The radiation patterns of all elements have been measured (see Section 3.3.5) and these patterns are used as input for the algorithm. Subsequently, the algorithm determines the excitation for each element such that the array pattern fulfills the constraints of the mask, while at the same time minimizing the radiation coming from directions other than the main lobe.

The algorithm determines weights for each element without any constraint on the values of the excitations. Since not every complex excitation can be found, due to non-linearities and quantization (see Fig. 3.17), the combination of excitations resulting in the smallest error possible was chosen. The error is in this case defined as the absolute value of the difference between the optimum excitation and the chosen excitation, summed over all elements.

To illustrate the capabilities of the phased array and the algorithm, uv-plots of array radiation pattern measurements are shown for six different beamforming scenarios in Fig. 3.20. The location of the desired scan angle and achieved maximum are indicated by the red cross and purple dot, respectively. As can be seen in Fig. 3.20, in some cases, the desired scan angle and achieved maximum are off by a few degrees. However, the radiation pattern at the desired

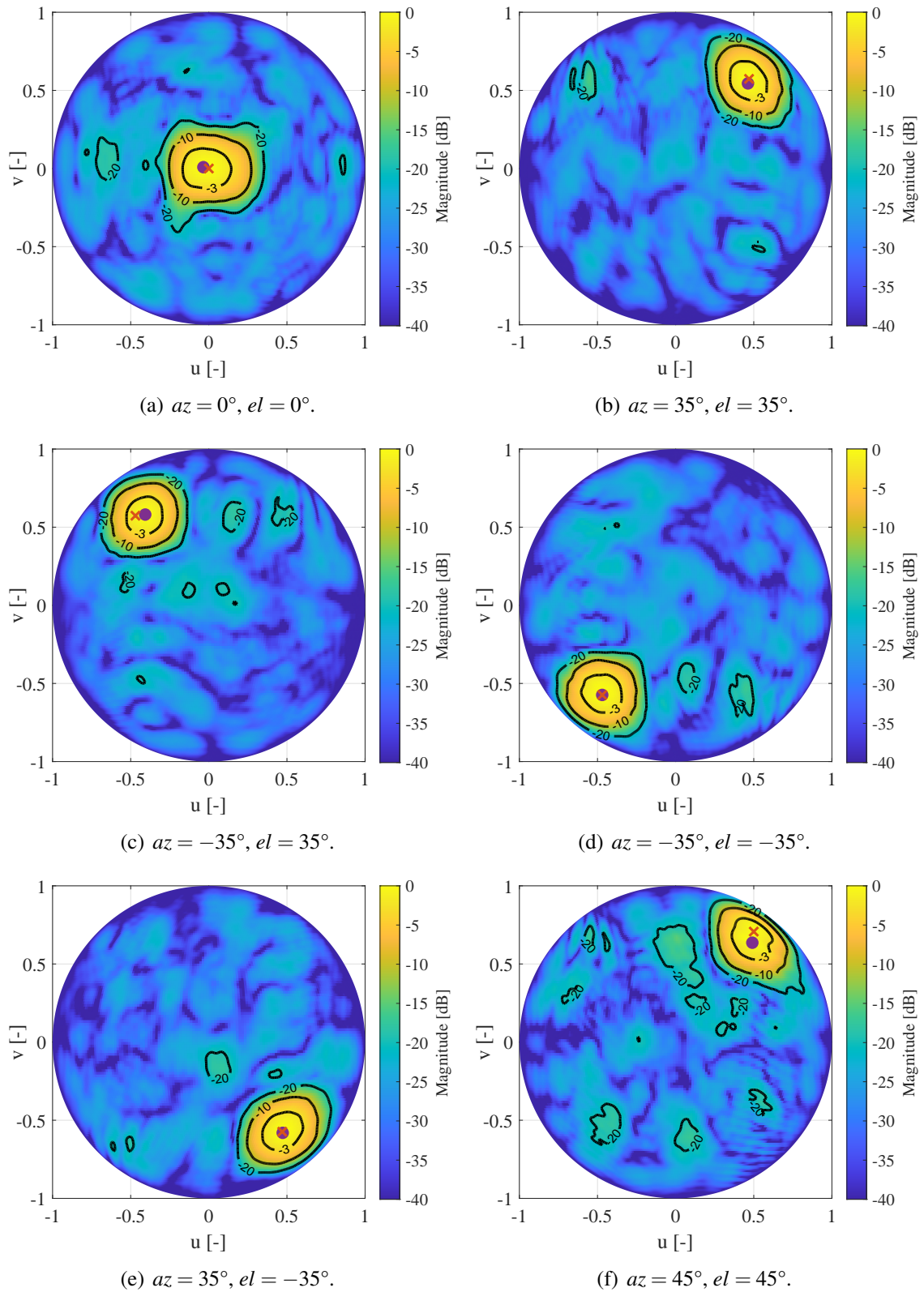


**Figure 3.20:** Measured radiation patterns for different beamforming scenarios. The goal was point the beam in a certain direction and simultaneously reach an SLL of -20 dB. The target and the achieved maximum are indicated by the red cross and purple dot, respectively.

scan angle is always within the  $-3$  dB contour with respect to the measured maximum. In fact, in all the assessed beamforming scenarios ( $-45^\circ \leq az \leq 45^\circ$ ,  $-45^\circ \leq el \leq 45^\circ$ ) this was the case.

An additional goal was to have an SLL of  $-20$  dB or lower in each of the beamforming scenarios. In each of the measured patterns in Fig. 3.20, contours are drawn for  $-3$ ,  $-10$  and  $-20$  dB. Hence, apart from the contours around the main lobe, the contours shown in Fig. 3.20 indicate the locations of side lobes exceeding  $-20$  dB. In all six scenarios, contours are present outside of the main lobe region, implying that the target SLL of  $-20$  dB is not accomplished. Likewise, an SLL of  $-20$  dB was hardly met in the 361 assessed beamforming scenarios, since almost always some small regions exceeded the limit. Especially at scan angles of  $40^\circ$  onwards, the performance deteriorates and more side lobes start to exceed  $-20$  dB, as can be seen in Fig. 3.20(f), for instance.

The discrepancies in desired and achieved radiation pattern is most likely caused by load pull effects. As can be seen in Fig. 3.18, the achieved element excitation changes under the effect of other elements. This effect is deterministic and can, in principle, be taken into account. However, much more measurements have to be performed to completely compensate for load pull effects. Therefore, if a strict SLL is required in the intended application, it is recommended that either the mutual coupling between the elements has to be reduced, the IC has to be made less sensitive to load pulling, or a combination of both.

### 3.4.2 Phase calibration and EIRP

If the SLL is not of interest, and solely the radiated power towards a user should be maximized, a phase calibration is sufficient. In the left column of Fig. 3.21, the phase of each individually excited element along the array is shown for three different frequencies when no phase shift is applied by the ICs. The large phase deviation over the elements implies that the radiation from the individual elements would not completely constructively interfere if all elements are excited simultaneously. The phase has been measured in a far-field setup where the distance between the antennas was 1.5 m. The distance between the center of the array to the center of a corner element is 26 mm. This makes the maximum difference in path length from any element to the opposite antenna 0.23 mm. At a frequency of 29.5 GHz, this corresponds to a phase difference of  $8^\circ$ . In the left column of Fig. 3.21, however, the deviation in phase is much higher than  $8^\circ$ , implying that the phase deviation is caused by the array itself instead of being a measurement artifact.

To compensate for the deviations in measured phase, an iterative searching routine was performed. First, the phase of an uncalibrated element is determined. Based on the measured phase, an estimate of the required phase setting is calculated in an attempt to achieve a certain phase reference, for instance  $0^\circ$ . In this case, the estimate is based on the phase shift of an ideal 6-bit phase shifter. If the phase setting is set, the element is measured again and compared to the reference phase of  $0^\circ$ . This procedure is repeated until a desired accuracy is reached, and is repeated for every element. Moreover, since the array contains all kind

of frequency-dependent components, such a calibration procedure has to be repeated for different frequencies if the array will be operating at different frequency bands. The results of this calibration procedure are illustrated in the right column of Fig. 3.21. As can be seen, the phase deviation is much smaller compared to the uncalibrated array and is below  $2^\circ$  on average.

In Fig. 3.22, the improvement in gain of a calibrated versus an uncalibrated array is shown. In this case, a phase calibration has been performed for three different frequencies, and the improvement has been measured over a wider frequency range. As expected, the improvement in gain in the center of the frequency range is highest when the calibration was performed at 28.0 GHz. Similarly, the improvement in the lower part and upper part of the frequency band is highest when the calibration was performed at 26.5 and 29.5 GHz, respectively. Moreover, although a phase calibration can, in principle, be performed for only one frequency, Fig. 3.22 shows that the gain can be increased over a much wider frequency range.

Since the aim of a phase-only calibration is to maximize the power towards a user, the EIRP, which is defined as input power times realized gain, of the array at P1dB has been determined. For this measurement, first a phase calibration was carried out. A standard gain horn (SGH) having a known gain was positioned opposite to the array at a distance of 1.5 m. Then, a sweep on the input power of the array was performed to determine for what input power the array reaches compression. Subsequently, the gain of the array was determined using a relative-distance sweep as described in Chapter 4. This procedure is repeated for seven frequencies and both polarizations, and the resulting EIRP at P1dB is shown in Fig. 3.23 using the solid lines. Error bars are included that indicate the  $2\sigma$ -confidence intervals. These error bars are based on the uncertainty of the used power meter, the reference load which was used to calibrate the power meter, and the uncertainty in the determined gain of the array. As can be seen in the figure, an EIRP in the order of 54 to 55 dBm was measured. Based on CST simulations and the datasheet of the IC, an EIRP in the order of 58 dBm was expected. This discrepancy of 3 to 4 dBm is most likely due to the following two reasons. As shown in Fig. 3.16, the ICs reach P1dB for different input powers. As a result, when the array reaches compression, some ICs are beyond their P1dB, whereas other ICs are still in their linear regime. This implies that if all ICs would reach compression for the same input power, the measured EIRP at P1dB would have been higher. Moreover, the measured gain of the array is 1 to 2 dBi lower compared to the expected gain. Effects due to mutual coupling (i.e., changing active impedance of the elements and load pulling) are probably the cause of this reduction in gain.

### 3.4.3 Online calibration

During operation, environmental effects and aging of the electronics impact the performance of the antenna array over time. To compensate for these effects, the array has to be recalibrated periodically. The procedures described in Section 3.4.1 and 3.4.2 are suitable to calibrate the array in a measurement facility, but cannot be used to calibrate the array once installed in the

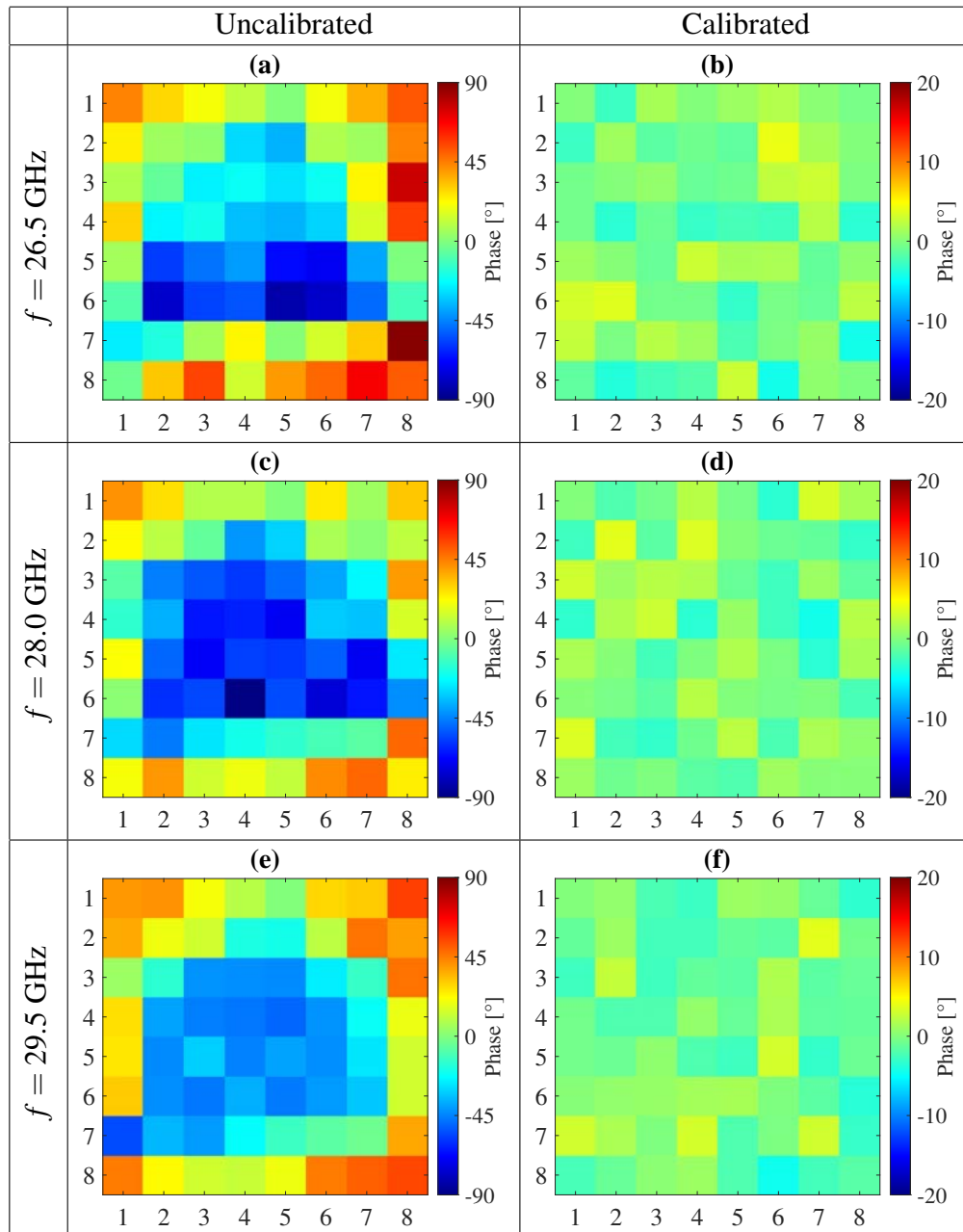


**Figure 3.21:** Measured phases of all 64 elements when no calibration is performed (left column) and when a phase calibration is performed (right column). The array has been calibrated on three different frequencies.

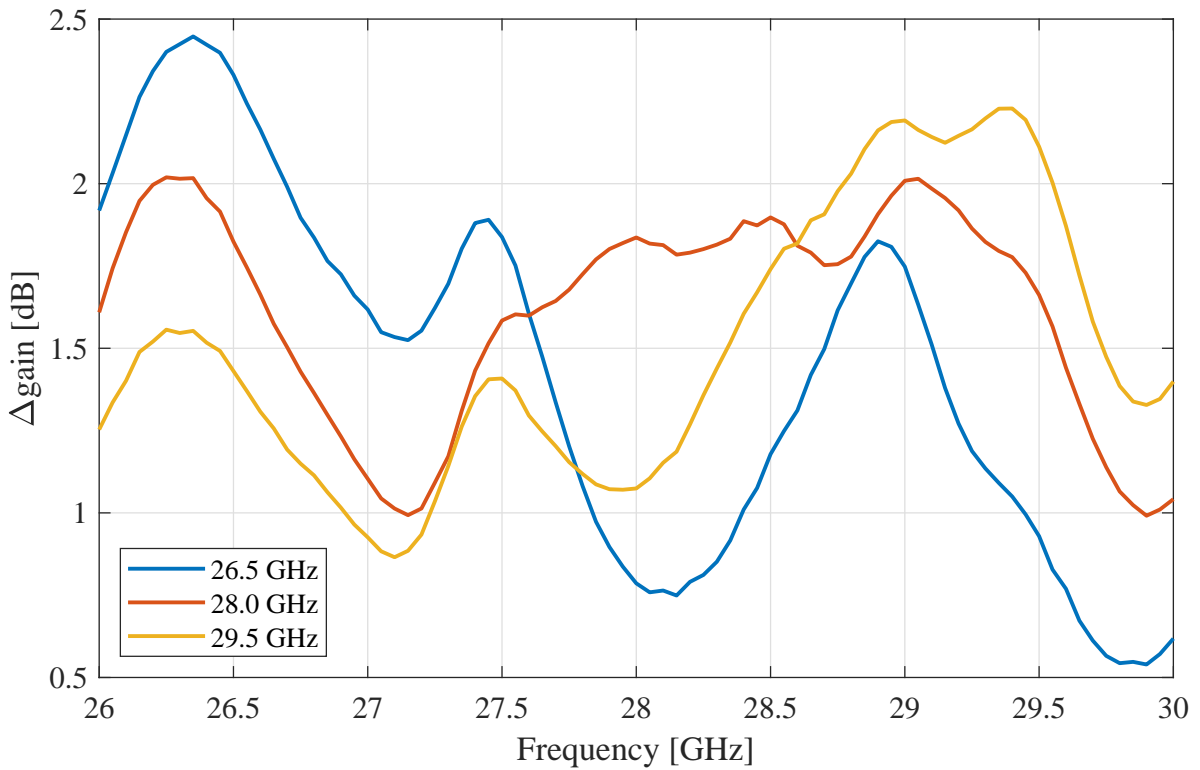


**Figure 3.22:** The improvement in gain of the phased array when phase calibration is performed for three different frequencies.

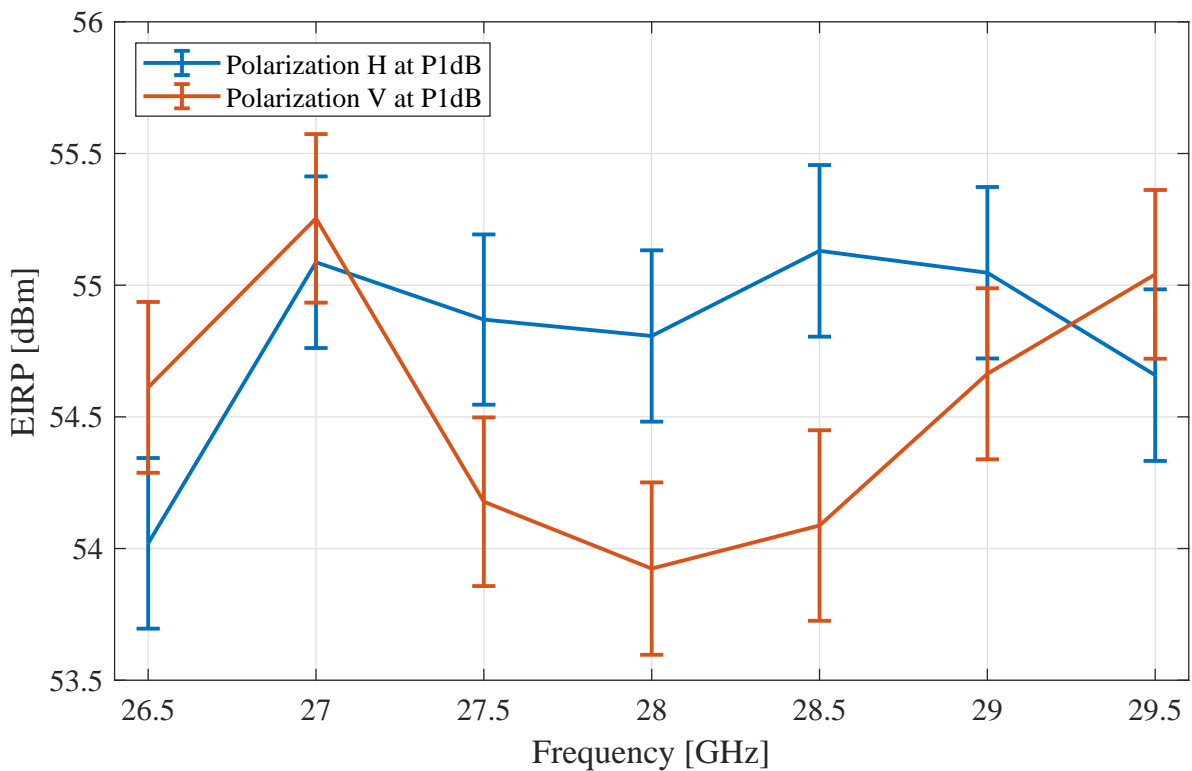


**Figure 3.23:** Determined EIRP at the 1-dB compression point for the horizontal and vertical polarization. The error bars indicate the  $2\sigma$ -confidence intervals.

field. Hence, another method has to be considered for online calibration.

One of the methods to perform online calibration requires a separate probe antenna to be embedded in the array or to be installed close to the array [36]. In the realized phased array, the ICs belonging to one polarization can be put in transmit mode, and simultaneously the ICs belonging to the other polarization can be put in receive mode. This means that the antennas of, for instance, the vertical polarization can be used as a probe to calibrate the horizontal polarization, and vice versa.

The online calibration procedure demonstrated using the presented phased array is as follows. First, the phase calibration as shown in Section 3.4.2 is performed on the horizontal polarization of the array while in transmit mode. After that, a center element of the vertical polarization is used as probe, and the response of each calibrated element of the horizontal polarization is measured sequentially. Although the IC connected to the probe is subject to drift over time, the effect of drift by the probe is present in all the measurements and can be discarded by storing the complex ratios of these measurements instead of the absolute measurements. Once the array is installed in the field and the response of the ICs has been drifting as a result of temperature, for instance, the probe is again used to measure the response of every element sequentially. In turn, the phase settings are adjusted until the measured complex ratios equal the stored complex ratios, bringing the array back in a calibrated state.

To mimic the situation of drifting ICs, a small random offset has been added to the phase settings of a calibrated array. In the left column of Fig. 3.24, the resulting phases measured using a far-field measurement setup are shown for three different frequencies. The random offset was chosen such that the maximum phase difference among the elements was limited to  $40^\circ$ . After the online calibration procedure was finished, the phases shown in the right column of Fig. 3.24 were measured. As can be seen, the resulting phase differences are comparable to the phase differences of the calibrated array as shown in Fig. 3.21. The phases shown in Fig. 3.24 have been measured in a far-field setup, but note that these measurements have not been used in the calibration procedure. These measurements are solely performed to show the effect of the calibration procedure on the phase of each element.

The significant mutual coupling present in the array in combination with the high dynamic range of the available vector network analyzer (VNA) allowed for using solely a center element as probe. If, however, less mutual coupling is present and/or the dynamic range of the measurement equipment is limited, this online calibration procedure can be split over multiple sections that overlap. For instance, the 8-by-8 array could be split in four sections of 4-by-4 subarrays. In each subarray, a separate probe is used that particular subarray. Since these subarrays are smaller than the full array, a lower dynamic range is required to calibrate each subarray. To calibrate a subarray with respect to another, one element has to be measured by both subarrays. This calibration method would require slightly more time, resulting in additional down time of the system. However, since the mutual coupling has shown to cause significant impact on the ICs and EEPs (see Section 3.3.4 and 3.3.5), a mutual coupling reduction is recommended at the cost of a slight increase of down time.

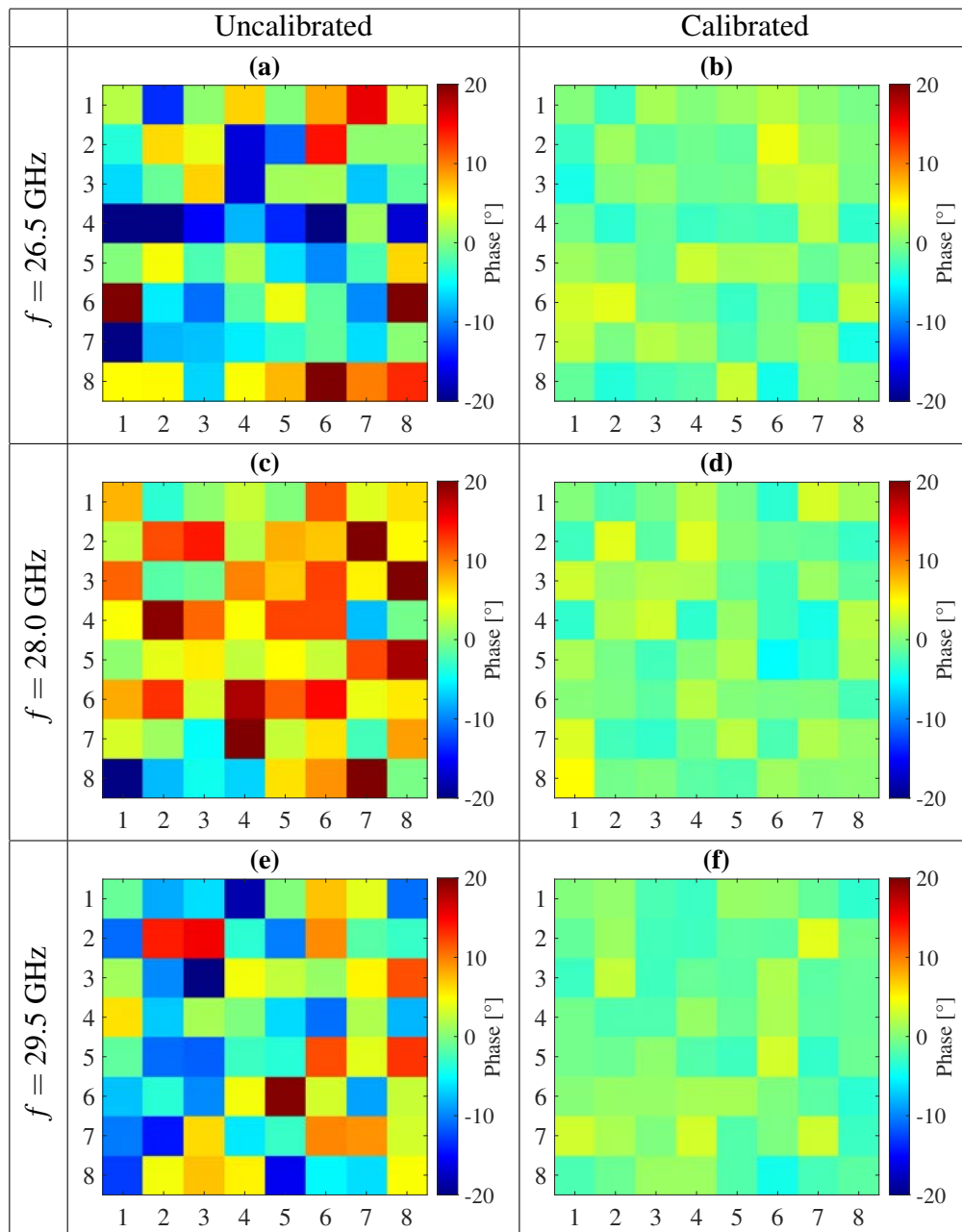


**Figure 3.24:** Measured phases of all 64 elements when no calibration is performed (left column) and when a phase calibration is performed (right column) using an online calibration procedure. The array has been calibrated on three different frequencies.



## 3.5 Conclusion

In this chapter, the design, characterization and calibration of a 28 GHz 8-by-8 analog dual-polarized active phased array is presented. The array is the university's first prototype of a 5G mm-wave active phased array and is developed as testbed to experiment with OTA characterization and phased array calibration methods. Design considerations are presented and the implementation of the BFN is shown in detail. Since the antenna module is highly integrated, characterizing components individually is impossible. Instead, OTA measurement results are shown that are used to deduce the performance of the BFN and the ICs under the influence of mutual coupling, for instance. Furthermore, three calibration methods are shown, which can be used to enhance the performance of the phased array.

In Section 3.4, it is shown that the array is functional, i.e., the main lobe of the array can be pointed in desired directions and an EIRP in the order of 54 to 55 dBm is achieved at P1dB. However, throughout the chapter, it is shown that some aspects of the phased array can be improved. For instance, the BFN does not perform as desired, resulting in a lower EIRP at the array's P1dB. To solve this, the use of Wilkinson junctions instead of T-junctions is proposed, at the price of increased complexity and cost. Moreover, the PCB was slightly warped, causing a non-uniform thermal connection among all ICs. Possible measures to balance the thermal conductivity are to introduce more copper symmetry in the PCB which reduces warpage, to create a heat sink that is made conformal to the heights of the ICs, or to strengthen the IC's connection to the PCB such that the PCB can be straightened by force without breaking the solder joints. Furthermore, load pulling caused by mutual coupling showed to have a significant effect on the complex response of the ICs. Also the EEPs showed to suffer from mutual coupling. To cope with these issues, measures can be introduced to reduce the mutual coupling from one element to another and make the antenna element less dependent on its direct environment, in turn, improving the performance of the array.



# Accurate Gain Measurement Technique for Limited Antenna Separations<sup>1</sup>

---

## 4.1 Introduction

One of the most important parameters of an antenna is its gain. In the last decades, several measurement techniques were developed to accurately determine the gain of an antenna, such as for instance the state-of-the-art extrapolation measurement technique [58]. Less rigorous measurement techniques often use the Friis equation to determine the antenna gain [59], [60]. By using the Friis equation, some assumptions are made that cannot be satisfied in any practical measurement setup. First of all, the receive antenna is assumed to be excited by a plane wave. In every practical setup, however, the distance between the transmit and receive antenna is finite. Due to the spherical nature of the radiated waves, the limited separation between the two antennas results in a non-uniform phase distribution over the area of the receive antenna. Second, the antennas are assumed to be a point source or sink and the distance between the antennas has to be known. An antenna has a certain size, which makes it sometimes unclear what should be regarded as the antenna's reference point. In turn, this generates an uncertainty in the distance between the antennas. Lastly, a free-space environment without any scattering is assumed. In every measurement setup, however, reflections are inevitable, creating multipath components or standing waves between the antennas, potentially disturbing the measurement.

In practice, it is often assumed that the first two assumptions are met when the antennas are separated by the commonly known Fraunhofer distance [61]. In [62], it is shown that if a maximum error as low as 0.05 dB is desired, without applying a proximity correction, the aperture-to-aperture distance between the assessed SGHs should be as large as 16 times the Fraunhofer distance. However, in [63] it is shown that if not the aperture-to-aperture distance

---

<sup>1</sup>This chapter is based on [P5].

is used, but instead the phase centers are chosen as the reference points of the antennas, the proximity correction is basically reduced to 0.02 dB if the antennas are separated by the Fraunhofer distance. In [64]-[68], more experimental results are shown indicating that accurate results can be obtained at one or two times the Fraunhofer distance when using the phase centers as reference points. In these papers, different approaches are taken in order to determine the phase centers. In [63], [64] a separate measurement requiring a different setup is used to determine the phase centers, whereas in [65]-[67], the used phase centers are based on simulations. In [68], an explanation of how the phase centers are determined is omitted.

In this chapter, a novel measurement technique is presented that allows for accurate gain measurements for limited antenna separations. This far-field technique requires the measurements to be performed for multiple separations between the antennas. The method relies on relative distances (i.e., changes in distance), instead of knowing the exact absolute distance between the antennas. Using this method, the amplitude center of the antennas can be found. This reduces the error in the estimation of the distance between the antennas, subsequently reducing the error in determined gain. Moreover, it can be assessed at what antenna separation far-field conditions are met, allowing for accurate far-field measurements at minimum antenna separations. This allows for accurate gain measurements in measurement setups where the distance between the antennas is limited, as in for instance the small anechoic chambers which are typically used for the characterization of mm-wave antennas [69], [70]. Furthermore, reflections caused by scatterers are (partly) averaged since multiple measurements are performed. Using three  $K_a$ -band aperture antennas, measurement data have been acquired and the gain of the three antennas has been determined. It is shown that, without relying on simulated data or having to perform a separate measurement, the gain of the antennas can be determined accurately for separations of one to two times the Fraunhofer far-field distance.

The outline of the chapter is as follows. In Section 4.2, a discussion on the definition of the phase center and amplitude center is given. Section 4.3 is devoted to the presented gain measurement technique. In Section 4.4, measurement results are shown. Moreover, a model is presented to interpret the obtained results. In Section 4.5, the performance of the technique is evaluated and compared to the extrapolation measurement technique. Finally, in Section 4.6, the conclusion is presented.

## 4.2 Phase and amplitude center

In [63]-[68], the phase center is used as the antenna's reference point. The definition of the phase center is as follows [71]: "the location of a point associated with an antenna such that if it is taken as the center of a sphere the radius of which extends into the far field, the phase of a given field component over the surface of the radiation sphere is essentially constant, at least over that portion of the surface where the radiation is significant." This definition is ambiguous, as the resulting location depends on which portion of the radiation sphere is assessed. For instance, in [63], it is shown that depending on the choice of angular

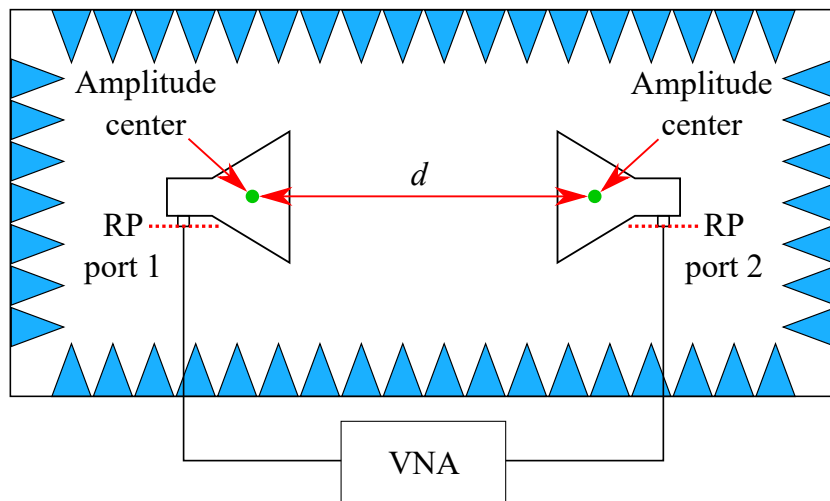


**Figure 4.1:** Schematic of a typical gain measurement setup, including the definition of the reference plane (RP) of each port. The amplitude centers are indicated by the green dots, and the distance  $d$  between the antennas is defined from amplitude center to amplitude center.

region ( $1^\circ \leq \theta \leq 10^\circ$ ) and principal cut, the determined phase center location of a SGH can vary up to four wavelengths. On top of that, to determine the phase center, a separate measurement [63], [64] or simulation [65]-[67] is required, which is generally undesired.

Instead of using the phase center, also the amplitude center can be used as the reference point of the antenna. In [72], the amplitude center is defined as follows: “a point from which the field amplitude varies relatively close to the inverse distance variation in a specified direction over some distance range.” The concepts of the phase and amplitude center are related as they both describe a point where the radiation seemingly originates from. Based on the definition, however, for a given direction, the amplitude center can be uniquely determined when the separation of the two antennas is ‘large enough’ such that far-field conditions are met. This essentially means that the phase variation of the non-uniform phase distribution over the aperture of the receiver has to be insignificant. In turn, this implies that the distance is ‘large enough’ and that far-field conditions are met when increasing the antenna separation, hence, making the phase distribution over the aperture more uniform, does not alter the calculated gain of the antenna. Moreover, the definition of the amplitude center relies only on radiation from a specified direction. Therefore, finding the amplitude center does not require knowledge (either simulated or measured) of the radiation pattern in another direction than the direction of interest, as is the case for finding the phase center. Due to these advantages, the amplitude center as described in [72] is adopted as the antenna’s reference point in this thesis for determining the antenna gain.

### 4.3 Antenna gain measurement technique

The presented gain measurement technique is based on the Friis equation and is a variation of the three-antenna method [60]. In Fig. 4.1, a schematic of a typical gain measurement setup

for the three-antenna method is shown. Two unknown antennas are positioned opposite to each other and are placed in an anechoic chamber. Both antennas are connected to a calibrated VNA such that the reference planes (RPs) are located at the input ports of the antennas. Then, the Friis equation can be cast in the following form

$$\frac{P_r}{P_t} = |S_{21}|^2 = G_r G_t \left( \frac{\lambda_0}{4\pi d} \right)^2. \quad (4.1)$$

Here,  $P_r$  and  $P_t$  are the power levels at the RPs of the receiving and transmitting antenna, respectively, and  $S_{21}$  represents the measured forward S-parameter. The wavelength in free-space is denoted by  $\lambda_0$ ,  $d$  is the distance between the amplitude centers of the two antennas, and  $G_r$  and  $G_t$  represent the realized gains of the receiving and transmitting antenna, respectively. By performing one single measurement for one given distance, (4.1) can be used to solve for the product of both realized gains (often referred to as realized pair gain). By performing three measurements using three (unknown) antennas, the realized pair gain of each antenna pair can be determined.<sup>2</sup> Subsequently, the realized gain of each AUT can be calculated.

Typically, the amplitude center of the used antennas is not exactly known. In a conventional three-antenna-method measurement, this leads to an increased uncertainty in  $d$ . However, if multiple measurements are performed, while one of the antennas is translated, this uncertainty in  $d$  can be reduced. This is done by relying on the relative distances (i.e., changes in distance) between the positions of the antenna that is translated instead of on the absolute distance between the antennas. To show this, the distance between the antennas is from this point onwards denoted by  $d = d_0 + \Delta d$ . Here,  $d_0$  is the unknown distance between the amplitude centers of the antennas of the first measurement. The term  $\Delta d$  represents the relative distance of the translated antenna and can be treated as a measurable (known) variable. By writing  $d = d_0 + \Delta d$ , (4.1) can be written as

$$G_r G_t = \left( |S_{21}| (d_0 + \Delta d) \right)^2 \left( \frac{4\pi}{\lambda_0} \right)^2. \quad (4.2)$$

The realized gain of an antenna is a far-field parameter, and is thus per definition independent of  $d$ . This means that if far-field conditions are met, both sides of (4.2) are constant. By performing multiple measurements with different antenna separations, both  $d_0$  and the realized pair gain can be determined.

In Fig 4.2, the workflow of a relative-distance sweep and a physical interpretation of the parameter  $d_0$  and variable  $\Delta d$  is depicted. Figure 4.2(a) represents the first measurement of the relative-distance sweep, indicating the meaning of  $d_0$ . Subsequently, as shown in Fig. 4.2(b), AUT 2 is translated by some measurable distance  $\Delta d$  and the second measurement is performed. This process continues until sufficient measurements are performed. In Section 4.5,

---

<sup>2</sup>In (4.1), it is assumed that both antennas are linearly polarized and that the polarizations are matched. If the orientation of the polarization of the antennas is unknown and/or one of the three antennas is elliptically polarized, up to six measurements have to be performed to fully characterize the gain of the antennas [58].

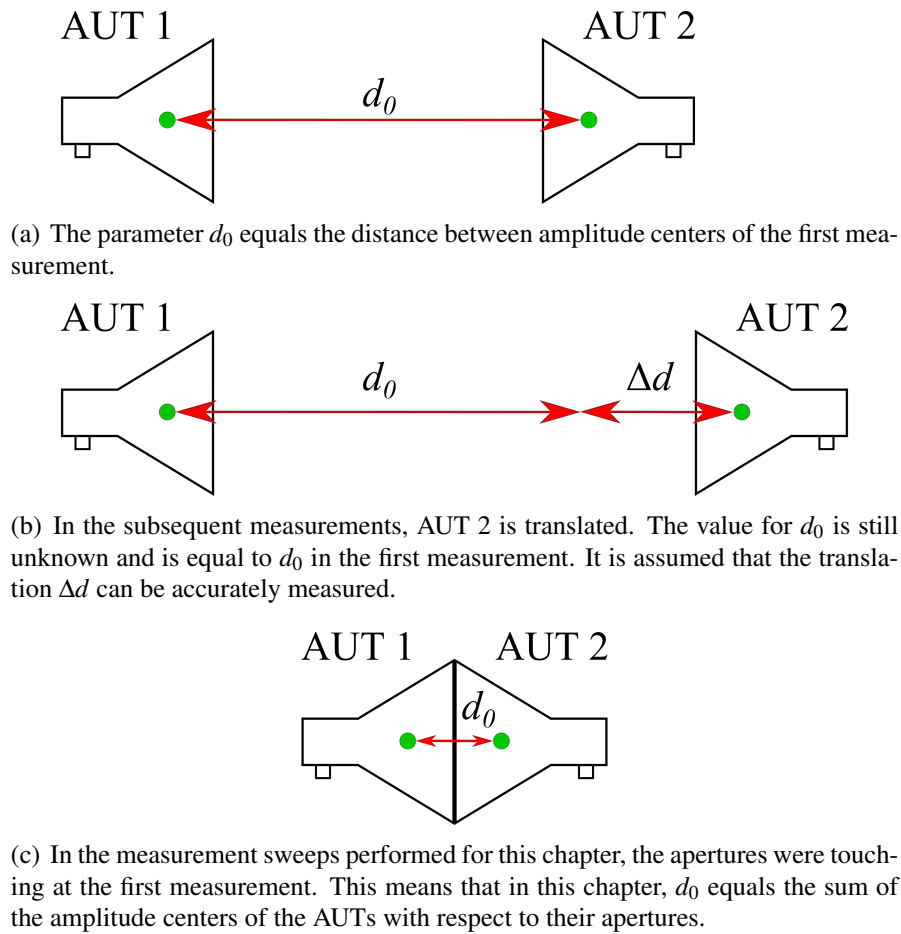


**Figure 4.2:** Schematic of the workflow of a relative-distance sweep measurement, including the definition of  $d_0$  and  $\Delta d$ .

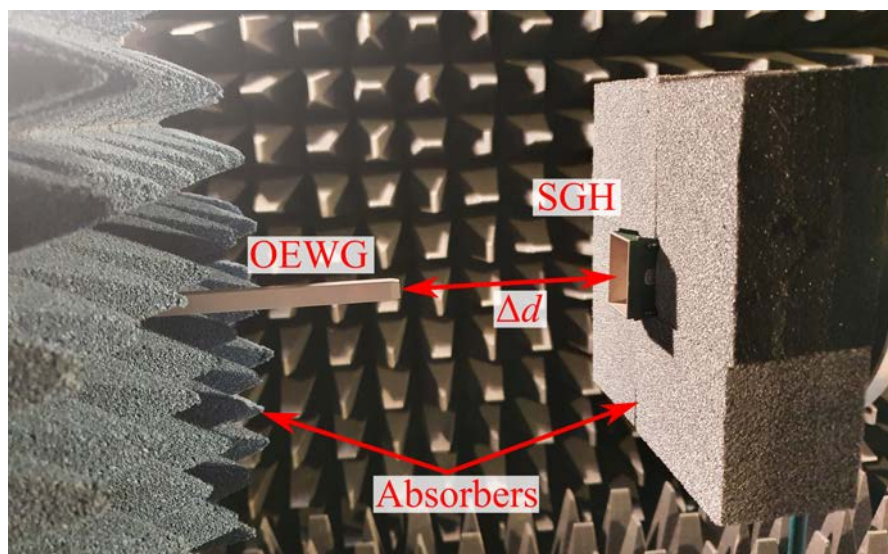


**Figure 4.3:** Measurement setup with the  $K_a$ -band OEWG and SGH. The distance sweep started when the aperture planes of the OEWG and SGH coincided, hence,  $\Delta d$  equals in this measurement the aperture-to-aperture distance.

the meaning of sufficient in the context of the presented gain measurement technique is discussed.

In the measurement sweeps performed for this chapter, the apertures were always touching at the first measurement. Needless to say, far-field conditions are not achieved when the apertures are touching and the Friis equation is not valid in that case. Having the apertures to touch at the first measurement, however, helps to show the principle of the measurement technique and is not a requisite for utilizing the presented technique. Additionally, having the apertures to touch at the first measurement means that in this chapter,  $d_0$  equals the sum of the amplitude centers of the AUTs with respect to their apertures, as illustrated in Fig. 4.2(c).

## 4.4 Measurement results

### 4.4.1 Relative-distance sweep: OEWG and SGH

To illustrate how  $d_0$  can be determined, a measurement using a relative-distance sweep has been performed. In this measurement, an open-ended waveguide and SGH operating at K<sub>a</sub>-band were positioned opposite to each other (see Fig. 4.3), and the distance between the apertures was linearly increased from 0 to 1 m, in steps of 2 mm.<sup>3</sup> As a post-processing step, the realized pair gain has been calculated using (4.2) for different estimations of  $d_0$ , denoted by  $\hat{d}_0$ , and the results at 40 GHz are shown in Fig. 4.4.

The realized pair gain calculated using  $\hat{d}_0 = 0$  is shown in blue in Fig. 4.4. Choosing  $\hat{d}_0 = 0$  means that in this measurement, the amplitude center of the antennas is estimated to be at the aperture. This implies that for this estimation of  $\hat{d}_0$ , the distance between the antennas is measured from aperture to aperture. It is evident to see that the determined realized pair gain show an increasing trend with respect to an increase in separation. This implies that either the non-uniform phase distribution is still significant, the choice of  $\hat{d}_0$  is poor, or a combination of both. In red, the calculated realized pair gain is shown for  $\hat{d}_0 = 25$  mm, which is a third of the flare length of the SGH. If the amplitude center of the OEWG is assumed to be at its aperture, this choice of  $\hat{d}_0$  corresponds to estimating the amplitude center of the SGH to be 25 mm inside of the SGH. The red line shows a trend of decreasing pair gain for increasing  $\Delta d$ , preventing an exact determination of the realized pair gain.

In yellow, the resulting pair gain is shown where  $\hat{d}_0$  was determined by a linear least-squares fitting routine. Since the pair gain is by definition independent from separation, this routine determines the value for  $\hat{d}_0$  such that the difference between  $|S_{21}|(\hat{d}_0 + \Delta d)$  and a constant is minimized. In other words,  $\hat{d}_0$  is chosen such that it minimizes the residual of the fit of  $|S_{21}|(\hat{d}_0 + \Delta d)$  to a constant. For small antenna separations, the non-uniform phase distribution is significant. Hence, in this fitting routine, only data have been used where  $\Delta d$  (i.e., the aperture-to-aperture distance) exceeded the Fraunhofer distance, which is 0.48 m and

---

<sup>3</sup>The large amount of 501 measurement points and the small step size of 2 mm is taken to show the principle of the measurement technique, and is not required by the technique, see Section 4.5.



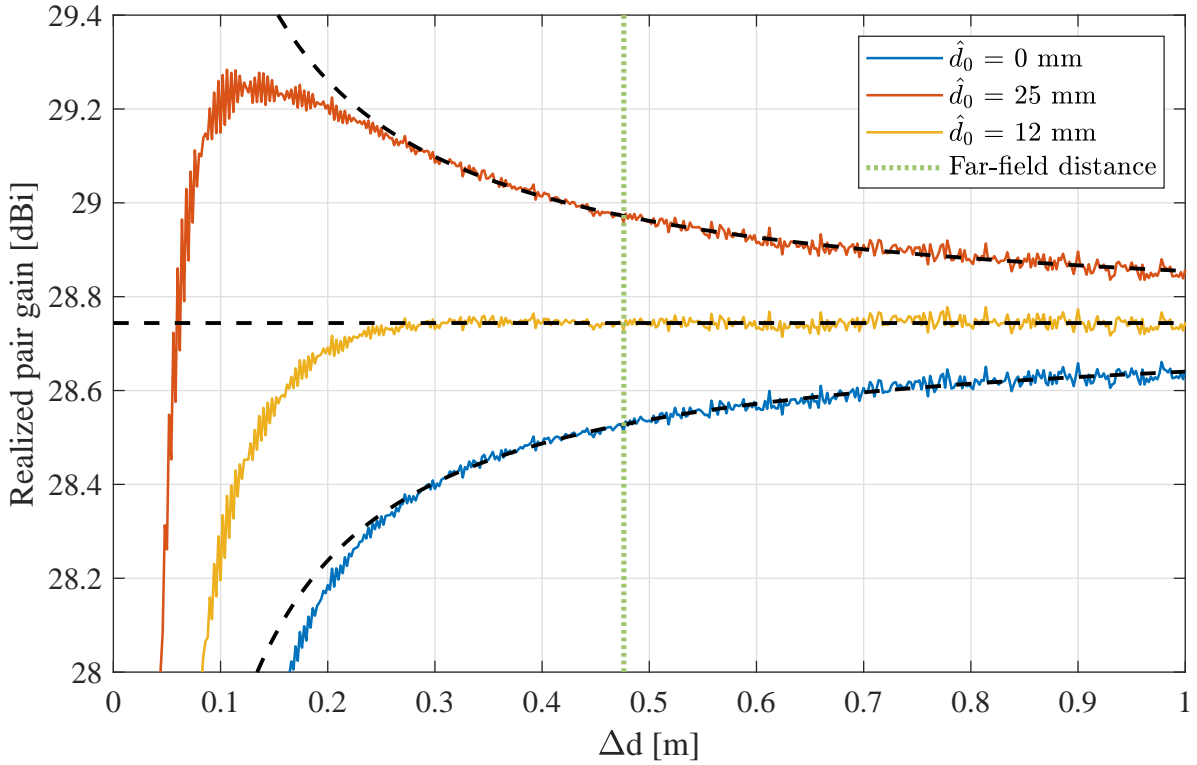


**Figure 4.4:** Determined realized pair gain of an OEWG and a SGH for different estimations of  $\hat{d}_0$ ,  $f = 40$  GHz. The blacked dashed lines are calculated using the isotropic radiator model presented in Section 4.4.2.

is indicated by the green dotted line. The parameter  $\hat{d}_0$  was determined to be 12 mm, and it can be seen in Fig. 4.4 that the calculated pair gain does not show an increasing or decreasing trend for separations larger than the Fraunhofer distance. In fact, already from a separation of 0.3 m, far-field conditions appear to be met. The deviations present in the measurement data are most likely due to scatterers in the anechoic chamber and small errors in the exact translation  $\Delta d$ .

#### 4.4.2 Isotropic radiator model

To better interpret the obtained results for  $\hat{d}_0 = 0$  mm and  $\hat{d}_0 = 25$  mm in Fig. 4.4, a mathematical model is constructed where the antennas are treated as isotropic radiators. In Fig. 4.5, a schematic of the model is depicted. Perfect spherical waves that obey the inverse-square law are originating from the transmitter, which is indicated by the yellow dot. The receiver, indicated by a black dot, is positioned a distance  $d_a$  away from the transmitter. Since the receiver is treated as a point object, no phase curvature is present along the receiving aperture. This means that the transfer from one point object to the other can be written as follows

$$|S_{21}|^2 = \frac{A_{\text{iso}}}{d_a^2} = \left( \frac{\lambda_0}{4\pi d_a} \right)^2, \quad (4.3)$$

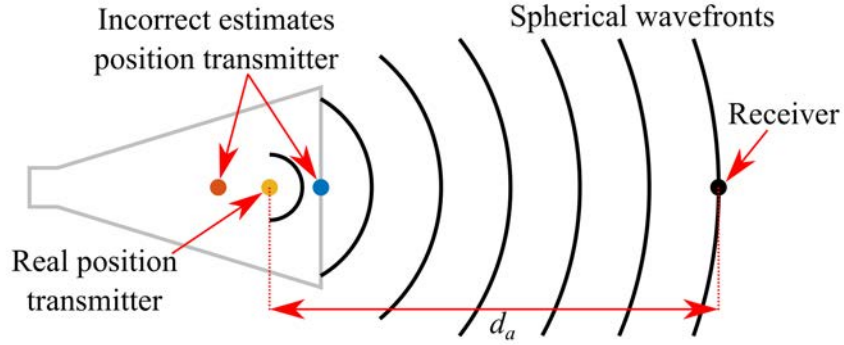


**Figure 4.5:** Schematic of a mathematical model where the antennas are treated as point object with an isotropic radiation pattern, transmitting perfect spherical wavefronts. The position of the transmitter (yellow) is typically not exactly known, so the distance can be underestimated (blue) or overestimated (red).

where  $A_{\text{iso}}$  is the effective aperture of an isotropic radiator [59]. Suppose that we want to determine the pair gain of the isotropic radiators using (4.1), but the distance is not exactly known and an estimate of  $d_a$  has to be made. This estimate is denoted by  $\hat{d}_a = d_a + \delta d$ , with  $\delta d$  being the error in the estimate. By inserting (4.3) and the estimate  $\hat{d}_a$  in (4.1), the following equation can be derived

$$\begin{aligned} \hat{G}_r \hat{G}_t &= \left( \frac{\lambda_0}{4\pi d_a} \right)^2 (d_a + \delta d)^2 \left( \frac{4\pi}{\lambda_0} \right)^2 \\ &= \left( \frac{d_a + \delta d}{d_a} \right)^2 \\ &= \left( 1 + \frac{\delta d}{d_a} \right)^2, \end{aligned} \quad (4.4)$$

where  $\hat{G}_r \hat{G}_t$  is the estimated realized pair gain for the distance estimation  $\hat{d}_a$ .

With this mathematical model in place, let's observe what happens for different estimations of the exact value for  $d_a$ . If the distance is correctly estimated, i.e.,  $\delta d = 0$ , the result is achieved that, independent from antenna separation, the pair gain of the isotropic radiators is equal to unity, which is to be expected. If, however, the real distance is larger than the estimated distance ( $\delta d < 0$ ), it can be seen in (4.4) that the estimated realized pair gain is smaller than one. Vice versa, if the real distance is smaller than the estimated distance ( $\delta d > 0$ ), the estimated realized pair gain is larger than one. Moreover, regardless of sign, for a fixed  $\delta d$  and increasing  $d_a$ , the estimated pair gain eventually converges to unity.

The presented model is analogous to not knowing the amplitude center of a physical antenna and, therefore, underestimating or overestimating the distance between the antennas. Every colored solid line in Fig. 4.4 is accompanied by a dashed black line. These black lines are constructed using the aforementioned mathematical model and are proportional to (4.4). Hence, they represent the determined gain of antennas that, independent of separation, can be treated as point objects, for different errors in the estimation of the absolute distance be-

tween these point objects. These errors are  $-12$  mm,  $13$  mm and  $0$  mm, and correspond to the differences in  $\hat{d}_0$  with respect to the estimation found by least-squares fitting routine. The similar trend observed in the model and the measured data from a separation of about  $0.3$  m indicates that the increase and decrease in determined realized pair gain shown by the blue and red line, respectively, follow the inverse-square law and thus the antennas can be treated as point objects. This implies that, for separations larger than  $0.3$  m, the blue and red line in Fig. 4.4 are dependent on antenna separation because of a poor choice of reference points, and not due to the non-uniform phase distribution over the aperture of the receiving antenna.

Note that the black dashed lines in Fig. 4.4 converge to the same pair gain for increasing separation. This indicates that the blue and red line also converges to the same pair gain, essentially making the determined pair gain independent from the choice of  $\hat{d}_0$  for a large value of  $\Delta d$ . This observation is compatible with the statement that if the separation between the antennas is taken to be large enough, the choice of reference point becomes insignificant [63], [73]. However, especially with the rise of small anechoic chambers for the characterization of, for instance, 5G mm-wave phased arrays, separating the antennas by very large distances is impossible [69], [70]. As can be observed in Fig. 4.4, for limited separations in the order of the Fraunhofer distance, a poor choice of absolute distance can lead to an error in the order of  $0.2$  dB in the realized pair gain. This emphasizes the importance of choosing a proper reference point when antennas are measured in anechoic chambers where separations in the order of the Fraunhofer distance can only be achieved.

### 4.4.3 Relative-distance sweep: SGH and SGH

A similar sweep as described in Section 4.4.1 is performed with two SGHs. In this measurement, the sweep was from  $0$  to  $1.3$  m, in steps of  $1$  mm.<sup>4</sup> The pair gain has been determined for different choices of  $\hat{d}_0$  and the results are shown in Fig. 4.6. The values of  $\hat{d}_0$  are selected in the same way as described in Section 4.4.1. The distance between the antennas is measured from aperture to aperture for  $\hat{d}_0 = 0$  mm. For  $\hat{d}_0 = 50$  mm, the amplitude center is taken to be  $25$  mm inside both the SGHs, which equals a third of the SGH's flare length. It can be seen that for these two choices of  $\hat{d}_0$ , the determined pair gain depends on  $\Delta d$ , indicating a poor choice of  $\hat{d}_0$ . Based on the least-squares fitting routine introduced in Section 4.4.1, a  $\hat{d}_0$  of  $33.3$  mm is determined at first. Since far-field conditions were met from  $\Delta d = 0.3$  m onwards for the measurement with the OEWG and SGH shown in Fig. 4.4, initially, data were used in the fit to estimate  $d_0$  of the measurement with two SGHs that exceeded  $\Delta d = 0.3$  m. The resulting pair gain is shown in Fig. 4.6 in purple. It is evident to see that the determined pair gain is not constant with respect to separation. In fact, a regular pattern in the trend can be identified. Around  $\Delta d = 0.3$  m, the determined realized pair gain is below  $42.5$  dBi, as indicated by the black dotted line. From about  $\Delta d = 0.4$  m to  $\Delta d = 0.9$  m, the pair gain exceeds

---

<sup>4</sup>The large amount of 1301 measurement points and the small step size of  $1$  mm is taken to show the principle of the measurement technique, and is not required by the technique, see Section 4.5.

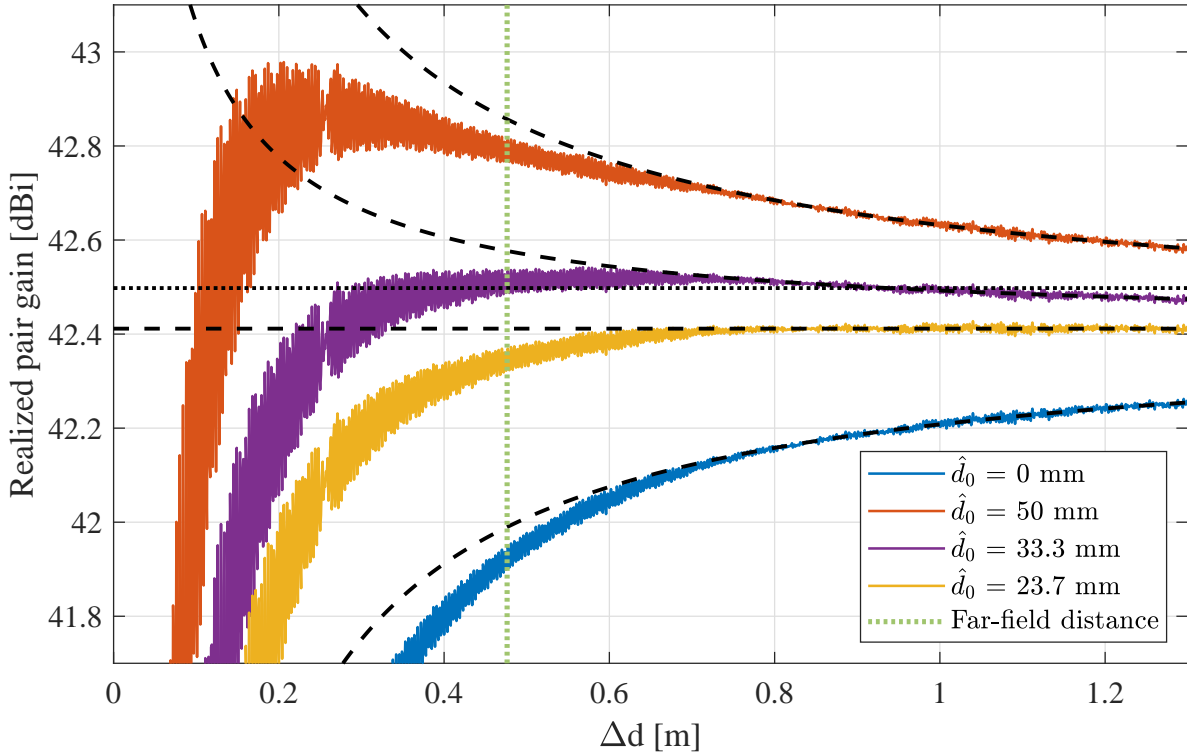


**Figure 4.6:** Determined realized pair gain of two SGHs for different estimations of  $\hat{d}_0$ ,  $f = 40$  GHz. The blacked dashed lines are calculated using the isotropic radiator model presented in Section 4.4.2. The black dotted line is meant as visual reference.

42.5 dBi, and from  $\Delta d = 0.9$  m it drops again below 42.5 dBi. This regular pattern being present indicates that far-field conditions are not yet met from  $\Delta d = 0.3$  m.

Since no estimate of  $d_0$  can be found that results in far-field conditions, it can be concluded that the non-uniform phase distribution over the receiver's aperture is still significant for separations as small as 0.3 m. By iteratively reducing the dataset and omitting the measurement points for the smallest separations, the regular pattern in the residual between the fit and a constant decreased and eventually disappeared. It was observed that from a separation of 0.8 m, far-field conditions were met with a  $\hat{d}_0$  of 23.7 mm as indicated in yellow in Fig. 4.6. It can be seen in the figure that the yellow line does not show a structural increase or decrease with respect to increasing  $\Delta d$ , indicating that both the non-uniform phase distribution is insignificant and that a suitable estimate for  $d_0$  is found. In Fig. 4.7, a flowchart of the used approach is shown.

In Fig. 4.6, every solid line is accompanied by a converging black dashed line. These black lines are constructed using the model presented in Section 4.4.2. Also here, the black lines represent the determined realized pair gain of the antenna pair when the antennas are treated as point objects, for different errors in the estimation of the absolute distance between these point objects. The high degree of similarity from  $\Delta d = 0.8$  m onwards indicates that the solid lines corresponding to all three choices for  $\hat{d}_0$  converge to the same pair gain. This strengthens the choice of  $\hat{d}_0 = 23.7$  mm.

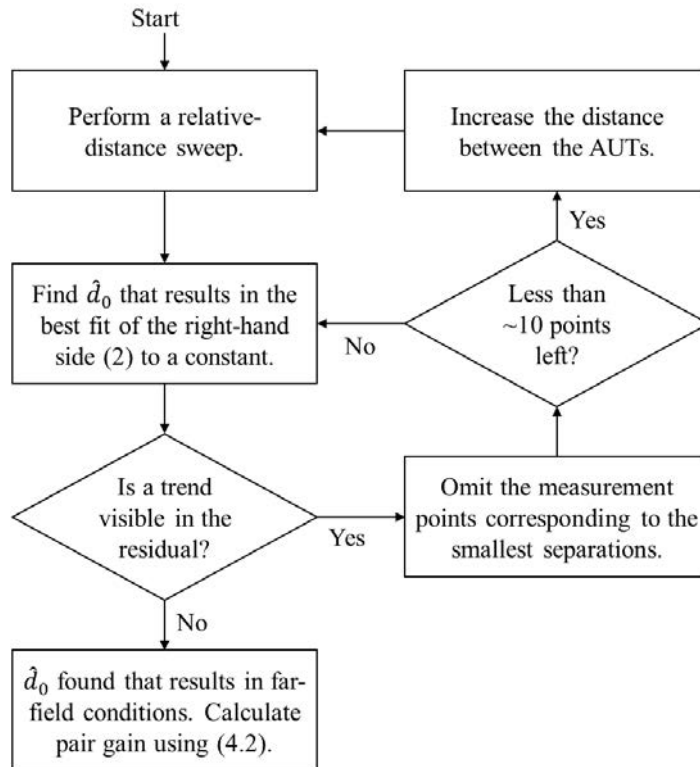


**Figure 4.7:** Flowchart of the measurement technique to estimate  $\hat{d}_0$  and the pair gain of one antenna pair.

To determine the Fraunhofer distance, it is commonly accepted to use the largest dimension of the largest AUT and is, therefore, independent of the other AUT. In both experiments described, the largest antenna was the same SGH, so for both the experiments the Fraunhofer distance was 0.48 m. Note that in Fig. 4.4 it is shown that in the measurement with the OEWG and SGH, far-field conditions are met from 0.3 m, whereas in Fig. 4.6, far-field conditions are met from 0.8 m onwards. This implies that although the Fraunhofer distance is independent of the smallest AUT, in practice, it depends on both AUTs from which distance far-field conditions can be reached.

#### 4.4.4 Determining the realized gain

The results in Fig. 4.4 and 4.6 show the determined realized pair gain of the AUTs. The goal of the presented gain measurement technique is eventually to determine the realized gain of an individual antenna. To determine the gain of an antenna using the three-antenna-method, first, the pair gain of each combination of three (unknown) antennas has to be determined. The three antennas that are used to acquire the data for this chapter are shown in Fig. 4.8. Two of the antennas are identical K<sub>a</sub>-band SGHs from Flann Microwave (model 22240-20 [74]), and the other AUT is a K<sub>a</sub>-band OEWG from NSI-MI Technologies (model ANT-WGP-26.5-40 [75]). Absorber material has been used to prevent reflections from the antenna mounts

and flanges, as can be seen in the figure. Since the two SGHs are identical, the measurement results of each of the SGHs in combination with the OEWG shows very similar results. To prevent repetition of results, therefore, only the measurement results at 40 GHz for two of the three required distance sweeps are shown (see Fig. 4.4 and 4.6).

The true realized gain of the AUTs is not known. The gain values provided by the datasheet are based on a calculation and have a relatively large maximum possible error of  $\pm 0.3$  dB [76], making these values not a suitable reference. Instead, based on the dimensions provided in the datasheet, a 3D model of the SGH was constructed to perform a full-wave simulation and is used as comparison. Since not all details of the antennas are available, and errors in manufacturing are not taken into account in the simulation models, the simulation results are not treated as a reference, but as a plausibility check for the results obtained. The simulations were performed using CST Microwave Studio and the models are shown in Fig. 4.9. The metal conductors are made out of aluminum ( $\rho = 3.56 \times 10^7$  S/m) and the absorbers are modeled by a surface impedance sheet having an impedance equal to the wave impedance of free space ( $Z_{\text{abs}} = 377 \Omega$ ). Since the details of the 2.92 mm coaxial to WR28 waveguide transitions are not known, these adapters are not modeled, causing the RP of the simulation and measurement not to be at the same location, as can be seen in Fig. 4.10.

The simulated realized gain of the SGH is shown in Fig. 4.11 in purple. Moreover, the determined realized gain of both SGHs is shown in the figure as well. The difference in the measured gain of both SGHs is less than 0.02 dB on average, and is maximum around 0.06 dB at the very end of the frequency band. Although the SGHs are identical, a deviation in the order of 0.02 dB on average is expected and can be attributed to manufacturing tolerances and uncertainties in the measurements. Moreover, the simulated and measured realized gain show the same trend, but there is still a reasonably large offset of about 0.2 dB on average present. As mentioned, the adapter is lacking in the simulation model. Therefore, a back-to-back measurement of the adapter has been performed, and half the insertion loss of this measurement has been subtracted from the simulation results in order to compensate for the adapter.<sup>5</sup> The result is shown in Fig. 4.11, and a good agreement is present, strengthening the validity of the acquired results.

The measured realized gain of the OEWG is shown in Fig. 4.12 in blue. A peak-to-peak ripple in the order of 0.4 dB is visible on the realized gain. The reflection coefficient of the OEWG had been measured as well, and the ripple on the realized gain was found to be present mainly due to the impedance mismatch of the OEWG. Since no information on the adapter is available and the OEWG consists of one metal piece making a back-to-back measurement of the adapter impossible, considering the absolute gain of the simulation and measurement of the OEWG results in a better comparison. In red and yellow, the measured and simulated absolute gain of the OEWG are shown. Still some discrepancies are present. This is mainly

---

<sup>5</sup>Strictly speaking, the full S-parameter matrix associated with this adapter has to be taken into account to compensate for the adapter. However, since the measured reflection coefficients of the back-to-back measurements were below  $-20$  dB, the  $S_{11}$  and  $S_{22}$  of the adapter were assumed to be zero.

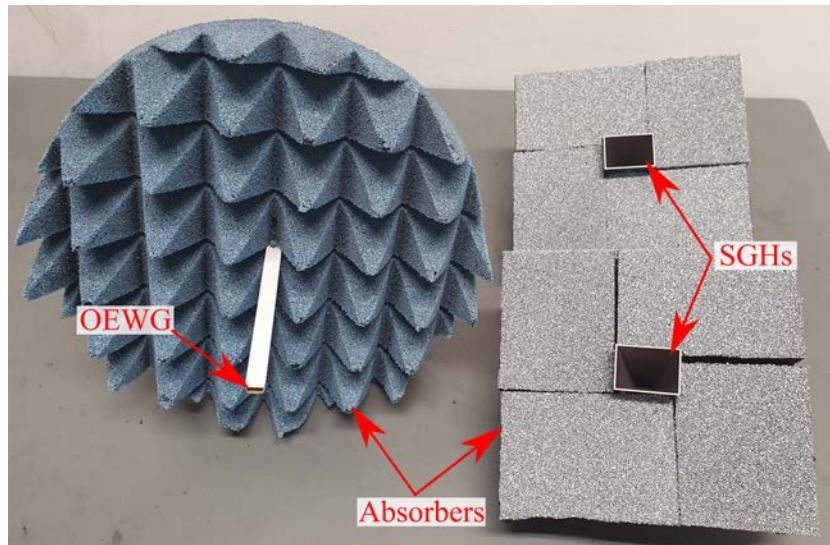


**Figure 4.8:** The three  $K_a$ -band AUTs, including absorbing material to prevent reflections from the antenna mounts and flanges.

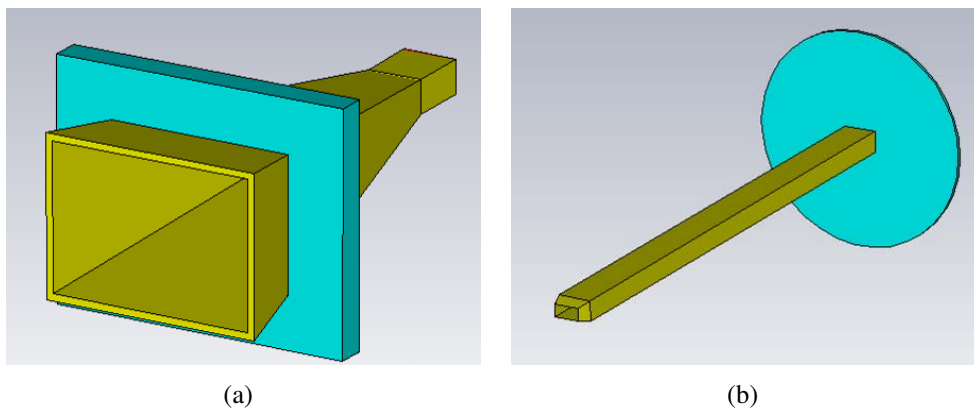


**Figure 4.9:** CST models of the (a) SGH and (b) OEWG.

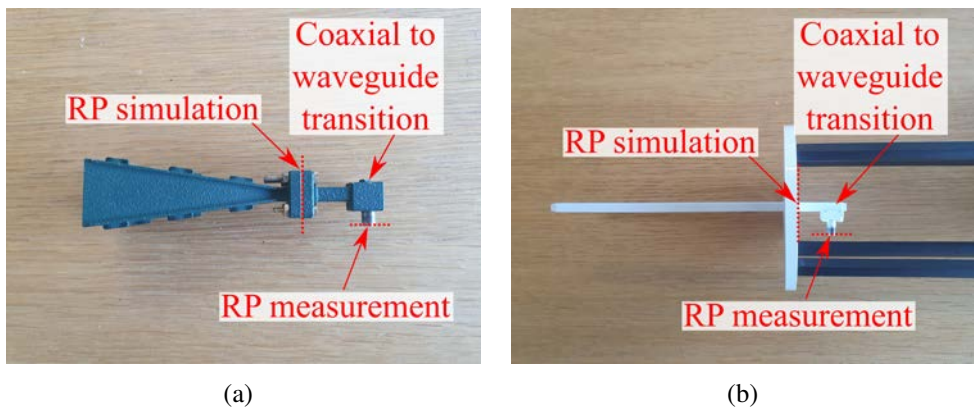


**Figure 4.10:** Side view of the (a) SGH and (b) OEWG, indicating the RPs in the measurement and in the simulation.

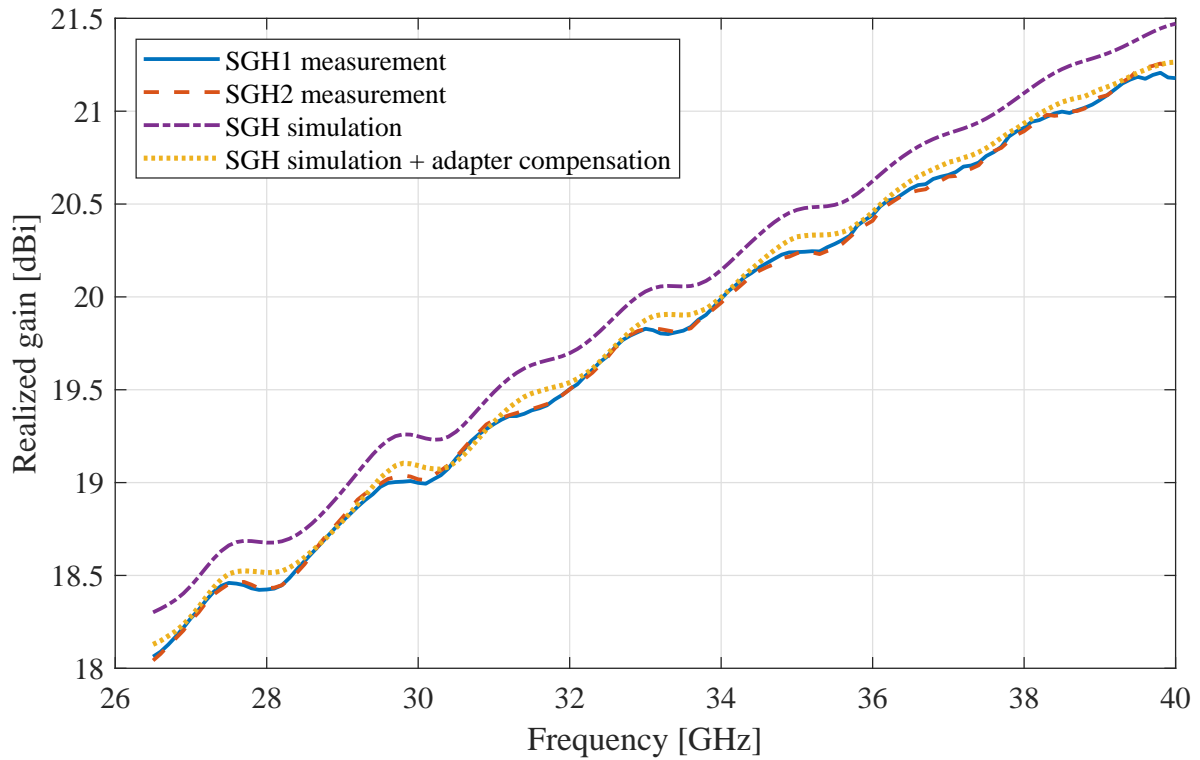


**Figure 4.11:** Simulated and measured realized gain of the SGHs.

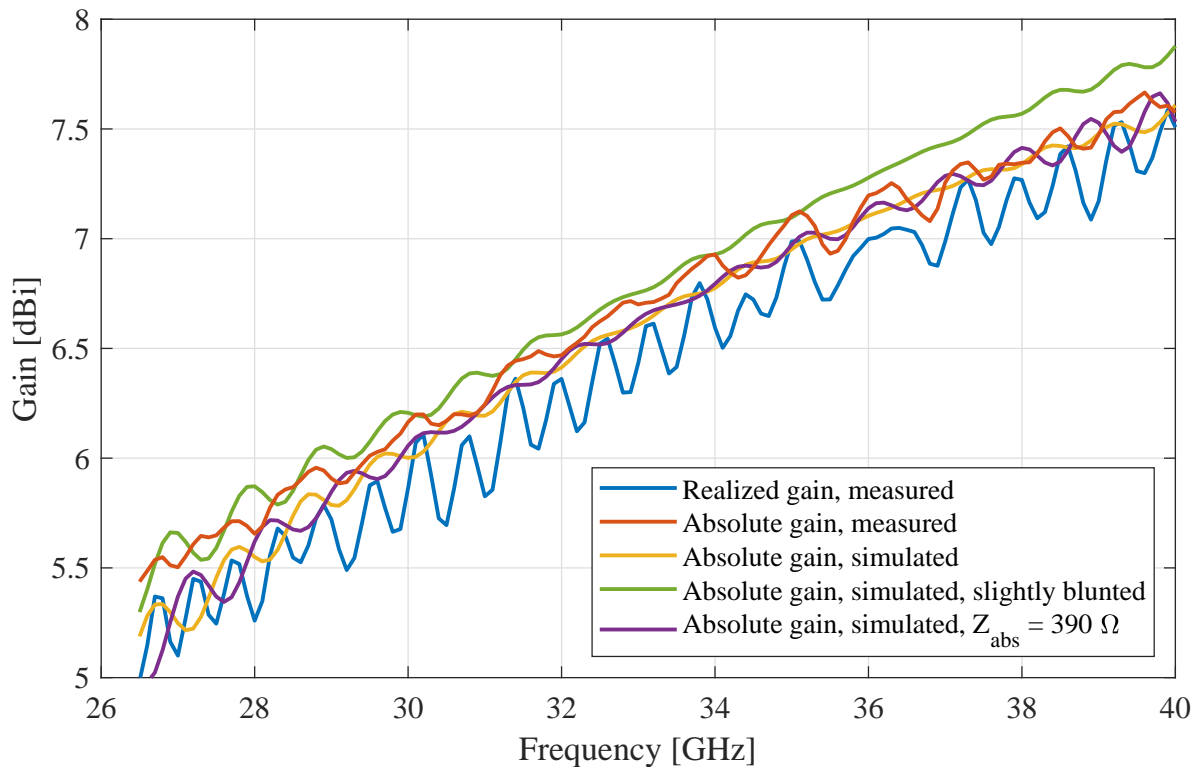


**Figure 4.12:** Simulated and measured gains of the OEWG. Three simulated gains are depicted in order to show the sensitivity of the resulting gain with respect to small changes in the simulation setup.



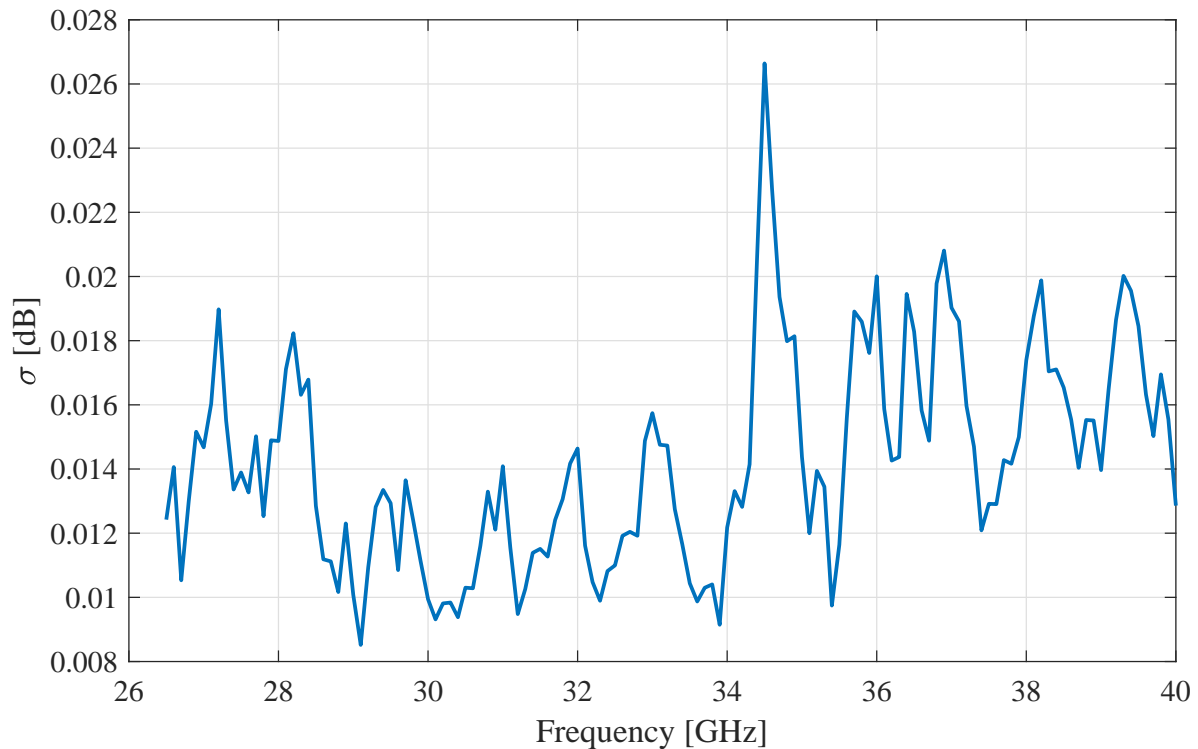


**Figure 4.13:** Uncertainty of the fitted parameter (i.e., the realized gain).

the result of the sensitivity of the determined gain to small changes in the simulation setup. For instance, in green, the simulated absolute gain is shown for the case where the edge of the tapered metal piece at the aperture is slightly blunted. As another example, in purple, the absolute gain is shown where the impedance of the absorbing material is changed to  $390 \Omega$ . These slight adaptations to the simulation model show the sensitivity of the OEWG simulation model on the resulting gain, indicating that such a simulation is not suited for a detailed comparison. Despite that, the measured and the three simulated absolute gains show the same trend and are the same order of magnitude, which shows that the acquired measured results are trustworthy.

In Fig. 4.13, the standard deviation of the uncertainty on the realized gain due to the fitting process is shown. As can be seen in the figure, the uncertainty is less than 0.015 dB on average and has a maximum of 0.027 dB around 34.5 GHz. This uncertainty includes errors in the exact translation of the antenna, cable bending uncertainties, VNA drift, multipath scattering due to the non-ideal anechoic environment and reflections between both antennas. It does not include uncertainties in the values of the calibration standards and uncertainties in the alignment of the antennas. For some frequencies, especially around 34.5 GHz, the fitting uncertainty is dominated by the reflections between both antennas. Since these reflections are deterministic, they could be included in the model, resulting in a decreased fitting uncertainty. However, this results in additional complexity and is outside the scope of this chapter.

As mentioned, the true realized gain of the AUTs is not known. Hence, the determined gains shown in this section cannot be validated. Due to uncertainties in the values of the

calibration standards of the VNA and uncertainties in the alignment of the antennas, for instance, the true realized gain of the AUTs might very well be different from the realized gains reported in this section. However, it should be emphasized that although the reported realized gains cannot be validated, the compliance with the definition of the realized pair gain (and thus realized gain) being constant with respect to separation, as shown in Fig. 4.4 and 4.6, does validate that far-field conditions are met. This, in turn, validates the presented measurement technique.

## 4.5 Evaluation of the gain measurement technique

### 4.5.1 Comparison to different choices of reference points

The curves in Fig. 4.4 and 4.6 showed the impact of the choice of reference points (i.e., different estimations of  $\hat{d}_0$ ) on the determined realized pair gain for one frequency. In Fig. 4.14, the difference in determined realized gain over the entire  $K_a$ -band for different choices of reference points is shown, for three separations. The determined gain of the SGHs shown in Fig. 4.11 is here treated as the reference. The reference points of the antennas are once again chosen to be at the aperture (blue), at 1/3 of the SGH's flare length (red) and determined by the fitting routine (yellow). The solid, dashed and dotted lines represent a separation of 1, 1.5 and 2 times the Fraunhofer far-field distance, respectively. This separation is measured from aperture to aperture. As expected, for increased separation, the differences go towards zero. However, as can be seen in the figure, for a separation as small as the Fraunhofer distance, the error in gain can be in the order of 0.2 dB or higher if the choice of reference point is poor.

### 4.5.2 Comparison phase and amplitude center

For each of the three combinations of antennas, a value for  $d_0$  is determined for each frequency. For  $\Delta d = 0$ , the apertures were touching, which means that in the presented measurements  $d_0$  represents the sum of the amplitude centers of both antennas with respect to their apertures. Similar to how the gain of the individual antennas can be determined by manipulating the three determined pair gains, the amplitude center of the individual antennas can be extracted by manipulating the three sums of amplitude centers. In Fig. 4.15, the determined amplitude center of the two assessed SGHs are shown in blue and red. Note that the distance being positive means that the amplitude center is inside the SGH.

In Section 4.2, a short discussion on the difference between the amplitude center and phase center is given. Since both concepts describe a point where radiation seemingly originates from, the question might arise if the same antenna gains as shown in Fig. 4.11 and Fig. 4.12 could have been acquired if a simulated or measured phase center was used. Since the position of the phase center of an antenna is not uniquely defined as it depends on 'the portion of the surface of the radiation sphere where radiation is significant,' two extremes are evaluated. Typically, the region corresponding to the half-power beamwidth (HPBW) of the antenna is

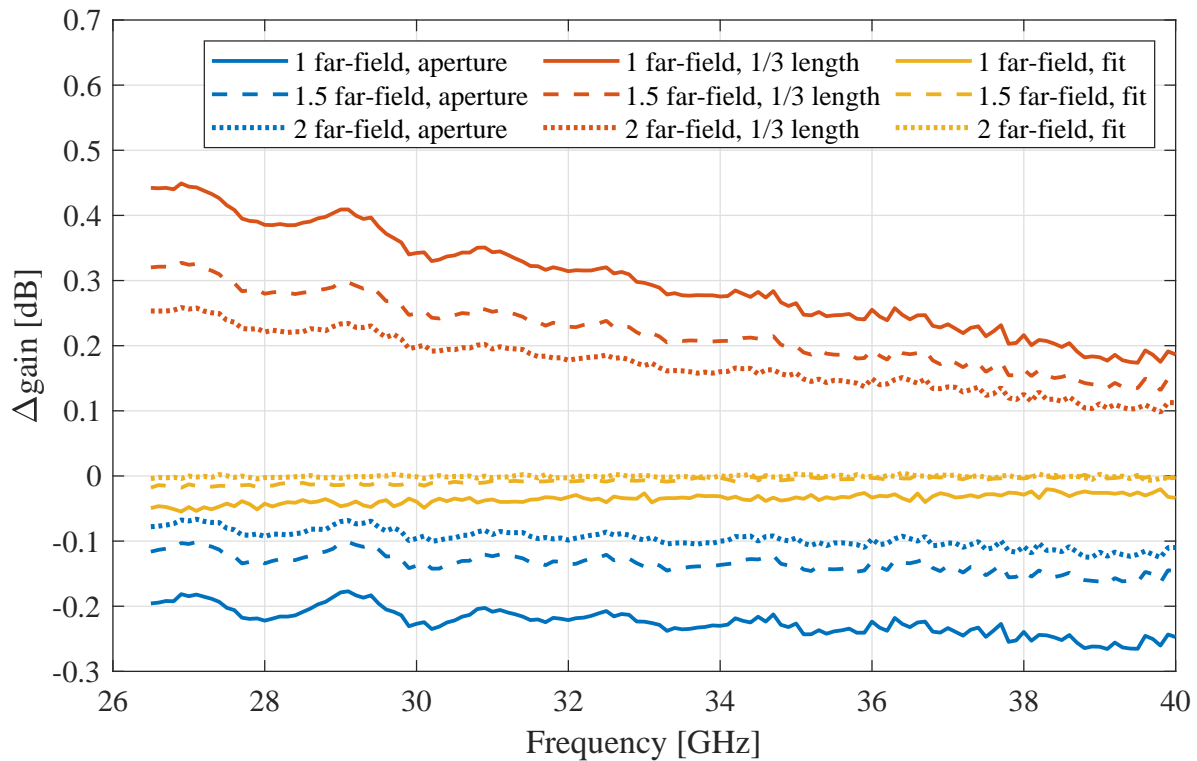


**Figure 4.14:** Improvement of the gain estimation of one of the SGHs by the presented gain measurement technique over choosing the reference point at the aperture (blue) or at 1/3 of the flare length (red) for different separations. The solid, dashed and dotted lines represent a separation (measured from aperture to aperture) of 1, 1.5 and 2 times the Fraunhofer far-field distance, respectively.

regarded as the significant region [63]. The HPBW was minimally  $15^\circ$  in both the E- and H-plane over the entire frequency band, so an angular region of  $\pm 7.5^\circ$  is used to determine the phase center. On the other hand, the minimum angular region that can be used to determine the phase center in CST is  $\pm 1^\circ$ , so the calculated phase center using that angular region is evaluated as well. In Fig. 4.15, the simulated phase centers of the SGH are also shown. Although the phase center is not uniquely defined, both simulated phase center curves show a very similar trend to the determined amplitude centers of the SGHs. This implies that taking the distance between the antennas based on a simulated phase center, the determined realized gain would not differ significantly from the determined realized gain shown in Fig. 4.11.

Likewise, in Fig. 4.16, the measured amplitude center and simulated phase centers of the OEWG are shown. It can be clearly seen that the two different choices of angular region that were assessed give rise to two completely different phase centers as function of frequency. At some frequencies, the difference is in the order of a wavelength. Additionally, the measured amplitude center shows totally different behavior, indicating that for an OEWG, the absolute distance can be off by a wavelength if this distance is based on a simulated phase center. In turn, this can result in an error of 0.2 dB in the determined gain of the AUTs for a separation in the order of the Fraunhofer distance.

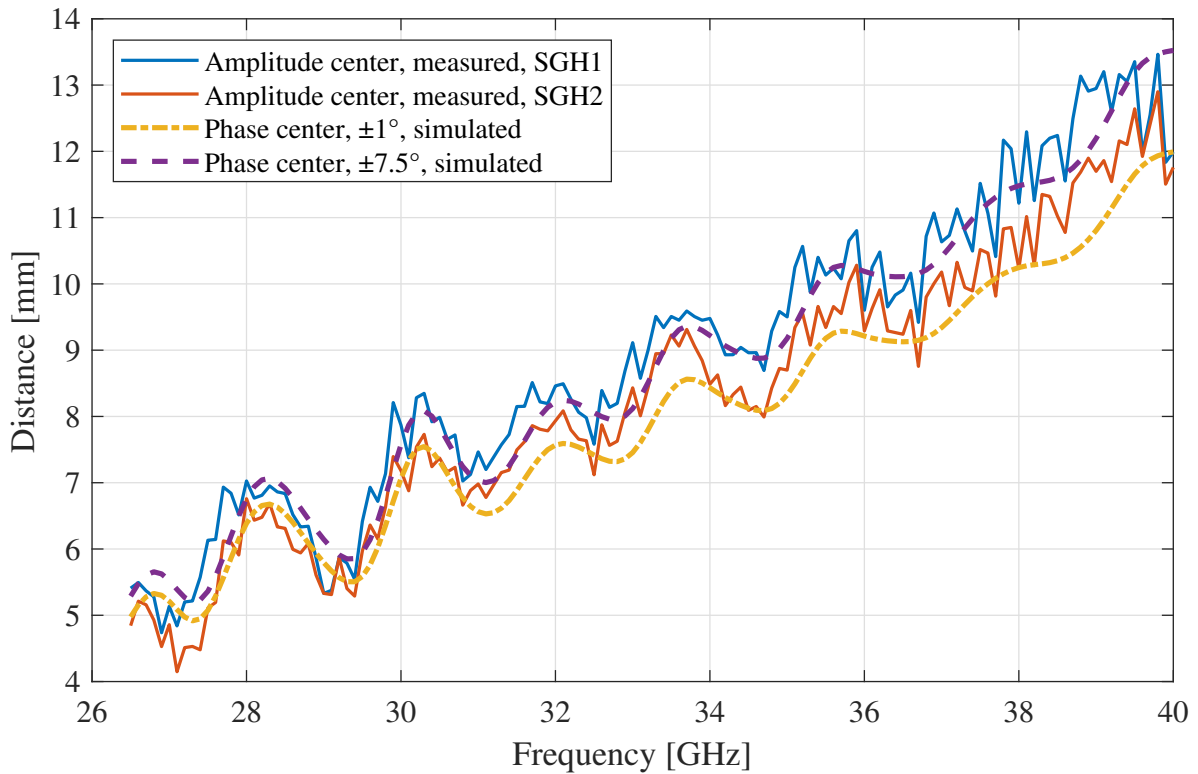


**Figure 4.15:** Measured amplitude centers and simulated phase centers of the SGHs.

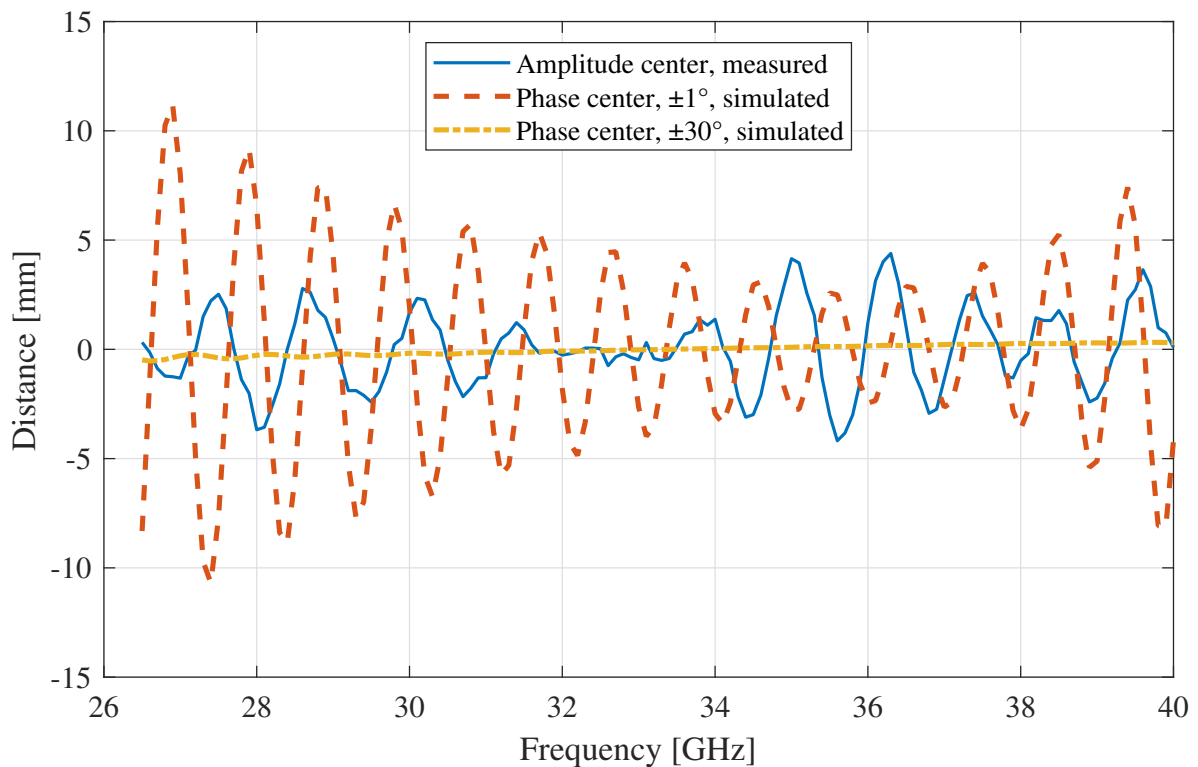


**Figure 4.16:** Measured amplitude center and simulated phase centers of the OEWG.

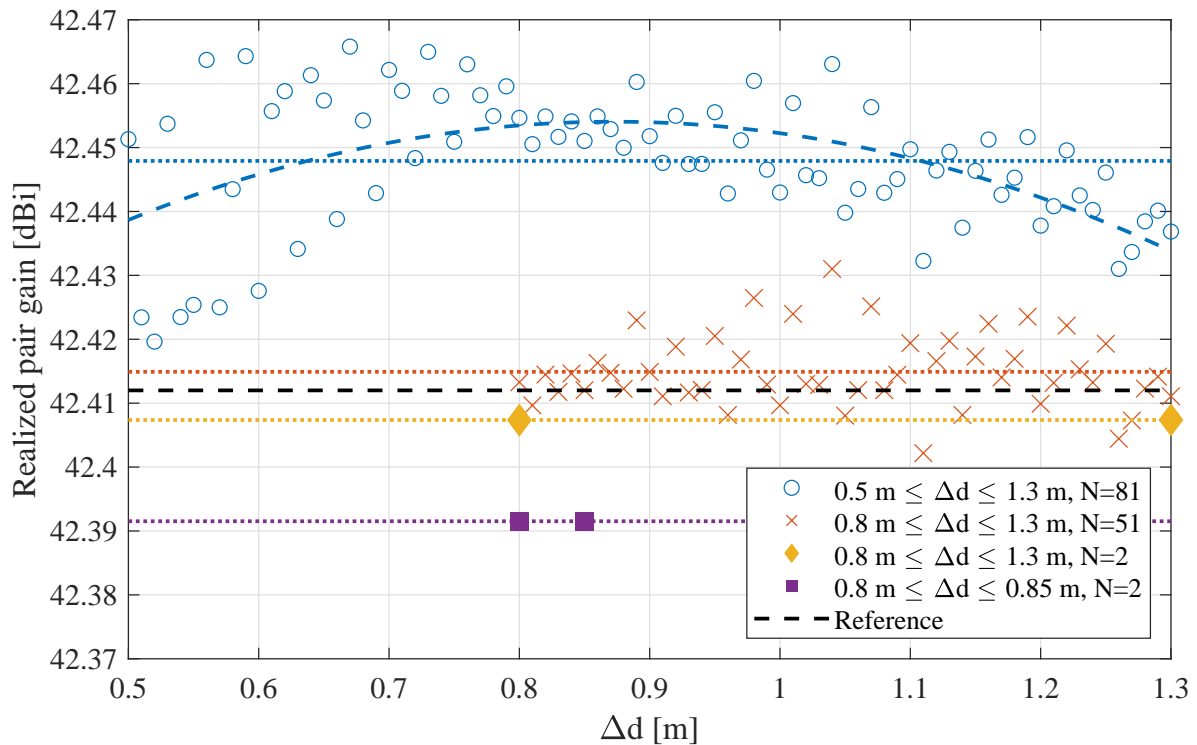


**Figure 4.17:** Comparison of the determined gain for different truncated datasets.

### 4.5.3 Number of measurements in the distance sweep

Although from a separation of 0.3 m and 0.8 m onwards the yellow lines in Fig. 4.4 and 4.6, respectively, do not show an increasing or decreasing trend, still the yellow lines are not completely flat. This is most likely due to scattering from the environment, reflections from the opposite antenna and uncertainties in the exact displacement of the translated antenna. An advantage of the presented measurement method is that since multiple measurements are taken, these effects tend to average out. For this work, the transfer between the AUTs has been measured for hundreds of different separations to properly show the principle of the presented measurement technique. For practical purposes, it would be convenient if accurate results could be obtained with far fewer measurements.

In theory, only two measurements are required to determine the two unknowns which are present in (4.2). A third measurement is required to assess whether far-field conditions are met, thus verifying that the non-uniform phase distribution is insignificant. Due to non-ideal measurement conditions, as for instance scattering, more measurement points are recommended. It is impractical to define in general how many measurements are required in order to achieve a certain accuracy, as this mainly depends on the measurement setup. However, based on the data acquired for this chapter, some guidelines can be drafted.

The following results are based on the data presented in Fig. 4.6. It is shown in Fig. 4.6 that far-field conditions were met from 0.8 m onwards. However, it is in general not known from which antenna separation far-field conditions are met. In Fig. 4.17, the pair gain determined

by the fitting routine is shown for different truncated datasets. As a first step, the dataset is truncated representing a measurement from 0.5 m to 1.3 m with a step size of 10 mm (81 points). The fitting routine is used to estimate  $d_0$ , and the determined pair gain for each of the individual measurement points is illustrated in Fig. 4.17 using the blue circles, with an average indicated by the blue dotted line. By looking at the difference between the individual measurement points and the average determined pair gain, a regular pattern in the residual can be observed. To illustrate this, a quadratic fit to this dataset has been added in Fig. 4.17, depicted by the blue dashed lines. This regular pattern in the residual indicates that far-field conditions are not met for this dataset. Therefore, the dataset is truncated further to 0.8 m to 1.3 m, having a step size of 10 mm (51 points), and the result is shown using the red crosses. No clear recognizable pattern in the residual is present, indicating that far-field conditions are met for this dataset.

As a next step, the dataset is reduced to two points, and the results are shown using yellow diamonds (0.5 m separation) and purple squares (50 mm separation). The determined pair gain is even for two measurement points very close to the pair gain determined by the full dataset, which is illustrated by the black dashed line and denoted by ‘Reference’. This implies that when far-field conditions are met, and no significant scatterers are present, having two measurement points can be sufficient to determine the pair gain to great accuracy. However, still it is recommended to take more measurement points than two. With only two points it is not possible to verify whether far-field conditions are met because the residual between the fit and individual measurement points will always be zero, as can be seen in Fig. 4.17.

#### 4.5.4 Connection to the extrapolation measurement technique

In this chapter, the Friis equation is used to model the interaction between two antennas. Wacker’s equation offers a more rigorous description than the Friis equation and is used in the extrapolation measurement technique [58], [73]. When using this measurement technique, a similar relative-distance sweep as used in the presented method is performed. Subsequently, the data is fitted to a polynomial that accounts for the phase curvature over the receiver’s aperture and standing waves between the antennas. Moreover, as claimed in [73], the pair gain determined using the extrapolation method is independent of the choice of reference point. Whereas this is true, it might not be immediately clear how the choice of reference point affects the fit of the extrapolation method.

To conceptually show the connection of the extrapolation method to the presented method, the polynomial in Wacker’s equation that describes the zeroth order of scattering is fitted to the data acquired in the measurement using the OEWG and SGH (see Section 4.4.1) at 40 GHz from  $\Delta d = 0.3$  m to  $\Delta d = 1$  m for different choices of  $d_0$ . The absolute value of the zeroth order of scattering can be written down as follows

$$|S_{21}| = \frac{\lambda_0}{4\pi d} \sum_{n=0}^{\infty} \frac{A_n}{d^n} = \frac{\lambda_0}{4\pi d} \left( A_0 + \frac{A_1}{d} + \frac{A_2}{d^2} + \dots \right), \quad (4.5)$$

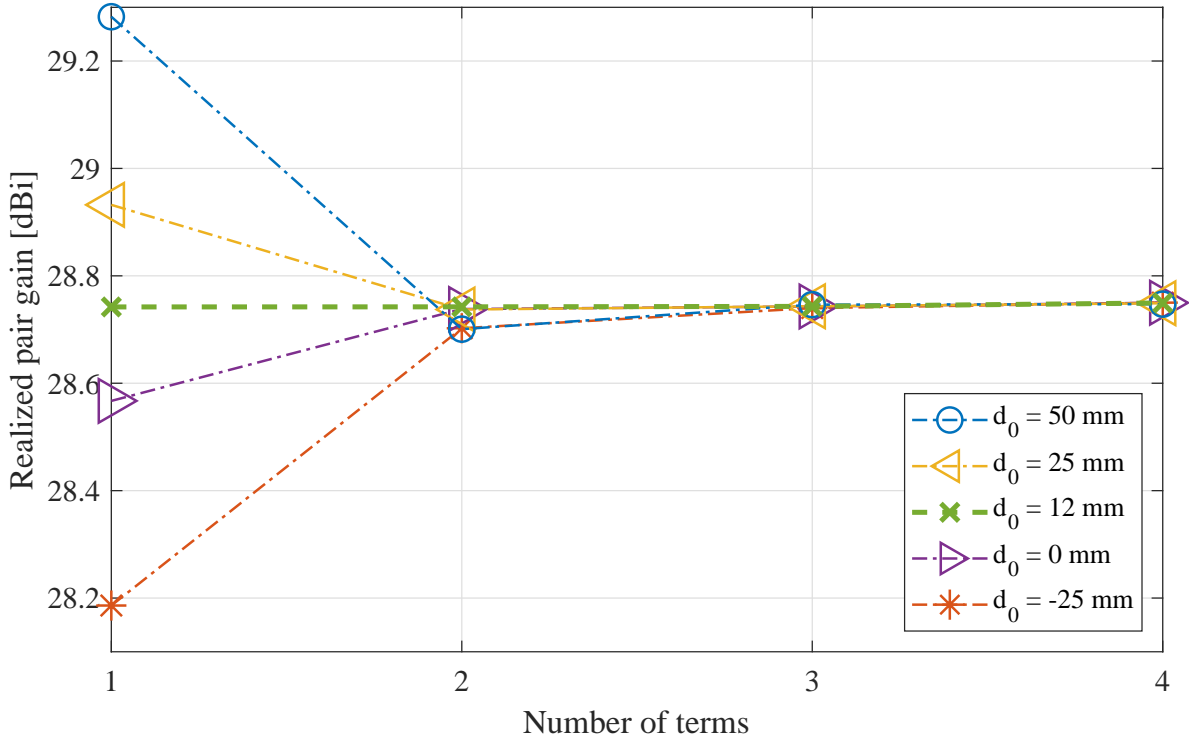


**Figure 4.18:** Comparison of the pair gain determined from (4.5) for different number of terms and for different values of  $d_0$ .

with  $A_n$  the constants that are to be determined by a least-squares fit. The constant  $A_0$  represents the square root of the pair gain. Hence, determining  $A_0$  is the objective when using the extrapolation method. If the distance  $d$  is large, only the first term of the polynomial is significant such that we arrive at the Friis equation. Note that  $d = \Delta d + d_0$ , so the constants  $A_n$  determined by (4.5) are implicitly a function of  $d_0$ .

Equation (4.5) contains infinitely many terms. Thus, selecting the optimum number of terms is not always a trivial task. In Fig. 4.18, the pair gain for different number of terms and for different values of  $d_0$  is shown. It can be seen in the figure that if the model only consists of one term, all choices of  $d_0$  result in a different pair gain. If a three-term or four-term model is selected, all five choices of  $d_0$  result to the same pair gain, verifying the claim the pair gain determined using the extrapolation method is independent of  $d_0$ . The pair gain for a  $d_0$  of 12 mm is independent of the number of terms, implying that a one-term model is suitable for  $d_0 = 12$  mm. Hence, the number of terms required to fit the data accurately can be reduced by making a good estimate of  $d_0$ , reducing the risk of overfitting, in turn.

In this example, only data are considered that complied with the inverse-square law and higher-order scattering terms were omitted. To thoroughly show the impact of choosing a reference point on the ability to fit Wacker's equation to the data and avoid the risk of overfitting, those effects have to be taking into account as well. This is, however, beyond the scope of the chapter.

## 4.6 Conclusion

In this chapter, a novel gain measurement technique based on a relative-distance sweep is presented. Using this measurement technique, the distance between amplitude centers of the antennas can be found. Knowing the absolute distance between the antennas allows for accurate gain measurements to be performed at limited separations. Moreover, performing measurements at multiple different distances allows for assessing whether or not the non-uniform phase curvature over the receiver's aperture has a significant impact on the determined gain, and thus whether the distance between the antennas has to be increased in order to achieve far-field conditions. Furthermore, since multiple measurements are taken, scattering and errors in the exact displacement of the translated antenna tend to average out, hence, reducing the error in the determined gain. These properties make the presented gain measurement technique suitable for accurate gain determination in anechoic chambers where the separation between the antennas is limited, as is for instance the case in the small chambers that are used for the characterization of 5G mm-wave phased arrays.



# Contactless Characterization of Millimeter-Wave Integrated Antennas<sup>1</sup>

---

## 5.1 Introduction

The short wavelength associated with the 5G mm-wave frequency band results typically in individual antenna elements having a size in the order of 5 mm. This miniaturization opens up the possibility to create an AoC or AiP [77]-[89], potentially reducing manufacturing costs and decreasing RF losses. Processes suitable for high-volume manufacturing of AoCs or AiPs are currently under development. Being able to measure typical antenna parameters, such as the input impedance or the antenna gain, is useful to validate models which are used to design integrated antennas produced using high-volume manufacturing processes. The OTA characterization methods presented in Chapter 3 were used to deduce the performance of several individual components in a phased array. However, the gain or the input impedance of an individual antenna element could not be extracted using the presented methods.

Adding a connector or using on-wafer probes to connect directly to the antenna requires a separate prototype, resulting in additional complexity and associated costs. Moreover, as reported in [90]-[96], the use of on-wafer probes often results in a change of antenna characteristics. For instance, in [90]-[95], it is shown that on-wafer probes have a significant influence on the gain and the radiation pattern of mm-wave antennas. Furthermore, [95], [96] report that the calibration procedure of on-wafer probes is not a straightforward task, making accurate input impedance measurements rather difficult.

To overcome these issues, a different method to characterize the antenna of an AoC or AiP is desired. In [97], [98], a polarimetric radar-cross-section (RCS) measurement method is introduced with which a complete set of antenna parameters, including input impedance, gain and scattering properties, can be obtained in a contactless manner. While determining scatter-

---

<sup>1</sup>This chapter is based on [P3].

ing properties of an antenna can be very important for radar applications, determining these properties for antennas used in communication systems is most often not relevant. Moreover, to perform this type of polarimetric RCS measurement, an extensive calibration procedure including two specific calibration targets are required [99]. In [100]-[105], [P12], a simplified version of the polarimetric RCS measurement method presented in [97], [98] has been used to determine antenna parameters using contactless OTA measurements. Basically, two variants of this CCM can be distinguished. In [100]-[103], [P12], the first variant was used to determine solely the input impedance of the AUT in a wireless fashion. This method does not require any calibration procedure. Using the second variant, both the input impedance and gain of the AUT could be determined [104], [105]. In this case, it is required to calibrate the setup by a straightforward 1-port SOL calibration, and an RA having a known gain has to be used. In Section 5.2, the two variants are discussed in detail.

Both variants have been successfully applied to antennas operating up to 5 GHz [101]-[105]. In [100], the CCM has been applied to an antenna operating in X-band. However, the authors indicate that accurate results in and beyond X-band are difficult to achieve, mainly due to the low received signal strengths and uncertainties in the position of the AUT.

In this chapter, the uncertainties of the CCM are examined and a model is presented to assess the impact of these uncertainties in far-field conditions. Using this model, the measurement setup is optimized in order to get reliable results with the CCM. The CCM is applied to an OEWG operating in the  $K_a$ -band. It is shown that using the CCM, the input impedance and realized gain of the OEWG can be successfully determined in the entire  $K_a$ -band. This makes the CCM potentially useful for the characterization of integrated mm-wave antennas.

The outline of this chapter is as follows. In Section 5.2, both variants of the contactless characterization method are explained. In Section 5.3, a model of the CCM including its uncertainties is presented. Section 5.4 is devoted to the used measurement setup and its limitations. In Section 5.5, the measurement results are shown and discussed. In Section 5.6, an outlook towards complex radiation pattern measurements is given. Finally, in Section 5.7, the conclusion is presented.

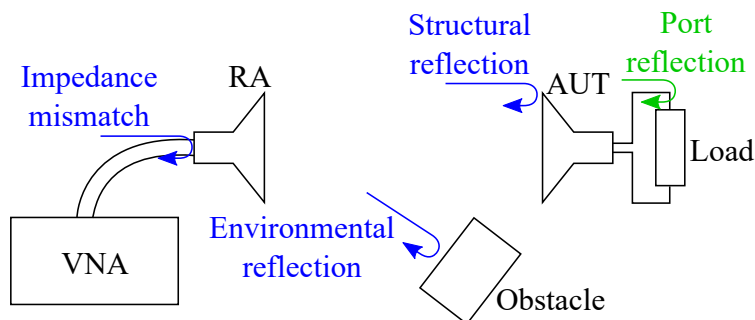


**Figure 5.1:** Schematic of the measurement setup.

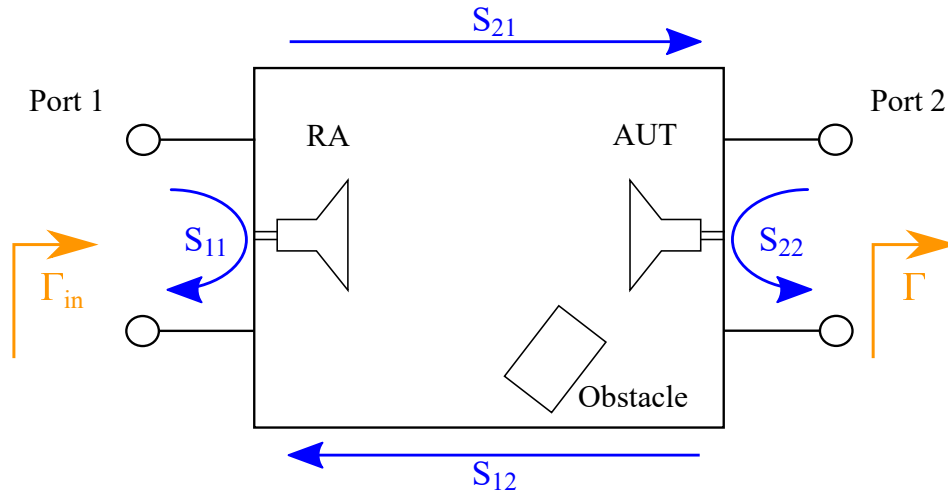


Figure 5.2: Two-port representation of the measurement setup.

## 5.2 Contactless characterization method

In Fig. 5.1, a schematic of the measurement setup for the CCM is shown. An RA is connected to a VNA and is used to illuminate the AUT. All EM waves that are reflected back to the RA contribute to the signal measured by the VNA. Examples of these contributions are the impedance mismatch of the RA, reflections due to reflective surfaces of the measurement environment and AUT, and a reflection at the port of the AUT. The key aspect of the CCM is that different loads connected to the AUT will only affect the latter reflection. By performing three measurements with three different known loads connected to the AUT, the parameters of interest can be retrieved as shown in the following subsections.

### 5.2.1 Determining the input impedance using the CCM

In the first variant of the CCM, only the input impedance of the AUT can be determined. If it is assumed that both antennas are linearly polarized, then the setup of Fig. 5.1 can be modeled as a two-port network. This is depicted in Fig. 5.2. The VNA is connected to port 1, whereas a known load having reflection coefficient  $\Gamma$  is connected to port 2. The measured reflection coefficient at port 1, denoted as  $\Gamma_{in}$ , can then be calculated using

$$\Gamma_{in} = S_{11} + \frac{S_{12}S_{21}\Gamma}{1 - S_{22}\Gamma}. \quad (5.1)$$

In (5.1), three unknowns can be identified, namely  $S_{11}$ ,  $S_{22}$ , and the product  $S_{12}S_{21}$ . This means that three measurements have to be performed in order to determine these three unknowns. As shown in [102], [103], [P12], the following set of equations can be used in order to extract the S-parameters of the two-port shown in Fig. 5.2

$$\begin{pmatrix} S_{11} \\ S_{22} \\ S_{12}S_{21} - S_{11}S_{22} \end{pmatrix} = \begin{pmatrix} 1 & \Gamma_{Z_1}^{in} \Gamma_{Z_1} & \Gamma_{Z_1} \\ 1 & \Gamma_{Z_2}^{in} \Gamma_{Z_2} & \Gamma_{Z_2} \\ 1 & \Gamma_{Z_3}^{in} \Gamma_{Z_3} & \Gamma_{Z_3} \end{pmatrix}^{-1} \begin{pmatrix} \Gamma_{Z_1}^{in} \\ \Gamma_{Z_2}^{in} \\ \Gamma_{Z_3}^{in} \end{pmatrix}. \quad (5.2)$$

Here,  $\Gamma_{Z_1}^{\text{in}}$ ,  $\Gamma_{Z_2}^{\text{in}}$  and  $\Gamma_{Z_3}^{\text{in}}$  represent the measured reflection coefficient at port 1, while terminating port 2 with known loads having reflection coefficients  $\Gamma_{Z_1}$ ,  $\Gamma_{Z_2}$  and  $\Gamma_{Z_3}$ , respectively.

To solely determine the input impedance, the VNA does not have to be calibrated. Calibrating the VNA will only affect the determined  $S_{11}$ ,  $S_{21}$  and  $S_{12}$ -parameters and will leave  $S_{22}$  unaffected because the reference plane of port 2 is already at the desired location. Moreover, the obstacles as shown in Fig. 5.1 are hardly influencing the  $S_{22}$ -parameter if they are positioned in the far-field of the AUT, making the use of an expensive anechoic chamber not necessary [P12].

## 5.2.2 Determining the realized gain using the CCM

The two-port representation in Fig. 5.2 is similar to the representation of a typical realized gain measurement. If both ports are connected to a calibrated VNA, and the realized gain of the RA is known, the realized gain of the AUT can be determined using the Friis equation. The Friis equation can be cast in the following form<sup>2</sup>

$$|S_{21}|^2 = G_{\text{RA}} G_{\text{AUT}} \left( \frac{\lambda_0}{4\pi d} \right)^2. \quad (5.3)$$

Here,  $\lambda_0$  is the wavelength in free-space,  $d$  is the distance between the antennas, and  $G_{\text{RA}}$  and  $G_{\text{AUT}}$  are the realized gains of the RA and the AUT, respectively. By performing a single  $S_{21}$ -measurement, the realized gain of the AUT can be determined by solving (5.3). In addition, if the AUT is rotated, the radiation pattern can be determined as well.

This method to determine the realized gain of an unknown antenna having a suitable interface to connect a cable or waveguide has been used for decades. However, this method is difficult to adopt for integrated antennas. In the case of an integrated antenna, the  $S_{21}$ -parameter can be determined using the set of equations given in (5.2). Port 1 has to be connected to the VNA, which now needs to be calibrated. A known load has to be connected to port 2. Again, three measurements have to be performed to solve (5.2), but using this second variant of the CCM, both the input impedance and realized gain can be extracted from the measurement data. Since both the input impedance and realized gain can be determined, the gain (also called absolute gain) can be calculated as well.

Note that the described procedure requires that  $S_{21}$  and  $S_{12}$  are equal. When using a monostatic setup (i.e., only one RA is used) this requirement is fulfilled. In [100], [102], [103], [105], a bistatic setup (i.e., two RAs are used) is adopted in an attempt to get a larger dynamic range. If a bistatic setup is used,  $S_{21}$  and  $S_{12}$  (as defined in Fig. 5.2) are not equal in general. Hence, using a bistatic setup can lead to errors in the determined realized gain of the AUT. Therefore, a monostatic setup is used to acquire the data shown in this chapter.

---

<sup>2</sup>In (5.3), it is assumed that both antennas are linearly polarized and that the polarizations are matched. If the RA is linearly polarized, but the AUT is elliptically polarized, two measurements have to be performed to fully characterize the gain of the AUT.

In Fig. 5.1 and 5.2, an obstacle is present to resemble environmental reflections. Whereas static obstacles hardly influence the resulting input impedance, the determined realized gain can be significantly affected by environmental reflections. Therefore, just like in a conventional gain measurement, the use of an anechoic chamber is a necessity for reliable gain measurements using the CCM.

### 5.3 Analysis of the CCM in far-field conditions

Compared to conventional input impedance and gain measurements, the CCM introduces a few additional measurement uncertainties. First of all, the CCM requires three measurements instead of one. It is mandatory that the AUT remains at the same position during the three measurements. However, since the loads attached to the AUT have to be changed, this is not always guaranteed while performing the CCM. Secondly, the reflection coefficients of the three used terminations have to be known. If this is not the case, the determined input impedance and gain of the AUT could significantly deviate from its true values. Lastly, the CCM relies on OTA transmission. This results in additional FSPL, which will, in turn, make the results of the CCM more susceptible to noise and drift compared to conventional methods. In the following subsections, a model is presented and is used to assess the impact of these additional measurement uncertainties. Based on this model, a suitable distance between the RA and AUT can be found, as shown in Section 5.4.

Different measurement setups require different accuracies. Therefore, in the upcoming subsections, instead of establishing bounds on the uncertainties to ensure accurate results, only the effects of the uncertainties are shown. The reader can implement the model and judge him/herself which uncertainties are tolerable in their own setup.

#### 5.3.1 Reflected signal of interest

The port reflection at the AUT (see Fig. 5.1) is crucial for the CCM and will be referred to as the reflected signal of interest (RSI). The RSI cannot be measured individually since the VNA is not able to distinguish the RSI from any other (static) reflection. A vector representation of the relation between the RSI  $\Gamma_{\text{RSI}}$  for different loads, measured reflection coefficient  $\Gamma_{\text{in}}$  and the static reflections  $\sum \Gamma_{\text{S}}$  is shown in Fig. 5.3. In Fig. 5.3(a)-(c), the situation is shown when a perfect short, open and load, respectively, is connected to an antenna with an input impedance equal to the reference impedance. Figure 5.3(d)-(f) depicts the relation between the vectors when a perfect short, open or load, respectively, is connected to an antenna having a real input impedance that is higher than the reference impedance. Note that in this case the magnitude of the RSI is different when a short or an open is connected to the antenna.

If the measurement environment remains static, the difference between  $\Gamma_{\text{in}}$  and  $\Gamma_{\text{RSI}}$  is independent of the reflection coefficient of the load  $\Gamma$ . The contribution of the static reflections in the measured reflection coefficient will, therefore, only contribute to the determined  $S_{11}$  of the 2-port network illustrated in Fig. 5.2, and will leave  $S_{12}$ ,  $S_{21}$  and  $S_{22}$  unaffected. In other

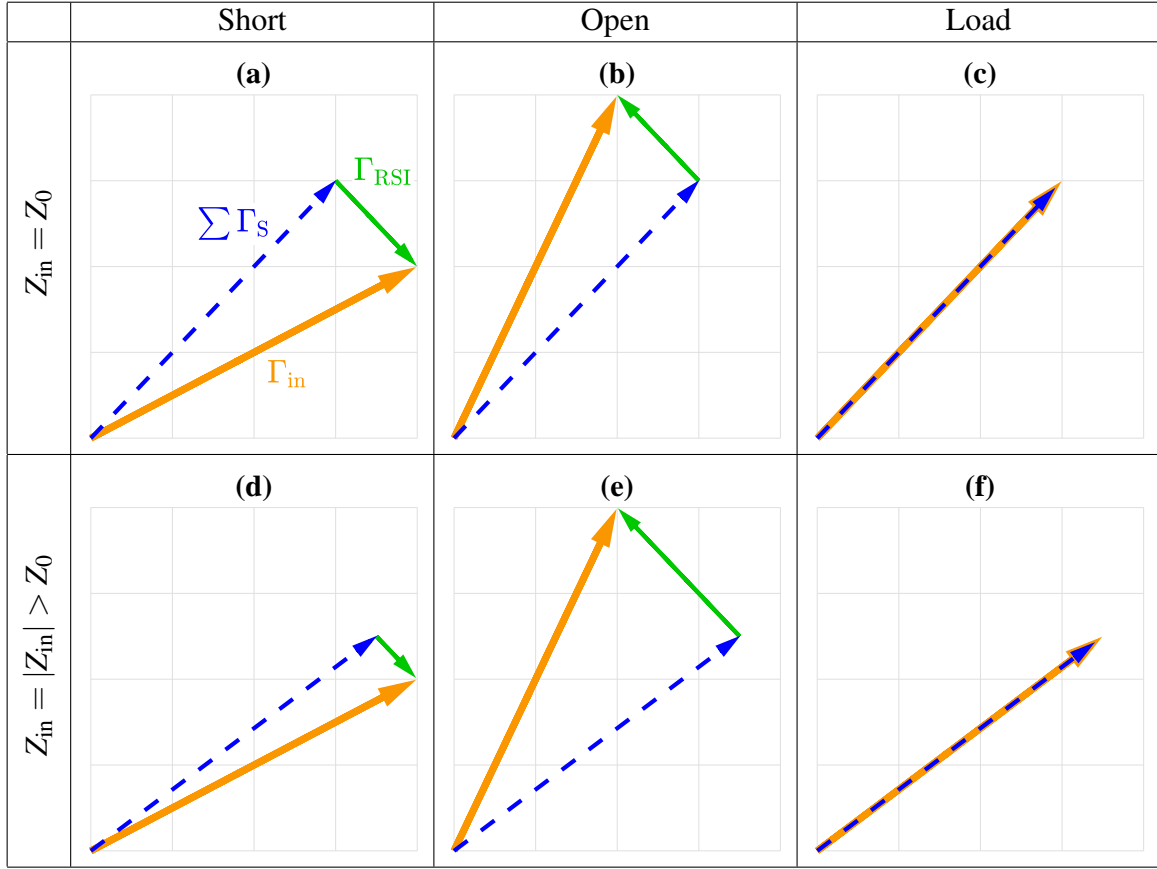


**Figure 5.3:** Qualitative vector representation of the relation between the measured reflection coefficient  $\Gamma_{in}$  (orange), the static reflections  $\sum \Gamma_s$  (blue), and the RSI  $\Gamma_{RSI}$  (green) for different terminations and different antenna input impedances.

words, all required information to determine the input impedance and realized gain of the AUT is present in the RSI. Therefore, the sensitivity of the CCM can be assessed by solely considering the RSI. In first order,<sup>3</sup> the RSI can be calculated as follows

$$\Gamma_{RSI} = |S_{21}^c|^2 G_{RA} \left( \frac{\lambda_0}{4\pi d} \right)^2 e^{-j2k_0 d} G_{AUT} \frac{\Gamma}{1 - S_{22}\Gamma}. \quad (5.4)$$

Here,  $S_{21}^c$  represent the transmission through the cable connecting the VNA and RA, and  $k_0$  represents the wavenumber in vacuum. The realized gain and input reflection coefficient of the AUT ( $G_{RA}$  and  $S_{22}$ , respectively) are generally unknown. Simulation data or an educated guess can be used to calculate the expected RSI.

If (5.4) is used to calculate the RSI three times for three different loads, the input impedance and realized gain of the AUT can be determined by feeding the results of (5.4)

<sup>3</sup>Like in the Friis equation, multipath reflections or standing waves are not considered in (5.4). Moreover, the phase progression in the cable and by the antennas is omitted since that is assumed constant throughout the three measurements.

in (5.2) and (5.3).<sup>4</sup> As expected, the resulting input reflection coefficient and realized gain of the AUT will exactly match the chosen values for  $S_{22}$  and  $G_{RA}$  in (5.4). To assess the impact of uncertainties in the setup, deviations can be artificially introduced in (5.4) and the error on the resulting input impedance and realized gain can be examined, as is shown in the following subsections. To show this, simulation data of a probe-fed square patch antenna operating around 30 GHz are used. The input impedance and realized gain of the patch are shown in Fig. 5.4 and 5.5, respectively, and denoted by ‘Reference.’ Moreover, for the realized gain of the RA, a WR-28 OEWG with 100% aperture efficiency is assumed and the distance between AUT and RA is 10 cm.

### 5.3.2 Displacement errors

To estimate the impact of displacement errors, two assumptions were made. Firstly, it is assumed that the positioning error of the AUT will only affect the RSI, and the static reflections  $\sum \Gamma_S$  will remain unchanged. Secondly, the errors are assumed to be in the longitudinal direction only. Both assumption allow usage of (5.4) and the displacement error is introduced by calculating the RSI for the different loads twice using distance  $d$ , and once using distance  $d + \Delta d$ ,  $\Delta d$  being the displacement error. In Fig. 5.4 and 5.5, the effect of a displacement error of 0.5 mm and 1 mm is shown. Both displacement errors give rise to a negative real impedance for some frequencies. This clearly shows that a displacement error as small as 0.5 mm results in incorrect results since a negative real impedance is unphysical for a passive device. For a displacement error of 1 mm, the realized gain is off by more than 2.5 dB at 30 GHz. For  $\Delta d = 0.5$  mm, the results are better, but still an error of 0.9 dB in the determined realized gain can be found at around 30 GHz. Hence, keeping the AUT stationary during the three measurements is of utmost importance.

### 5.3.3 Load uncertainty

If the reflection coefficients of the loads are not accurately known, the set of equations in (5.2) and (5.4) can be used to determine the impact of this uncertainty. In order to do this assessment, a different value for  $\Gamma$  has to be chosen in (5.2) and (5.4). In (5.2), the nominal value of the loads has to be used, whereas in (5.4) the load can be varied in order to assess the impact. In Fig. 5.4 and 5.5, the impact of a wrong assumption on a 50  $\Omega$  load is shown. Since the loads used in the measurement setup are connectorized, the reflection coefficient of these loads could be accurately determined. Therefore, this uncertainty will not be considered in the remainder of the chapter.

---

<sup>4</sup>Note that the cable losses included in (5.4) also have to be included in (5.3).

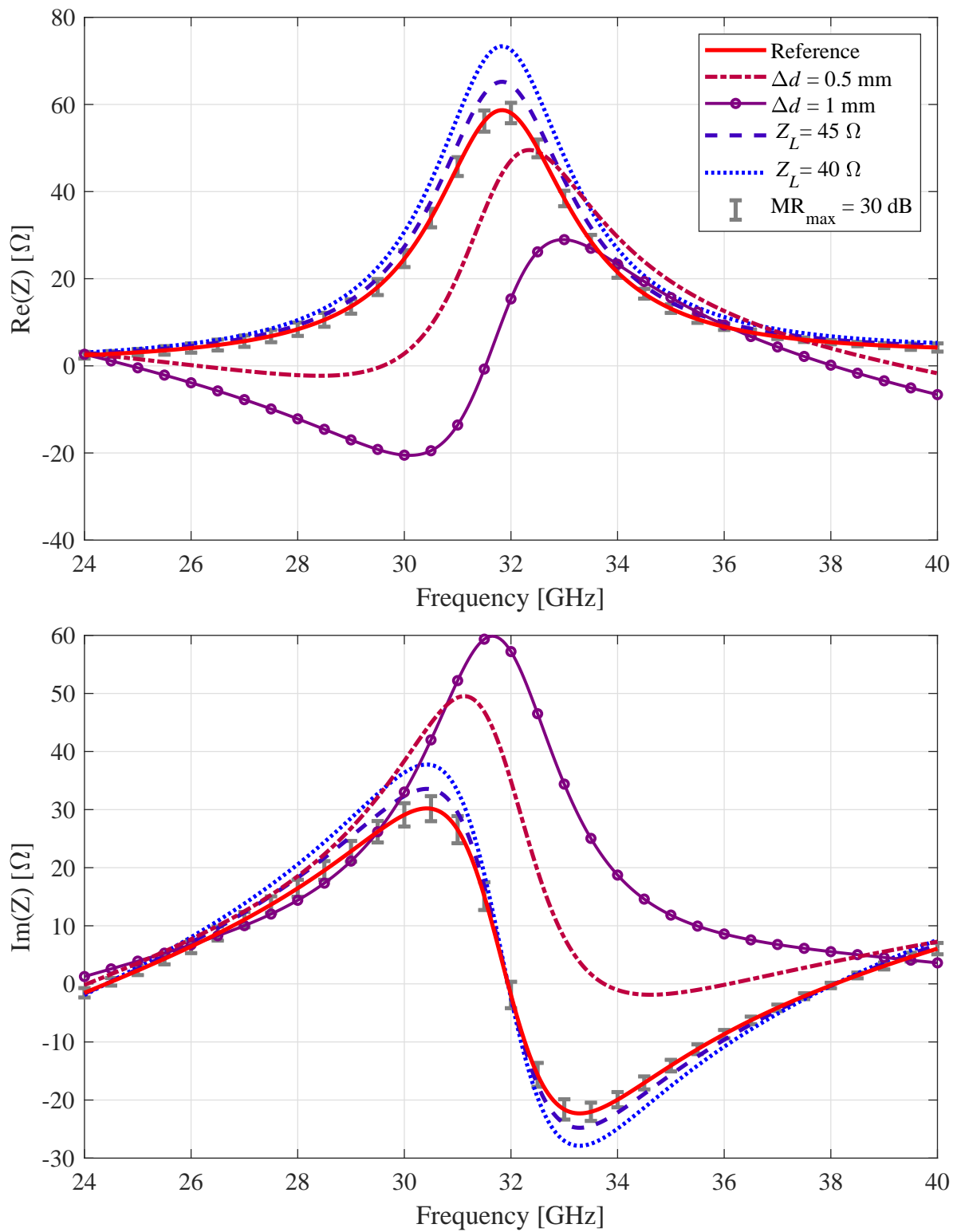


**Figure 5.4:** Determined real (top) and imaginary (bottom) part of the input impedance of a patch antenna for different artificially introduced errors.



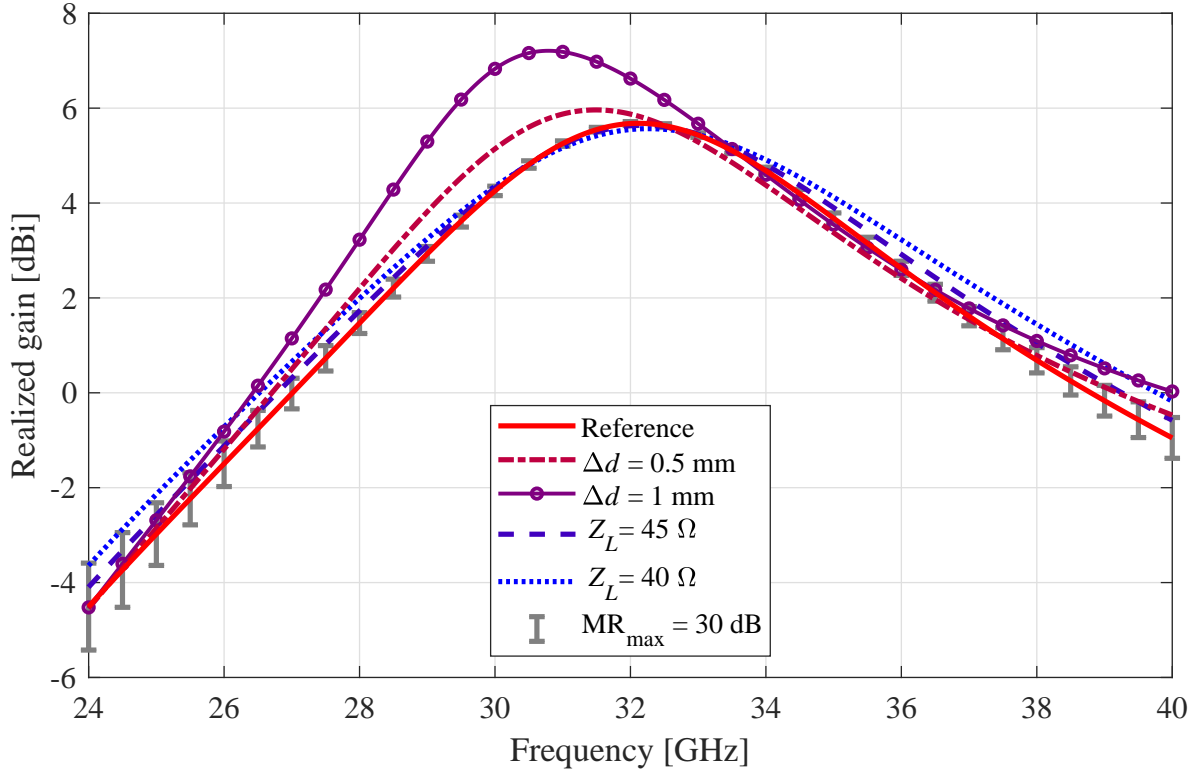


**Figure 5.5:** Determined realized gain of a patch antenna for different artificially introduced errors.

### 5.3.4 Impact of noise and drift

Every electronic measurement device adds thermal noise to its measured signal. Furthermore, all measurement devices and setups are subject to a time-dependent drift. Both the noise and drift add an uncertainty to the measurement. Although the nature of the noise and drift are different, the added uncertainty of both effects can be assessed by adding a random complex vector to (5.4). Note that this random complex vector has to be different for each of the three terminations.

The effect of noise and/or drift is shown in Fig. 5.4 and 5.5 using error bars. The size of these error bars denote the  $2\sigma$ -confidence intervals. Here, the noise and/or drift is chosen such that the maximum measurement range (MR), denoted as  $MR_{\max}$ , is around 30 dB. This means that the power of the random complex vector added to (5.4) is 30 dB lower than the maximum expected RSI power. Since the realized gain of the patch is frequency dependent, the power of the RSI is dependent on frequency. This means that since the noise and/or drift are fixed, the MR is a function of frequency. For instance, it can be seen in Fig. 5.5 that the uncertainty is higher for lower realized gain, which is the result of a lower MR due to a lower RSI power.

An error of 0.3 dB in the realized gain due to noise and/or drift is considered to be acceptable. The error bars at 27 and 38.5 GHz in Fig. 5.5 correspond to 0.3 dB. At these frequencies, the realized gain has dropped by 5.5 dB, making the MR approximately 24.5 dB. Therefore,

an MR of 24.5 dB is considered to be acceptable in the remainder of this chapter.

Note that the MR is relative, and that the value of the added noise and/or drift vector can only be fixed if the cables losses are defined. In the results shown in Fig. 5.4 and 5.5, the effect of the cables is ignored, i.e.,  $S_{21}^c = 1$ . In this case, the maximum RSI is around  $-67.5$  dB, so the added noise and/or drift vector is around  $-97.5$  dB.

### 5.3.5 Optimal distance between the RA and AUT

To perform a reliable input impedance measurement, no scatterers should be present in the vicinity of the AUT. For the CCM, by definition, an RA is positioned opposite to the AUT. To minimize the effect of the RA on the input impedance of the AUT, the distance between the RA and AUT should be sufficiently large. To determine the realized gain of the AUT, the Friis equation is used. This equation is only valid for antennas operating in far-field conditions. Furthermore, the Friis equation only takes into account the line-of-sight contribution and does not account for standing waves between the RA and AUT. This essentially means that either both the structural reflection and the reflection due to the impedance mismatch (see Fig. 5.1) should be sufficiently low, or the distance between the antennas should be sufficiently large. On the other hand, the CCM is subject to significant FSPL. If the distance between the RA and AUT is doubled, the power of the RSI will drop as much as 12 dB. Increasing the distance will make the CCM more susceptible to noise and drift. Therefore, the most suitable distance for the CCM is as large as possible to ensure reliable measurement data, but is limited by the noise power and drift of the system. As discussed in the previous subsection, an MR of 24.5 dB or higher seems to lead to reasonable results, so based on that value a suitable distance can be found.

## 5.4 Experimental evaluation

### 5.4.1 Measurement setup

In Fig. 5.6, the CCM setup is shown. The RA is connected to the VNA and is positioned opposite to the AUT. The RA illuminates the AUT and the reflected signal is measured. This measurement is repeated three times, each time with a different known load connected to the AUT. The male short, open and load of the Maury Microwave 8770CK11 calibration kit have been used for these measurements. Because no switch up to 40 GHz was available at the measurement facility, the loads had to be changed manually. To minimize the positioning error caused by manually changing the loads, the AUT was fixated using tie wraps, as can be seen in the figure.

### 5.4.2 Choice of RA and AUT

Measurement results in recent publications show that the realized gain of integrated antennas can vary between 0 dBi and 14 dBi [77]-[87]. Since the CCM is meant for integrated antennas, an AUT having a realized gain in the same order is desired. Therefore, a WR-28 OEWG, having a realized gain of about 6 dBi, has been chosen for both RA and AUT. An absorber has been placed around the waveguide of the AUT to minimize the reflections of the load and of the metal construction used to keep the antenna into place. Likewise, absorbing material was positioned on the waveguide of the RA to mitigate the reflection from the flange and mounting structure.

### 5.4.3 Stability of the measurement setup

Since the loads had to be changed manually, the stability of the whole system has been examined. In the first stability test, the setup shown in Fig. 5.6 has been used. The VNA was connected to the RA, and the reflection coefficient has been measured for 20 minutes. Changing a load takes about 30 seconds, meaning that the three measurements required for the CCM take about 1 minute. The average drift after 1 minute was found to be in the order of  $-95$  dB. In the second stability test, the same setup was used, but now the calibration standard connected to the AUT was removed and put back every minute to determine the effect of manually changing the calibration standard. This sequence was performed using all three different calibration standards. Subsequent measurements again showed a difference in the order of  $-95$  dB on average. This indicates that the stability of the system is dominated by a time-dependent drift and that the positioning error caused by manually changing the load is negligible in the used setup.

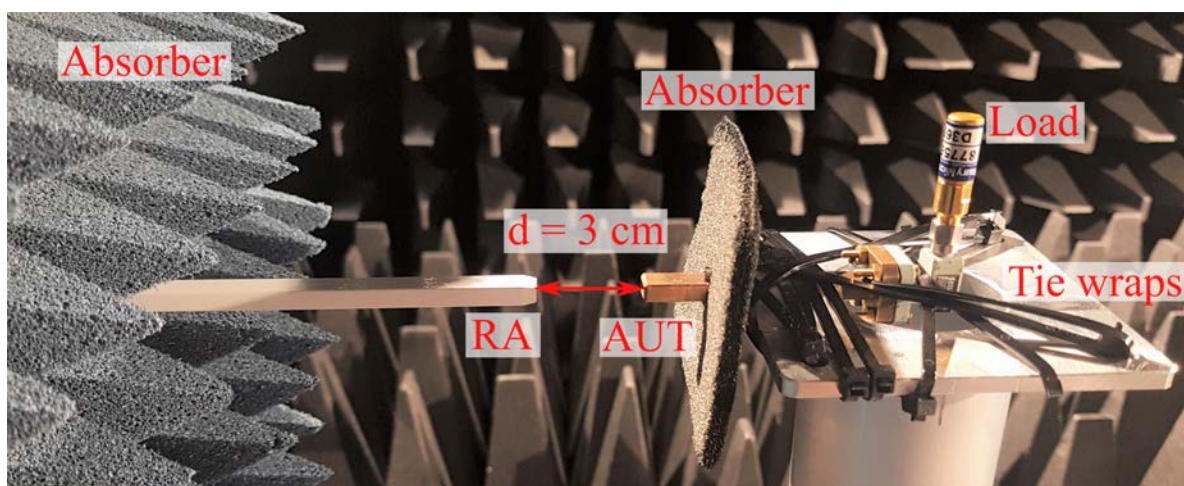


**Figure 5.6:** Setup for the contactless characterization method.

**Table 5.1:** Losses and gains in the measurement setup.

	$f = 24$ GHz	$f = 40$ GHz
Total cable losses	23.7 dB	31.0 dB
Total free-space path loss	59.2 dB	68.1 dB
Total realized antenna gain	18.9 dBi	28.3 dBi
Expected RSI (short & open)	-64.0 dB	-70.8 dB

#### 5.4.4 Impact of noise

The VNA is an N5225A PNA Microwave Network Analyser from Keysight Technologies. With an output power of 13 dBm and an intermediate frequency bandwidth (IFBW) of 100 Hz, the noise floor of the VNA is around  $-120$  dB. This means that the noise generated by the VNA is negligible compared to the observed drift of the setup.

#### 5.4.5 Distance between the RA and AUT

The most suitable distance between the RA and AUT is dependent on the expected signal strength of the RSI in relation to the drift and noise of the setup. Based on Section 5.3.4, an MR of 24.5 dB was found to be suitable. Using (5.3), a distance of 3 cm between RA and AUT has been determined. This is larger than the Fraunhofer distance of a WR-28 OEWG, which is 1.7 cm at 40 GHz. In Table 5.1, the values of the losses and gain are summarized. In this calculation, a perfect matched AUT (i.e.,  $S_{22} = 0$ ) has been assumed. By comparing the drift values reported in Section 5.4.3 to the expected RSI values, it can be concluded that the system has an MR of about 31 dB at lower frequencies, whereas it is around 24 dB at higher frequencies.

### 5.5 Measurement results

In order to experimentally verify the CCM, two reference measurements have been performed. In the first reference measurement, the AUT was directly connected to a calibrated VNA and its input impedance was determined in a connected manner. For this reference measurement, the AUT was mounted in the anechoic chamber without any scatterers in its vicinity. For the second reference measurement, a 2-port SOLT calibration was performed. The antennas were positioned opposite to each other in the same way as shown in Fig. 5.6, but the AUT was connected to port 2 of the VNA, rather than to a calibration standard. Using the conventional gain measurement method as described in Section 5.2.2, the realized gain of the AUT was determined.

Since both the RA and AUT are OEWDs, the realized gain is assumed to be equal. Additionally, since the separation between the antennas is almost twice the Fraunhofer distance,

it had been assumed that the antennas were operating in far-field conditions. Moreover, as shown in Chapter 4, for an accurate gain measurement, the amplitude center has to be taken into account when determining the distance  $d$  between the antennas. In the upcoming results, the amplitude center was assumed to be at the aperture of the OEWDs. All three assumptions lead to an error in the determined realized gain. However, both the reference measurement and the CCM use the aforementioned assumptions, allowing a direct comparison of both methods.

In Fig. 5.7, the determined input impedance of both the reference measurement and the CCM are shown. It can be seen that the measurements are in good agreement. Both curves follow the same trend and have peaks and troughs at the same locations. Figure 5.8 shows the determined realized gain and phase. Also here a high degree of resemblance can be found between the reference measurement and the CCM. The maximum gain deviation is lower than 0.2 dB, whereas the phase deviation remains below  $3^\circ$ .

Although the results in Fig. 5.7 and 5.8 are in good agreement, some discrepancies can be found. As mentioned in Section 5.4.3, some time had passed in between measurements, causing the system to drift slightly, affecting the accuracy of the CCM. In addition, the CCM is very sensitive to positioning errors. Although the error caused by manually changing the load did not seem dominant, it remains a source of uncertainty.

If the CCM is going to be used for integrated antennas, three different terminations and a switch have to be implemented on the integrated circuit. With a switch, the setup will be completely static, eliminating a possible alignment error. Moreover, the measurement time can be significantly reduced, mitigating the observed time-dependent drift of the measurement setup. On the other hand, in the present case, the reflection coefficient of the loads were measured with high precision. If the CCM will be used for integrated antennas, the on-chip terminations will be subject to manufacturing tolerances and, hence, less accurately known.

## 5.6 Complex radiation pattern measurement

A radiation pattern measurement of an integrated antenna can be performed with an on-board RF source and a spectrum or power analyzer attached to the RA. However, determining the phase of the radiation pattern is not possible using this method. Especially since integrated antennas are likely to be used in antenna arrays, verification of the phase distribution of the radiating elements can be desired. As mentioned in Section 5.2.2, in theory, the complex radiation pattern of the AUT can be determined in a wireless fashion. The results in Fig. 5.8 indicate that indeed an accurate measurement of the magnitude and phase of a radiation pattern is possible using the presented CCM. It should be emphasized, however, that the MR of the system should be higher compared to a gain measurement, since otherwise it will not be possible to detect nulls in the radiation pattern. This can, for instance, be achieved by reducing the cables losses, or by performing the measurements faster to reduce the drift. Moreover, in traditional radiation pattern measurements, the measurements are often performed in a dynamic

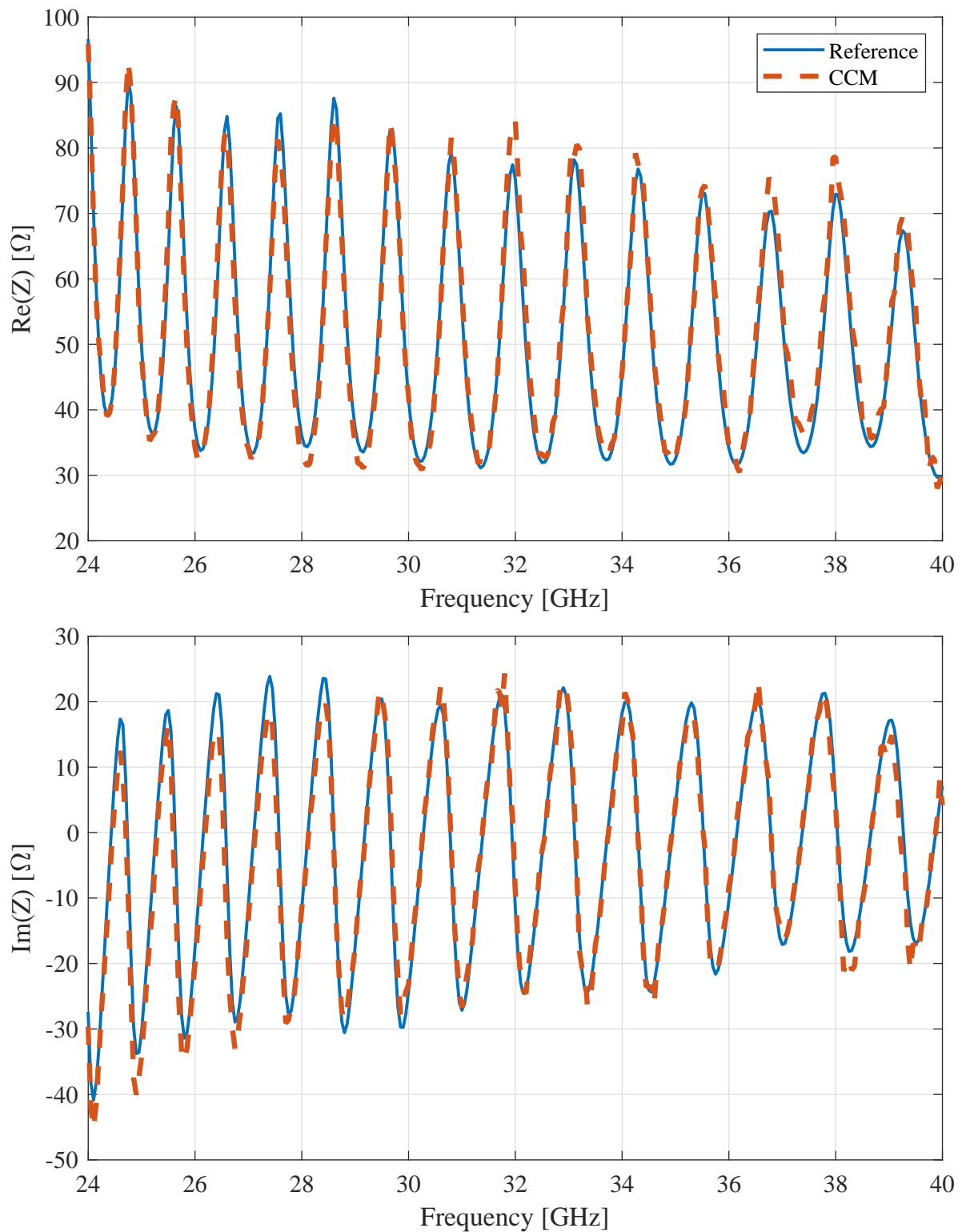


**Figure 5.7:** Real (top) and imaginary (bottom) part of the input impedance using a connected measurement (blue) and the CCM (red).

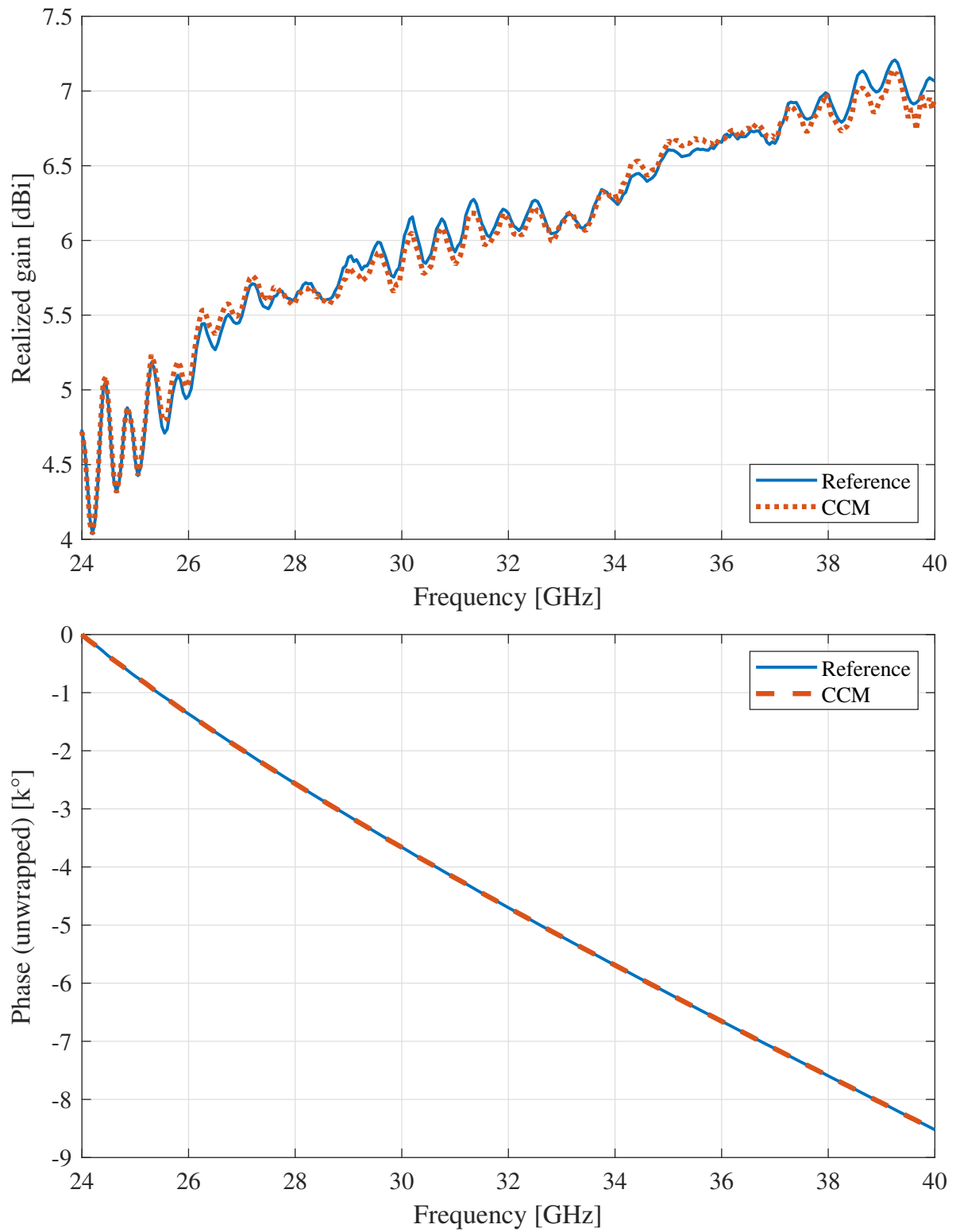


**Figure 5.8:** Realized gain (top) and phase (bottom) using a two-port calibrated setup (blue) and the CCM (red).

environment. Instead of taking a measurement at every angle while the equipment remains stationary, either the RA or AUT is continuously moving throughout the measurements. Since the CCM is very sensitive to positioning errors, it should be noted that a complex radiation pattern measurement might have to be performed in a static environment, i.e., the equipment has to remain stationary at every angle while performing the three required measurements per angle.

## 5.7 Conclusion

In this chapter, the uncertainties of the CCM in far-field conditions are examined and a model is presented to assess the impact of these uncertainties. Moreover, the CCM has been used to determine the input impedance and realized gain of an OEWG operating in the  $K_a$ -band, and a good match between the reference measurement and CCM is achieved. Being able to measure these typical antenna parameters is useful to validate models which are used to design integrated antennas produced using high-volume manufacturing processes. In order to do perform the CCM on an integrated mm-wave antenna, three different terminations and a switch have to be implemented on the IC. In this case, both the misalignment and drift issues discussed in this chapter will be mitigated. The on-chip terminations will be subject to manufacturing tolerances and, hence, less accurately known compared to the terminations used in the experiments described in this chapter. The model presented in this chapter can be used to investigate the impact of this uncertainty. In turn, this uncertainty has to be taken into account in the validation of the models used to design integrated antennas produced using high-volume manufacturing processes.



# Antenna Functionality Testing for High-Volume AoC & AiP Manufacturing<sup>1</sup>

---

## 6.1 Introduction

In a cost-effective high-volume IC manufacturing facility, the majority of the tasks are completely automated. To bring a (packaged) IC from one station to the next, pick-and-place handlers using suctions are often utilized. These handlers typically are embedded in a system which can be used to test and verify the functionality of the IC [106]. As mentioned in Chapter 5, one of the current trends in the IC development is the integration of antennas on-chip or in the package of the IC. In Section 5.2.2, an elaborate method to accurately characterize an integrated antenna is presented. This method, however, does require calibration, an anechoic chamber, and a large dynamic range. This method is, therefore, not attractive for high-volume production testing. In Section 5.2.1, a method is introduced with which only the reflection coefficient of an unknown and possibly integrated antenna can be measured in a contactless manner. An advantage of this method is that it does not require any calibration.

In [100]-[103], this method has been used to determine the reflection coefficient of an antenna which was positioned in an anechoic chamber. Anechoic chambers suited for high-frequency RF measurements are expensive and the used absorbers typically are covered by carbon dust. ICs are usually manufactured in a clean room, making the use of common RF absorbers in an IC testing facility not practical, if not impossible. It is experimentally verified in [P12], that the use of an anechoic chamber is not a necessity to acquire accurate results using this variant of the CCM, making it an attractive method for high-volume testing.

In [100]-[103], [P12], the reported separation between the measurement antenna and the AUT has always been larger than the far-field distances of either antenna. However, reducing the separation between the antennas relieves dynamic range requirements of measurement

---

<sup>1</sup>This chapter is based on [P4].

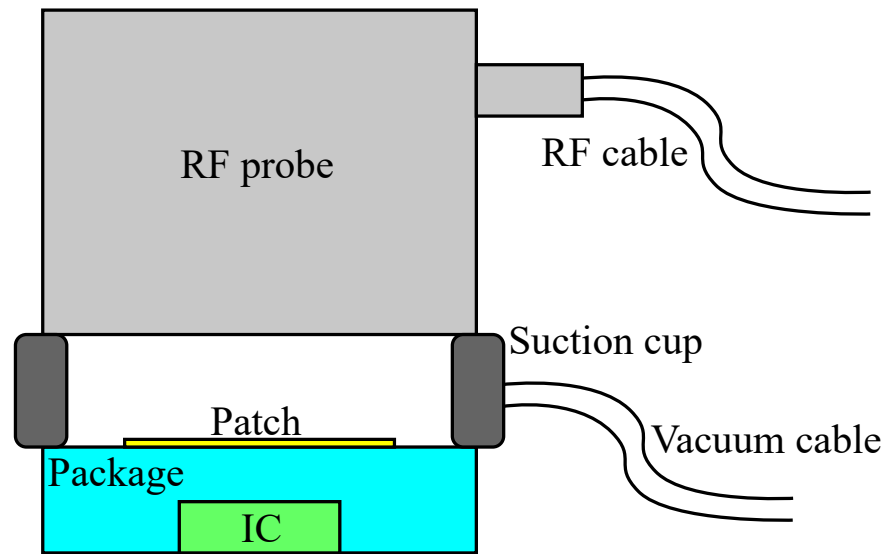


**Figure 6.1:** Concept of a probe combining the RF testing and the pick-and-place functionality.

equipment and would allow for more compact testing solutions. Traditionally, pick-and-place handling systems are not equipped with an OTA testing functionality, but with the upcoming trend of integrating the antenna with the IC, it might even be beneficial that such testing functionality will be included in a pick-and-place handler. For instance, an RF probe could be embedded in the pick-and-place handler, combining both the RF testing and pick-and-place functionality. The concept of such a novel probe is shown in Fig. 6.1 and is patented in [P19].

In this chapter, the concept of using the CCM in combination with the probe illustrated in Fig. 6.1 is assessed from an RF point of view. It is investigated whether the CCM can be used in near-field conditions, since this will enable compact testing solutions and potentially relief dynamic range requirements. In this case, coupling between the RF probe and the AUT is inevitable. Hence, the sensitivity of the CCM due to the position and alignment errors of the probe is examined. To perform this assessment, positional tolerances of cost-effective commercial available pick-and-place handlers are used. The effect of vibrations in the measurement system is also examined. To generalize the obtained results, the assessment is performed on three different integrated antenna structures. Moreover, measurement results around 33 GHz using a connectorized patch antenna are shown, which experimentally verify the validity of using the CCM in near-field conditions at mm-wave frequencies.

The outline of this chapter is as follows. Section 6.2 is devoted to modeling the characterization method in near-field conditions and adding imperfections to the measurement setup. In Section 6.3, the measurement setup and results are shown. In Section 6.4, the conclusion is presented.

## 6.2 Analysis of the CCM in near-field conditions

### 6.2.1 Setup of the CST model

Equation (5.4) can be used to calculate the RSI and this RSI can subsequently be used to assess the sensitivity of the CCM in far-field conditions. However, to assess the sensitivity of the CCM in near-field conditions, a full-wave electromagnetic model has been made using CST Microwave Studio. In first instance, a patch antenna has been used as AUT. Mainly because of its planar low-profile structure, this type of antenna is widely used in integrated antenna studies (see for instance [82]-[85]) and, therefore, a straightforward choice as a starting point for this assessment. In Fig. 6.2(a), a model of the via-fed patch is shown. The patch is square and its length and width are 2.5 mm. The relative permittivity and loss tangent of the substrate is 3 and 0.025, respectively. The length, width and thickness of the substrate is 4 mm, 4 mm, and 0.3 mm, respectively. Without loss of generality and to reduce computation time, the patch, ground plane and feed are made of perfect electric conductor (PEC) material, and the patch and ground plane are given zero thickness. In order to get a well-matched antenna at  $f_c = 32$  GHz, the position of the via is 0.65 mm out of the center of the patch.

A WR-28 OEWG is chosen as RA. The CST model of the OEWG is depicted in Fig. 6.2(b). The wall thickness is chosen to be 0.5 mm, and the OEWG is modeled using PEC material as well. The combination of AUT and RA is shown in Fig. 6.2(c). The centers of both antennas are aligned and the nominal distance between the two antennas is chosen to be 2 mm.

### 6.2.2 Distance between the AUT and RA

The CCM relies on OTA transmission, which can result in large FSPL. The port reflection, which is the signal of interest, travels twice the distance between the AUT and RA. If far-field conditions are achieved, this means that every doubling in distance results in 12 dB additional FSPL. Therefore, the distance between the AUT and RA has a significant impact on the required dynamic range of the measurement setup. Since the intended application is a cost-effective high-volume testing procedure, it is advantageous to have a method that does not require the test equipment to have a large dynamic range. Moreover, if losses such as the FSPL are reduced, the IFBW of the VNA can be increased, allowing reduced measurement times.

In [100]-[103], the reported separation between the AUT and RA has been always larger than the far-field distances of both antennas. However, as shown in this section, it is possible to place the antennas in each other's near-field region and the reflection coefficient can still be accurately determined using the CCM.

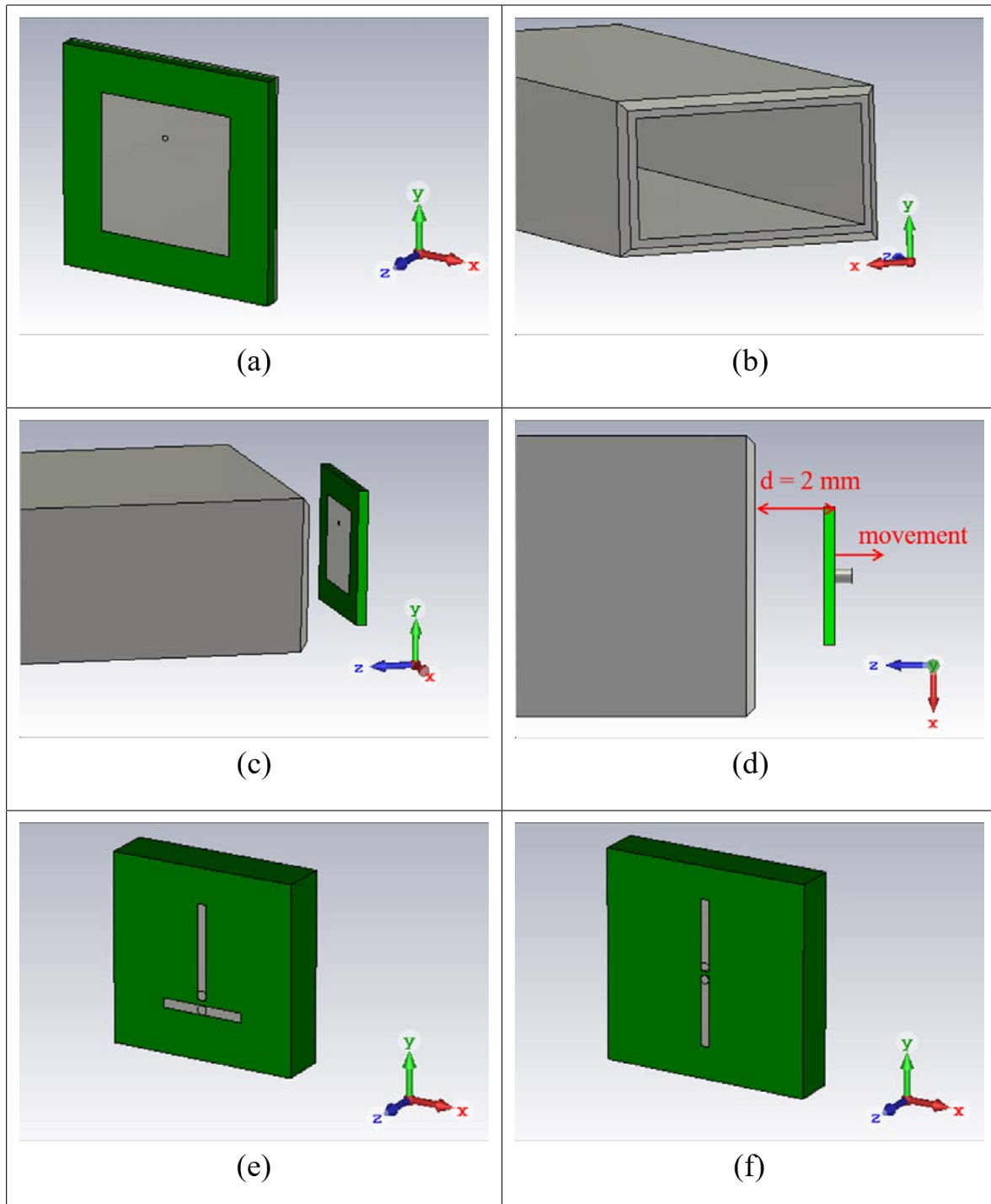


**Figure 6.2:** CST models showing the (a) patch, (b) OEWG, (c) CCM setup, (d) CCM setup mimicking vibrations, (e) monopole and (f) dipole.

The far-field of the used patch at its center frequency of 32 GHz is given by<sup>2</sup>

$$R_{\text{AUT}} = \frac{2D_{\text{AUT}}^2}{\lambda_c} = 2.7 \text{ mm}, \quad (6.1)$$

where  $D_{\text{AUT}}$  is the diagonal of the square patch, and  $\lambda_c$  the wavelength in free-space at the center frequency of 32 GHz. The diagonal  $D_{\text{RA}}$  of the WR-28 OEWG is 7.95 mm, meaning that the far-field of the used RA at the center frequency of the patch is as follows

$$R_{\text{RA}} = \frac{2D_{\text{RA}}^2}{\lambda_c} = 13.5 \text{ mm}. \quad (6.2)$$

The magnitude of the input reflection coefficient of the patch in a free-space environment is shown in Fig. 6.3 and is denoted by ‘Reference.’ Additionally, the determined reflection coefficient using the CCM is shown for a separation of the patch and OEWG of 1 mm, 2 mm and 3 mm. By putting the antennas close to one another, the reflection coefficient of the antennas will be altered due to reflections of both antennas. The discrepancies shown in Fig. 6.3 are due to this effect. Although the AUT and RA are close, Fig. 6.3 shows that the effect of the OEWG on the patch is small, hence, the error introduced by putting the antennas in each other’s near-field region is small for this setup.

In Fig. 6.3 and subsequent figures, a gray area is used to highlight a tolerable error introduced by the setup. This tolerable error is in this chapter defined by  $\pm 10\%$  of the accepted power of the reference, which is proportional to  $(1 - |S_{11}^{\text{ref}}|^2)$ , with  $S_{11}^{\text{ref}}$  being the reflection coefficient of the patch in the free-space environment depicted in Fig. 6.2(a).

### 6.2.3 Sensitivity to positioning errors

In the previous subsection, the centers of the patch and OEWG were perfectly aligned. It is likely, however, that in a high-volume testing facility, most of the samples will not be perfectly aligned to the RA. Therefore, the sensitivity to positioning errors has been assessed. For this assessment, the patch has been translated, mimicking positioning errors, whereas the OEWG remains at its position. The translations  $\Delta d_x$  and  $\Delta d_y$  are in the positive x- and y-direction, respectively.

In Fig. 6.4, the results for translations are shown. The translations of 100  $\mu\text{m}$  are based on tolerances of commercial available pick-and-place handlers. It can be seen that the positioning errors lead to small differences in input reflection coefficient. Both curves of the translation errors remain within the 10% error margin over the entire frequency band. Also here, the discrepancies shown in Fig. 6.4 are caused by the OEWG which alters the characteristics of the patch.

---

<sup>2</sup>Strictly speaking, the radiation of the patch is caused by fringe fields which slightly increases  $D_{\text{AUT}}$ , and thus increases  $R_{\text{AUT}}$ . Without altering the conclusion of this chapter and for the sake of simplicity, the diagonal of the patch will be used to determine the far-field distance of the patch in this chapter.

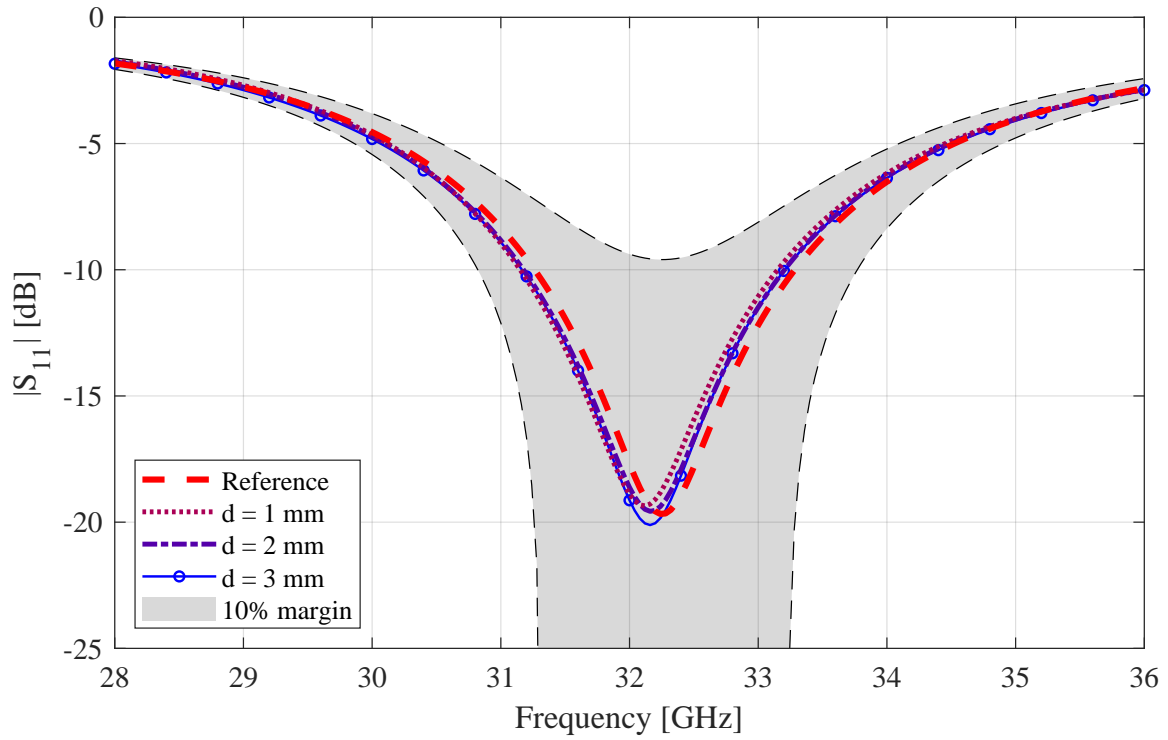


**Figure 6.3:** Reflection coefficient for different distances between the patch and OEWG.

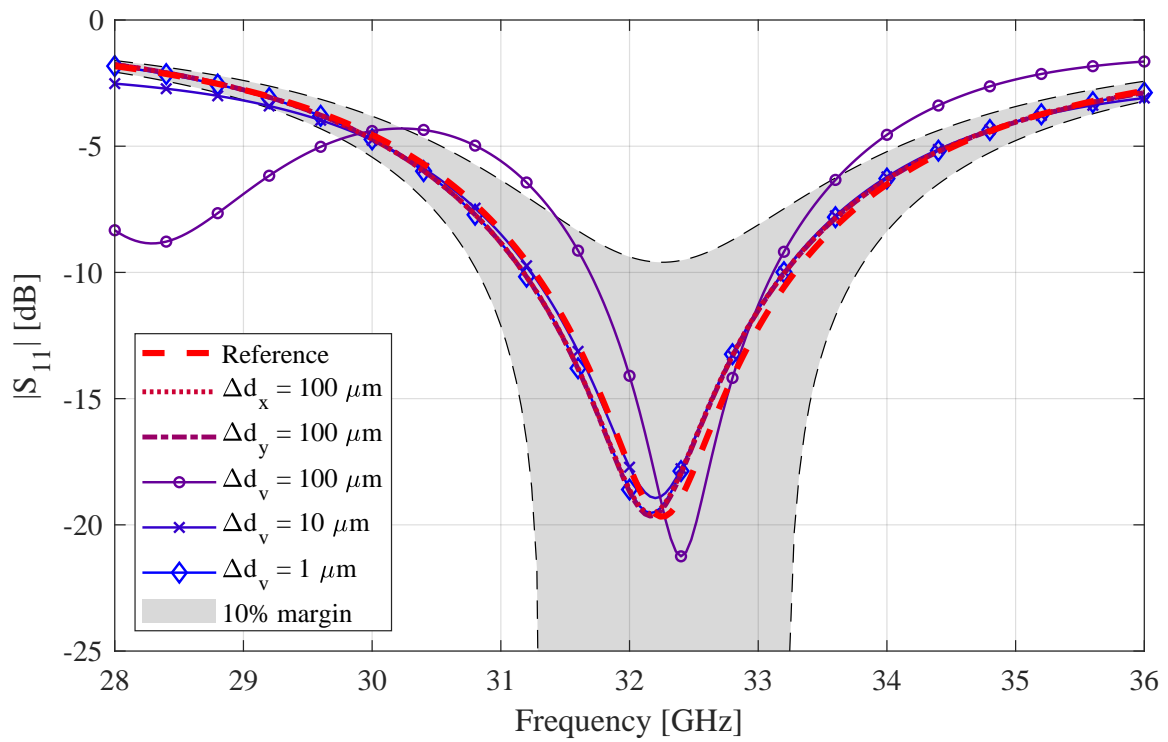


**Figure 6.4:** Reflection coefficient for different imperfections in the measurement setup, such as alignment errors and vibrations.

### 6.2.4 Sensitivity to a dynamic setup

For the CCM, three measurements are required, each with a different termination connected to the AUT. In the previous subsections, the setup is assumed to be static. However, it could be that during the three measurements, the measurement setup slightly changes. To assess the sensitivity of the CCM to environmental changes, the effect of a vibration in the system is mimicked. In the first simulation, a short is connected to the patch and the distance between the patch and the OEWG is 2 mm. In the second and third simulation, the patch has been terminated to an open and 50  $\Omega$  load, and the distance between the patch and the OEWG has been increased by  $\Delta d_v$  and  $2\Delta d_v$ , respectively. The simulation setup and the movement of the patch are depicted in Fig. 6.2(d). In Fig. 6.4, the results are shown for  $\Delta d_v = 100 \mu\text{m}$ ,  $\Delta d_v = 10 \mu\text{m}$  and  $\Delta d_v = 1 \mu\text{m}$ . A deviation of  $\Delta d_v = 100 \mu\text{m}$  clearly leads to incorrect results. An error of  $\Delta d_v = 10 \mu\text{m}$  leads to better results, but even for this small deviation, the results are not bounded by the 10% error margin region, as can be seen at the left edge of the graph. Only when the error is as small as  $\Delta d_v = 1 \mu\text{m}$ , accurate results can be achieved and the determined reflection coefficient remains within the 10% error margin region. Hence, it is important to mitigate any vibration in the measurement setup when performing the CCM.

### 6.2.5 Integrated monopole and dipole antenna

To see whether the obtained results can also be acquired using antennas different from a patch, two other antenna structures were assessed. For this assessment, a monopole and dipole antenna are selected since these structures are found in multiple studies on integrated antennas [86]-[89]. In Fig. 6.2(e) and 6.2(f), a planar monopole and dipole antenna are shown, respectively. The monopole antenna consists of an arm with a length of 2 mm and a ground with a length of 1.75 mm, in order to have the center frequency around 32 GHz. To have the dipole well-matched to 32 GHz, both arms of the dipole have a length of 1.73 mm. The width of the metal strips of both antennas is 0.1 mm, and the gap between the metal strips is 0.15 mm. The relative permittivity and loss tangent are the same as for the patch. The length, width and thickness of the substrate of the monopole is 4 mm, 4 mm and 1 mm, and 5 mm, 5 mm and 1 mm of the dipole. To reduce computation time, all metals are PEC, and the antennas are given zero thickness. The far-field distances of the monopole and dipole at 32 GHz are 1.26 mm and 2.76 mm, respectively.

In Fig. 6.5, the reflection coefficient of the monopole in free space is shown and denoted by ‘Reference.’ Moreover, the determined reflection coefficient of the monopole in a CCM configuration is shown for different separations between the OEWG and monopole. It can be seen that for a separation of 1 mm, the OEWG affects the monopole and the determined reflection coefficient of the monopole is not bounded by the 10% error margin. For a separation of 3 mm, 4 mm or 5 mm, the OEWG hardly affects the monopole and the determined reflection coefficients are bounded by the 10% error margin, as can be seen in Fig. 6.5. Although a separation of 3 mm is larger than the far-field of the monopole, the monopole is still well

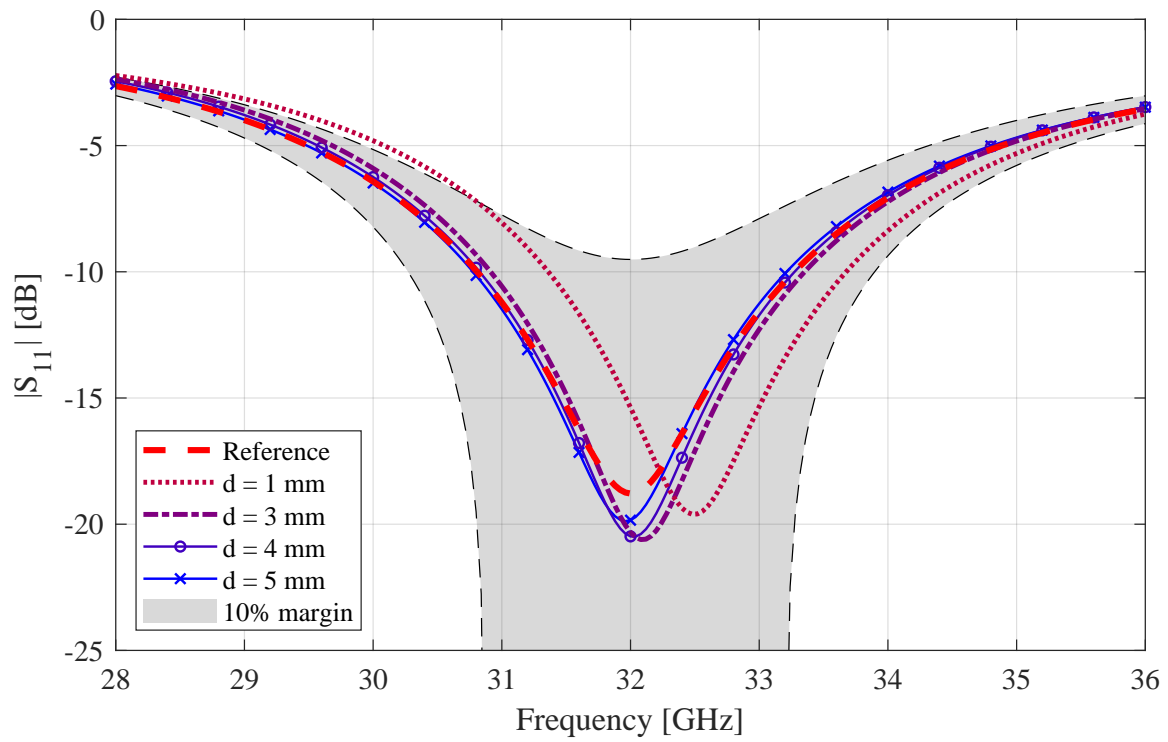


**Figure 6.5:** Reflection coefficient for different distances between the monopole and OEWG.

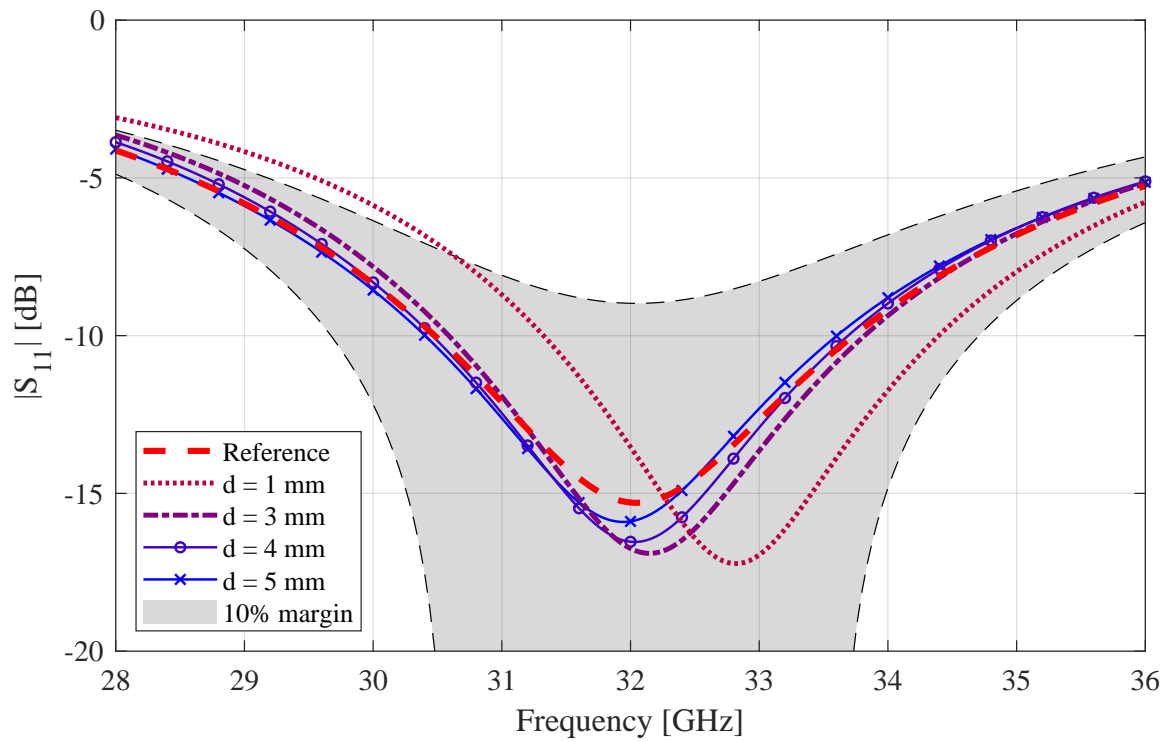


**Figure 6.6:** Reflection coefficient for different distances between the dipole and OEWG.



within the near-field of the OEWG.

The results while using a dipole antenna as AUT are shown in Fig. 6.6. Also here, a separation of the OEWG and dipole of only 1 mm detunes the dipole. When the distance between the OEWG and dipole is 3 mm, 4 mm or 5 mm, it can be seen in Fig. 6.6 that the effect of the OEWG on the dipole is negligible and the determined reflection coefficients are bounded by the 10% error margin. Also in this case, the separation of 3 mm is larger than the far-field of the dipole, but the dipole is still well within the near-field of the OEWG.

The sensitivity of the CCM to alignment errors and vibrations while characterizing the monopole and dipole is also examined. Similar results as shown in Fig. 6.4 were acquired. For both the monopole and dipole, an alignment error in the order of 100  $\mu\text{m}$  shows very little deviation, and the determined reflection coefficient stays within the 10% error margin. A vibration in the order of 10 to 100  $\mu\text{m}$  in the setup leads to incorrect results. When the vibration is limited to 1  $\mu\text{m}$ , the reflection coefficient does not exceed the 10% error margin. Graphs showing this have been omitted to prevent repetition of results.

## 6.3 Measurement results

In order to verify the simulation results, two different types of measurements have been performed. In the first measurement, the AUT has been directly connected to a calibrated VNA and its reflection coefficient has been measured. In Fig. 6.7, the AUT and the reference plane of the measurement is shown. This measurement serves as a reference. The AUT is an inset-fed square patch antenna with an edge length of 2.3 mm and is placed on top of a 508  $\mu\text{m}$  thick RO4003C substrate. The patch is matched at 33 GHz, and the far-field at that frequency is 2.32 mm. In the second type of measurement, the CCM is performed. The measurement setup for the CCM is shown in Fig. 6.8. Because no switch up to 37 GHz was available at the measurement facility, the loads required for the three measurements had to be changed manually. To minimize vibrations caused by manually changing the loads, the AUT was fixated to a stiff metal base. The OEWG is connected to an uncalibrated VNA and three measurements are performed, each with a different termination connected to the AUT. For each set of three measurements, the position of the OEWG was varied to mimic positioning errors.

In Fig. 6.9, the measurement results are shown. It can be seen that the five curves, which are determined using the CCM, follow the reference well and all five curves are within the 10% error bounds. Some discrepancies can be found, however. First of all, although the AUT is fixated and the terminations were changed with care, it is not guaranteed that the AUT does not change its position slightly in between the measurements. Second, manually changing the loads requires some time, allowing the measurement setup to slightly drift. If this method will be performed using integrated antennas with onboard terminations, as mentioned in Chapter 5, both effects will be mitigated. At last, the OEWG does detune the AUT by being in close proximity. Hence, using the CCM in near-field conditions yields a trade-off between accuracy of the measurement and the dynamic range required by the system.

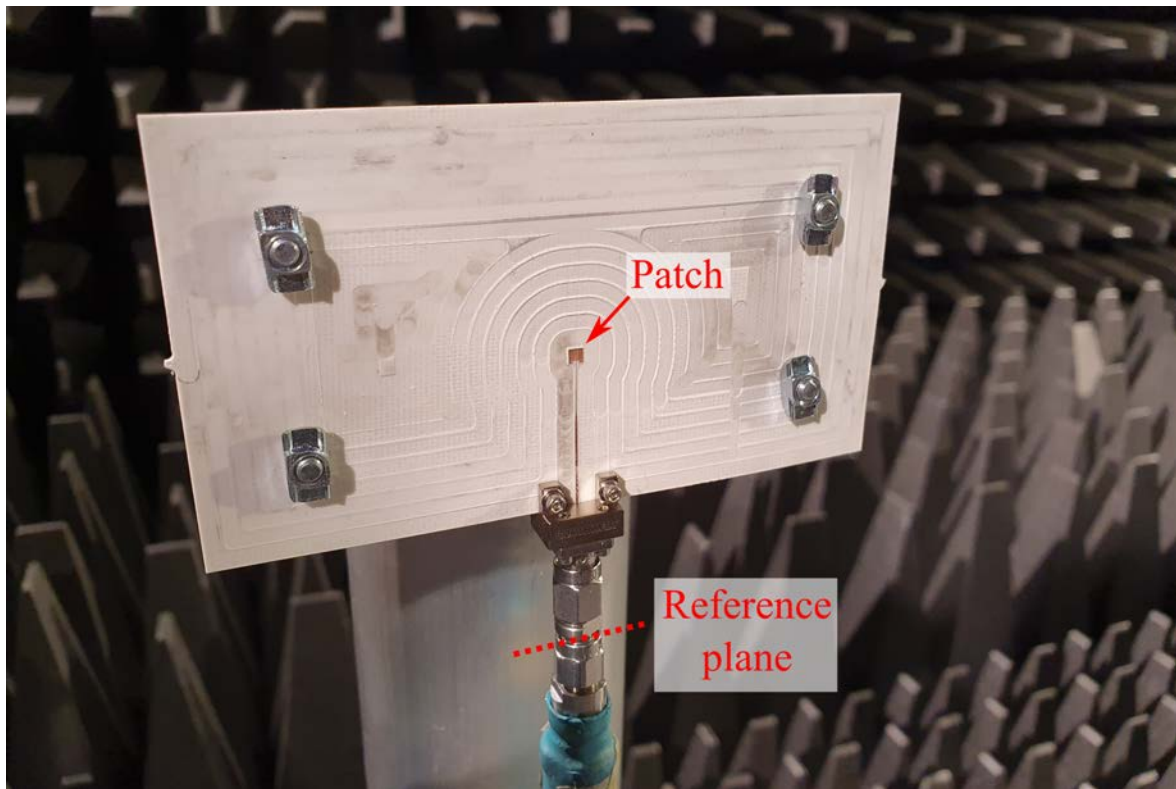


Figure 6.7: Setup for the directly connected reference measurement.

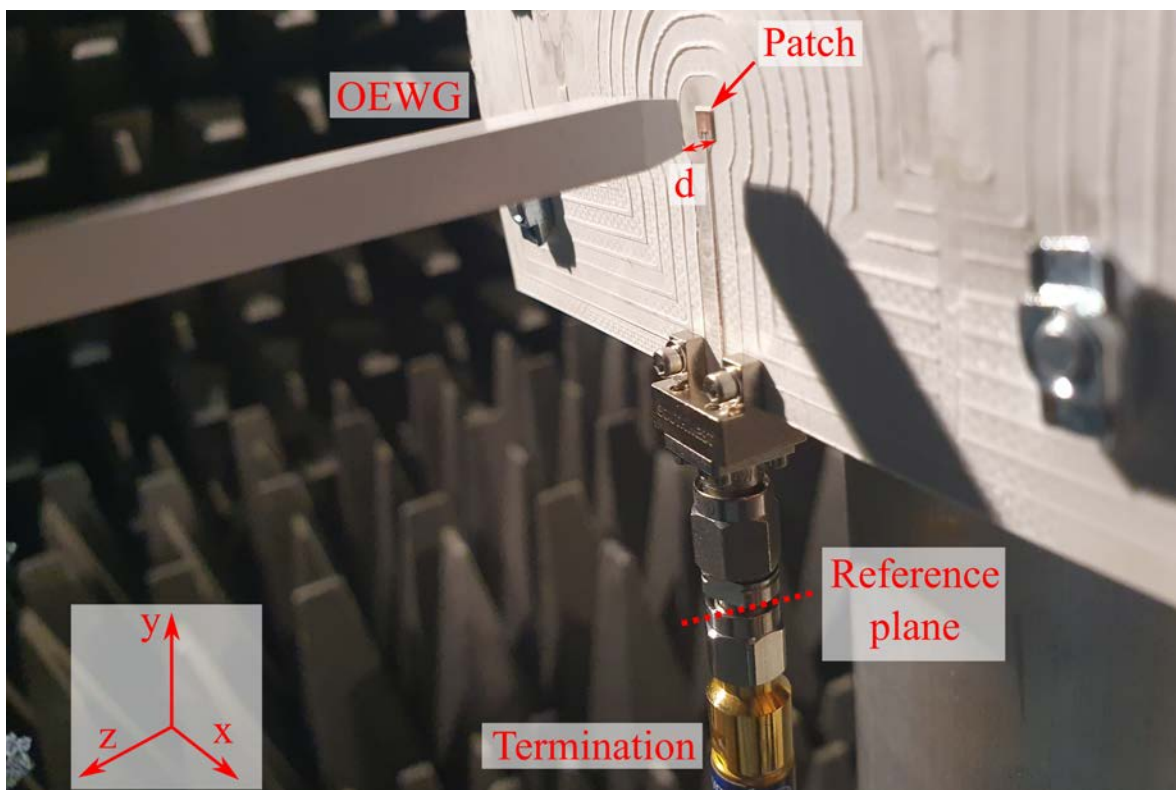
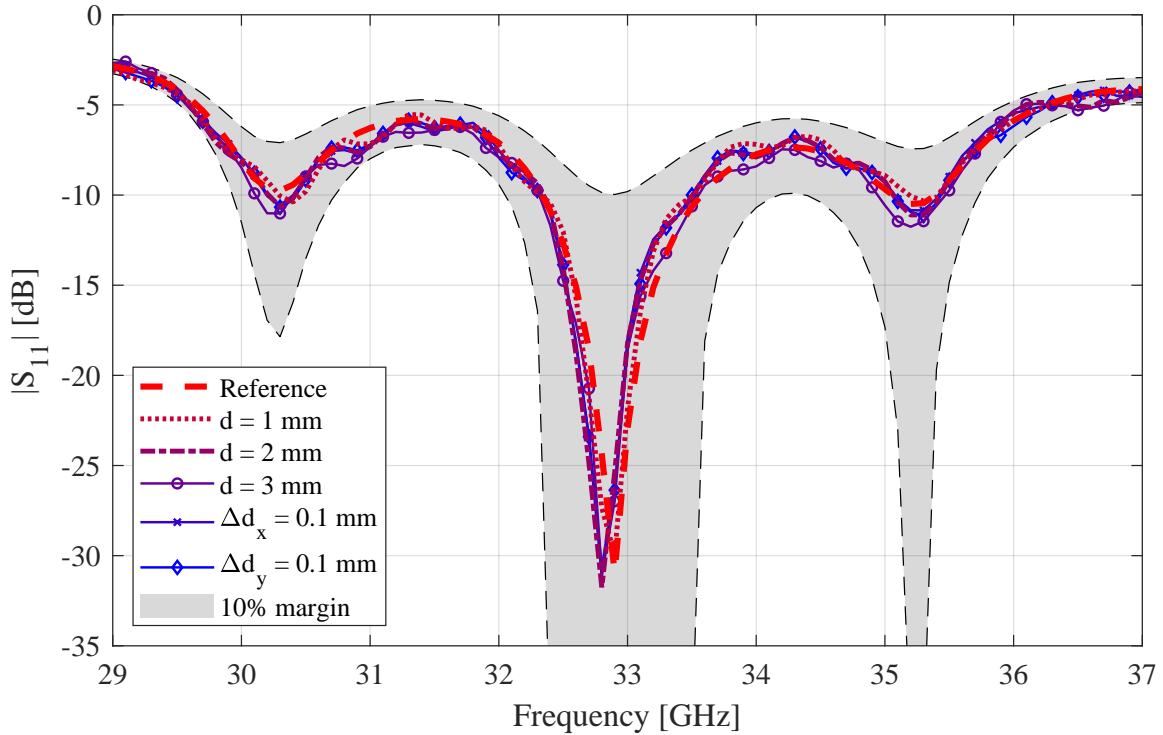


Figure 6.8: Setup for the CCM.



**Figure 6.9:** Experimentally determined reflection coefficient for different positions of the AUT, relative to the OEWG.

## 6.4 Conclusion

In this chapter, the practicality of the CCM operating in near-field conditions is presented, having the application of a cost-effective high-volume testing procedure for integrated antennas in mind. This method can be used to determine the reflection coefficient of an unknown, and possibly integrated, antenna with OTA measurements and does not require calibration. Using simulations, it is shown that an RA can be positioned in the near-field of the integrated antenna if the AUT is a patch antenna. If the AUT is a dipole or monopole, the distance between the OEWG and AUT has to be increased, but the AUT can still be positioned in the near-field of the OEWG, reducing the FSPL significantly. This relieves dynamic range requirements of the measurement equipment and allows for reduced measurement times. Furthermore, it is shown that the impact of the OEWG on the reflection coefficient of positioning errors are not severe, as long as the setup is stationary throughout all three measurements, which are required for the CCM. However, if the setup is not stationary in between measurements due to, for instance, vibrations, the 10% error bounds used in this chapter are readily exceeded when the displacement is in the order of 10  $\mu\text{m}$  or higher. If the vibrations are limited to 1  $\mu\text{m}$ , accurate results can be achieved. Moreover, results around 33 GHz using a connectorized patch antenna are shown, which experimentally verify the validity of using the CCM in near-field conditions.

The assessment has been limited to only three types of antennas. To generalize the con-

clusions drawn in this chapter, this assessment has to be performed on more antenna types. Moreover, since the intended application is a testing procedure for integrated antennas, the method has to be verified for integrated antennas as well. As mentioned in Chapter 5, the required on-chip terminations are subject to manufacturing tolerances which give rise to an uncertainty in the determined input impedance and reflection coefficient of the AUT. If this method will be used to characterize integrated antennas, this uncertainty has to be included in measurement results.

# Modeling of Artificial Magnetic Conductors for AoC Applications<sup>1</sup>

---

## 7.1 Introduction

The short wavelength associated with the 5G mm-wave frequency band allows for individual antenna elements the size in the order of 5 mm. A typical IC is similar in size which opens up the possibility to create the antenna on-chip or in-package. Designing the antenna on-chip makes direct matching to on-chip amplifiers possible, allowing us to leave the standard 50  $\Omega$  interface impedance [107], [108]. This will also reduce the number of RF transitions required and decrease the associated losses [107], [108].

The IC manufacturing process is highly optimized to maximize the performance of the electronics, but is typically not well suited for antennas. For instance, the dielectric loss induced by the IC's silicon is generally high and impacts the radiation efficiency of the antenna significantly [109]. Additionally, the IC is typically placed on a ground plane or heat sink to distribute the generated heat [P13], which may detune the antenna at the same time.

AMCs can be used to design or create an operational AoC, as can be seen in [110]-[114]. Roughly, two different methodologies can be identified in the current research on AMCs for AoC applications. On one hand, the AMC can be fully constructed in the metal stack of the IC, and can be used to shield the antenna completely from the lossy silicon substrate [110]. The limited thickness of the metal stack of a typical (Bi-)CMOS process, however, can impose an issue in terms of the bandwidth of the AMC, especially for frequencies in the 5G mm-wave spectrum. On the other hand, to increase the bandwidth, the silicon substrate of the IC can be included in the design of the AMC, at the expense of additional losses. Examples of AMCs where the lossy silicon is part of the structure can be found in [111]-[114].

In most cases, the AMC is designed for normal incident plane waves only. In a lot of

---

<sup>1</sup>This chapter is based on [P2], [P7], [P9] and [P10].

applications, the AMC is close to the radiating source, meaning that the AMC will also be excited by oblique incident plane waves. In general, the resonance frequency of the AMC changes for different angles of incidence and polarization [115]. In [116]-[118], it is shown that with additional effort, it is possible to stabilize the resonance frequency as function of angle of incidence and polarization. However, still the results show some deviations in resonance frequency, and often the simulated and measured results are limited to incident angles up to  $67.5^\circ$ .

In this chapter, the utilization of AMCs for AoC applications is examined. A limit on the bandwidth of AMCs is derived. The dielectric losses of AMCs are assessed and a design approach for minimum dielectric losses is presented. Based on the derived limit on the bandwidth and the design approach for minimum dielectric losses, a realization of an AoC, consisting of a monopole and a double-layer AMC, is shown. Moreover, a design approach for angular stable AMCs for oblique incident TM plane waves is presented, and its response is compared to a 2D surface impedance sheet.

The outline of this chapter is as follows. In Section 7.2, a built-up of a typical (Bi-)CMOS IC is shown. In Section 7.3, a circuit model of an AMC is presented. In Section 7.4, the bandwidth of an AMC is discussed and a limit is derived. Section 7.5 is devoted to the dielectric losses of an AMC and a design approach to minimize these losses is presented. In Section 7.6, an example of an AoC utilizing an AMC is shown. Section 7.7 is devoted to an angular stable AMC for TM plane wave excitations. Finally, in Section 7.8, the conclusion is presented.

## 7.2 IC manufacturing process

In Fig. 7.1, a cross-section of a typical IC using a (Bi-)CMOS process is shown. The metal stack consists of a few different metal layers, embedded in silicon dioxide. These metal layers can be used to create all kind of metal structures, hence, the AMC can be constructed by using one or more of these layers. Silicon dioxide has a relative permittivity of about  $\epsilon_r = 4$  and is generally assumed to be lossless. The state-of-the-art (Bi-)CMOS processes have a metal stack of around  $10 \mu\text{m}$ . The metal in the top layer is often the thickest, so to reduce metal losses in the antenna, the antenna is usually placed in the top metal layer.

The metal stack is positioned on top of the silicon substrate. Silicon has a relative permittivity of typically  $\epsilon_r = 11.9$  and a resistivity (conductivity) of about  $\rho = 20 \Omega\text{cm}$  ( $\sigma = 5 \text{ Sm}^{-1}$ ). Often, the silicon substrate has a thickness of approximately  $250 \mu\text{m}$ , but can, in principle, be ground down to several tens of micrometers.

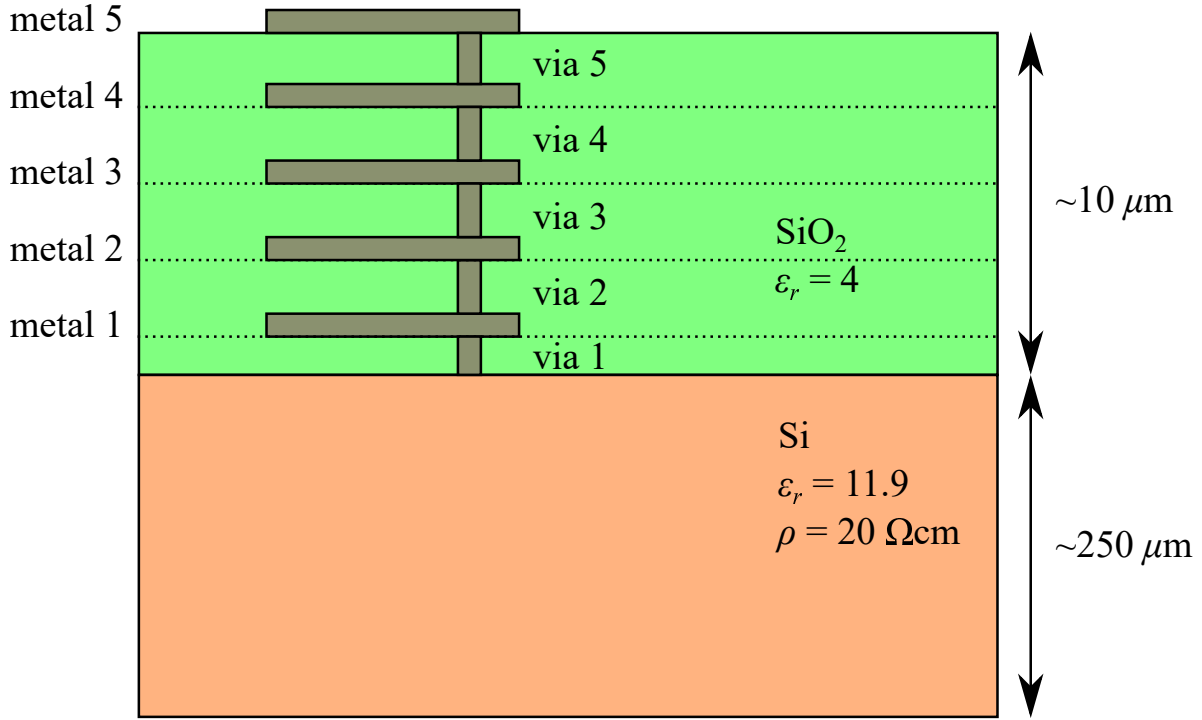


**Figure 7.1:** Sketched cross-section of a typical (Bi-)CMOS IC. Not to scale.

## 7.3 Equivalent circuit models of AMCs

### 7.3.1 Modeling of an AMC having a lossless substrate

Many AMCs are constructed by a grounded dielectric slab, covered by a periodic grid of metal structures. Different types of periodic grids can be found in literature. For instance, the periodic grid can be constructed by using a single layer of patches [110], two layers of patches [119] or more sophisticated patterns such as Hilbert curves [120]. Examples of AMCs using these different types of periodic grids are shown in Fig 7.2. Each type of periodic grid has its own advantages and disadvantages. However, one property that all these different types of physical structures have in common, is that these grids are dominantly capacitive, and can, typically be represented in an equivalent circuit model by a capacitor.

When the presence of the periodic grid is ignored for a moment, it can be identified that, for normally incident plane waves, the grounded dielectric is essentially a transmission line (TL) terminated with a short. Therefore, for plane waves of normal incidence, a unit cell of an AMC can be represented by the equivalent circuit model in Fig. 7.3(a). The operation principle of an AMC is explained in this subsection assuming a lossless TL and lossless metal. The lossless metal assumption will persist in the remainder of this chapter.

The input impedance of the TL,  $Z_{TL}$  in Fig. 7.3(a), can be calculated using

$$Z_{TL} = jZ_1 \tan(k_1 h). \quad (7.1)$$

Here,  $k_1 = \omega \sqrt{\epsilon_1 \mu_1} = 2\pi/\lambda_1$  is the wave number in the dielectric,  $h$  represents the thickness

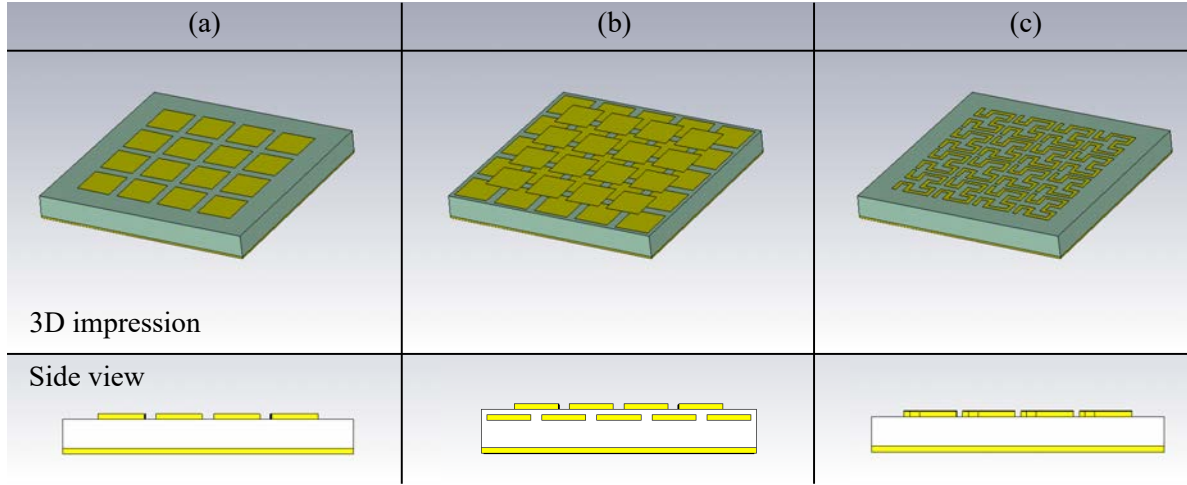


**Figure 7.2:** Examples of AMCs where the periodic grid consists of (a) one layer of patches, (b) two layers of patches, and (c) Hilbert curves. In the 3D impression of (b), the dielectric between the two layers of patches is removed for visualization purposes.

of the dielectric, and  $Z_1 = \sqrt{\mu_1/\epsilon_1}$  is the characteristic impedance of the dielectric. For small  $k_1 h$  (i.e.,  $h \ll \lambda_1$ ), the small-angle approximation of the tangent function can be used. Therefore, (7.1) can be written as

$$Z_{TL} \approx jZ_1 k_1 h = j\sqrt{\frac{\mu_1}{\epsilon_1}} \omega \sqrt{\epsilon_1 \mu_1} h = j\omega \mu_1 h = j\omega L_{TL}. \quad (7.2)$$

It can be seen in (7.2) that an electrically small TL shows inductive behavior. This means that the TL in Fig. 7.3(a) can be substituted for an inductor having an inductance value of  $L_{TL} = \mu_1 h$ . The new equivalent circuit model is illustrated in Fig. 7.3(b). The surface impedance  $Z_s$  of the AMC, thus including the parallel capacitor of the periodic grid, can now be calculated using

$$Z_s = Z_C || Z_{TL} = \frac{j\omega L_{TL}}{1 - \omega^2 L_{TL} C}. \quad (7.3)$$

For a normal incident plane wave, the reflection coefficient can be found using

$$\Gamma = \frac{Z_s - Z_0}{Z_s + Z_0}, \quad (7.4)$$

where  $Z_0$  is the characteristic impedance of the medium above the AMC. By inspecting (7.3), it can be seen that a certain resonance frequency  $\omega_0 = 1/\sqrt{LC}$  can be found where  $Z_s \rightarrow \infty$ . If this condition is satisfied, it can be seen in (7.4) that  $\Gamma = +1$ , meaning that a lossless in-phase reflection is achieved. Therefore, the lossless AMC behaves as a perfect magnetic conductor (PMC) for that particular frequency.

### 7.3.2 Modeling of an AMC having a lossy substrate

In the previous subsection, the operation principle of an AMC having a lossless substrate is explained, and a possible way of modeling its behavior is given. Although now a lossy



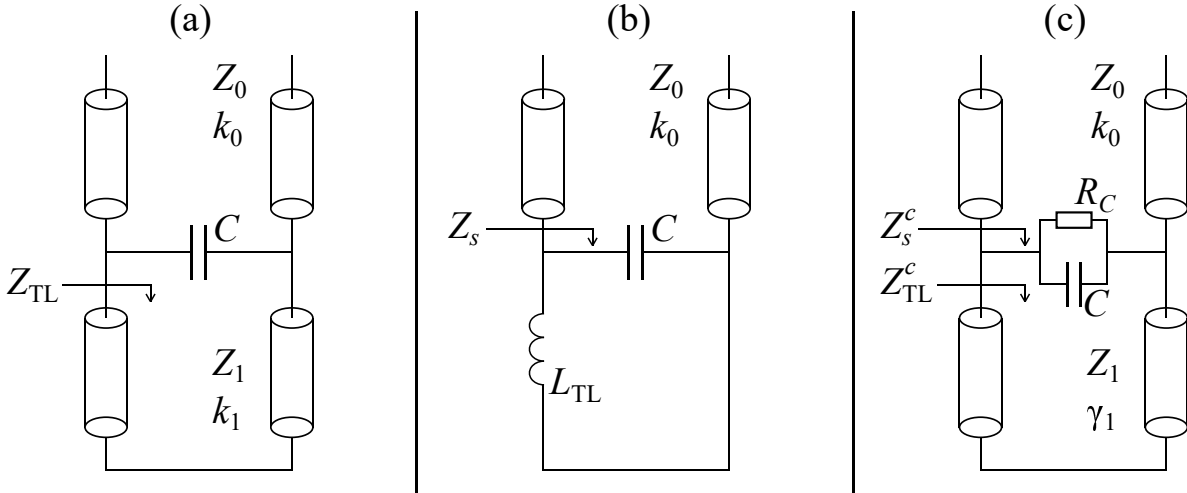


**Figure 7.3:** Equivalent circuit models of a unit cell of (a) a lossless AMC, (b) a lossless AMC using the small-angle approximation, and (c) a lossy AMC.

substrate is included in the AMC design, the principle remains the same; a structure having a large surface impedance has to be engineered in order to achieve an in-phase reflection. The reflection coefficient of a lossy AMC at resonance will not be +1, however, since dielectric losses reduce the reflected power. To distinguish different effects, the total dielectric losses are divided in two different loss mechanisms.

First of all, propagation through a lossy medium will take place, causing propagation losses. This loss is predictable and can be calculated using TL theory. The equivalent circuit model of a unit cell of an AMC with a lossy dielectric can be drawn as illustrated in Fig. 7.3(c). The input impedance of a lossy TL, terminated with a short, can be expressed as

$$Z_{TL}^c = Z_1 \tanh(\gamma_1 h), \quad (7.5)$$

with  $Z_1$  and  $\gamma_1$  the complex-valued characteristic impedance and propagation constant of the TL, respectively. In the case of normally incident plane waves,  $Z_1$  and  $\gamma_1$  can be written as

$$Z_1 = \sqrt{\frac{j\omega\mu_1}{\sigma_1 + j\omega\epsilon_1}},$$

$$\gamma_1 = \sqrt{j\omega\mu_1(\sigma_1 + j\omega\epsilon_1)}. \quad (7.6)$$

Second, the capacitive grid will have fringe fields which couple into the lossy substrate, giving rise to additional dielectric losses. Hence, the resistance  $R_C$  is added in parallel to the capacitor in the equivalent circuit model in Fig. 7.3(c) to model the losses induced by the fringe fields. The surface impedance of a lossy AMC can now be calculated using

$$Z_s^c = (Z_C || R_C) || Z_{TL}^c = \frac{R_C Z_{TL}^c}{R_C + Z_{TL}^c (j\omega R_C C + 1)}. \quad (7.7)$$

It is difficult to determine the exact value of  $R_C$ , hence, the inclusion of  $R_C$  in the equivalent circuit model in Fig. 7.3(c) will be used in a qualitative way, rather than a quantitative way.

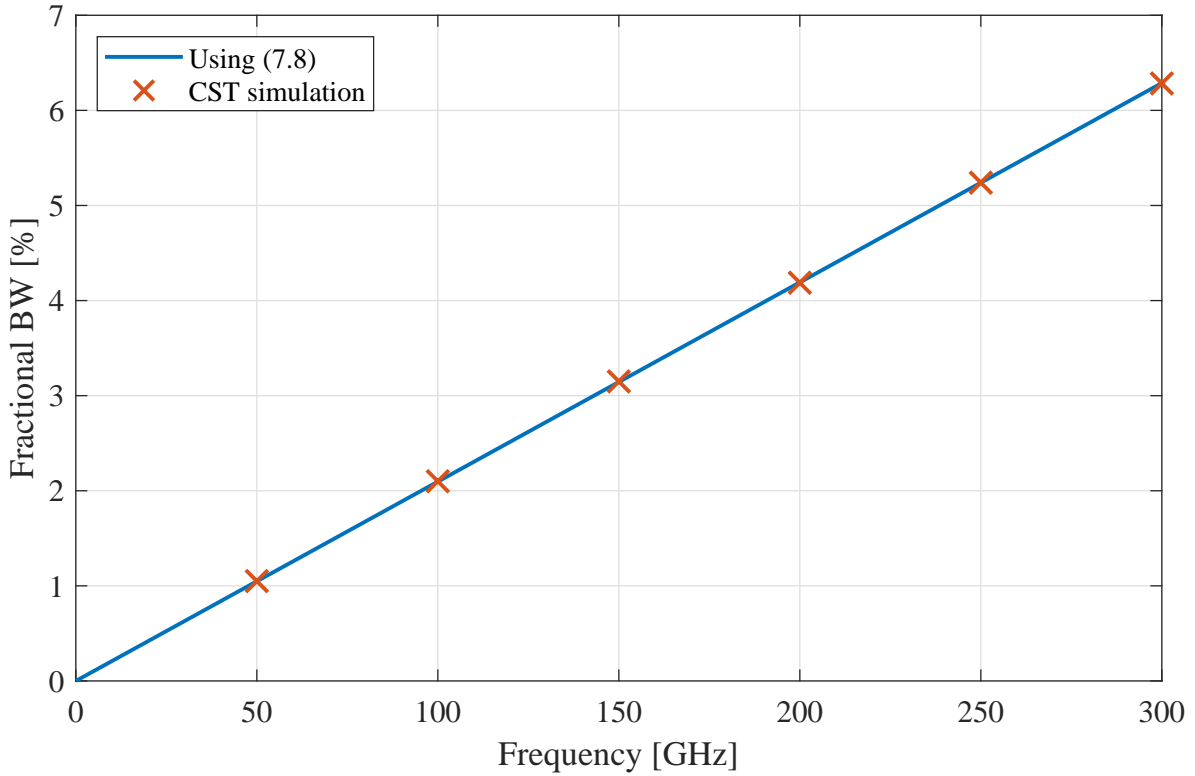


**Figure 7.4:** Fractional bandwidth versus frequency for an AMC in the metal stack.

Note that the losses caused by the propagation through a lossy medium are inevitable. The losses caused by the fringe fields of the capacitive grid could, in principle, be fully mitigated. Therefore, for a given lossy substrate thickness, a theoretical minimum loss can be determined by imposed  $R_C \rightarrow \infty \Omega$ . Intuitive ways to reduce the losses caused by the fringe fields, and thus increasing  $R_C$ , are presented in Section 7.5.

## 7.4 Bandwidth of AMCs

One of the key parameters of an AMC is the bandwidth. Typically, the bandwidth of an AMC is defined from  $\angle\Gamma = +90^\circ$  to  $\angle\Gamma = -90^\circ$  [121]. In the upcoming subsections, the bandwidth of two different types of AMCs for AoC applications is determined. In the first case, the AMC is constructed in the metal stack of the IC and is considered lossless. In the second case, the silicon substrate is part of the AMC, meaning that the AMC is lossy.

### 7.4.1 Bandwidth of an AMC in the metal stack

The bandwidth of the lossless LC circuit model in Fig. 7.3(b) can be calculated using

$$\text{BW}_{\text{frac}} = \frac{\omega_0 L_{\text{TL}}}{Z_0}. \quad (7.8)$$

For a complete derivation of (7.8), the reader is referred to Appendix C.

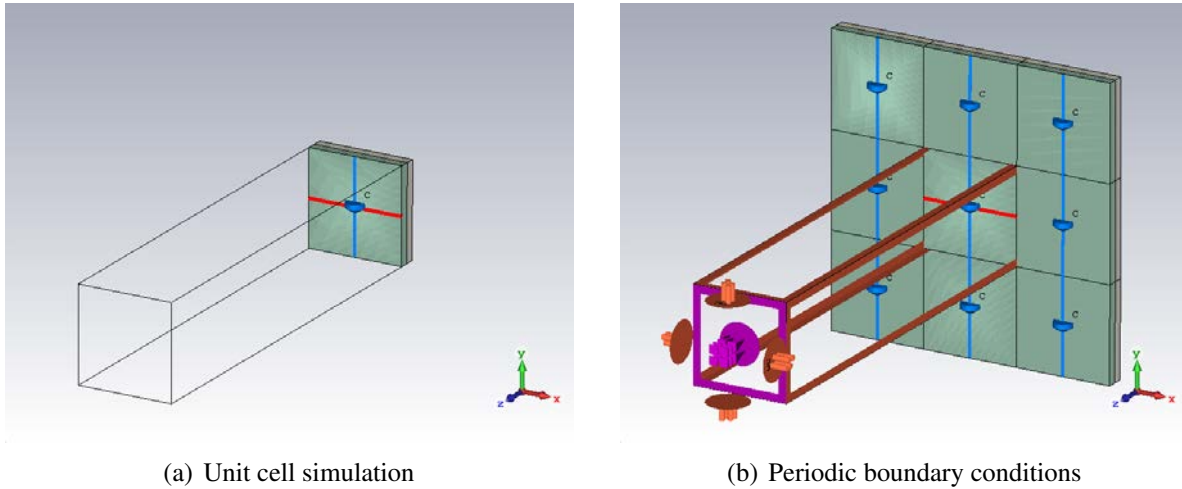


**Figure 7.5:** CST simulation setup showing the (a) unit cell simulation and (b) its periodic boundary conditions. The unit cell structure consists of a PEC ground plane, a metal stack of  $10\ \mu\text{m}$ , and a lumped capacitor. The structure is excited by a normal incident plane wave.

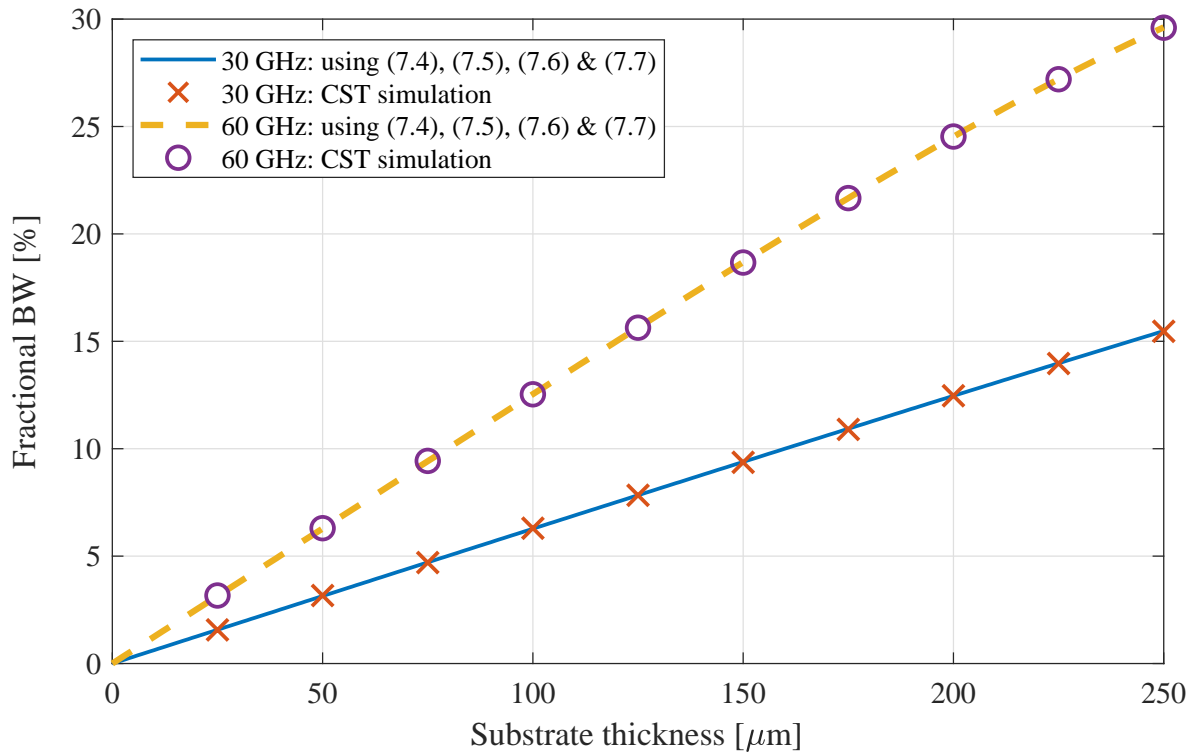
Using the typical (Bi-)CMOS manufacturing values mentioned in Section 7.2, the fractional bandwidth of an AMC constructed in the metal stack can be calculated using (7.8). In Fig. 7.4, the resulting bandwidth for the entire mm-wave spectrum is shown using the blue solid line.

To verify this way of modeling, a unit cell of an AMC has been simulated in CST Microwave Studio. In Fig. 7.5, the CST simulation model is shown. The periodic capacitive grid is modeled by a perfect lumped capacitor and is placed on top of the metal stack. The results of the CST simulations<sup>2</sup> are visualized in Fig. 7.4 by the red crosses. As one can see, the simulated CST results completely overlap the results of (7.8), justifying the chosen way of modeling.

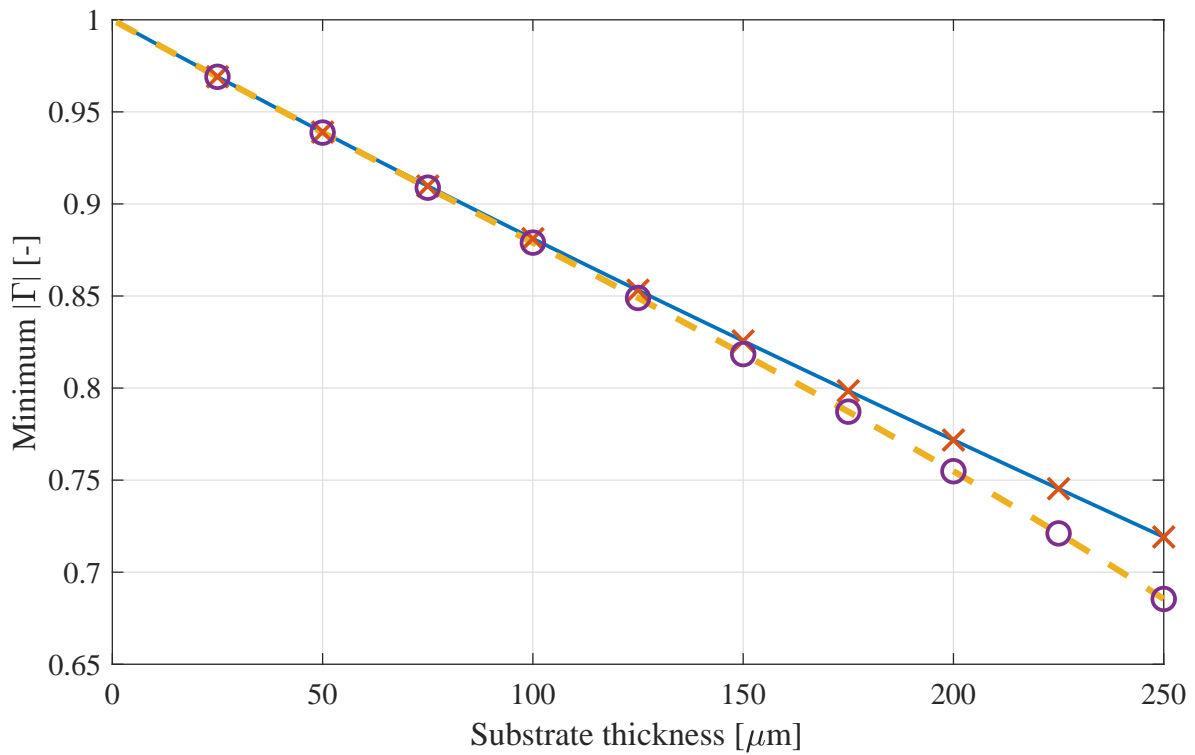
As can be seen in Fig. 7.4, the fractional bandwidth for low frequencies is rather limited, hence, it seems almost impossible to design practically useful AMCs constructed in the metal stack for the frequencies in the 5G mm-wave frequency band. However, depending on the desired fractional bandwidth, the utilization of AMCs in the metal stack for frequencies in the central and upper region of the mm-wave spectrum may be practical.

To calculate the results which are shown in Fig. 7.4,  $Z_0$  is taken to be the characteristic impedance of free space. However, note that so far no assumption is made on the value of  $Z_0$ . It can be seen in (7.8), that the fractional bandwidth increases for decreasing  $Z_0$ . Therefore, the fractional bandwidth of an AMC can generally be increased by putting a dielectric having a high relative permittivity on top of the AMC.

<sup>2</sup>Note that when using a plane wave excitation in CST, the port is automatically positioned  $\lambda_c/4$  away from the structure, with  $\lambda_c$  being the wavelength corresponding to the center frequency. This is typically done to prevent interaction between the structure and the port. Therefore, in order to extract the reflection phase at the surface of the AMC, the reference plane has to be shifted by  $\lambda_c/4$  towards the surface of the AMC structure.



(a) Fractional bandwidth versus substrate height.



(b) Minimum amplitude of the reflection coefficient versus substrate height.

**Figure 7.6:** (a) Fractional bandwidth and (b) minimum  $|\Gamma|$  versus substrate height for 30 and 60 GHz.

### 7.4.2 Bandwidth of an AMC utilizing the silicon substrate

As presented in the previous subsection, constructing an AMC in the metal stack for frequencies in the lower region of the mm-wave spectrum seems not very promising due to the limited fractional bandwidth. As can be seen in (7.8), the fractional bandwidth of a lossless AMC can be increased by increasing  $L_{TL}$ . Increasing  $L_{TL}$  yields increasing the length of the equivalent TL. One way of increasing this length, is to use the silicon substrate as equivalent TL.

Equation (7.8) has been derived for a lossless AMC. By combining (7.4), (7.5), (7.6) and (7.7), an expression for the reflection coefficient of a lossy AMC can be found. By following the same approach as presented in the Appendix C, an expression for the fractional bandwidth for lossy AMCs can be found. However, this will give rise to a tedious expression, and is omitted here. Alternatively, the reader is encouraged to numerically calculate the fractional bandwidth by following the approach presented in the Appendix C.

In the case of a lossy AMC, the losses are of high importance. The absolute value of the reflection coefficient is a measure of the induced losses; the power that is not reflected by the AMC is essentially dissipated in the lossy silicon substrate. Although the induced loss for a fixed substrate height is, in general, a function of frequency, only the maximum loss (i.e., the minimum value of  $|\Gamma|$ ) will be used as benchmark in the following considerations. This happens to be at resonance.

In Fig. 7.6, results are shown for an AMC using the silicon substrate. Figure 7.6(a) shows the fractional bandwidth as function of silicon substrate height for a resonance frequency of 30 and 60 GHz. As can be seen in Fig. 7.6(a), the fractional bandwidth increases approximately linearly with respect to substrate height. By increasing the substrate height, the equivalent inductance of the TL increases, hence, the fractional bandwidth increases as well. On the other hand, increasing the substrate height also gives rise to a lower reflection coefficient, resulting in higher induced losses, as can be seen in Fig. 7.6(b). Figure 7.6 clearly visualizes a trade-off. By using the silicon substrate to increase the fractional bandwidth, also the losses will increase.

To verify this way of modeling, a unit cell of an AMC has been simulated in CST. The CST model is similar to the model depicted in Fig. 7.5, but the properties of the dielectric are replaced by the properties of silicon, and a sweep over the dielectric thickness is performed. The periodic grid is modeled by using a perfect lumped capacitor (i.e., the losses due to fringe fields are ignored) and is placed on top of the silicon substrate. The results of the CST simulations are visualized in Fig. 7.6 by the markers. As one can see, the simulated CST results completely overlap the results of combining (7.4) to (7.7), justifying the chosen way of modeling.

## 7.5 Minimizing the dielectric losses of an AMC

To achieve a reasonable fractional bandwidth for an on-chip AMC operating in the 5G mm-wave band, the lossy silicon substrate has to be included. For a fixed substrate height, the

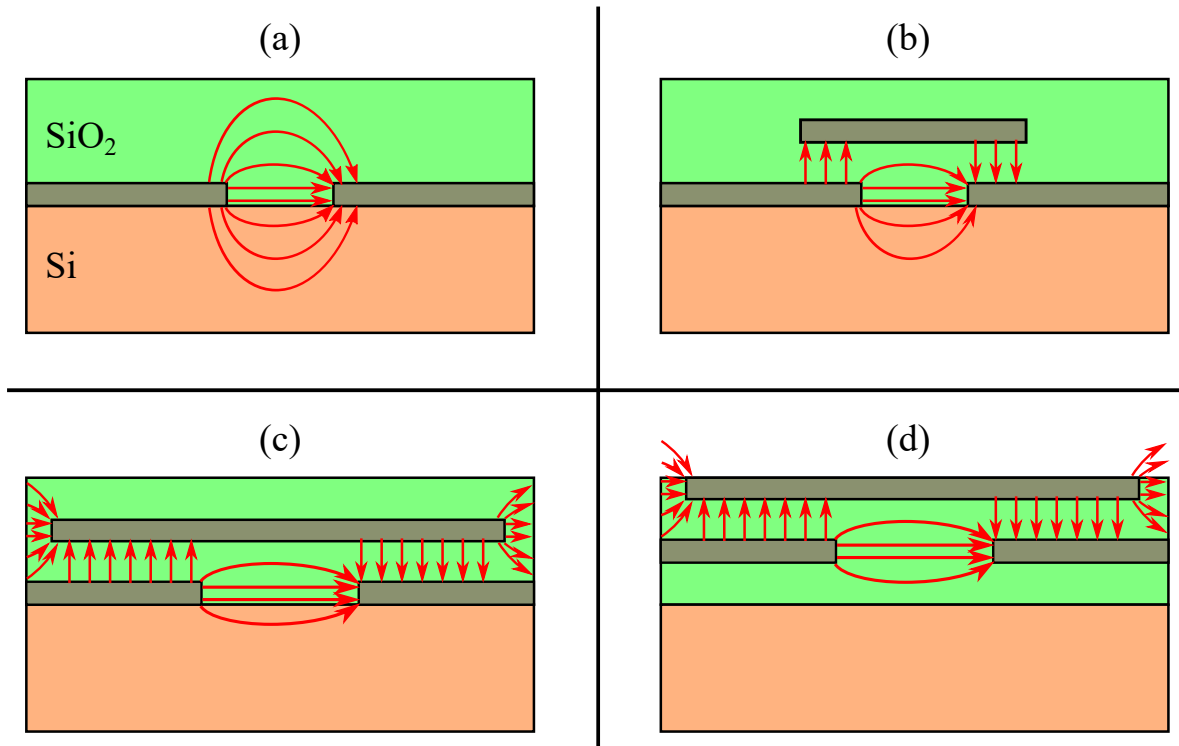


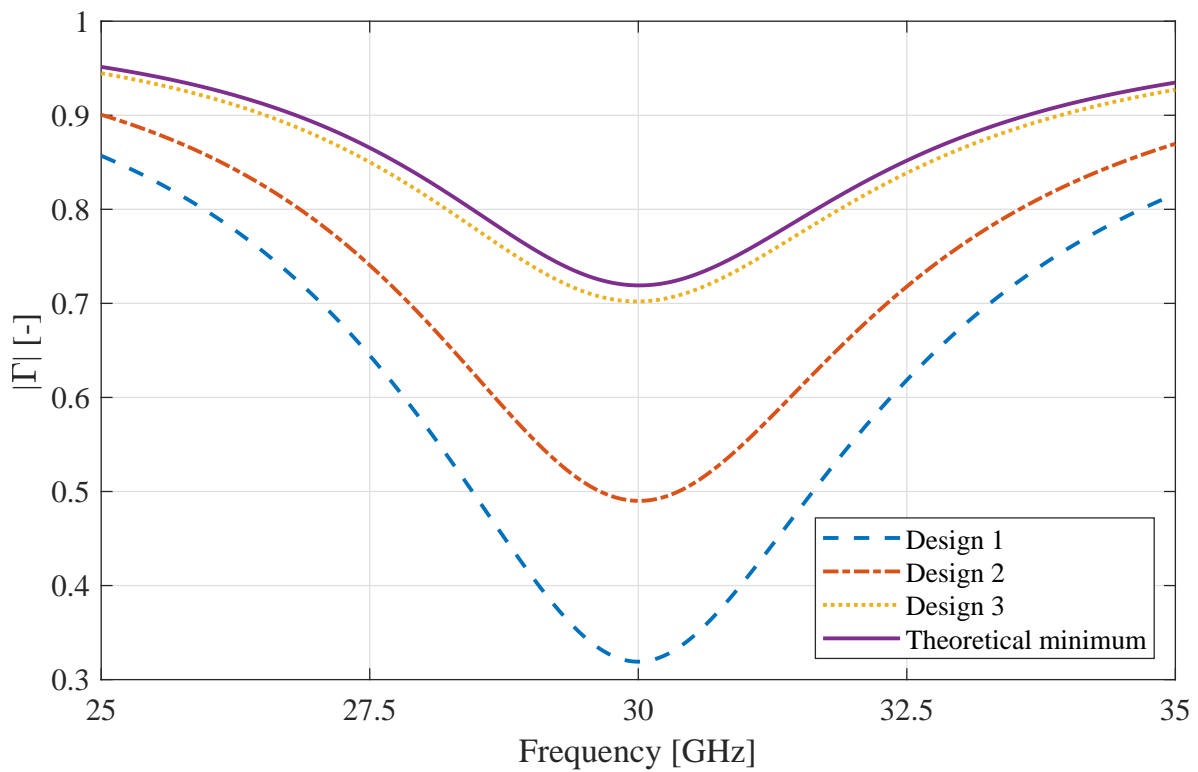
**Figure 7.7:** Qualitative visual representation of the fringe fields (in red) in a unit cell of different AMCs; (a) single-layer patch, (b) double-layer patch design 1, (c) double-layer patch design 2, and (d) double-layer patch design 3.

dielectric losses caused by the propagation through a lossy medium are inevitable. The losses caused by the fringe fields of the capacitive grid could, in principle, be fully mitigated. Hence, a theoretical minimum loss of the AMC can be calculated using the equivalent circuit model of Fig. 7.3(c) by choosing  $R_C \rightarrow \infty$ .

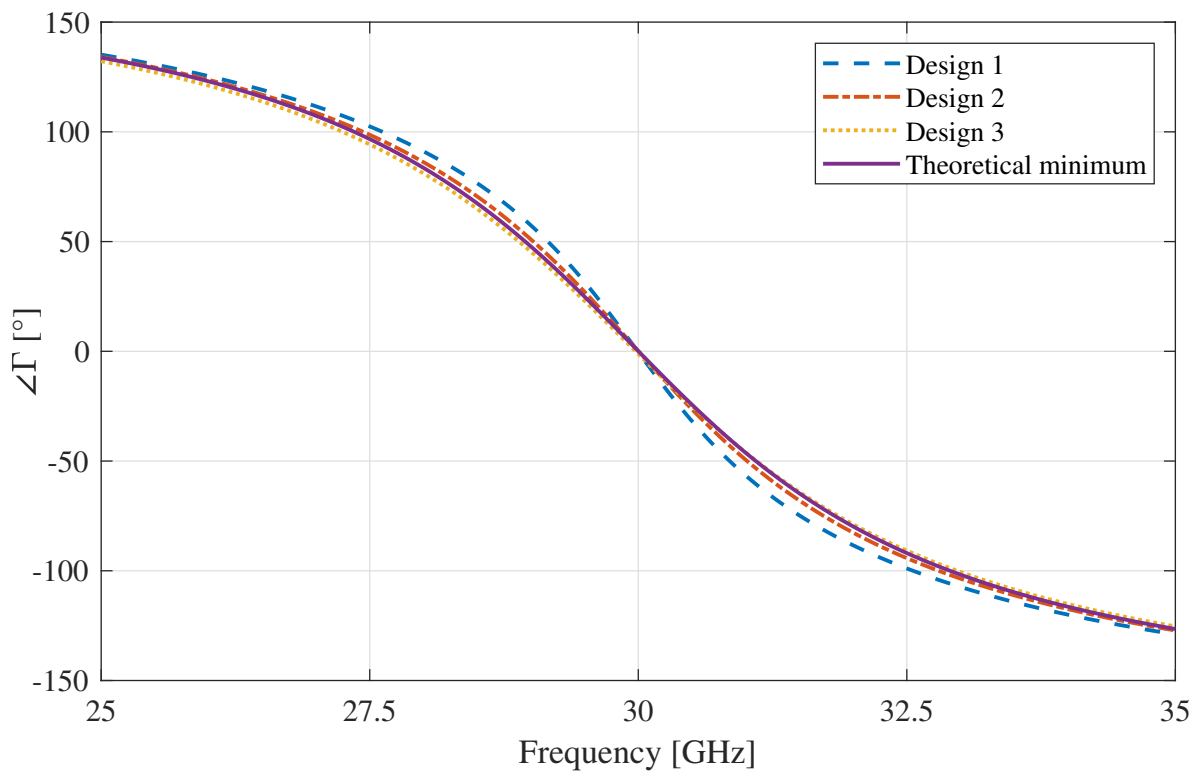
One of the most basic AMC structures one can find in literature is a single-layer square patch AMC. In [122], it was already reported that this structure is very lossy when having silicon as substrate. In fact, the AMC even loses the property of reflecting in-phase due to the high dielectric losses. In Fig. 7.7(a), the fringe fields of a unit cell of such a structure, when used on a chip, are illustrated. It is clear to see that a lot of fringe fields couple into the silicon, which gives rise to high losses and is obviously disadvantageous.

Other structures can be used which might reduce the fringe fields coupling into the silicon, and thus reduce the losses. An example of such a structure is the double-layer AMC as reported in [119]. Double-layer AMCs are typically used to increase the capacitance of a unit cell, which leads to smaller unit cells. Since the dominant capacitance is positioned between two layers, it is also expected that the dielectric losses will be reduced since the fringe fields coupling into the silicon will be weaker.

One example of a double-layer patch and its fringe fields is illustrated in Fig. 7.7(b). In this case, the gap between the patches in the lower layer is chosen much smaller than the gap between the patches in the upper layer.



(a) Reflection amplitude.



(b) Reflection phase.

**Figure 7.8:** Reflection (a) amplitude and (b) phase of different double-layer AMC structures versus frequency.

This structure has been simulated in CST. The material properties and dimensions given in Section 7.2 have been used and the geometry of the periodic grid of patches was tuned to have an in-phase reflection at 30 GHz. The simulated reflection coefficient is illustrated in Fig. 7.8(a) and denoted by ‘Design 1.’ The reflection phase can be observed in Fig. 7.8(b).

Although ‘Design 1’ exhibits the in-phase reflection behavior at 30 GHz, the amplitude of the reflection coefficient is low, meaning that the losses are high. In an attempt to reduce these losses, the gap between the patches in the upper layer is decreased. The gap between the patches in the lower layer is increased to keep the in-phase reflection at 30 GHz. This will lead to weaker fringe fields coupling into the silicon due to the smaller capacitance formed by the lower layer of patches. This is illustrated in Fig. 7.7(c). The resulting amplitude and phase of the reflection coefficient can be observed in Fig. 7.8(a) and 7.8(b), respectively, and are denoted by ‘Design 2.’

Despite the fact that the losses are decreased, the reflection coefficient is still way below the theoretical minimum reflection coefficient, as can be seen in Fig. 7.8(a). To decrease the losses due to the fringe fields even further, the AMC is shifted to the upper layers of the metal stack. This situation is depicted in Fig. 7.7(d). Again, the resulting amplitude and phase of the reflection coefficient can be observed in Fig. 7.8(a) and 7.8(b), respectively, and are now denoted by ‘Design 3.’ As expected, not a lot of fringe fields will couple into the silicon, so the reflection coefficient is approaching the reflection coefficient corresponding to the theoretical minimum loss.

The simulations were carried out with a silicon substrate having a thickness of 250  $\mu\text{m}$ . Although the losses caused by the TL are inevitable, they can still be reduced by grinding down the silicon substrate. This will, however, lead to a smaller operational bandwidth, as reported in Section 7.4.

## 7.6 Realization of an AoC including an AMC

In Section 7.4, the conclusion is drawn that an AMC in the metal stack does not provide enough bandwidth for the 5G mm-wave frequency band. Therefore, the silicon substrate has to be included in the AMC design, at the cost of additional losses. In Section 7.5, a design approach is presented that keeps the dielectric loss to a minimum. Based on these two findings, an AoC, consisting of a monopole and a double-layer AMC, has been designed [P2]. A photograph of the realized AoC is shown in Fig. 7.9.

As reported in [P2], the utilization of the double-layer AMC increased the simulated realized gain of the AoC by minimally 2.4 dB and maximally 3.3 dB in the frequency band ranging from 50 to 60 GHz. No AoC without an AMC was available to us, so no comparison could be made and this claim could not be supported by measurement results. However, the measured input impedance of the AoC is shown to be in good agreement with the simulated input impedance. This strongly supports the validity of the simulation model used in [P2], and, hence, the usage of an AMC to increase the realized gain of an AoC.



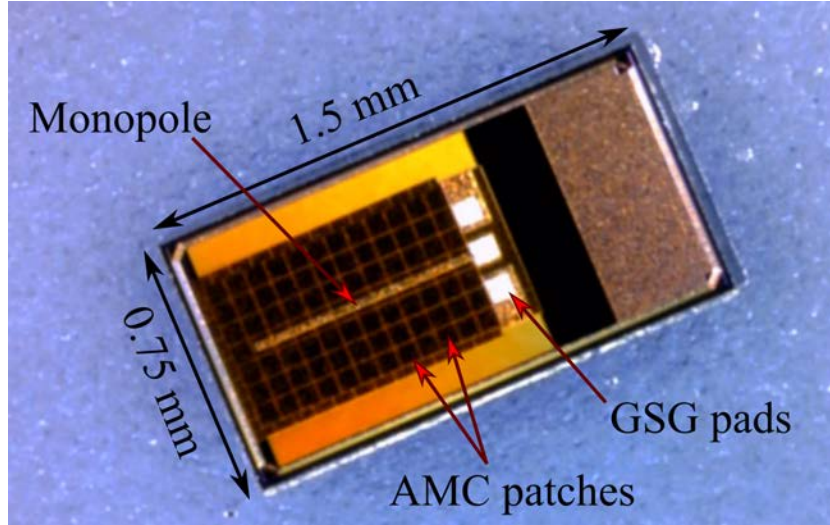


**Figure 7.9:** Realization of an AoC consisting of a monopole and an AMC [P2].

## 7.7 Angular stable AMC for TM plane wave excitations

In the analysis so far, the excitation of AMCs has been restricted to normal incident plane waves only. In most applications, however, the AMC is positioned very close to the radiating element, so the excitation is far from plane waves of normal incidence. This complicates the design of AMCs for AoC applications. For instance, in [P2], the initial AMC dimensions were determined by a normal incident plane wave unit cell simulation. After integration with the monopole, the dimensions of the AMC were optimized using full-wave electromagnetic simulations. These simulations are often computationally intensive since the AMCs typically exhibit important sub-wavelength features. This makes optimizing the monopole in combination with the AMC very time consuming.

The complexity of these full-wave electromagnetic simulations could be reduced if an AMC structure is used which is angular stable and mimics the behavior of a 2D surface impedance sheet. In that case, the complex 3D AMC structure could be substituted by a 2D surface impedance sheet, mitigating the sub-wavelength details of the AMCs. In the upcoming subsection, a design procedure for an angular stable AMC for TM plane wave excitations is presented. Moreover, the response of the complex 3D AMC structure is compared to the response of a 2D surface impedance sheet.

### 7.7.1 Design procedure and simulation results

The equivalent inductance  $L_{TL}$  and capacitance  $C$  depicted in Fig. 7.3(b) depend, in general, on the angle of incidence  $\theta$  [115]. Therefore, also the resonance frequency  $\omega_0$  is dependent on  $\theta$ . In this section, a procedure is presented that enables the design of an angular stable AMC for TM plane wave excitations.

The starting point for the angular stable AMC is the double-layer AMC structure. In [119], a circuit model of a double-layer AMC is presented, which enables the fast calculation of the

dimensions of the AMC for a certain resonance frequency and given substrate. This calculated resonance frequency is only valid for normal incident plane waves [119]. To compensate for the angular dependency of  $L_{TL}$  and  $C$  (defined in Fig. 7.3(b)), it has been found that a via can be used. The via connects the ground plane and the lower patch layer of the double-layer AMC. A top and side view of the double-layer AMC, including the vias, is visualized in Fig. 7.10(a) and 7.10(b), respectively. A unit cell is illustrated using the red dashed line. Figure 7.10(c) and 7.10(d) show the unit cell model in CST. In Fig. 7.10(c), the ground plane, four quarters of a via, and the lower layer of quarter patches of the double-layer AMC are shown. In Fig. 7.10(d), also the dielectric and the upper patch are visualized.

By varying the thickness of the via, the added inductance can be adjusted. In this research, it is empirically found that for a via with a radius of  $P/5$ , with  $P$  being the periodicity of the unit cell, the angular dependency of the capacitive grid and TL is exactly compensated by the angular dependency of the via. To support this claim, a full-wave simulation model was constructed using CST.

In Fig. 7.11, the reflection phase of the AMC as function of angle of incidence and frequency is shown using the solid lines. In the figure, it can be observed that the resonance frequency remains constant as function of incident angle, so this AMC structure can be regarded as an angular stable AMC for TM plane waves. The reflection phase for transverse electric (TE) plane waves is shown in Fig. 7.11(b). Here it can be seen that the resonance frequency increases as the incident angle increases.

### 7.7.2 Comparison to 2D surface impedance sheets

Although the presented AMC is a complex structure, the simulation of the unit cell is computationally not intensive. If the structure is simulated in a real application, and several unit cells are positioned in the model, the simulation can become computationally very intensive. It would, therefore, be advantageous if the 3D AMC structure, with all its sub-wavelength details, could be replaced by a less complex structure, like a 2D surface impedance sheet for instance.

To compare the AMC with a 2D surface impedance sheet, the surface impedance of the AMC for normal incident plane waves,  $Z_{s\perp}$ , has been extracted using (7.4). Using CST, a 2D surface impedance sheet has been defined, having  $Z_{s\perp}$  as its impedance. The response of the 2D sheet to oblique incident plane waves is shown in Fig. 7.11 using the dashed lines. In Fig. 7.11(a) it can be seen that the response of the AMC and the 2D sheet are exactly the same for TM plane wave excitations. Figure 7.11(b), however, shows a discrepancy between the response of the AMC and the 2D sheet for the TE case. This means that, if in the application only (or mainly) TM plane waves will be incident on the AMC structure, the full-wave simulation model can be simplified by using a 2D surface impedance sheet instead of the 3D structure.

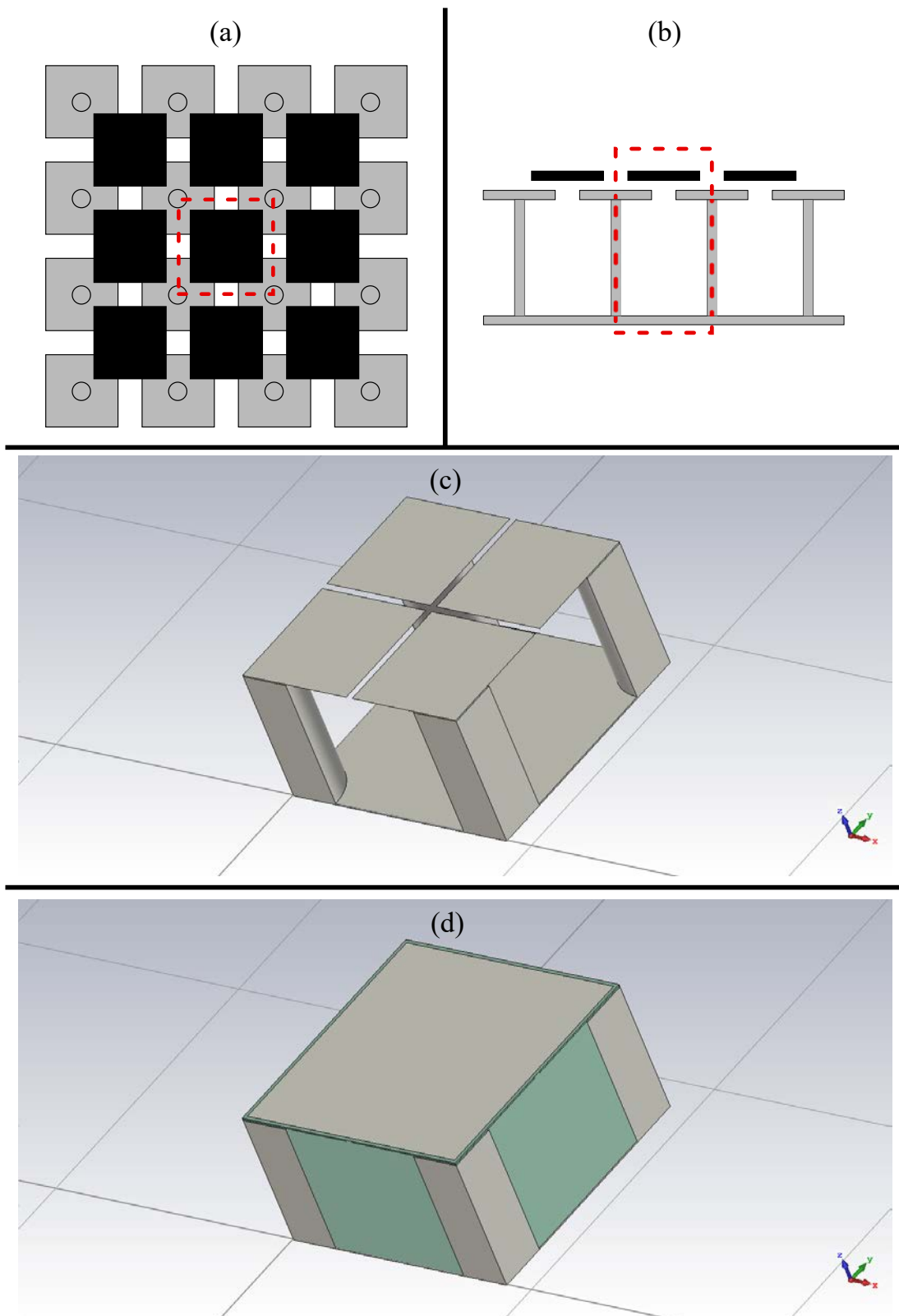
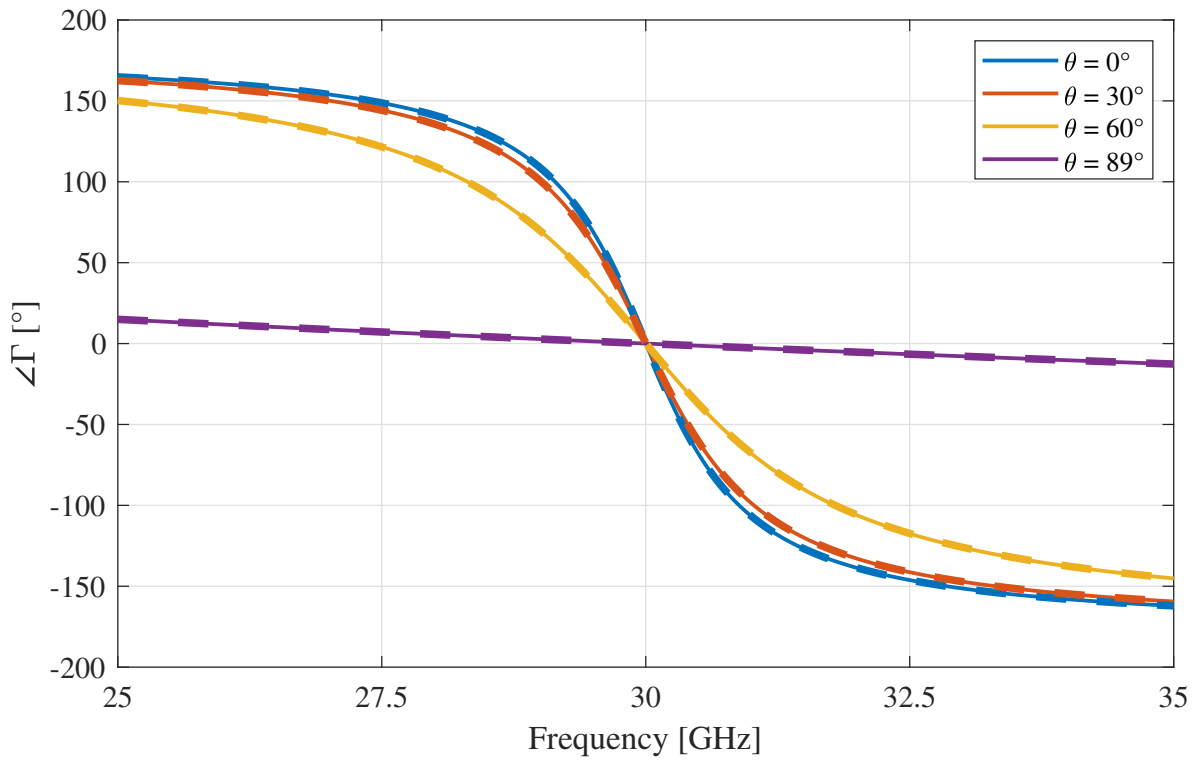
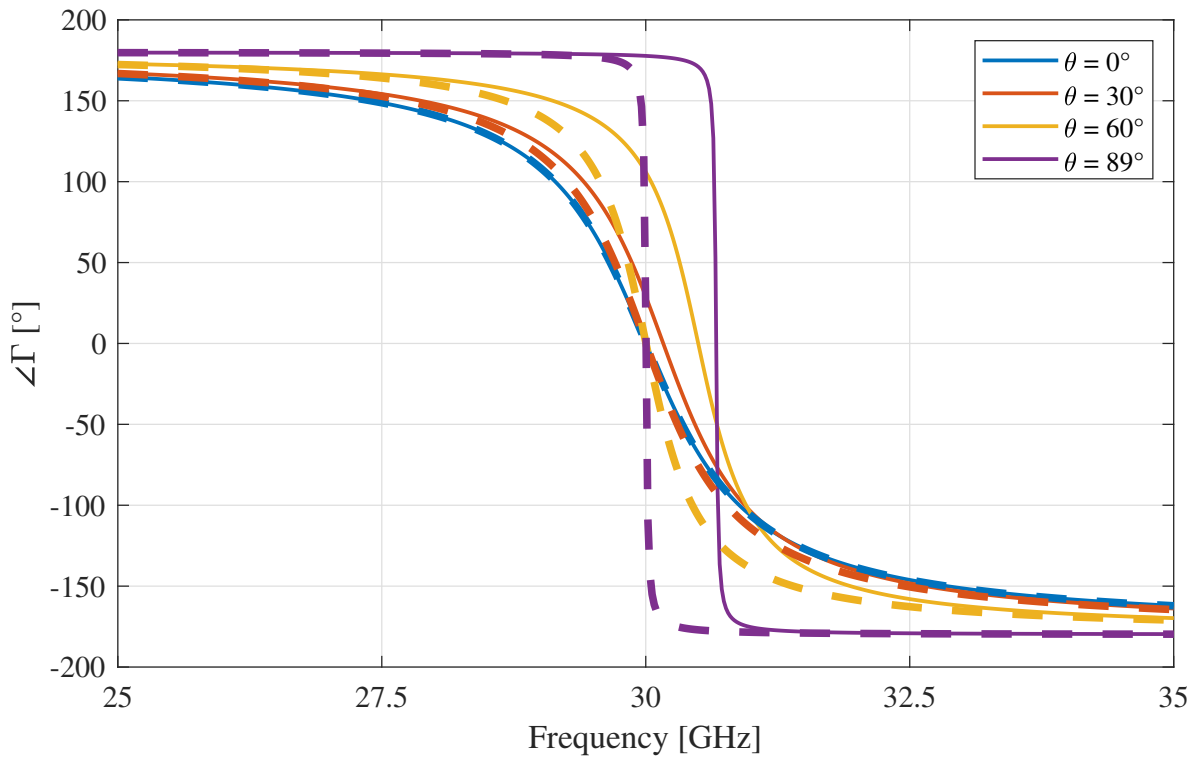


**Figure 7.10:** (a) top view and (b) side view of the double-layer AMC including the vias (not to scale). (c) & (d) unit cell of the designed AMC in CST. In (c), the dielectric and the top layer are removed for visualization purposes only.



(a) Reflection phase for TM plane waves.



(b) Reflection phase for TE plane waves.

**Figure 7.11:** Reflection phase as function of frequency and incident angle of oblique (a) TM and (b) TE plane waves of the 3D AMC structure (solid) and 2D impedance sheet (dashed).

## 7.8 Conclusion

In this chapter, the utilization of AMCs for AoC applications is investigated and modeling techniques are presented, with the aim of stimulating future research to enable low-loss AoCs using AMCs. A limit on the bandwidth of an AMC, excited by a normal incident plane wave, is derived. It is shown that an AMC constructed in the metal stack does not provide enough bandwidth for the 5G mm-wave frequency band. Therefore, the silicon substrate has to be included in the AMC design, at the cost of additional losses. A design approach is presented that keeps the dielectric loss to a minimum. Based on these two findings, an AoC, consisting of a monopole and a double-layer AMC, has been designed. The utilization of the double-layer AMC increased the simulated realized gain of the AoC by minimally 2.4 dB and maximally 3.3 dB in the frequency band ranging from 50 to 60 GHz. Moreover, the full-wave electromagnetic simulations of AMCs are computational intensive since the AMCs typically exhibit important sub-wavelength features. A design procedure for an angular stable AMC for TM plane wave excitations is presented. The response of the AMC and a 2D surface impedance sheet are exactly the same for TM plane wave excitations, potentially simplifying future full-wave electromagnetic simulations.



## CHAPTER EIGHT

# Conclusions and recommendations

---

Mobile cellular communication plays a vital role in today's society. To prevent congestion in our current cellular infrastructure, the 4G cellular network has to be upgraded, resulting in the current deployment of 5G. Before a large-scale roll-out of the 5G mm-wave cellular network is possible, several hurdles have to be overcome first. The increased path loss and attenuation associated with the exploitation of mm-waves demands new antenna concepts for 5G mm-wave base stations. One promising concept for a new 5G mm-wave base station antenna system is a phased array. The main goal of this thesis is to address challenges with respect to the design and OTA characterization of these new phased array systems operating at mm-waves.

Array radiation patterns having desired radiation characteristics, such as having a certain SLL or a null at a certain angle, can be obtained by properly exciting each individual antenna element in the array. Due to errors in the phase and amplitude of the element excitations, the array pattern gets distorted. In Chapter 2, the impact of these errors on the array radiation pattern is assessed. It is shown that the magnitude of a distorted array amplitude pattern follows a Beckmann distribution instead of the conventionally assumed Rician distribution. This result can be utilized by engineers or regulatory agencies to, based on desired radiation characteristics, define specifications on tolerable excitation errors by the ICs of a phased array to ensure compliance with future 5G protocols. In this model, the excitation errors are treated as uncorrelated errors. For a better estimation of the distribution of the array amplitude pattern's magnitude of high-volume manufactured phased array systems, the effect of correlation has to be taken into consideration as well.

In Chapter 3, the design and realization of a 28 GHz 8-by-8 dual-polarized analog active phased array is presented. The array is the university's first prototype of a 5G mm-wave active phased array and is developed as a testbed to experiment with OTA characterization and phased array calibration methods. It is shown that the array is functional, i.e., the main lobe of the array can be pointed in desired directions and an EIRP in the order of 54 to 55 dBm is achieved at the 1-dB compression point. The array being dual-polarized allows for performing an

online calibration procedure once the array is installed in the field, ensuring reliable operation over time. How often the array should be calibrated is unclear as it depends on the influence of the environment and on future 5G protocols. Using several OTA characterization techniques, it is also shown throughout the chapter that some aspects of the phased array can be improved. For instance, the BFN does not perform as desired, resulting in a lower EIRP at the array's P1dB. To solve this, the use of Wilkinson junctions instead of T-junctions is proposed, at the price of increased complexity and cost. Moreover, the PCB was slightly warped, causing a poor thermal connection to some ICs. Possible measures to balance the thermal conductivity are to introduce more copper symmetry in the PCB which reduces warpage, to create a heat sink that is made conformal to the heights of the ICs, or to strengthen the IC's connection to the PCB such that the PCB can be straightened by force without breaking the solder joints. Furthermore, load pulling caused by mutual coupling showed to have a significant effect on the amplitude and phase of the RF signals generated by the ICs. Also the EEPs showed to suffer from mutual coupling. To cope with these issues, measures can be introduced to reduce the mutual coupling from one element to another and make the antenna element less dependent on its direct environment. These recommendations can, in turn, improve future realizations of 5G mm-wave base station antenna systems.

The limited size of typical 5G mm-wave arrays allows for antenna measurement ranges that are small in size and simultaneously can achieve far-field conditions. To determine the gain of an antenna accurately (i.e., having a maximum error in the order of 0.05 dB) for antenna separations in the order of one to two times the Fraunhofer distance, a good estimate of the distance between the amplitude centers of the antennas is required. In Chapter 4, a novel antenna gain measurement method based on a relative-distance sweep is presented. Using this technique, the distance between the amplitude centers of the two antennas can be determined, allowing for an accurate gain determination. Since multiple measurements are performed, scattering and errors in the exact position of the translated antenna tend to average out, hence, reducing the error in the determined gain. Moreover, this sweep can be used to determine whether or not the non-uniform phase distribution over the aperture of the receiver is significant. This, in turn, allows for accurate far-field measurements at minimum antenna separations. This also improves the accuracy of other OTA measurements requiring far-field conditions, such as EVM or BER measurements, for instance, ultimately enhancing the reliability of the 5G cellular network. Furthermore, it is shown in the chapter that although the Fraunhofer distance is independent of the smallest antenna in the measurement setup, the minimum antenna separation required to achieve far-field conditions depends on both antennas. This suggests that the often used Fraunhofer distance is not adequate and motivates the search for a new equation that can be used to calculate the antenna separation required to achieve far-field conditions.

The antenna system shown in Chapter 3 is highly integrated, but the individual antenna element and IC are still designed separately and are both matched to  $50 \Omega$ . The short wavelength associated with the 5G mm-wave frequency band, however, results typically in individual antenna elements having a size in the order of a typical IC. This miniaturization opens up



the possibility to create an AoC or AiP, potentially reducing manufacturing costs, decreasing RF losses and allowing us to leave the standard  $50\ \Omega$  impedance interface. Processes suitable for high-volume manufacturing of AoCs or AiPs are currently under development. In Chapter 5, a characterization method is presented that allows for determining the input impedance and gain of an integrated antenna without having to connect the integrated antenna to a measurement device. The method is verified using a connectorized mm-wave OEWG. In order to perform the CCM on an integrated mm-wave antenna, three different terminations and a switch have to be implemented on the IC. The on-chip terminations will be subject to manufacturing tolerances and, hence, less accurately known compared to the terminations used in the experiments described in Chapter 5. In this case, it is recommended to assess the effect of the tolerances of the manufacturing process to see whether or not the antenna characteristics can be determined reliably. The model presented in the chapter can be used to investigate the impact of these manufacturing tolerances. As the presented method enables the characterization of mm-wave integrated antennas, it can be used to (in)validate models used to design the AoCs and AiPs using new high-volume manufacturing technologies. In turn, these integrated antennas can be used as building blocks for antenna arrays. As these integrated antennas could be used for every type of array topology (small, large, dense, sparse, etc.), such a building block could save a tremendous amount of design time, which cuts costs and reduces the time-to-market for future antenna arrays.

The method presented in Chapter 5 does require calibration, an anechoic chamber, and a large dynamic range. Whereas the method is suited for validating a high-volume manufacturing process, having these requirements is not beneficial for antenna functionality testing of the individual (packaged) dies. In Chapter 6, a variant of the CCM presented in Chapter 5 is shown. Using this variant, solely the reflection coefficient can be determined in a contactless manner. This variant does not require an anechoic chamber or calibration, and can be used while the antennas are in each other's near-field region, drastically reducing the required dynamic range of the measurement system. Due to these advantages it is possible to create compact antenna functionality testing solutions for mass-produced integrated antennas, ensuring reliability of the products. Using simulations, it is shown that an RA can be positioned in the near-field of the integrated antenna if the AUT is a patch antenna. If the AUT is a dipole or monopole, the distance between the OEWG and AUT has to be increased, but the AUT can still be positioned in the near-field of the OEWG. To generalize these observations, this assessment has to be performed on more antenna types in the future. In the chapter, results around 33 GHz using a connectorized patch antenna are shown, which experimentally verify the validity of using the CCM in near-field conditions. Since the intended application is a testing procedure for integrated antennas, the method has to be verified for integrated antennas as well. As mentioned in Chapter 5, the required on-chip terminations are subject to manufacturing tolerances which give rise to an uncertainty in the determined input impedance and reflection coefficient of the AUT. If this method will be used to characterize integrated antennas, this uncertainty has to be included in measurement results.

In Chapter 7, the utilization of AMCs for AoC applications is investigated and modeling

techniques are presented. These modeling techniques are presented with the aim of stimulating future research to enable the production of low-loss AoCs using AMCs. A limit on the bandwidth of an AMC, excited by a normal incident plane wave, is derived. It is shown that an AMC constructed in the metal stack does not provide enough bandwidth for the 5G mm-wave frequency band. As a consequence, the silicon substrate has to be included in the AMC design, at the cost of additional losses. A design approach is presented that keeps the dielectric loss to a minimum. A double-layer AMC has been designed based on these two findings. After integration of this AMC with a monopole, the dimensions of the AMC were optimized using full-wave electromagnetic simulations. The utilization of the AMC increased the simulated realized gain of the AoC by minimally 2.4 dB and maximally 3.3 dB in the frequency band ranging from 50 to 60 GHz. The full-wave simulations to optimize AMCs are computational intensive since AMCs typically exhibit important sub-wavelength features. To enable faster design cycles, better design tools and methods for AMCs are desired. A design procedure for an angular stable AMC for TM plane wave excitations is presented in Chapter 7. The response of the angular stable AMC and a 2D surface impedance sheet are exactly the same for TM plane wave excitations, potentially simplifying future full-wave electromagnetic simulations. The AMC is not angular stable for TE plane wave excitation, however, leaving room for improvement of the presented design procedure.

# Derivation of Statistical Quantities of the Array Amplitude Pattern

---

## A.1 Introduction

In this appendix, the results as presented in (2.8), (2.9), (2.10), (2.11) and (2.13) are derived. For these derivations, the following properties are used.

If random variables  $A$  and  $B$  are independent, the following holds

$$E[AB] = E[A]E[B]. \quad (\text{A.1})$$

For a Gaussian distributed random variable  $\delta$  having zero mean and a variance of  $\sigma^2$  (i.e.,  $\delta \sim \mathcal{N}(0, \sigma^2)$ ), the following relations hold

$$E[\delta] = 0, \quad (\text{A.2a})$$

$$E[\delta^2] = \sigma^2, \quad (\text{A.2b})$$

$$E[\cos(\delta)] = e^{-\frac{\sigma^2}{2}}, \quad (\text{A.2c})$$

$$E[\sin(\delta)] = 0, \quad (\text{A.2d})$$

$$E[\sin(\delta)\cos(\delta)] = 0, \quad (\text{A.2e})$$

$$E[\cos^2(\delta)] = E\left[\frac{1 + \cos(2\delta)}{2}\right] = \frac{1}{2} + \frac{1}{2}e^{-2\sigma^2}, \quad (\text{A.2f})$$

$$E[\sin^2(\delta)] = E[1 - \cos^2(\delta)] = \frac{1}{2} - \frac{1}{2}e^{-2\sigma^2}. \quad (\text{A.2g})$$

Furthermore, the following well-known trigonometric identity is used

$$\sin^2 \theta + \cos^2 \theta = 1. \quad (\text{A.3})$$

## A.2 Mean value

The mean value of  $X$ , as defined in (2.7), can be written as

$$\begin{aligned}
 E[X] &= E \left[ \sum_{n=1}^N A_n (1 + \delta_{an}) (\cos \delta_{pn} \cos C_n - \sin \delta_{pn} \sin C_n) \right] \\
 &= \sum_{n=1}^N A_n E \left[ (\cos \delta_{pn} \cos C_n - \sin \delta_{pn} \sin C_n) \right] \stackrel{(A.1), (A.2a)}{\leftarrow} \\
 &= e^{-\frac{\sigma_p^2}{2}} \sum_{n=1}^N A_n \cos C_n \stackrel{(A.2c), (A.2d)}{\leftarrow} \\
 &= e^{-\frac{\sigma_p^2}{2}} \operatorname{Re}[F_0].
 \end{aligned} \tag{A.4}$$

By performing a similar derivation, the mean value of  $Y$ , as defined in (2.7), can be found to be

$$E[Y] = e^{-\frac{\sigma_p^2}{2}} \operatorname{Im}[F_0]. \tag{A.5}$$

## A.3 Variance

By definition, the variance of a random variable  $X$  is

$$\operatorname{Var}(X) = E[(X - E[X])^2] = E[X^2] - E[X]^2. \tag{A.6}$$

The calculation for the second term of the right-hand side of (A.6) is straightforward using the expression found in (A.4)

$$E[X]^2 = e^{-\sigma_p^2} (\operatorname{Re}[F_0])^2. \tag{A.7}$$

Solving the first term of the right-hand side of (A.6), however, is not that straightforward. In order to do that,  $X^2$  will be first rewritten and divided into two different summations. In one of the summations, only the contributions where  $n = m$  are taken into account, whereas in the other summation  $n \neq m$  will be considered.

$X^2$  can be written as

$$\begin{aligned}
X^2 &= \left( \sum_{n=1}^N A_n (1 + \delta_{an}) (\cos \delta_{pn} \cos C_n - \sin \delta_{pn} \sin C_n) \right)^2 \\
&= \sum_{n=1}^N \sum_{m=1}^N A_n A_m (1 + \delta_{an}) (1 + \delta_{am}) \\
&\quad (\cos \delta_{pn} \cos C_n - \sin \delta_{pn} \sin C_n) (\cos \delta_{pm} \cos C_m - \sin \delta_{pm} \sin C_m) \\
&= \sum_{n=1}^N A_n^2 (1 + \delta_{an})^2 (\cos \delta_{pn} \cos C_n - \sin \delta_{pn} \sin C_n)^2 \quad \left. \vphantom{\sum_{n=1}^N} \right\} \text{I} \\
&\quad + \sum_{n=1}^N \sum_{m=1, m \neq n}^N A_n A_m (1 + \delta_{an}) (1 + \delta_{am}) \\
&\quad (\cos \delta_{pn} \cos C_n - \sin \delta_{pn} \sin C_n) (\cos \delta_{pm} \cos C_m - \sin \delta_{pm} \sin C_m), \quad \left. \vphantom{\sum_{n=1}^N} \right\} \text{II} \quad (\text{A.8})
\end{aligned}$$

and therefore  $E[X^2]$  can be written as

$$E[X^2] = E[\text{I}] + E[\text{II}]. \quad (\text{A.9})$$

I and II will be solved independently. The expected value of I can be written as

$$\begin{aligned}
E[\text{I}] &= E \left[ \sum_{n=1}^N A_n^2 (1 + \delta_{an})^2 (\cos \delta_{pn} \cos C_n - \sin \delta_{pn} \sin C_n)^2 \right] \\
&= \sum_{n=1}^N A_n^2 (1 + \sigma_a^2) \leftarrow_{(\text{A.1}), (\text{A.2a}), (\text{A.2b})} \\
&\quad E \left[ \cos^2 \delta_{pn} \cos^2 C_n - 2 \cos \delta_{pn} \cos C_n \sin \delta_{pn} \sin C_n + \sin^2 \delta_{pn} \sin^2 C_n \right] \\
&= (1 + \sigma_a^2) \sum_{n=1}^N A_n^2 \left( \frac{1}{2} + \frac{1}{2} e^{-2\sigma_p^2} \cos^2 C_n - \frac{1}{2} e^{-2\sigma_p^2} \sin^2 C_n \right) \leftarrow_{(\text{A.2e}), (\text{A.2f}), (\text{A.2g}), (\text{A.3})} \\
&= (1 + \sigma_a^2) \sum_{n=1}^N A_n^2 \left( \frac{1}{2} + e^{-2\sigma_p^2} \cos^2 C_n - \frac{1}{2} e^{-2\sigma_p^2} \right). \leftarrow_{(\text{A.3})}
\end{aligned} \quad (\text{A.10})$$

$E[\text{II}]$  can be expressed by

$$\begin{aligned}
E[\text{II}] &= E \left[ \sum_{n=1}^N \sum_{m=1, m \neq n}^N A_n A_m (1 + \delta_{an})(1 + \delta_{am}) \right. \\
&\quad \left. (\cos \delta_{pn} \cos C_n - \sin \delta_{pn} \sin C_n)(\cos \delta_{pm} \cos C_m - \sin \delta_{pm} \sin C_m) \right] \\
&= \sum_{n=1}^N \sum_{m=1, m \neq n}^N A_n A_m \stackrel{\text{(A.1), (A.2a)}}{\leftarrow} \\
&\quad E \left[ (\cos \delta_{pn} \cos C_n - \sin \delta_{pn} \sin C_n) \right] E \left[ (\cos \delta_{pm} \cos C_m - \sin \delta_{pm} \sin C_m) \right] \\
&= e^{-\sigma_p^2} \sum_{n=1}^N \sum_{m=1, m \neq n}^N A_n A_m \cos C_n \cos C_m \stackrel{\text{(A.2c), (A.2d)}}{\leftarrow} \\
&= e^{-\sigma_p^2} (\text{Re}[F_0])^2 - e^{-\sigma_p^2} \sum_{n=1}^N A_n^2 \cos^2 C_n. \tag{A.11}
\end{aligned}$$

By combining (A.6), (A.7), (A.9), (A.10) and (A.11), an expression for the variance of the real part of the array amplitude pattern can be found

$$\text{Var}(X) = \frac{1}{2} (1 + \sigma_a^2) (1 - e^{-2\sigma_p^2}) \sum_{n=1}^N A_n^2 + \left( (1 + \sigma_a^2) e^{-2\sigma_p^2} - e^{-\sigma_p^2} \right) \sum_{n=1}^N A_n^2 \cos^2 C_n. \tag{A.12}$$

A similar derivation can be done in order to find the variance of the imaginary part of the array amplitude pattern, which turns out to be as follows

$$\text{Var}(Y) = \frac{1}{2} (1 + \sigma_a^2) (1 - e^{-2\sigma_p^2}) \sum_{n=1}^N A_n^2 + \left( (1 + \sigma_a^2) e^{-2\sigma_p^2} - e^{-\sigma_p^2} \right) \sum_{n=1}^N A_n^2 \sin^2 C_n. \tag{A.13}$$

## A.4 Correlation

The correlation coefficient  $\rho_{xy}$  between random variables  $X$  and  $Y$  with expected values  $\mu_x$  and  $\mu_y$  and standard deviations  $\sigma_x$  and  $\sigma_y$  is defined as

$$\rho_{xy} = \frac{\text{cov}(X, Y)}{\sigma_x \sigma_y} = \frac{\text{cov}(X, Y)}{\sqrt{\text{Var}(X) \text{Var}(Y)}}, \tag{A.14}$$

with

$$\text{cov}(X, Y) = E[(X - \mu_x)(Y - \mu_y)] = E[XY] - \mu_x \mu_y. \tag{A.15}$$

Expressions of  $\mu_x$ ,  $\mu_y$ ,  $\text{Var}(X)$  and  $\text{Var}(Y)$  have already been found in (A.4), (A.5), (A.12) and (A.13) respectively. Therefore,  $E[XY]$  is the only unknown of (A.14) and (A.15). The steps

that have to be performed to get  $E[XY]$  are quite similar to the steps performed to get  $E[X^2]$ . Also here, the argument (i.e.,  $XY$ ) will first be rewritten in two different summations. In one of the summations, only the contributions where  $n = m$  are taken into account, whereas in the other summation  $n \neq m$  will be considered.

$XY$  can be written as

$$\begin{aligned}
XY &= \sum_{n=1}^N \sum_{m=1}^N A_n A_m (1 + \delta_{an})(1 + \delta_{am})(\cos \delta_{pn} \cos C_n - \sin \delta_{pn} \sin C_n) \\
&\quad (\cos \delta_{pm} \sin C_m + \sin \delta_{pm} \cos C_m) \\
&= \sum_{n=1}^N A_n^2 (1 + \delta_{an})^2 (\cos^2 \delta_{pn} \cos C_n \sin C_n - \sin^2 \delta_{pn} \cos C_n \sin C_n \\
&\quad - \cos \delta_{pn} \sin \delta_{pn} \sin^2 C_n + \cos \delta_{pn} \sin \delta_{pn} \cos^2 C_n) \quad \left. \vphantom{\sum_{n=1}^N} \right\} \text{III} \\
&\quad + \sum_{n=1}^N \sum_{m=1, m \neq n}^N A_n A_m (1 + \delta_{an})(1 + \delta_{am})(\cos \delta_{pn} \cos C_n \\
&\quad - \sin \delta_{pn} \sin C_n)(\cos \delta_{pm} \sin C_m + \sin \delta_{pm} \cos C_m), \quad \left. \vphantom{\sum_{n=1}^N} \right\} \text{IV} \quad (\text{A.16})
\end{aligned}$$

and therefore  $E[XY]$  can be written as

$$E[XY] = E[\text{III}] + E[\text{IV}]. \quad (\text{A.17})$$

III and IV will be solved independently. The expected value of III can be written as

$$\begin{aligned}
E[\text{III}] &= E \left[ \sum_{n=1}^N A_n^2 (1 + \delta_{an})^2 (\cos^2 \delta_{pn} \cos C_n \sin C_n - \sin^2 \delta_{pn} \cos C_n \sin C_n \right. \\
&\quad \left. - \cos \delta_{pn} \sin \delta_{pn} \sin^2 C_n + \cos \delta_{pn} \sin \delta_{pn} \cos^2 C_n) \right] \\
&= (1 + \sigma_a^2) \sum_{n=1}^N A_n^2 E \left[ (\cos^2 \delta_{pn} \cos C_n \sin C_n \overset{\leftarrow}{\text{(A.1),(A.2a),(A.2b)}}} \right. \\
&\quad \left. - \sin^2 \delta_{pn} \cos C_n \sin C_n - \cos \delta_{pn} \sin \delta_{pn} \sin^2 C_n + \cos \delta_{pn} \sin \delta_{pn} \cos^2 C_n) \right] \\
&= (1 + \sigma_a^2) e^{-2\sigma_p^2} \sum_{n=1}^N A_n^2 \cos C_n \sin C_n. \overset{\leftarrow}{\text{(A.2e),(A.2f),(A.2g)}} \quad (\text{A.18})
\end{aligned}$$

$E[\text{IV}]$  can be expressed by

$$\begin{aligned}
E[\text{IV}] &= E \left[ \sum_{n=1}^N \sum_{m=1, m \neq n}^N A_n A_m (1 + \delta_{an})(1 + \delta_{am})(\cos \delta_{pn} \cos C_n - \sin \delta_{pn} \sin C_n) \right. \\
&\quad \left. (\cos \delta_{pm} \sin C_m + \sin \delta_{pm} \cos C_m) \right] \\
&= \sum_{n=1}^N \sum_{m=1, m \neq n}^N A_n A_m E[(\cos \delta_{pn} \cos C_n - \sin \delta_{pn} \sin C_n)] \stackrel{(A.1), (A.2a)}{\leftarrow} \\
&\quad E[(\cos \delta_{pm} \sin C_m + \sin \delta_{pm} \cos C_m)] \\
&= e^{-\sigma_p^2} \sum_{n=1}^N \sum_{m=1, m \neq n}^N A_n A_m \cos C_n \sin C_m \stackrel{(A.2c), (A.2d)}{\leftarrow} \\
&= e^{-\sigma_p^2} \sum_{n=1}^N \sum_{m=1}^N A_n A_m \cos C_n \sin C_m - e^{-\sigma_p^2} \sum_{n=1}^N A_n^2 \cos C_n \sin C_n. \tag{A.19}
\end{aligned}$$

By combining (A.15), (A.17), (A.18) and (A.19), an expression for  $E[XY]$  can be found

$$\begin{aligned}
E[XY] &= \left( (1 + \sigma_a^2) e^{-2\sigma_p^2} - e^{-\sigma_p^2} \right) \sum_{n=1}^N A_n^2 \cos C_n \sin C_n + e^{-\sigma_p^2} \sum_{n=1}^N \sum_{m=1}^N A_n A_m \cos C_n \sin C_m \\
&= \left( (1 + \sigma_a^2) e^{-2\sigma_p^2} - e^{-\sigma_p^2} \right) \sum_{n=1}^N A_n^2 \cos C_n \sin C_n + e^{-\sigma_p^2} \text{Re}[F_0] \text{Im}[F_0]. \tag{A.20}
\end{aligned}$$

Then, by combining (A.4), (A.5), (A.15) and (A.20), an expression of the covariance between  $X$  and  $Y$  can be found

$$\text{cov}(X, Y) = \left( (1 + \sigma_a^2) e^{-2\sigma_p^2} - e^{-\sigma_p^2} \right) \sum_{n=1}^N A_n^2 \cos C_n \sin C_n. \tag{A.21}$$

By substituting (2.10), (2.11) and (2.13) into (2.12), an expression for the correlation coefficient  $\rho_{xy}$  can be found. This will give rise to a tedious expression and this expression has been omitted in this appendix. For implementation purposes, it is recommended to calculate the variances of  $X$  and  $Y$ , and the covariance between  $X$  and  $Y$ , and substitute the results in (2.12), rather than implementing (2.12) in one single expression.



# Derivation of a Beamforming Algorithm for Arbitrary Antenna Arrays

---

## B.1 Introduction to the algorithm

In [15], a beamforming algorithm is presented that can be used to calculate the excitation coefficients to shape the radiation pattern of an arbitrary array in one planar cut. The algorithm presented in this appendix is based on the algorithm in [15] and can be used to calculate the excitations to shape the full radiation pattern of an arbitrary antenna array. This algorithm was used to generate the coefficients for the radiation pattern measurements shown in Fig. 3.20.

In the algorithm, the excitation coefficients are found using an iterative procedure. In the first step, the main lobe is pointing in the desired direction, while the radiation coming from other directions is minimized. After the first step, an iterative method ensures that the side lobes are suppressed to a certain level, while maintaining the main beam in its desired direction. The algorithm is derived as follows.

The array field pattern  $F(\theta, \phi)$  of an arbitrary antenna array having  $N$  antenna elements can be written as

$$F(\theta, \phi) = \underline{\omega}^\dagger \underline{v}(\theta, \phi). \quad (\text{B.1})$$

Here, the dagger  $\dagger$  is defined as the Hermitian transpose operator,  $\underline{\omega}$  represents an  $N \times 1$ -vector containing the complex weights of the  $N$  individual antenna elements and  $\underline{v}(\theta, \phi)$  the steering vector, which is defined as

$$\underline{v}(\theta, \phi) = \begin{bmatrix} g_1(\theta, \phi) \\ g_2(\theta, \phi) \\ \vdots \\ g_N(\theta, \phi) \end{bmatrix}. \quad (\text{B.2})$$

Here,  $g_n(\theta, \phi)$  is the complex embedded element field pattern of the  $n^{\text{th}}$  antenna element.

The complex field patterns of the individual antenna elements have to be extracted from simulation software or have to be measured. In both cases, the pattern will consist of samples. The samples of the complex E-field patterns have to be equally spaced in the  $\theta$  and  $\phi$ -direction in terms of degrees. The number of samples in the  $\theta$  and  $\phi$ -direction are indicated with  $L_\theta$  and  $L_\phi$  respectively. Furthermore, the  $k^{\text{th}}$  sample in the  $\theta$ -direction is indicated by  $\theta_k$  and the  $l^{\text{th}}$  sample in the  $\phi$ -direction is indicated by  $\phi_l$ .

## B.2 Steering the main lobe and minimizing radiation

Finding the excitations  $\underline{\omega}_0$  that minimizes the radiation from other directions than the main lobe can be expressed as follows

$$\underline{\omega}_0 = \min_{\underline{\omega}} \underline{\omega}^\dagger \mathbf{A} \underline{\omega}, \quad (\text{B.3})$$

with  $\mathbf{A}$  the covariance matrix defined as

$$\mathbf{A} = \sum_{k=1}^{L_\theta} \sum_{l=1}^{L_\phi} e(k, l) \mathbf{V}_{kl} \sin(\theta_k), \quad (\text{B.4})$$

with

$$\mathbf{V}_{kl} = \underline{v}(\theta_k, \phi_l) \underline{v}^\dagger(\theta_k, \phi_l), \quad (\text{B.5})$$

and

$$e(k, l) = \begin{cases} 0 & \text{if } (\theta, \phi) = (\theta_k, \phi_l) \text{ is in the main lobe,} \\ 1 & \text{otherwise.} \end{cases} \quad (\text{B.6})$$

In this formula, a few things have to be clarified. The goal is to minimize the unwanted radiation. The total unweighted contribution to the radiation pattern is collected by the covariance matrix  $\mathbf{A}$ . In order to capture only the unwanted radiation, instead of also taking into account the radiation of the main lobe, the function  $e(k, l)$  is introduced. This function is equal to zero in the region inside the main lobe, so the desired radiation is not included in the covariance matrix  $\mathbf{A}$ . This means that an expectation of the location and the beamwidth of the main lobe is required.

Since the algorithm is developed using spherical coordinates, a correcting factor needs to be included. This is resembled by the  $\sin(\theta_k)$ -term in (B.4).

In other words, all the contributions of the unweighted field patterns are summed in (B.4), except for the contributions where the main lobe is present. Subsequently, the weights that minimize these contributions, and thus minimize (B.3), are determined.

To make sure that the main lobe is pointing towards its desired direction, some constraints have to be formulated. First of all, to not end up with a trivial solution, the radiation pattern has to be equal to an number other than zero (for instance, one) in the direction of pointing.

Moreover, the radiation pattern has to have a local maximum in the direction of pointing. This can be achieved by forcing the real part of the partial derivatives of the radiation pattern with respect to  $\theta$  and  $\phi$  to be zero.<sup>1</sup> This can be expressed in the following way

$$\begin{aligned} F(\theta_0, \phi_0) &= \underline{\omega}^\dagger \underline{v}(\theta_0, \phi_0) = \underline{\omega}^\dagger \underline{v}_0 = 1, \\ \operatorname{Re} \left[ \frac{\partial F(\theta, \phi)}{\partial \theta} \Big|_{(\theta, \phi) = (\theta_0, \phi_0)} \right] &= \operatorname{Re} \left[ \underline{\omega}^\dagger \frac{\partial \underline{v}(\theta, \phi)}{\partial \theta} \Big|_{(\theta, \phi) = (\theta_0, \phi_0)} \right] = \operatorname{Re}[\underline{\omega}^\dagger \underline{v}_0^{\partial \theta}] = 0, \\ \operatorname{Re} \left[ \frac{\partial F(\theta, \phi)}{\partial \phi} \Big|_{(\theta, \phi) = (\theta_0, \phi_0)} \right] &= \operatorname{Re} \left[ \underline{\omega}^\dagger \frac{\partial \underline{v}(\theta, \phi)}{\partial \phi} \Big|_{(\theta, \phi) = (\theta_0, \phi_0)} \right] = \operatorname{Re}[\underline{\omega}^\dagger \underline{v}_0^{\partial \phi}] = 0, \end{aligned} \quad (\text{B.7})$$

with  $\theta_0$  and  $\phi_0$  the  $\theta$  and  $\phi$ -coordinate of the desired pointing angle, with  $\underline{v}_0$  a shorthand notation of  $\underline{v}(\theta, \phi)$  evaluated at  $(\theta, \phi) = (\theta_0, \phi_0)$ , and with  $\underline{v}_0^{\partial \theta}$  and  $\underline{v}_0^{\partial \phi}$  a shorthand notation of the partial derivative of  $\underline{v}(\theta, \phi)$  with respect to  $\theta$  and  $\phi$ , respectively, evaluated at  $(\theta, \phi) = (\theta_0, \phi_0)$ .

### B.3 Solving the real counterpart

The minimization problem formulated in (B.3) in combination with the constraints defined in (B.7) form a complex minimization problem, and there is no direct solution. However, this problem can be transformed in a real minimization problem, such that a solution can be found [123]. The real counterpart of the minimization problem and its constraints formulated in (B.3) and (B.7), respectively, is as follows

$$\underline{\tilde{\omega}}_0 = \min_{\underline{\tilde{\omega}}} \underline{\tilde{\omega}}^T \tilde{\mathbf{A}} \underline{\tilde{\omega}}, \quad (\text{B.8})$$

under the constraints

$$\begin{aligned} \underline{\tilde{\omega}}^T \tilde{\underline{v}}_0 &= 1, \\ \underline{\tilde{\omega}}^T \tilde{\underline{v}}_0 &= 0, \\ \underline{\tilde{\omega}}^T \tilde{\underline{v}}_0^{\partial \theta} &= 0, \\ \underline{\tilde{\omega}}^T \tilde{\underline{v}}_0^{\partial \phi} &= 0, \end{aligned} \quad (\text{B.9})$$

---

<sup>1</sup>To be mathematically more precise, the second-order partial derivatives with respect to  $\theta$  and  $\phi$  should also be constrained to be negative in order to ensure a local maximum [15]. However, this constraint is omitted since in most practical situations this is satisfied.

with superscript  $T$  defined as the transpose operator, and with

$$\begin{aligned}
\tilde{\underline{\omega}}_0 &= \begin{bmatrix} \text{Re}[\underline{\omega}_0] \\ \text{Im}[\underline{\omega}_0] \end{bmatrix}, \\
\tilde{\underline{\omega}} &= \begin{bmatrix} \text{Re}[\underline{\omega}] \\ \text{Im}[\underline{\omega}] \end{bmatrix}, \\
\tilde{\underline{\mathbf{A}}} &= \begin{bmatrix} \text{Re}[\underline{\mathbf{A}}] & -\text{Im}[\underline{\mathbf{A}}] \\ \text{Im}[\underline{\mathbf{A}}] & \text{Re}[\underline{\mathbf{A}}] \end{bmatrix}, \\
\tilde{\underline{v}}_0 &= \begin{bmatrix} \text{Re}[\underline{v}_0] \\ \text{Im}[\underline{v}_0] \end{bmatrix}, \\
\hat{\underline{v}}_0 &= \begin{bmatrix} -\text{Im}[\underline{v}_0] \\ \text{Re}[\underline{v}_0] \end{bmatrix}, \\
\tilde{\underline{v}}_0^{\partial\theta} &= \begin{bmatrix} \text{Re}[\underline{v}_0^{\partial\theta}] \\ \text{Im}[\underline{v}_0^{\partial\theta}] \end{bmatrix}, \\
\tilde{\underline{v}}_0^{\partial\phi} &= \begin{bmatrix} \text{Re}[\underline{v}_0^{\partial\phi}] \\ \text{Im}[\underline{v}_0^{\partial\phi}] \end{bmatrix}.
\end{aligned} \tag{B.10}$$

These linear constraints can be formulated as follows

$$\tilde{\underline{\mathbf{C}}}^T \tilde{\underline{\omega}} = \tilde{\underline{f}}, \tag{B.11}$$

with

$$\tilde{\underline{\mathbf{C}}} = \begin{bmatrix} \tilde{\underline{v}}_0 & \hat{\underline{v}}_0 & \tilde{\underline{v}}_0^{\partial\theta} & \tilde{\underline{v}}_0^{\partial\phi} \end{bmatrix}, \tag{B.12}$$

and

$$\tilde{\underline{f}} = [1 \ 0 \ 0 \ 0]^T. \tag{B.13}$$

The closed-form solution to this linear constraint minimization problem is

$$\tilde{\underline{\omega}}_0 = \tilde{\underline{\mathbf{A}}}^{-1} \tilde{\underline{\mathbf{C}}} (\tilde{\underline{\mathbf{C}}}^T \tilde{\underline{\mathbf{A}}}^{-1} \tilde{\underline{\mathbf{C}}})^{-1} \tilde{\underline{f}}. \tag{B.14}$$

## B.4 Suppressing the side lobes

By solving (B.14), it is only ensured that the main lobe is at the desired angle, and minimizes the radiation outside the main lobe region. The goal is not to minimize the radiation at other angles than the main lobe, however, but is to minimize the maximum side lobe. This can be done by equalizing the side lobes [124]. To do this, an iterative process is proposed. In each iteration new weights will be calculated. This can be written as

$$\underline{\omega}_{n+1} \leftarrow \underline{\omega}_n + \Delta \underline{\omega}_n. \tag{B.15}$$

Although new weights have to be found to equalize the side lobes, the constraints which are defined in (B.7) still have to be met. Also, while the weights are being changed, the added radiation coming from directions other than the main lobe must be kept to a minimum. This can be expressed as follows

$$\Delta \underline{\omega}_n = \min_{\Delta \underline{\omega}} \Delta \underline{\omega}^\dagger \mathbf{A} \Delta \underline{\omega}, \quad (\text{B.16})$$

under the constraints

$$\begin{aligned} \Delta \underline{\omega}^\dagger \underline{v}_0 &= 0, \\ \text{Re}[\Delta \underline{\omega}^\dagger \underline{v}_0^{\partial \theta}] &= 0, \\ \text{Re}[\Delta \underline{\omega}^\dagger \underline{v}_0^{\partial \phi}] &= 0. \end{aligned} \quad (\text{B.17})$$

To ensure that the side lobes will be suppressed to a certain level, some extra constraints have to be defined. To prevent having an underdetermined system, only a limited amount of extra constraints can be defined. Since the variable  $\Delta \underline{\omega}$  is vector of the size  $N \times 1$  and is complex, in principle, a maximum of  $N$  constraints in the complex domain can be defined. Two constraints in the real domain have the same complexity as one constraint in the complex domain, meaning that in the problem defined in (B.17) is equivalent to two constraints in the complex domain. This means that, in principle,  $M_{\max} = N - 2$  side lobes can be controlled in each iteration. The first step is to find the locations of the highest side lobes in the radiation pattern. Once these locations are known, the following constraint can be introduced to suppress the  $i^{\text{th}}$  side lobe

$$\Delta \underline{\omega}^\dagger \underline{v}_i = f_i, \quad (\text{B.18})$$

with

$$\begin{aligned} f_i &= (R - |c_i|) \frac{c_i}{|c_i|}, \\ c_i &= \underline{\omega}_n^\dagger \underline{v}_i, \\ \underline{v}_i &= \underline{v}(\theta_i, \phi_i), \\ i &= 1, 2, \dots, M \leq M_{\max}, \end{aligned} \quad (\text{B.19})$$

with  $\theta_i$  and  $\phi_i$  the  $\theta$  and  $\phi$ -coordinate of the location of the  $i^{\text{th}}$  side lobe,  $R$  is the desired side lobe level and  $M$  the amount of side lobes to be suppressed. Next to that,  $c_i$  is the value of the  $i^{\text{th}}$  side lobe and  $f_i$  resembles the residual amount needed for the  $i^{\text{th}}$  side lobe to achieve the desired side lobe level.

In the same way as in the previous section, the real counterpart of the new complex minimization problem can be found. This can be expressed as follows

$$\Delta \tilde{\omega}_n = \min_{\Delta \tilde{\omega}} \Delta \tilde{\omega}^T \tilde{\mathbf{A}} \Delta \tilde{\omega}, \quad (\text{B.20})$$

under the constraints

$$\begin{aligned}
\Delta\tilde{\omega}^T \tilde{v}_0 &= 0, \\
\Delta\tilde{\omega}^T \hat{v}_0 &= 0, \\
\Delta\tilde{\omega}^T \tilde{v}_0^{\partial\theta} &= 0, \\
\Delta\tilde{\omega}^T \tilde{v}_0^{\partial\phi} &= 0, \\
\Delta\tilde{\omega}^T \tilde{v}_i &= \tilde{f}_i, \\
\Delta\tilde{\omega}^T \hat{v}_i &= \hat{f}_i,
\end{aligned} \tag{B.21}$$

with

$$\begin{aligned}
\Delta\tilde{\omega}_n &= \begin{bmatrix} \text{Re}[\Delta\omega_n] \\ \text{Im}[\Delta\omega_n] \end{bmatrix}, \\
\Delta\tilde{\omega} &= \begin{bmatrix} \text{Re}[\Delta\omega] \\ \text{Im}[\Delta\omega] \end{bmatrix}, \\
\tilde{f}_i &= \text{Re}[f_i], \\
\hat{f}_i &= \text{Im}[f_i], \\
\tilde{v}_i &= \begin{bmatrix} \text{Re}[v_i] \\ \text{Im}[v_i] \end{bmatrix}, \\
\hat{v}_i &= \begin{bmatrix} -\text{Im}[v_i] \\ \text{Re}[v_i] \end{bmatrix}.
\end{aligned} \tag{B.22}$$

In line with the previous section, these linear constraints can then be formulated as follows

$$\tilde{\mathbf{C}}_n^T \Delta\tilde{\omega} = \tilde{\mathbf{f}}_n, \tag{B.23}$$

with

$$\tilde{\mathbf{C}}_n = \begin{bmatrix} \tilde{v}_0 & \hat{v}_0 & \tilde{v}_0^{\partial\theta} & \tilde{v}_0^{\partial\phi} & \tilde{v}_1 & \tilde{v}_2 & \dots & \tilde{v}_M & \hat{v}_1 & \hat{v}_2 & \dots & \hat{v}_M \end{bmatrix}, \tag{B.24}$$

and

$$\tilde{\mathbf{f}}_n = [0 \ 0 \ 0 \ 0 \ \tilde{f}_1 \ \tilde{f}_2 \ \dots \ \tilde{f}_M \ \hat{f}_1 \ \hat{f}_2 \ \dots \ \hat{f}_M]^T. \tag{B.25}$$

The closed-form solution to this linear constraint minimization problem is

$$\Delta\tilde{\omega}_n = \tilde{\mathbf{A}}^{-1} \tilde{\mathbf{C}}_n (\tilde{\mathbf{C}}_n^T \tilde{\mathbf{A}}^{-1} \tilde{\mathbf{C}}_n)^{-1} \tilde{\mathbf{f}}_n. \tag{B.26}$$

By solving (B.26) iteratively, coefficients can be generated that ensure the beam to be pointed towards  $(\theta, \phi) = (\theta_0, \phi_0)$  and an SLL of  $R$ . This iterative algorithm was used to generate the coefficients for radiation pattern measurements shown in Fig. 3.20. To generate these weights, in general, no more than ten iterations were required.

## Derivation of the Bandwidth of a Lossless Artificial Magnetic Conductor

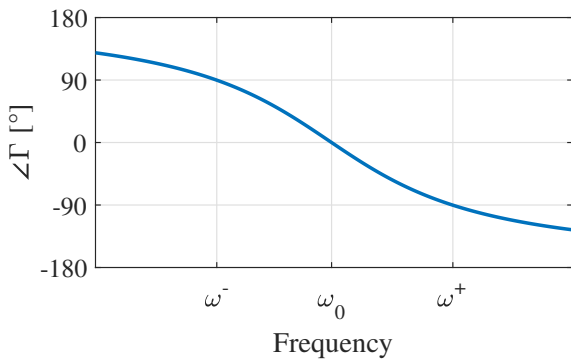
---

In this appendix, the derivation of the bandwidth of a lossless AMC is presented. As mentioned in Section 7.4, the bandwidth of an AMC is typically defined from  $\angle\Gamma = +90^\circ$  to  $\angle\Gamma = -90^\circ$  [121]. Hence, to solve for the bandwidth, an expression of the frequency corresponding to  $\angle\Gamma = +90^\circ$  and  $\angle\Gamma = -90^\circ$ , denoted by  $\omega^-$  and  $\omega^+$ , respectively, has to be determined. In Fig. C.1(a), the reflection phase of a typical AMC is shown. Note that the frequency corresponding to  $\angle\Gamma = +90^\circ$  is lower than the resonance frequency, whereas the frequency corresponding to  $\angle\Gamma = -90^\circ$  is higher than the resonance frequency.

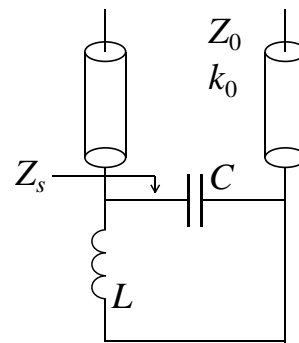
In Fig. C.1(b), the equivalent circuit model of a lossless AMC is shown. The equivalent surface impedance  $Z_s$  of this parallel LC circuit can be written as

$$Z_s = Z_C || Z_L = \frac{j\omega L}{1 - \omega^2 LC}. \quad (\text{C.1})$$

If a structure having surface impedance  $Z_s$  is excited by a plane wave of normal incidence,



(a) Reflection phase of a typical AMC.



(b) Equivalent circuit model of a lossless AMC.

**Figure C.1**

the reflection coefficient can be calculated using

$$\Gamma = \frac{Z_s - Z_0}{Z_s + Z_0} = \frac{Z_0(\omega^2 LC - 1) + j\omega L}{Z_0(1 - \omega^2 LC) + j\omega L} = \frac{A + j\omega L}{-A + j\omega L}, \quad (\text{C.2})$$

with  $A = Z_0(\omega^2 LC - 1)$  and  $Z_0$  being the characteristic impedance of the medium directly above the surface. The angle of the reflection coefficient can be expressed as

$$\angle \Gamma = \angle(A + j\omega L) - \angle(-A + j\omega L). \quad (\text{C.3})$$

The parameter  $A$  is positive for frequencies above the resonance frequency. To determine the angular frequency corresponding to  $\angle \Gamma = -90^\circ (= -\pi/2)$ , (C.3) can be written as

$$\angle \Gamma = \tan^{-1}\left(\frac{\omega L}{A}\right) - \left(\pi - \tan^{-1}\left(\frac{\omega L}{A}\right)\right) = 2 \tan^{-1}\left(\frac{\omega L}{A}\right) - \pi = -\pi/2. \quad (\text{C.4})$$

By using  $A = Z_0(\omega^2 LC - 1)$ , (C.4) can be rewritten as

$$\omega^2 Z_0 LC \tan\left(\frac{\pi}{4}\right) - \omega L - Z_0 \tan\left(\frac{\pi}{4}\right) = \omega^2 Z_0 LC - \omega L - Z_0 = 0. \quad (\text{C.5})$$

Equation (C.5) is a quadratic equation and can be solved in an analytic way. The following values of  $\omega$  can be found

$$\omega_{1,2}^+ = \frac{\frac{1}{Z_0 C} \pm \sqrt{\frac{1}{(Z_0 C)^2} + \frac{4}{LC}}}{2}. \quad (\text{C.6})$$

Since only positive frequencies are of interest, (C.6) can be reduced to

$$\omega^+ = \frac{\frac{1}{Z_0 C} + \sqrt{\frac{1}{(Z_0 C)^2} + \frac{4}{LC}}}{2}. \quad (\text{C.7})$$

Likewise, the parameter  $A$  is negative for frequencies below the resonance frequency. To determine the angular frequency corresponding to  $\angle \Gamma = +90^\circ (= +\pi/2)$ , (C.3) can be written as

$$\angle \Gamma = \tan^{-1}\left(\frac{\omega L}{A}\right) - \left(\pi - \tan^{-1}\left(\frac{\omega L}{A}\right)\right) = 2 \tan^{-1}\left(\frac{\omega L}{A}\right) + \pi = \pi/2. \quad (\text{C.8})$$

By using  $A = Z_0(\omega^2 LC - 1)$ , (C.8) can be rewritten as

$$\omega^2 Z_0 LC \tan\left(-\frac{\pi}{4}\right) - \omega L - Z_0 \tan\left(-\frac{\pi}{4}\right) = -\omega^2 Z_0 LC - \omega L + Z_0 = 0. \quad (\text{C.9})$$

Equation (C.9) is a quadratic equation and can be solved in an analytic way. The following values of  $\omega$  can be found

$$\omega_{1,2}^- = \frac{-\frac{1}{Z_0 C} \pm \sqrt{\frac{1}{(Z_0 C)^2} + \frac{4}{LC}}}{2}. \quad (\text{C.10})$$



Since only positive frequencies are of interest, (C.10) can be reduced to

$$\omega^- = \frac{-\frac{1}{Z_0 C} + \sqrt{\frac{1}{(Z_0 C)^2} + \frac{4}{LC}}}{2}. \quad (\text{C.11})$$

The resonance frequency  $\omega_0$  is defined as

$$\omega_0 = \frac{1}{\sqrt{LC}}. \quad (\text{C.12})$$

By taking the results of (C.7) and (C.11), the bandwidth and the fractional bandwidth of a lossless AMC can be calculated using

$$\begin{aligned} \Delta\omega &= \omega^+ - \omega^- = \frac{1}{Z_0 C} = \frac{\omega_0^2 L}{Z_0}, \\ \text{BW}_{\text{frac}} &= \frac{\Delta\omega}{\omega_0} = \frac{1}{Z_0 C \omega_0} = \frac{\omega_0 L}{Z_0}. \end{aligned} \quad (\text{C.13})$$



# List of Publications

---

## Journal publications

- [P1] **A. J. van den Biggelaar**, U. Johannsen, P. Mattheijssen and A. B. Smolders, “Improved Statistical Model on the Effect of Random Errors in the Phase and Amplitude of Element Excitations on the Array Radiation Pattern,” in *IEEE Transactions on Antennas and Propagation*, vol. 66, no. 5, pp. 2309-2317, May 2018.
- [P2] Q. Liu, **A. J. van den Biggelaar**, U. Johannsen, M. C. van Beurden and A. B. Smolders, “On-chip Metal Tiling for Improving Grounded mm-Wave Antenna-on-Chip Performance in Standard Low-Cost Packaging,” in *IEEE Transactions on Antennas and Propagation*, vol. 68, no. 4, pp. 2638-2645, April 2020.
- [P3] **A. J. van den Biggelaar**, E. Galesloot, A. C. F. Reniers, A. B. Smolders and U. Johannsen, “Verification of a Contactless Characterization Method for Millimeter-Wave Integrated Antennas,” in *IEEE Transactions on Antennas and Propagation*, vol. 68, no. 5, pp. 3358-3365, May 2020.
- [P4] **A. J. van den Biggelaar**, D. P. P. Daverveld, A. C. F. Reniers, A. B. Smolders and U. Johannsen, “Determining the Input Reflection Coefficient of Integrated Antennas Using Over-the-Air Measurements in Near-Field Conditions,” in *International Journal of Microwave and Wireless Technologies*, accepted for publication.
- [P5] **A. J. van den Biggelaar**, S. J. Geluk, B. F. Jamroz, D. F. Williams, A. B. Smolders, U. Johannsen and L. A. Bronckers, “Accurate Gain Measurement Technique for Limited Antenna Separations,” in preparation.
- [P6] A. Elsakka, A. Farsaei, **A. J. van den Biggelaar**, A. C. F. Reniers, M. N. Johansson, R. Maaskant, U. Johannsen, O. Iupikov, M. Ivashina and A. B. Smolders, “A mm-Wave Phased-Array-Fed Torus Reflector Antenna with  $\pm 30^\circ$  Scan Range for 5G Massive-MIMO Base-Station Applications,” in preparation.

## Conference publications

- [P7] **A. J. van den Biggelaar**, U. Johannsen and A. B. Smolders, “Assessment on the Bandwidth of Artificial Magnetic Conductors for Antenna-on-Chip Applications,” *12th European Conference on Antennas and Propagation (EuCAP 2018)*, London, 2018, pp. 1-5.
- [P8] A. Elsakka, T. A. H. Bressner, **A. J. van den Biggelaar**, A. Al-Rawi, U. Johannsen, M. V. Ivashina and A. B. Smolders, “On the Use of Focal-Plane Arrays in mm-Wave 5G Base Stations,” *12th European Conference on Antennas and Propagation (EuCAP 2018)*, London, 2018, pp. 1-4.
- [P9] **A. J. van den Biggelaar**, U. Johannsen and A. B. Smolders, “Assessment on the Dielectric Losses of Artificial Magnetic Conductors for Antenna-on-Chip Applications,” *48th European Microwave Conference (EuMC 2018)*, Madrid, 2018, pp. 272-275.
- [P10] **A. J. van den Biggelaar**, U. Johannsen and A. B. Smolders, “Angular Stable Artificial Magnetic Conductor for Oblique Incident TM Plane Waves,” *The Loughborough Antennas and Propagation Conference (LAPC 2018)*, Loughborough, 2018, pp. 1-4.
- [P11] **A. J. van den Biggelaar**, U. Johannsen, M. Geurts and A. B. Smolders, “Assessment on the Frequency Dependent Performance of Active Phased Arrays for 5G,” *13th European Conference on Antennas and Propagation (EuCAP 2019)*, Krakow, 2019, pp. 1-4.
- [P12] **A. J. van den Biggelaar**, D. P. P. Daverveld, A. C. F. Reniers, U. Johannsen and A. B. Smolders, “Assessment of a Contactless Characterization Method for Integrated Antennas,” *49th European Microwave Conference (EuMC 2019)*, Paris, 2019, pp. 1016-1019.
- [P13] Y. Aslan, C. E. Kiperly, **A. J. van den Biggelaar**, U. Johannsen and A. Yarovoy, “Passive Cooling of mm-Wave Active Integrated 5G Base Station Antennas Using CPU Heatsinks,” *16th European Radar Conference (EuRAD 2019)*, Paris, 2019, pp. 121-124.
- [P14] **A. J. van den Biggelaar**, C. J. C. Vertegaal, U. Johannsen, M. Geurts and A. B. Smolders, “Post-Manufacturing Calibration Procedure for Medium-Sized Silicon-Based Active Phased Arrays for mm-Wave Wireless Communications,” *14th European Conference on Antennas and Propagation (EuCAP 2020)*, Copenhagen, 2020, pp. 1-5.
- [P15] **A. J. van den Biggelaar**, A. Al-Rawi, U. Johannsen and A. B. Smolders, “64 Element Active Phased Array as Focal Plane Array Feed for Reflector Antennas for mm-Wave Wireless Communications,” *14th European Conference on Antennas and Propagation (EuCAP 2020)*, Copenhagen, 2020, pp. 1-5.
- [P16] **A. J. van den Biggelaar**, B. F. Jamroz, D. F. Williams, A. B. Smolders and U. Johannsen, “Correction of the Measured Phase of the Radiation Pattern of Millimeter-Wave Antennas,” *2020 Antenna Measurement Techniques Association Symposium (AMTA)*, Newport, Rhode Island, 2020, accepted for publication.
- [P17] **A. J. van den Biggelaar**, C. J. C. Vertegaal, U. Johannsen, M. Geurts and A. B. Smolders, “Realization of a 5G Millimeter-Wave Dual-Polarized Active Phased Array,” *2021*

*IEEE-APS Topical Conference on Antennas and Propagation in Wireless Communications (APWC)*, Honolulu, Hawaii, 2021, accepted for publication.

## Other publications

- [P18] **A. J. van den Biggelaar**, A. B. Smolders, C. B. de Paula, D. C. S. de Silva and J. J. Bazzo, *Cognitive Technologies*, “A Fast and Efficient 3D Beamforming Algorithm for Cognitive Radio Networks,” Springer, 2017.
- [P19] U. Johannsen, A. C. F. Reniers and **A. J. van den Biggelaar**, “Wireless testing pick and place probe,” US Provisional Patent, November 2019.



# Bibliography

---

- [1] International Telecommunication Union (ITU), Country ICT Data, “Mobile-cellular subscriptions 2000-2018,” July 2020. [Online]. Available: <https://www.itu.int/en/ITU-D/Statistics/Pages/stat/default.aspx>.
- [2] Ericsson, “Ericsson Mobility Report, November 2019” & “Ericsson Mobility Visualizer,” July 2020. [Online]. Available: <https://www.ericsson.com/en/mobility-report/>.
- [3] J. G. Andrews, S. Buzzi, W. Choi, S. V. Hanly, A. Lozano, A. C. K. Soong and J. C. Zhang, “What Will 5G Be?,” in *IEEE Journal on Selected Areas in Communications*, vol. 32, no. 6, pp. 1065-1082, June 2014.
- [4] NGMN Alliance, “NGMN 5G White paper,” July 2020. [Online]. Available: <https://www.ngmn.org/work-programme/5g-white-paper.html>.
- [5] Huawei Technologies, “White Paper: 5G Network Architecture - A High-Level Perspective,” July 2020. [Online]. Available: <https://www.huawei.com/en/industry-insights/outlook/mobile-broadband/insights-reports/5g-network-architecture>.
- [6] Ericsson, “This is 5G,” July 2020. [Online]. Available: <https://www.ericsson.com/en/5g/what-is-5g>.
- [7] A. Ghosh, A. Maeder, M. Baker and D. Chandramouli, “5G Evolution: A View on 5G Cellular Technology Beyond 3GPP Release 15,” in *IEEE Access*, vol. 7, pp. 127639-127651, 2019.
- [8] 3rd Generation Partnership Project (3GPP), Reference 21.915, “Release 15: 3GPP TR 21.915 V15.0.0,” July 2020. [Online]. Available: <https://portal.3gpp.org/desktopmodules/Specifications/SpecificationDetails.aspx?specificationId=3389>.
- [9] 3rd Generation Partnership Project (3GPP), Reference 38.815, “Release 15: 3GPP TR 38.815 V15.0.0,” July 2020. [Online]. Available: <https://portal.3gpp.org/desktopmodules/Specifications/SpecificationDetails.aspx?specificationId=3298>.
- [10] Y. Liu, X. Chen, Z. Zhong, B. Ai, D. Miao, Z. Zhao, J. Sun, Y. Teng and H. Guan, “Waveform Design for 5G Networks: Analysis and Comparison,” in *IEEE Access*, vol. 5, pp. 19282-19292, 2017.
- [11] A. Hammoodi, L. Audah and M. A. Taher, “Green Coexistence for 5G Waveform Candidates: A Review,” in *IEEE Access*, vol. 7, pp. 10103-10126, 2019.

- [12] E. Bjornson, L. Van der Perre, S. Buzzi and E. G. Larsson, "Massive MIMO in Sub-6 GHz and mmWave: Physical, Practical, and Use-Case Differences," in *IEEE Wireless Communications*, vol. 26, no. 2, pp. 100-108, April 2019.
- [13] S. Rangan, T. S. Rappaport and E. Erkip, "Millimeter-Wave Cellular Wireless Networks: Potentials and Challenges," in *Proceedings of the IEEE*, vol. 102, no. 3, pp. 366-385, March 2014.
- [14] T. A. H. Bressner, A. Farsaei, M. Fozooni, U. Johannsen, M. N. Johansson and A. B. Smolders, "MIMO Performance Evaluation of Isotropic, Directional and Highly-Directional Antenna Systems for mm-Wave Communications," *13th European Conference on Antennas and Propagation (EuCAP 2019)*, Krakow, 2019, pp. 1-5.
- [15] C. Y. Tseng and L. J. Griffiths, "A Simple Algorithm to Achieve Desired Patterns for Arbitrary Arrays," in *IEEE Transactions on Signal Processing*, vol. 40, no. 11, pp. 2737-2746, Nov. 1992.
- [16] J. Ruze, "The Effect of Aperture Errors on the Antenna Radiation Pattern," in *Supplemento Nuovo Cimento*, vol. 9, pp. 364-380, 1952.
- [17] J. L. Allen, "Some Extensions of the Theory of Random Error Effects on Array Patterns," in *Phased Array Radar Studies*, MIT Lincoln Laboratory Technical Report, no. 236, 1961.
- [18] J. K. Hsiao, "Array Sidelobes, Error Tolerance, Gain and Beamwidth," in *NRL Report 8841*, Naval Research Laboratory, 1984.
- [19] J. L. Allen, "Effects of Errors on the Patterns of Arrays," in *The Theory of Array Antennas*, MIT Lincoln Laboratory Technical Report, no. 323, 1963.
- [20] R. E. Collin, *Antenna Theory Part 1*, "Random Errors in Arrays," 1st ed., McGraw-Hill Book Company, 1969.
- [21] R. J. Mailloux, *Phased Array Antenna Handbook*, "Array Error Effects," 2nd ed., Artech House, 2005.
- [22] R. C. Hansen, *Phased Array Antennas*, "Measurements and Tolerances," 2nd ed., John Wiley & Sons, 2009.
- [23] S. O. Rice, "Mathematical analysis of random noise," in *The Bell System Technical Journal*, vol. 24, no. 1, pp. 46-156, Jan. 1945.
- [24] Wolfram MathWorld, "Marcum Q-Function," July 2020. [Online]. Available: <http://mathworld.wolfram.com/MarcumQ-Function.html>.
- [25] P. Beckmann, "Statistical Distribution of the Amplitude and Phase of a Multiply Scattered Field," in *Journal of Research of the National Bureau of Standards*, vol. 66D, no. 3, 1961.
- [26] X. Gu, D. Liu, C. Baks, O. Tageman, B. Sadhu, J. Hallin, L. Rexberg and A. Valdes-Garcia, "A multilayer organic package with 64 dual-polarized antennas for 28GHz 5G communication," *2017 IEEE MTT-S International Microwave Symposium (IMS)*, Honolulu, HI, 2017, pp. 1899-1901.



- [27] B. Sadhu *et al.*, “A 28-GHz 32-Element TRX Phased-Array IC With Concurrent Dual-Polarized Operation and Orthogonal Phase and Gain Control for 5G Communications,” in *IEEE Journal of Solid-State Circuits*, vol. 52, no. 12, pp. 3373-3391, Dec. 2017.
- [28] K. Kibaroglu, M. Sayginer and G. M. Rebeiz, “An ultra low-cost 32-element 28 GHz phased-array transceiver with 41 dBm EIRP and 1.0–1.6 Gbps 16-QAM link at 300 meters,” *IEEE Radio Frequency Integrated Circuits Symposium (RFIC)*, Honolulu, HI, 2017, pp. 73-76.
- [29] R. Valkonen, “Compact 28-GHz phased array antenna for 5G access,” *2018 IEEE MTT-S International Microwave Symposium (IMS)*, Philadelphia, PA, 2018, pp. 1334-1337.
- [30] J. D. Dunworth *et al.*, “A 28GHz Bulk-CMOS dual-polarization phased-array transceiver with 24 channels for 5G user and basestation equipment,” *2018 IEEE International Solid - State Circuits Conference - (ISSCC)*, San Francisco, CA, 2018, pp. 70-72.
- [31] X. Gu, D. Liu, C. Baks, O. Tageman, B. Sadhu, J. Hallin, L. Rexberg, P. Parida, Y. Kwark and A. Valdes-Garcia, “Development, Implementation, and Characterization of a 64-Element Dual-Polarized Phased-Array Antenna Module for 28-GHz High-Speed Data Communications,” in *IEEE Transactions on Microwave Theory and Techniques*, vol. 67, no. 7, pp. 2975-2984, July 2019.
- [32] K. Kibaroglu, M. Sayginer, T. Phelps and G. M. Rebeiz, “A 64-Element 28-GHz Phased-Array Transceiver With 52-dBm EIRP and 8–12-Gb/s 5G Link at 300 Meters Without Any Calibration,” in *IEEE Transactions on Microwave Theory and Techniques*, vol. 66, no. 12, pp. 5796-5811, Dec. 2018.
- [33] M. Stoneback and K. Madsen, “A Planar All-Silicon 256-Element Ka-band Phased Array for High-Altitude Platforms (HAPs) Application,” *2018 IEEE MTT-S International Microwave Symposium (IMS)*, Philadelphia, PA, 2018, pp. 783-786.
- [34] K. Kibaroglu, M. Sayginer and G. M. Rebeiz, “A Low-Cost Scalable 32-Element 28-GHz Phased Array Transceiver for 5G Communication Links Based on a  $2 \times 2$  Beam-former Flip-Chip Unit Cell,” in *IEEE Journal of Solid-State Circuits*, vol. 53, no. 5, pp. 1260-1274, May 2018.
- [35] A. Nafe, M. Sayginer, K. Kibaroglu and G. M. Rebeiz, “ $2 \times 64$  Dual-Polarized Dual-Beam Single-Aperture 28 GHz Phased Array with High Cross-Polarization Rejection for 5G Polarization MIMO,” *IEEE MTT-S International Microwave Symposium (IMS)*, Boston, MA, USA, 2019, pp. 484-487.
- [36] I. Şeker, “Calibration methods for phased array radars,” *Proc. SPIE 8714, Radar Sensor Technology XVII, SPIE Defense, Security, and Sensing*, Baltimore, Maryland, 2013.
- [37] G. A. Hampson and A. B. Smolders, “A fast and accurate scheme for calibration of active phased-array antennas,” *IEEE Antennas and Propagation Society International Symposium. 1999 Digest.*, Orlando, FL, 1999, pp. 1040-1043 vol.2.
- [38] T. Takahashi, Y. Konishi, S. Makino, H. Ohmine and H. Nakaguro, “Fast Measurement Technique for Phased Array Calibration,” in *IEEE Transactions on Antennas and Propa-*

- gation, vol. 56, no. 7, pp. 1888-1899, July 2008.
- [39] H. M. Aumann, A. J. Fenn and F. G. Willwerth, "Phased array antenna calibration and pattern prediction using mutual coupling measurements," in *IEEE Transactions on Antennas and Propagation*, vol. 37, no. 7, pp. 844-850, July 1989.
- [40] H. Chou and D. Cheng, "Beam-Pattern Calibration in a Realistic System of Phased-Array Antennas via the Implementation of a Genetic Algorithm With a Measurement System," in *IEEE Transactions on Antennas and Propagation*, vol. 65, no. 2, pp. 593-601, Feb. 2017.
- [41] D. M. Pozar, *Microwave Engineering*, "Impedance Matching and Tuning," 2nd ed., John Wiley & Sons, 1998.
- [42] J. E. Rayas-Sanchez and V. Gutierrez-Ayala, "A general EM-based design procedure for single-layer substrate integrated waveguide interconnects with microstrip transitions," *2008 IEEE MTT-S International Microwave Symposium Digest*, Atlanta, GA, USA, 2008, pp. 983-986.
- [43] T. Teshirogi, M. Tanaka and W. Chujo, "Wideband circularly polarized array antenna with sequential rotations and phase shifts of elements," *International Symposium on Antennas and Propagation (ISAP85)*, Tokyo, 1985.
- [44] R. J. Mailloux, *Phased Array Antenna Handbook*, "Fundamental Results from Array Theory," 2nd ed., Artech House, 2005.
- [45] G. Gonzalez, *Microwave Transistor Amplifiers - Analysis and Design*, "Stability Considerations," 1st ed., Prentice-Hall, 1984.
- [46] Scythe, "Mugen MAX," July 2020. [Online]. Available: <http://www.scythe-eu.com/en/products/cpu-cooler/mugen-max.html>.
- [47] Dow, "DOWSIL SE 4422," July 2020. [Online]. Available: <https://www.dow.com/en-us/pdp.dowsil-se-4422.02507544z.html>.
- [48] T-Global Technology, "TG-A1250 Ultra Soft Thermal Pad," July 2020. [Online]. Available: <https://www.tglobalcorp.com/tg-a1250-ultra-soft-thermal-conductive-pad>.
- [49] Center for Wireless Technology Eindhoven (CWTe) - Eindhoven University of Technology (TU/e), "Anechoic Chamber," July 2020. [Online]. Available: <https://www.tue.nl/en/research/research-labs/center-for-wireless-technology/>.
- [50] NSI-MI, "Near-Field Systems," July 2020. [Online]. Available: <https://www.nsi-mi.com/products/system-solutions/near-field-systems>.
- [51] C. L. Dolph, "A Current Distribution for Broadside Arrays Which Optimizes the Relationship between Beam Width and Side-Lobe Level," in *Proceedings of the IRE*, vol. 34, no. 6, pp. 335-348, June 1946.
- [52] T. T. Taylor, "Design of line-source antennas for narrow beamwidth and low side lobes," in *Transactions of the IRE Professional Group on Antennas and Propagation*, vol. 3, no. 1, pp. 16-28, Jan. 1955.

- [53] R. J. Allard, D. H. Werner and P. L. Werner, "Radiation pattern synthesis for arrays of conformal antennas mounted on arbitrarily-shaped three-dimensional platforms using genetic algorithms," in *IEEE Transactions on Antennas and Propagation*, vol. 51, no. 5, pp. 1054-1062, May 2003.
- [54] T. Su and H. Ling, "Array beamforming in the presence of a mounting tower using genetic algorithms," in *IEEE Transactions on Antennas and Propagation*, vol. 53, no. 6, pp. 2011-2019, June 2005.
- [55] P. Demarcke, H. Rogier, R. Goossens and P. De Jaeger, "Beamforming in the Presence of Mutual Coupling Based on Constrained Particle Swarm Optimization," in *IEEE Transactions on Antennas and Propagation*, vol. 57, no. 6, pp. 1655-1666, June 2009.
- [56] A. Pirhadi, M. H. Rahmani and A. Mallahzadeh, "Shaped beam array synthesis using particle swarm optimisation method with mutual coupling compensation and wideband feeding network," in *IET Microwaves, Antennas & Propagation*, vol. 8, no. 8, pp. 549-555, 2014.
- [57] S. Liang, T. Feng and G. Sun, "Sidelobe-level suppression for linear and circular antenna arrays via the cuckoo search-chicken swarm optimisation algorithm," in *IET Microwaves, Antennas & Propagation*, vol. 11, no. 2, pp. 209-218, 2017.
- [58] A. Newell, R. Baird and P. Wacker, "Accurate measurement of antenna gain and polarization at reduced distances by an extrapolation technique," in *IEEE Transactions on Antennas and Propagation*, vol. 21, no. 4, pp. 418-431, July 1973.
- [59] H. T. Friis, "A Note on a Simple Transmission Formula," in *Proceedings of the IRE*, vol. 34, no. 5, pp. 254-256, May 1946.
- [60] "IEEE Standard Test Procedures for Antennas," in *ANSI/IEEE Std 149-1979*, ch. 12, pp. 78-98, 1979.
- [61] K. T. Selvan and R. Janaswamy, "Fraunhofer and Fresnel Distances: Unified derivation for aperture antennas," in *IEEE Antennas and Propagation Magazine*, vol. 59, no. 4, pp. 12-15, Aug. 2017.
- [62] R. R. Bowman, "Field strength above 1 GHz: Measurement procedures for standard antennas," in *Proceedings of the IEEE*, vol. 55, no. 6, pp. 981-990, June 1967.
- [63] S. Pivnenko, J.M. Nielsen and O. Breinbjerg, "Using the phase center of a Standard Gain Horn in antenna gain determination," *2008 Antenna Measurement Techniques Association Symposium (AMTA)*, Boston, MA, USA, 2008, pp. 334-340.
- [64] S. Pivnenko and O. Breinbjerg, "Fast and accurate measurement of on-axis gain and on-axis polarization at a finite distance," *7th European Conference on Antennas and Propagation (EuCAP 2013)*, Gothenburg, 2013, pp. 810-814.
- [65] K. Harima, M. Sakasai and K. Fujii, "Determination of gain for pyramidal-horn antenna on basis of phase center location," *2008 IEEE International Symposium on Electromagnetic Compatibility*, Detroit, MI, 2008, pp. 1-5.

- [66] K. Harima, "Accurate gain measurement for millimeter-wave horn and open-ended waveguide antennas," *2012 International Symposium on Antennas and Propagation (ISAP)*, Nagoya, 2012, pp. 1019-1022.
- [67] K. Harima, "Evaluating the effectiveness of applying the phase center for antenna measurements," *2017 IEEE Conference on Antenna Measurements & Applications (CAMA)*, Tsukuba, 2017, pp. 61-64.
- [68] T. W. Hertel, "Phase center measurements based on the three-antenna method," *IEEE Antennas and Propagation Society International Symposium. 2003 Digest.*, Columbus, OH, 2003, pp. 816-819 vol.3.
- [69] A. B. Smolders, A. C. F. Reniers, U. Johannsen and M. H. A. J. Herben, "Measurement and calibration challenges of microwave and millimeter-wave phased-arrays," *2013 International Workshop on Antenna Technology (iWAT)*, Karlsruhe, 2013, pp. 358-361.
- [70] Rohde & Schwarz, "R&S ATS1000 - Brochures and Data Sheets," July 2020. [Online]. Available: <https://www.rohde-schwarz.com/fi/brochure-datasheet/ats1000/>.
- [71] "IEEE Standard for Definitions of Terms for Antennas," in *IEEE Std 145-2013 (Revision of IEEE Std 145-1993)*, pp. 25, 6 March 2014.
- [72] J. Appel-Hansen, "Centers of structures in electromagnetism - a critical analysis," in *IEEE Transactions on Antennas and Propagation*, vol. 30, no. 4, pp. 606-610, July 1982.
- [73] A. J. Yuffa, "On Wacker's Essential Equation in the Extrapolation Measurement Technique," *2019 Antenna Measurement Techniques Association Symposium (AMTA)*, San Diego, CA, USA, 2019, pp. 1-5.
- [74] Flann Microwave, "Standard Gain Horns Series 240," July 2020. [Online]. Available: <https://flann.com/products/antennas/standard-gain-horns-series-240/>.
- [75] NSI-MI, "Waveguide Probes," July 2020. [Online]. Available: <https://www.nsi-mi.com/products/antenna-products/waveguide-probes/>.
- [76] W. T. Slayton, "Design and Calibration of Microwave Antenna Gain Standards," US Naval Research Laboratory, Washington DC, Report 4433, 1954.
- [77] S. Wi, J. Kim, N. Kang, J. Kim, H. Yang, Y. Kim and J. Yook, "Package-Level Integrated LTCC Antenna for RF Package Application," in *IEEE Transactions on Advanced Packaging*, vol. 30, no. 1, pp. 132-141, Feb. 2007.
- [78] M. Fakharzadeh and M. Mohajer, "An Integrated Wide-Band Circularly Polarized Antenna for Millimeter-Wave Applications," in *IEEE Transactions on Antennas and Propagation*, vol. 62, no. 2, pp. 925-929, Feb. 2014.
- [79] B. Cao, H. Wang, Y. Huang, J. Wang and H. Xu, "A Novel Antenna-in-Package With LTCC Technology for W-Band Application," in *IEEE Antennas and Wireless Propagation Letters*, vol. 13, pp. 357-360, 2014.
- [80] S. Liao and Q. Xue, "Dual Polarized Planar Aperture Antenna on LTCC for 60-GHz Antenna-in-Package Applications," in *IEEE Transactions on Antennas and Propagation*, vol. 65, no. 1, pp. 63-70, Jan. 2017.

- [81] M. Sun, Y. P. Zhang, Y. X. Guo, K. M. Chua and L. L. Wai, "Integration of Grid Array Antenna in Chip Package for Highly Integrated 60-GHz Radios," in *IEEE Antennas and Wireless Propagation Letters*, vol. 8, pp. 1364-1366, 2009.
- [82] A. E. I. Lamminen, J. Saily and A. R. Vimpari, "60-GHz Patch Antennas and Arrays on LTCC With Embedded-Cavity Substrates," in *IEEE Transactions on Antennas and Propagation*, vol. 56, no. 9, pp. 2865-2874, Sept. 2008.
- [83] S. Beer, H. Gulan, C. Rusch and T. Zwick, "Coplanar 122-GHz Antenna Array With Air Cavity Reflector for Integration in Plastic Packages," in *IEEE Antennas and Wireless Propagation Letters*, vol. 11, pp. 160-163, 2012.
- [84] E. Herth, N. Rolland and T. Lasri, "Circularly Polarized Millimeter-Wave Antenna Using 0-Level Packaging," in *IEEE Antennas and Wireless Propagation Letters*, vol. 9, pp. 934-937, 2010.
- [85] C. Jin, V. N. Sekhar, X. Bao, B. Chen, B. Zheng and R. Li, "Antenna-in-Package Design Based on Wafer-Level Packaging With Through Silicon Via Technology," in *IEEE Transactions on Components, Packaging and Manufacturing Technology*, vol. 3, no. 9, pp. 1498-1505, Sept. 2013.
- [86] P. H. Park and S. S. Wong, "An on-chip dipole antenna for millimeter-wave transmitters," *2008 IEEE Radio Frequency Integrated Circuits Symposium*, Atlanta, GA, 2008, pp. 629-632.
- [87] B. B. Adela, P. T. M. van Zeijl, U. Johannsen and A. B. Smolders, "On-Chip Antenna Integration for Millimeter-Wave Single-Chip FMCW Radar, Providing High Efficiency and Isolation," in *IEEE Transactions on Antennas and Propagation*, vol. 64, no. 8, pp. 3281-3291, Aug. 2016.
- [88] A. Shamim, M. Arsalan, L. Roy and K. N. Salama, "Co-design of on-chip antennas and circuits for a UNII band monolithic transceiver," *2010 IEEE Antennas and Propagation Society International Symposium*, Toronto, ON, 2010, pp. 1-4.
- [89] Z. Chen, Q. Liu, B. Smolders, P. Baltus and H. Gao, "30-GHz Co-designed Low-Noise Amplifier and Antenna-on-Chip for Wireless Applications," *2019 IEEE International Symposium on Radio-Frequency Integration Technology (RFIT)*, Nanjing, China, 2019, pp. 1-3.
- [90] K. Mohammadpour-Aghdam, S. Brebels, A. Enayati, R. Faraji-Dana, G. A. E. Vandebosch and W. DeRaedt, "RF Probe Influence Study in Millimeter-Wave Antenna Pattern Measurements," in *International Journal of RF Microwave Computer-Aided Engineering*, vol. 21, no. 4, pp. 413-420, 2011.
- [91] J. Murdock, E. Ben-Dor, F. Gutierrez and T. S. Rappaport, "Challenges and approaches to on-chip millimeter wave antenna pattern measurements," *2011 IEEE MTT-S International Microwave Symposium*, Baltimore, MD, 2011, pp. 1-4.
- [92] A. C. F. Reniers, A. R. van Dommele, M. D. Huang and M. H. A. J. Herben, "Disturbing effects of microwave probe on mm-Wave antenna pattern measurements," *8th European*

- Conference on Antennas and Propagation (EuCAP 2014)*, The Hague, 2014, pp. 161-164.
- [93] A. C. F. Reniers, A. R. van Dommele, A. B. Smolders and M. H. A. J. Herben, "The Influence of the Probe Connection on mm-Wave Antenna Measurements," in *IEEE Transactions on Antennas and Propagation*, vol. 63, no. 9, pp. 3819-3825, Sept. 2015.
- [94] Q. Liu, U. Johannsen, M. C. van Beurden and A. B. Smolders, "Antenna-on-Chip Radiation Pattern Characterization - Analysis of Different Approaches," *13th European Conference on Antennas and Propagation (EuCAP 2019)*, Krakow, 2019, pp. 1-5.
- [95] Q. Liu, A. C. F. Reniers, U. Johannsen, M. C. van Beurden and A. B. Smolders, "Influence of on-wafer probes in mm-wave antenna measurements," *12th European Conference on Antennas and Propagation (EuCAP 2018)*, London, 2018, pp. 1-5.
- [96] Q. Liu, A. C. F. Reniers, U. Johannsen, M. C. van Beurden and A. B. Smolders, "Improved Probing Reliability in Antenna-on-Chip Measurements," in *IEEE Antennas and Wireless Propagation Letters*, vol. 17, pp. 1745-1749, Sept. 2018.
- [97] E. Heidrich and W. Wiesbeck, "Features of advanced polarimetric RCS-antenna measurements," *Digest on Antennas and Propagation Society International Symposium*, San Jose, CA, USA, 1989, pp. 1026-1029 vol.2.
- [98] W. Wiesbeck and E. Heidrich, "Wide-band multiport antenna characterization by polarimetric RCS measurements," in *IEEE Transactions on Antennas and Propagation*, vol. 46, no. 3, pp. 341-350, March 1998.
- [99] G. Schone, S. Riegger and E. Heidrich, "Wideband polarimetric radar cross section measurement," 1988 IEEE AP-S. *International Symposium, Antennas and Propagation*, Syracuse, NY, USA, 1988, pp. 537-540 vol.2.
- [100] U. Johannsen, M. Spiritoy and A. B. Smolders, "Contactless measurement method for integrated mm-wave antennas," *5th European Conference on Antennas and Propagation (EuCAP 2011)*, Rome, 2011, pp. 797-801.
- [101] B. Monsalve, S. Blanch, J. Romeu and L. Jofre, "A contact-less small antenna characterization through impedance modulation," *3rd European Conference on Antennas and Propagation (EuCAP 2009)*, Berlin, 2009, pp. 696-698.
- [102] B. Monsalve, S. Blanch and J. Romeu, "Input impedance measurements of cell phone antennas using backscattering modulation," *6th European Conference on Antennas and Propagation (EuCAP 2012)*, Prague, 2012, pp. 1549-1551.
- [103] B. Monsalve, S. Blanch and J. Romeu, "Multiport Small Integrated Antenna Impedance Matrix Measurement by Backscattering Modulation," in *IEEE Transactions on Antennas and Propagation*, vol. 61, no. 4, pp. 2034-2042, April 2013.
- [104] O. Vicencio and J. Romeu, "Application of RCS measurement method for characterization of small antennas," *2008 IEEE Antennas and Propagation Society International Symposium*, San Diego, CA, 2008, pp. 1-4.

- [105] S. Bories, M. Hachemi, K. H. Khelifa and C. Delaveaud, "Small antennas impedance and gain characterization using backscattering measurements," *4th European Conference on Antennas and Propagation (EuCAP 2010)*, Barcelona, 2010, pp. 1-5.
- [106] M. Baba, "Pick and place for automatic test handler," U.S. patent 5290134A, December 3, 1991.
- [107] U. Johannsen, "Technologies for integrated millimeter-wave antennas," PhD thesis, Technische Universiteit Eindhoven, Eindhoven, The Netherlands, 2013.
- [108] H. M. Cheema and A. Shamim, "The last barrier: on-chip antennas," in *IEEE Microwave Magazine*, vol. 14, no. 1, pp. 79-91, Jan.-Feb. 2013.
- [109] Y. P. Zhang and D. Liu, "Antenna-on-Chip and Antenna-in-Package Solutions to Highly Integrated Millimeter-Wave Devices for Wireless Communications," in *IEEE Transactions on Antennas and Propagation*, vol. 57, no. 10, pp. 2830-2841, Oct. 2009.
- [110] M. Nafe, A. Syed and A. Shamim, "Gain enhancement of low profile on-chip dipole antenna via Artificial Magnetic Conductor at 94 GHz," *9th European Conference on Antennas and Propagation (EuCAP 2015)*, Lisbon, 2015, pp. 1-3.
- [111] H. T. Huang, B. Yuan, X. H. Zhang, Z. F. Hu and G. Q. Luo, "A circular ring-shape monopole on-chip antenna with artificial magnetic conductor," *2015 Asia-Pacific Microwave Conference (APMC)*, Nanjing, 2015, pp. 1-3.
- [112] X. Z. Liao, B. Yuan, X. H. Zhang, Z. F. Hu and G. Q. Luo, "Design of a 60GHz Antenna-on-chip with cross-shape Artificial Magnetic Conductor," *2015 Asia-Pacific Microwave Conference (APMC)*, Nanjing, 2015, pp. 1-3.
- [113] A. Barakat, A. Allam, H. Elsadek, A. B. Abdel-Rahman, S. M. Hanif and R. K. Pokharel, "Miniaturized 60 GHz triangular CMOS Antenna-on-Chip using asymmetric artificial magnetic conductor," *2015 IEEE 15th Topical Meeting on Silicon Monolithic Integrated Circuits in RF Systems*, San Diego, CA, 2015, pp. 92-94.
- [114] S. Pan, D. Wang, C. Guclu and F. Capolino, "High impedance layer for CMOS on-chip antenna at millimeter waves," *2011 IEEE International Symposium on Antennas and Propagation (APSURSI)*, Spokane, WA, 2011, pp. 903-906.
- [115] O. Luukkonen, "Artificial Impedance Surfaces," PhD thesis, Helsinki University of Technology, Espoo, Finland, 2009.
- [116] C. R. Simovski, S. A. Tretyakov and P. de Maagt, "Artificial high-impedance surfaces: theoretical analysis for oblique incidence," *IEEE Antennas and Propagation Society International Symposium. Digest. Held in conjunction with: USNC/CNC/URSI North American Radio Sci. Meeting (Cat. No.03CH37450)*, Columbus, OH, 2003, pp. 434-437 vol.4.
- [117] C. R. Simovski, P. de Maagt, S. A. Tretyakov, M. Paquay and A. A. Sochava, "Angular stabilisation of resonant frequency of artificial magnetic conductors for TE-incidence," in *Electronics Letters*, vol. 40, no. 2, pp. 92-93, 22 Jan. 2004.

- [118] C. R. Simovski, P. de Maagt and I. V. Melchakova, "High-impedance surfaces having stable resonance with respect to polarization and incidence angle," in *IEEE Transactions on Antennas and Propagation*, vol. 53, no. 3, pp. 908-914, March 2005.
- [119] A. Presse and A. Tarot, "Circuit Model of a Double-Layer Artificial Magnetic Conductor," in *IEEE Antennas and Wireless Propagation Letters*, vol. 15, pp. 1061-1064, 2016.
- [120] J. McVay, N. Engheta and A. Hoorfar, "High impedance metamaterial surfaces using Hilbert-curve inclusions," in *IEEE Microwave and Wireless Components Letters*, vol. 14, no. 3, pp. 130-132, March 2004.
- [121] A. P. Feresidis, G. Goussetis, S. Wang and J. C. Vardaxoglou, "Artificial magnetic conductor surfaces and their application to low-profile high-gain planar antennas," in *IEEE Transactions on Antennas and Propagation*, vol. 53, no. 1, pp. 209-215, Jan. 2005.
- [122] Q. Liu, Y. Xi, A. C. F. Reniers and A. B. Smolders, "Analysis of the reflection characteristics of a planar EBG structure on lossy silicon substrates," *10th European Conference on Antennas and Propagation (EuCAP 2016)*, Davos, 2016, pp. 1-4.
- [123] C. Y. Tseng, "Minimum variance beamforming with phase-independent derivative constraints," in *IEEE Transactions on Antennas and Propagation*, vol. 40, no. 3, pp. 285-294, March 1992.
- [124] R. C. Hansen, *Phased Array Antennas*, "Linear Array Pattern Synthesis," 2nd ed., John Wiley & Sons, 2009.



# Acknowledgments

---

Time flies when you're having fun! Four years have passed incredibly fast and I've learned so much during this period. It all started with an email I received from Bart Smolders; whether or not I was interested in doing a PhD. I almost replied that I wanted to start working in the industry, but then I thought, a conversation wouldn't hurt. With a lot of skepticism about doing a PhD I entered Bart's office, and I left with a lot of enthusiasm. I could safely say that this was a life-changing conversation and I definitely owe him my gratitude.

I couldn't be more lucky with my daily supervisor Ulf Johannsen. Every meeting was a pleasure and his questions and criticism improved my learning and the quality of my research. Although performing research can sometimes be tough and discouraging, the conversations and discussions with Ulf kept me enthusiastic and motivated every single day.

Another source of motivation and joy was the supervision of bachelor and master students. I look back to all student projects with great satisfaction and I'm grateful for the constructive collaboration I had with every student. In particular, I want to thank Niels Vertegaal, Daan Daverveld and Esmé Galesloot as their work and effort eventually resulted in one (or more) papers.

Of course I want to thank all colleagues (past and present) from the EM group for the great time I had. Having such a fantastic and diverse group of colleagues made me want to go to the university every single day and often resulted in interesting and joyful conversations. I do want to spend some extra words on a few colleagues, however. First off, Suzanne Kuijlaars, thanks for all administrative things you solved and the non-technical chats we had. The first experience I had with creating an antenna was with Ad Reniers during my bachelor end project. This project inspired me as a student to continue learning in the field of antennas. As colleagues, I enjoyed the conversations, technical discussions and collaboration we had in mainly antenna metrology. In the last year of my PhD, I also had the privilege to work with Sander Bronckers on a novel gain measurement technique, as presented in this thesis. I'm looking forward to continue the collaboration with you both in AntenneX.

After I visited some international conferences I realized that having NXP supporting my work did put me in a special position; being able to manufacture the phased array described in this thesis is unique and is often deemed too costly and risky by a lot of universities. This uncommon opportunity allowed me to develop myself in typically unexplored territory

and I want to thank NXP for supporting and funding my PhD project. I want to especially thank Marcel Geurts, Paul Mattheijssen and Johan Janssen for the discussions we had and the support they delivered throughout my project.

In May 2019, I received the exciting news that NIST was able to host me as a guest researcher for a period of six months. Although the coronavirus made me shorten my stay, I had an amazing time in Boulder. I would like to thank Dylan Williams and Kate Remley for making this awesome experience possible. Additionally, Ben Jamroz was of great help in both the technical discussions and making me feel at home during my stay in Boulder. Thanks a lot for that, Ben!

I was not able to write this thesis without the help of Rob Mestrom; thank you for the very clear template that you sent me. I also want to express my gratitude to the committee members and Tom van Nunen as they provided me high-quality reviews that improved the writing and content of this thesis.

At last, but certainly not least, I want to sincerely thank my parents. They fully supported me throughout my studies and always advised me on decisions that sometimes required a different mindset than a technical and rational one. Mam, dad, thanks for everything!

# Curriculum Vitae

---

Antonius Johannes (Teun) van den Biggelaar was born on the 9<sup>th</sup> of March, 1991, in Gemert, the Netherlands. Starting in 2009, he studied electrical engineering at Eindhoven University of Technology (TU/e). As part of his MSc program, he was an intern at Centro de Pesquisa e Desenvolvimento em Telecomunicações (CPqD) in Campinas, Brazil, and he performed his graduation project at ASML in Veldhoven, the Netherlands. In 2016, Teun received his MSc degree with distinction. His MSc thesis was selected as the best MSc thesis of the department of Electrical Engineering in the year 2016.



In 2016, Teun continued his academic career as a Doctoral Candidate in the Electromagnetics group of the department of Electrical Engineering, TU/e. During these four years, he worked on a project supported by NXP Semiconductors in Nijmegen, the Netherlands. The main results of this project are presented in this thesis. In addition to the strong collaboration with NXP, Teun had been a guest researcher at the National Institute of Standards and Technology (NIST) in Boulder, USA, for a period of six months.